

GAZI
JOURNAL OF
ENGINEERING
SCIENCES



GAZI

JOURNAL OF ENGINEERING SCIENCES

YAYIN KOORDİNATÖRÜ / PUBLICATION COORDINATOR

İsmail ŞAHİN

Gazi University, Ankara, Turkey
e-mail: editorgjes@gmail.com

EDİTÖR / EDITOR - IN – CHIEF

İsmail ŞAHİN

Gazi University, Ankara, Turkey
e-mail: editorgjes@gmail.com

YARDIMCI EDİTÖRLER / ASSOCIATE EDITORS

Harun GÖKÇE

Gazi University
e-mail: harungokce@gazi.edu.tr

Murat DÖRTERLER

Gazi University
e-mail: dorterler@gazi.edu.tr

ALAN EDİTÖRLERİ / SECTION EDITORS

Abdullah AKDOĞAN

Pamukkale University

Adem TEKEREK

Gazi University

Alper BÜYÜKKARAGÖZ

Gazi University

Amin MIRZAPOUR

Zanjan İslami Azad University

Ayhan AYTAÇ

National Defense University

Burçin ATILGAN TÜRKMEN

Bilecik Şeyh Edebali University

Bülent ÖZKAN

Gazi University

Erdem CÜCE

Recep Tayyip Erdoğan University

Fecir DURAN

Gazi University

Fatih ŞAHİN

Gazi University

G. Serdar TOMBUL

ASELSAN

Halil KARAKOÇ

Hacettepe University

Hüseyin GÖKÇE

Çankırı Karatekin University

Karolos J. KONTELEON

Aristotle University of Thessaloniki

M. Fatih IŞIK

Hitit University

M. Hanefi CALP

Karadeniz Technical University

M. Serkan YILDIRIM

Gazi University

Mustafa BOZ

Karabük University

Mustafa GÜNAY

Karabük University

Neslihan TOP

Gazi University

Nurullah YÜKSEL

Gazi University

Serhat KARAP

TUBİTAK-SAGE

Shaik SABOOR

Vellore Institute of Technology

Tayfun MENLİK

Gazi University

Umit ATİLA

Gazi University

Majid MEGHDADI

University of Zanjan, Iran

GAZI

JOURNAL OF ENGINEERING SCIENCES

YAYIN DANIŞMA KURULU / ADVISORY BOARD

Adnan SÖZEN

Gazi University, Turkey

Andrew PINKERTON

Lancaster University, England

Bekir Sami YILBAŞ

King Fahd University, Sudia Arabia

Farzollah MIRZAPOUR

University of Zanjan, Iran

Herbert M. REYNOLDS

Michigan State University, USA

Jamal KHATIB

University of Wolverhampton, England

John KINUTHIA

University of South Wales, England

Jonathan C. BORG

University of Malta, Malta

Hossam KISHAWY

University of Ontario Technology, Canada

Kürşad SEZER

Gazi University, Turkey

Mustafa KURT

Gazi University, Turkey

Reza Negarastani

RIETEX, England

Salman NISARNational University of Sci. and Tech.,
Pakistan**Shahin JALILI**

Tebriz University, Iran

Şakir TAŞDEMİR

Selçuk University, Turkey

Tahsin Tecelli ÖPÖZ

John Moores University, England

Yasir JOYA

GIK Institute, Pakistan

DİL EDİTORLERİ / LANGUAGE EDITORS

Türkçe/Turkish: V. Savaş YELOK (Hacı Bayram Veli University)**İngilizce/English:** H. Kürşad SEZER (Gazi University)

TEKNİK EDİTÖR / TECHNICAL EDITOR

Mert Efe CEYLANe-mail: editorgjes@gmail.com

BU SAYININ HAKEMLERİ / REVIEWER OF THIS ISSUE

Abdullah Beyaz	Mert Bekir Atsever
Bülent Özkan	Nuri Alper Metin
Emine Uçar	Onur Denizhan
Emre Alvur	Orhan Kaplan
Erman Kadir Öztekin	Serkan Savaş
Ferhat Atasoy	Tamer Güçlü
Gözde Altuntaş	Yavuz Ateş
Gültekin Uzun	Yunus Kayır
Harun Şen	Özlem Türkşen
Kemal Aydın	İbrahim Karademir
Mehmet Şimşek	İsmail Altın
Mehmet Fatih Işık	Şekip Esat Hayber



GAZİ

JOURNAL OF ENGINEERING SCIENCES

Gazi Journal of Engineering Sciences has been published three issues per year

CORRESPONDENCE ADDRESS :

Gazi Akademik Yayıncılık
Mustafa Kemal Mah. 2118 Cad. No:4C/140 Çankaya/Ankara
Tel: +90-312-9113311 Fax: +90-312-9113312
e-mail: editorgjes@gmail.com

GAZİ

JOURNAL OF ENGINEERING SCIENCES

İÇİNDEKİLER / CONTENTS

Dört Çubuk Mekanizmasında Bir Biyel Noktasında Sabit Hız Elde Etmeye Yönelik Bir Çalışma: Modellemesi, Sayısal Simülasyonu ve Deneysel Uygulaması

A Study on Four-Bar Mechanism with Constant Coupler Point Velocity: Modelling, Numerical Simulation and Experimental Application

Halit HULAKO, Orhan ÇAKAR1-15

Kredi Kartı Müşteri Kaybının Makine Öğrenmesi Yöntemleri Kullanılarak Tahmin Edilmesi

Predicting of Credit Card Customer Churn Using Machine Learning Methods

M. Hanefi CALP16-34

Grafen ve MWCNT Nanoparçacık Katkılı Poliüretan Yapıştırıcı ile Birleştirilmiş Epoksi Bazlı Karbon Fiber Takviyeli Kompozit Levhaların Tek Taraflı Bindirmeli Bağlantılarının Mekanik Özellikleri

Mechanical Properties of SLJs with Graphene and MWCNT Nanoparticle-Doped Hybrid Polyurethane Adhesives on Epoxy-Based Carbon Fiber Reinforced Composite Plates

Mehmet TONGUR, Necati ATABERK35-47

Makine Öğrenmesi Algoritmaları ile Şifreli Trafik Sınıflandırılması

Classification of Encrypted Traffic with Machine Learning Algorithms

Nur Betül DEMİREL, Aydın ERDEN48-68

Yapay Arı Kolonisi ve JAYA Algoritmaları Kullanarak Dağıtık Üretimin Optimal Yerleşimi ve Boyutlandırılması

Optimal Location and Sizing of Distributed Generation Using Artificial Bee Colony and JAYA Algorithms

Salih ERMİŞ, Oğuz TAŞDEMİR69-82

Hourly Analysis Program Kullanarak Net Sıfır Enerji Binası İçin Enerji Analizi: Bağdat'ta Bir Konut Binası Üzerine Bir Vaka Çalışması

The Energy Analysis for Net Zero Energy Building Using Hourly Analysis Program: A Case Study of a Residential Building In Baghdad

Lara Raad Jawad AL-SHAMMARİ, Mutlu TEKİR83-103

Radial Sistemde Aşırı Akım Rölesi Koordinasyonu için Geçiş Arama Optimizasyonu ve Parçacık Sürüsü Optimizasyonunun Karşılaştırmalı Performans Analizi

Comparative Performance Analysis of Transit Search Optimization and Particle Swarm Optimization for Overcurrent Relay Coordination in Radial System

İbrahim ARSLANOĞLU, Fatih Mehmet NUROĞLU, İsmail Hakkı ALTAŞ104-120

Karbon Yakalamada Nanoparçacık Katkılanmış MOF Kompozit Gömülü Karma Matris Membranların Uygulanması

Application of Nanoparticle-Doped MOF Composite-Embedded Mixed Matrix Membranes in Carbon Capture

Özge ÖSTÜRK SÖMEK121-134

GAZİ**JOURNAL OF ENGINEERING SCIENCES**

Rulman Üretimi Yapan Bir Firmada Orta Dönem Kapasite Planlama İçin Çok Amaçlı Matematiksel Model Önerisi

Multiobjective Mathematical Model Proposal For Mid-Term Capacity Planning In A Bearing Manufacturing Company

Begüm POLAT, Esra DİNLER, Alptekin DEMİRAY.....135-152

Tarım Araçları için Çok-Antenli RTK/GNSS, Taktiksel-Sınıf ve Düşük-Bütçeli IMU ile Yön Tahmini

Heading Estimation for Agricultural Vehicles with Multi-Antenna RTK/GNSS, Tactical-Grade and Low-Cost IMUs

Hasan DİLMAC, Veli ILCİ, Emirhan KAYA.....153-166

Taguchi Yöntemi ile 3B Baskılı PETG Bal Peteği Yapılarında Çekme Özelliklerinin Optimizasyonu: Hücre Boyutu ve Geometrik Yönelimin Etkisi

Optimization of Tensile Properties in 3D-Printed PETG Honeycomb Structures via Taguchi Method: Influence of Cell Size and Geometric Orientation

Ahmet Fatih YILMAZ.....167-178

GAZİ

JOURNAL OF ENGINEERING SCIENCES

A Study on Four-Bar Mechanism with Constant Coupler Point Velocity: Modelling, Numerical Simulation and Experimental Application

Halit Hülako^a, Orhan Çakar^b

Submitted: 30.10.2024 Revised: 10.02.2024 Accepted: 14.10.2025 doi:10.30855/gmbd.070525N01

ABSTRACT

In industry, the trace path of a point on the coupler link of four-bar mechanism is often utilized and sometimes it is desired that the coupler point moves on its path with constant velocity. This can be achieved by a variable crank speed. Processes requiring constant speed are often achieved by designing expensive complex mechanisms with high degrees of freedom without feedback control. This study considers the four-bar mechanism driven by a DC motor with constant coupler point velocity. MATLAB[®] is used to model and to simulate the system dynamics. We have successfully implemented an experimental application of coupler point speed control, a mechanism that is much needed in the industry, at a remarkably low cost. We developed a highly detailed simulation model that incorporates intricate system dynamics including bearing frictions. Additionally, motor parameters are predicted for the application through cost-effective estimation techniques. In order to show the efficiency of the method, some experimental studies are made besides the numerical simulations and the results are compared. Proportional plus integral plus derivative (PID) control action is used to control of the crank speed and it is shown that the desired coupler point velocity is achieved.

Keywords: Coupler Point, Four-Bar Mechanism, Crank Speed Control, Simscape Multibody Model

^a Hakkari University,
Engineering Faculty,
Dept. of Mechanical Engineering
30000 - Hakkari, Türkiye
Orcid: 0000-0001-8194-5433
e mail: halithulako@hakkari.edu.tr

^b Firat University,
Engineering Faculty,
Dept. of Mechanical Engineering
23000 - Elazığ, Türkiye
Orcid: 0000-0001-6947-3875
e mail: cakaro@firat.edu.tr

^{*}Corresponding author:
halithulako@hakkari.edu.tr

Dört Çubuk Mekanizmasında Bir Biyel Noktasında Sabit Hız Elde Etmeye Yönelik Bir Çalışma: Modellemesi, Sayısal Simülasyonu ve Deneysel Uygulaması

ÖZ

Endüstride, dört çubuklu bir mekanizmanın biyel kolundaki bir noktanın izlediği yol sıklıkla kullanılmakta ve bazen bu biyel noktasının yörüngesi üzerinde sabit hızla hareket etmesi istenmektedir. Bu, değişken krank hızı ile sağlanabilir. Sabit hız gerektiren süreçler, genellikle geri besleme kontrolü olmaksızın yüksek serbestlik derecesine sahip pahalı ve karmaşık mekanizmalar tasarlanarak gerçekleştirilir. Bu çalışma, biyel noktasının sabit hızını sağlamak üzere bir DC motoru tarafından tahrik edilen dört çubuklu bir mekanizmayı ele almaktadır. Sistem dinamiklerini modellemek ve simüle etmek için MATLAB[®] kullanılmıştır. Sanayinin büyük ölçüde ihtiyaç duyduğu biyel noktası hız kontrolünün deneysel bir uygulaması, dikkate değer derecede düşük bir maliyetle başarıyla gerçekleştirilmiştir. Detaylı bir simülasyon modeli geliştirilmiş ve bu model, yatak sürtünmeleri gibi karmaşık sistem dinamiklerini içermektedir. Ayrıca, uygulama için gerekli olan motor parametreleri, tahmin yöntemleriyle belirlenmiştir. Yöntemin etkinliğini göstermek için sayısal simülasyonların yanı sıra bazı deneysel çalışmalar yapılmış ve sonuçlar karşılaştırılmıştır. Krank hızını kontrol etmek için oransal, integral ve türev (PID) kontrol yöntemi kullanılmış ve istenilen biyel nokta hızının elde edildiği gösterilmiştir.

Anahtar Kelimeler: Biyel Noktası, Dört Çubuk Mekanizması, Krank Hız Kontrolü, Simscape Multibody Model

1. Introduction

Mass production machines generally have requirements such as high production speed, constant speed, product specific process trajectories and low cost. Four-bar mechanisms are widely used in industry and are classified as motion, function, or path generation based on requirements [1]. The mechanisms are designed assuming that the input link, i.e. crank, rotates at a constant speed. However, even if a constant voltage is supplied to the motor driving the crank of the four-bar mechanism, fluctuations occur around the desired speed of the crank due to the dynamics of the mechanism itself. To partially eliminate these speed fluctuations, a flywheel can be added to the crank mechanically. However, today, this is not sufficient, especially due to the need to use high-speed, light and flexible mechanisms. With the development of measurement tools and control engineering, these speed fluctuations can be eliminated more effectively by controlling the motor that drives the mechanism. For this purpose, the crank speed is measured instantaneously and compared with the reference value and the appropriate control signal is generated according to the present error and applied to the motor driving the mechanism to eliminate the speed fluctuation. Tao and Sadler [2] tried to eliminate the speed fluctuations occurring in the crank speed of a four-bar mechanism driven by a direct current (DC) electrical motor by implementing the well-known proportional plus integral plus derivative (PID) control action-based algorithms. Other control techniques, such as fuzzy logic [3], sliding mode control [4], moving sliding mode control [5], backstepping control [6], and a combination of these techniques [7,8], have also been used for the same purpose. Four-bar mechanisms that generate path are commonly used in the industry. These mechanisms typically utilize a point on the link, known as the coupler, and the path traced by this point is referred to as coupler curves. Fig. 1a shows the kinematic diagram of the four bar path generating mechanism and Fig. 1b shows the trajectory drawn by point C on the coupler link. The third link, or coupler, which connects the links 2 and 4 to each other, creates different curves based on the geometric position of the point C on it. When the input link is moves at a constant speed, the velocity of coupler point varies along the trajectory it follows, depending on the link lengths and the geometric position of C. In the industry, there are situations where it is desired that this point moves at a constant velocity in a specific portion or throughout the entire trajectory it follows. Designing mechanisms that can provide a constant speed in a specific region is possible [9,10]; however, due to the dynamics of the mechanism, this cannot be achieved accurately without control. While measuring the crank speed is easy in real applications, measuring the speed of a point moving along a trajectory is quite challenging and costly. In this regard, ensuring that the coupler point follows the trajectory at a constant speed can be achieved with a variable crank speed. This can be achieved by controlling the motor that drives the mechanism. For this purpose, a variable crank speed profile can be obtained from the kinematic relationship between the velocity of the coupler point and the crank speed. This velocity profile can be used as a reference to control the crank speed. Peón-Escalante et al. [11] tried to control the speed of the crank in a four-bar mechanism to ensure that a point on the coupler moves at a constant speed on the trajectory it follows. For this purpose, the dynamics of the four-bar mechanism driven by a DC motor were obtained analytically and the desired variable crank speed was tried to be achieved with the PID algorithm. Then Bañuelos et al. [12] presented their experimental studies on the same problem. In their work, they determined the velocity of the coupler point using real-time camera images and employed a PID control algorithm. Recently, Peón-Escalante et al. [13] applied Artificial Neural Network (ANN) based PID control scheme to the same problem. Denizhan and Chew explored linkage mechanisms for automotive applications, emphasizing the role of optimized spring configurations to reduce the force required to open and maintain hood positions. Their findings showed that extension and compression springs could effectively balance the hood while allowing ease of use [14]. The usual way of analysing mechanisms is to derive mathematical model of the system and solve them by numerical methods. However, especially for complex dynamic systems with high degrees of freedom, analyzing dynamics can be challenging. Another way to solve dynamic problems is through commercial simulation programs. MATLAB® provides a wide environment for such studies. With MATLAB® SIMULINK®, both the control structure and the dynamic model can be created and executed in the same environment using block structures. Multibody Simulation (MSM) formulates and solves the equation of motion after modeling the system with blocks such as forces, sensors, joints, and links [15]. This allows researchers to focus on their main studies without the need to derive the complex dynamic equations of the mechanism. For example, the complete dynamics of the robotic mechanism with 26 degrees of freedom were modelled by using MSM in [16]. The present study considers the problem of maintaining constant speed motion along the trajectory of a point on the coupler in a four-bar mechanism driven by a DC motor (see Fig. 1b). The MSM interface is used to model the dynamics of the system consisting DC motor-gearbox-four-bar linkage. However, the friction in the joints that has not been considered in other studies was taken into account. The crank speed was controlled using PID control technique with reference to the obtained variable crank speed profile for a specified coupler point velocity. In order to show the efficiency of the method, some

experimental case studies are made besides the numerical simulations. In the next section, the kinematic relationship between the velocity of the coupler point and the crank speed is determined. Then the system is modelled by using MSM tool and the numerical simulations and experimental case studies are given for the specific coupler point velocities with comparison. Subsequently, the results are discussed.

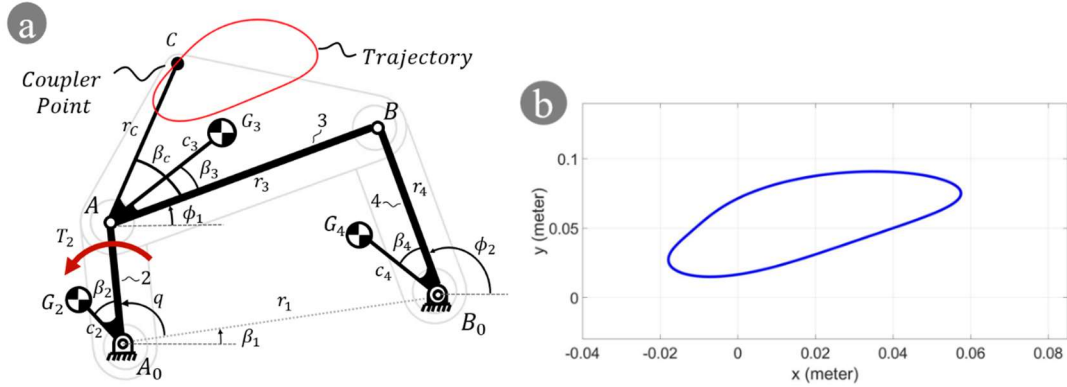


Fig. 1. (a) Kinematic diagram of the four-bar mechanism and (b) the tracking path of point C on the coupler link

2. Kinematic Modeling of System

In this section, the relationship between the coupler point velocity and the crank angular velocity is derived. The vector loop equation of the four-bar linkage mechanism given in Fig. 1a is:

$$\mathbf{A_0A} + \mathbf{AB} = \mathbf{A_0B_0} + \mathbf{B_0B} \quad (1)$$

and it can be written in the polar form as,

$$r_2 e^{iq} + r_3 e^{i\phi_1} = r_1 + r_4 e^{i\phi_2} \quad (2)$$

Two scalar equations can be written from Eq. (2) using Euler identity as follows:

$$f_1(q, \phi_1, \phi_2) = r_2 \cos q + r_3 \cos \phi_1 - r_1 - r_4 \cos \phi_2 = 0 \quad (3)$$

$$f_2(q, \phi_1, \phi_2) = r_2 \sin q + r_3 \sin \phi_1 - r_4 \sin \phi_2 = 0 \quad (4)$$

where r_i ($i=1,2,3,4$) represents length of links, q is position of input crank and ϕ_i , $i=1,2$ are positions of other links. For given q , ϕ_1 and ϕ_2 can be found by solving nonlinear equations given by Eq.(2) or Eqs.(3,4).

On the other hand, the angular velocities of links 2 and 3 $\dot{\phi}_1$ and $\dot{\phi}_2$ depending on the crank angular velocity \dot{q} are given as follows:

$$\dot{\phi}_1 = g_1 \dot{q}, \quad \dot{\phi}_2 = g_2 \dot{q} \quad (5)$$

where g_1 and g_2 are named as velocity influence coefficients and they are calculated as follows:

$$\mathbf{g} = -\mathbf{J}^{-1} \mathbf{f}' \quad (6)$$

where the bold characters are vectors and matrices and \mathbf{J} is Jacobian matrix, \mathbf{g} is velocity influence coefficients vector and \mathbf{f}' is the derivative of the constraint equations Eqs.(3,4) according to the input variable q and written in the form as:

$$\mathbf{g} = \{g_1, g_2\}^T, \mathbf{f}' = \left\{ \frac{\partial f_1}{\partial q}, \frac{\partial f_2}{\partial q} \right\}^T \quad (7)$$

$$J_{ij} = \frac{\partial f_i}{\partial \phi_j}, (i, j = 1, 2) \quad (8)$$

For the four-bar linkage \mathbf{J} ve \mathbf{f}' are given as follows [5]:

$$\mathbf{J} = \begin{bmatrix} -r_3 \sin \phi_1 & r_4 \sin \phi_2 \\ r_3 \cos \phi_1 & -r_4 \cos \phi_2 \end{bmatrix}, \mathbf{f}' = \begin{Bmatrix} -r_2 \sin q \\ r_2 \cos q \end{Bmatrix} \quad (9)$$

Solving Eq.(6) the velocity influence coefficients of four-bar linkages can be found as follows:

$$g_1 = -\frac{r_2 \sin(q - \phi_2)}{r_3 \sin(\phi_1 - \phi_2)} \quad (10)$$

$$g_2 = -\frac{r_2 \sin(q - \phi_1)}{r_4 \sin(\phi_1 - \phi_2)} \quad (11)$$

The next step is to express the angular velocity of the input crank \dot{q} depending on the velocity of the coupler point V_C . The position vector of the coupler point can be written in the polar form as:

$$\mathbf{A}_0 \mathbf{C} = \mathbf{A}_0 \mathbf{A} + \mathbf{A} \mathbf{C} \quad (12)$$

$$r_C = r_2 e^{iq} + r_C e^{i(\phi_1 + \beta_C)} \quad (13)$$

and the time derivative of Eq.(13) gives the coupler point velocity:

$$V_C = ir_2 \dot{q} e^{iq} + ir_C \dot{\phi}_1 e^{i(\phi_1 + \beta_C)} \quad (14)$$

and the real and imaginary parts are

$$V_C^x = -r_2 \dot{q} \sin q - r_C \dot{\phi}_1 \sin(\phi_1 + \beta_C) \quad (15)$$

$$V_C^y = r_2 \dot{q} \cos q + r_C \dot{\phi}_1 \cos(\phi_1 + \beta_C) \quad (16)$$

Finally, the angular velocity of the input crank can be found as follows:

$$\dot{q} = \sqrt{\frac{(V_C^x)^2 + (V_C^y)^2}{r_2^2 + r_C^2 g_1^2 + 2r_2 r_C g_1 \cos(q - \phi_1 - \beta_C)}} \quad (17)$$

The Eq.(17) gives the variable crank velocity for the given value of $V_C = \sqrt{(V_C^x)^2 + (V_C^y)^2}$ and it is reference for the control algorithm. Although the value of V_C is taken as constant during the trajectory in this study, it can be considered as partially constant or fully variable. It should be noted that, the necessary position and velocity values for the control will be determined by the mechanism model created in MSM environment, in this study. In the next section, the modelling of the linkage and control system in SIMULINK is given.

3. Modelling the System via MSM

The motion analysis is made in order to understand dynamic behaviour of a machine under the known external forces. This analysis is also called as forward dynamics or Wittenbauer's first problem. For this analysis, it is needed to derive equation of motion of the machine under consideration, first. There is a number of different ways to accomplish this, for example Exergian equation of motion for single degree of freedom

machines, and Lagrange Equations for single or multiple degree of freedom systems. On the other hand, today there are many commercial analysis programs and these offer researchers the opportunity to analyse without deriving the equation of motion. MATLAB® SIMULINK is a widely used tool where the system is simply modelled with blocks and connections. The mechatronic system under consideration in this study includes the four-bar linkage, DC motor-gearbox and the controller. The main block structure created in MSM is given in Fig.(2). The four-bar mechanism block has one input and four outputs. Input is DC motor torque and outputs are the position of links and the speed of crank. These outputs are the inputs of controller block. The controller block generates the control signal by comparing desired and present value of the crank speed. The DC motor block generates the control torque depending on the control signal and this torque drives the crank of mechanism from the torque input. In the next subsections, the detailed block structures of mechanism, DC motor with gearbox and controller are given.

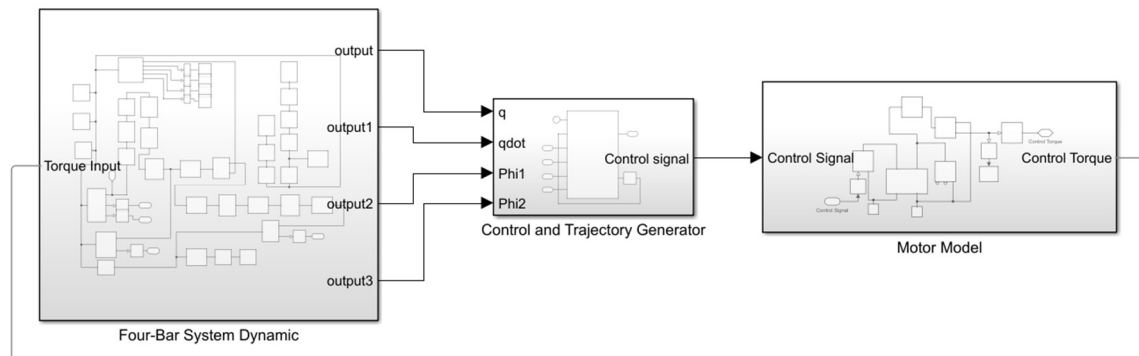


Fig. 2. Simulink® main model structure of a four-bar mechanism that follows a variable speed trajectory with DC motor control

3.1. Four-bar linkage model in MSM

The SIMULINK® block model of the four-bar linkage is shown in Fig.(3). Four-bar linkage consists of four rigid bodies (links) and four revolute joints. The rigid links can be created by using computer aided design (CAD) programs as well as using SIMULINK® library. The mass, mass moment of inertia, and mass centre of the linkage elements' physical parameters are automatically generated once the material parameters are defined. The revolute joints are defined between two links. The rigid transform blocks are used to define the position of the joints on the links taking the local coordinate of the relevant rigid link as reference. The damping and stiffness properties of joints can be defined in the joint blocks. However, the position and velocities of the links and the reaction forces in the joints during the motion can be determined from the joint blocks. For example, the outputs q and ω in the revolute joint 1-2 block are the angular position and the angular velocity of the link 2, respectively. In addition, the inner and outer ring bearing blocks are defined between the joint and the adjacent link compatible with the experimental case in this study. However, the frame of experimental system, DC motor body and couplings are transferred to SIMULINK model from CAD. It should be noted that Ports B and F are frame ports they represent the base and follower frames, respectively.

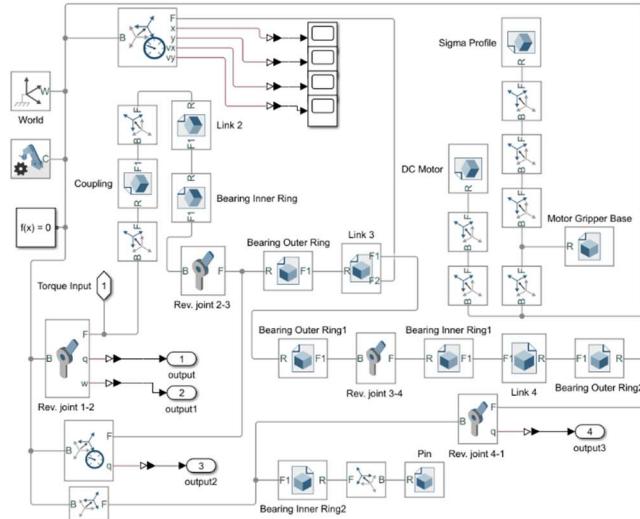


Fig. 3. Block diagram of the four-bar system dynamics subsystem

3.2. DC motor model in MSM

In this study it is considered that the mechanism is driven by a DC motor and a gear box as shown in Fig.(4). DC motor input voltage V_a , the torque generated by motor T_m and the torque at output of gearbox T_2 are given by Eqs.(18-20), respectively [2-5].

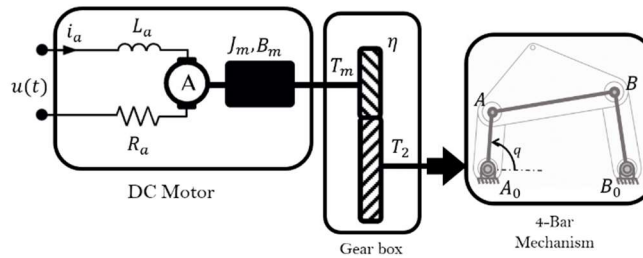


Fig. 4. DC motor-gearbox-four bar mechanism model

$$V_a = R_a i_a + L_a \frac{di_a}{dt} + nK_g \dot{q} \tag{18}$$

$$T_m = K_m i_a \tag{19}$$

$$T_2 = n(-nJ_m \ddot{q} - nB \dot{q} + T_m - T_f) \tag{20}$$

The definition of symbols used in Eqs.(18-20) are given as follows

Symbol	Unit	Description
R_a	Ω	Armature resistance
L_a	Henry	Armature inductance
i_a	A	Armature current
K_g	V-s	Motor voltage constant
n	-	Gear ratio
K_m	Nm/A	Motor torque constant
T_f	Nm	Lost torque due to friction in brushes, bearings, gearbox and so on.
J_m	kg-m ²	Mass moment of inertia of the rotor
B	Nm-s	Viscous damping coefficient in the bearings

DC Motor model is ready in SIMULINK® as a block and it is shown in Fig.(5) including gearbox block. All of the motor parameters defined above are set in the DC motor block. Input of the block is the control voltage and the output is the control torque. The torque is measured by a torque sensor at output of gearbox block.

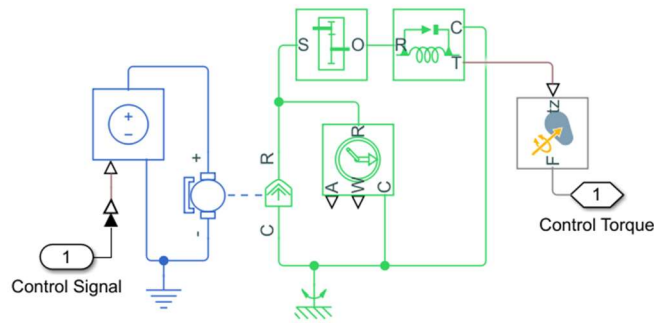


Fig. 5. DC Motor and gearbox block diagram

It should be stated that, MATLAB® Parameter Estimation toolbox can be used to estimate the actual DC motor parameters. The experimental performance outputs, such as the voltage and speed of the motor, are used to determine the motor parameters. DC motor parameters used in this study are determined MATLAB toolbox and then they are used in the simulations.

3.3. Speed trajectory generator and control

The control structure of the DC motor-four bar linkage is shown in Fig.(6). V_C^{des} is the desired velocity of the coupler point. The constant velocity of the coupler point is achieved with variable crank speed. The crank speed trajectory \dot{q}_{trj} is generated by using Eq.(17) where the necessary position parameters (q, ϕ_1, ϕ_2) are taken from the four-bar linkage block. However, the instantaneous speed of the crank \dot{q} is feed back to calculate speed error and the control signal $u(t)$ is generated by the controller. In this study PID controller is considered and the control signal is defined as

$$u(t) = K_p e(t) + K_d \frac{de(t)}{dt} + K_i \int_0^t e(t) dt \tag{21}$$

where K_p , K_d and K_i proportional, derivative and integral gains respectively, and $e(t)$ is the speed error defined as follows:

$$e(t) = \dot{q}_{trj} - \dot{q} \tag{22}$$

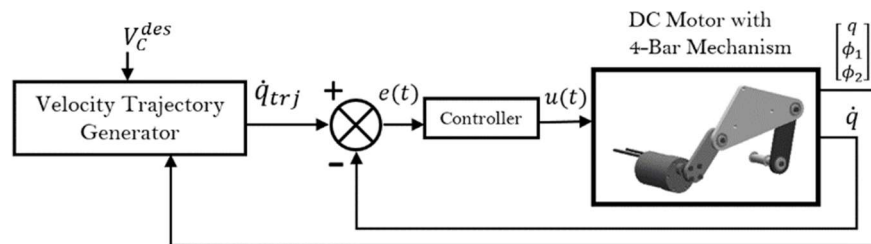


Fig. 6. The control structure of the DC motor-gearbox-four bar linkage

A MATLAB® function is prepared for the speed trajectory generator and the controller as a function block in MSM and given in Fig.(7).

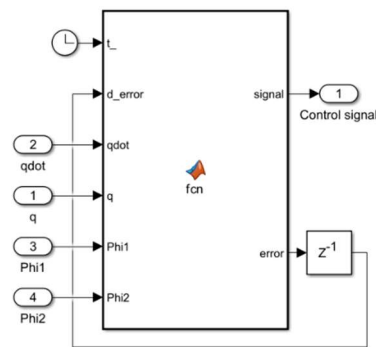


Fig. 7. The function block including trajectory generator and controller

In this way, the mechatronic system consists of DC motor-gearbox-fourbar linkage is modelled in MSM without deriving the complex equations of motions. In this study, some numerical simulations and experimental case studies have been made and the results are given in the followed two sections, respectively. In the applications, two different four-bar linkages named Model-1 and Model-2 are used. In the Model-2, the mass properties of the link 3 are changed in order to show the performance of the method. For the experimental studies, two four-bar mechanisms driven by a DC-Motor is manufactured and the same linkage and DC-motor parameters are used in both the numerical simulation and the experimental case studies.

4. Numerical Simulation

The parameters of Model-1 four-bar linkage and DC-motor used in the simulation are given in Table 1 and Table 2 respectively. 3D solid model of the four-bar linkage was created via SolidWorks and it is transferred to the Simscape as shown in Fig. 8. There is a gearbox with 1:50 gear ratio at the motor output. However, in the joints of the experimental system, the roller bearings with mass of 40 g are used and the mass of them are considered in the simulations. Also, the viscous friction in bearings is considered in the simulations. The viscous friction coefficient is determined by experimentally as $0.000745 \text{ Nm}/(\text{rad}/\text{sec})$. For this, one of the link is subjected to the free vibration like a pendulum while other link is fixed and the damping coefficient is determined from logarithmic decrement.

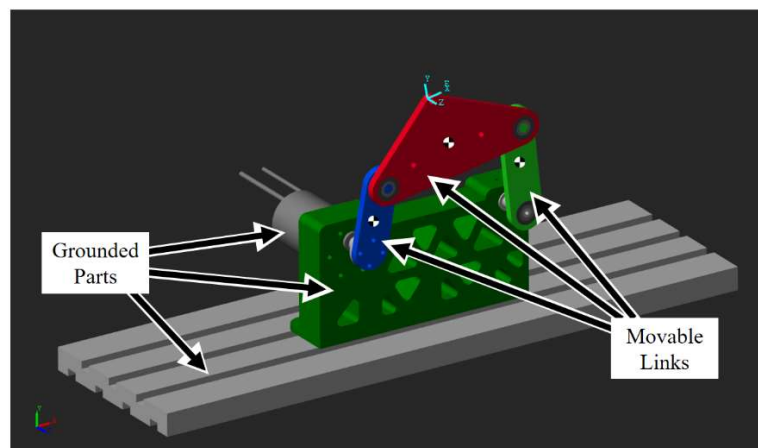


Fig. 8. 3D solid model of the four-bar linkage

Table 1. Four-bar linkage parameters

Mechanism parameters				
Parameters	Model 1-Link no (i)			
	1	2	3	4
r_i (mm)	108.91	42.26	96.44	58.78
c_i (mm)		21.13	0.04781	29.39
m_i (kg)		0.0461	0.1438	0.0546
J_i (kg-m ²)		1.55e-5	0.000125	2.91e-05
β_i (rad)	0.0	0.0	0.2268	0.0
β_c (rad)	r_c (mm)			
0.8318	58.11			

Table 2. DC motor parameters

DC Motor parameters						
R	L	K_m	K_g	J_m	T_f	B
(Ω)	(H)	(Nm/A)	(Vs)	(kgm ²)	(Nm)	(Nms)
4.2602	0.0538	0.0021	6.9724e-4	1.1236e-6	0.00	9.5486e-7
		Speed (rpm)	Voltage	Current		
Power (kW)	Torque (Nm)	(Gearbox output)	(V)	(A)		
0.04	1.47	330	12	<6.0		

The simulations are made for the constant coupler point velocities $V_c^{des} = 0.1$ and $V_c^{des} = 0.2$ m/sec. m/sec. PID parameters for Model 1 mechanism are determined by trial and error $K_p = 3.7$, $K_i = 7$ and $K_d = 2$, as this approach allowed practical tuning for desired performance. However, methods like pole placement could also be considered for systematic tuning to ensure stability across various operating conditions. The simulations are run for 5 seconds using the chosen Ode4 (Runge-Kutta) solver with a fixed time step of 0.0001 seconds. The comparison of the desired and calculated (measured) angular velocity trajectories and the crank velocity errors for the cases $V_c^{des} = 0.1$ m/sec and $V_c^{des} = 0.2$ m/sec are given in Fig. 9 and Fig. 10, respectively. It is seen that the desired and measured crank velocities match each other well along the entire trajectory, and the error for both cases are under 0.1 rad/sec after 1.5 sec and they tend to decrease over time due to control.

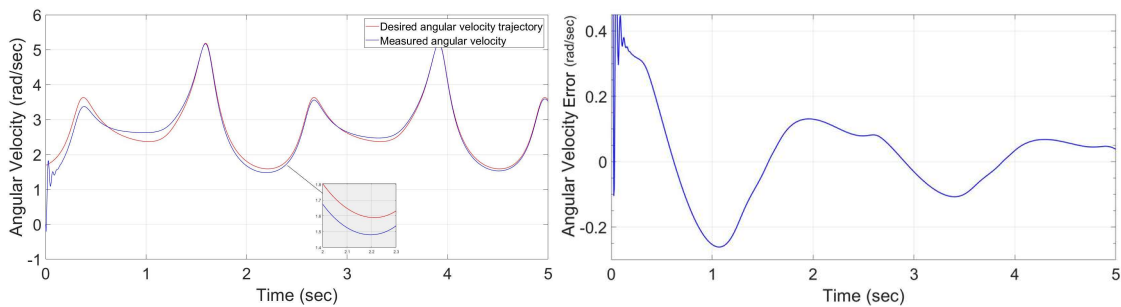


Fig. 9. a) Comparison of desired and calculated crank speeds and b) crank speed error of Model-1 mechanism for $V_c^{des} = 0.1$ m/sec

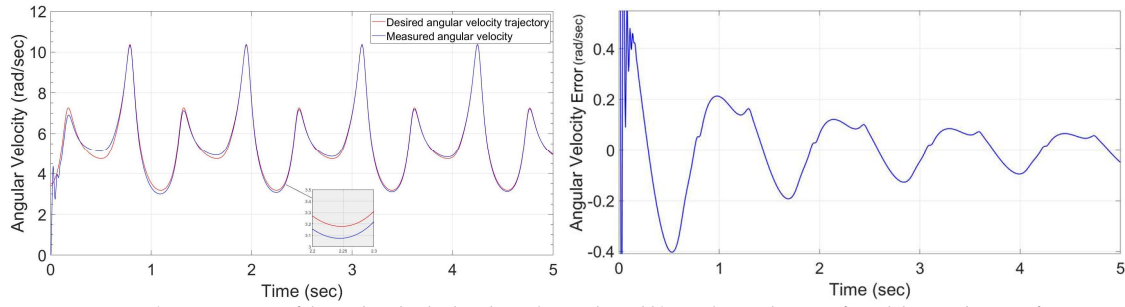


Fig. 10. a) Comparison of desired and calculated crank speeds and b) crank speed error of Model-1 mechanism for $V_C^{des} = 0.2 \text{ m/sec}$

In order to show the performance of the proposed method, a second simulation is conducted. In the second example, the mass and mass moment of inertia values of the link 3 are updated without changing the physical and geometrical properties of the other links such that $m_3 = 0.719 \text{ kg}$ and $J_3 = 0.000626 \text{ kg}\cdot\text{m}^2$. This model is named as Model-2. In this case, PID parameters are estimated as $K_p = 50$, $K_i = 30$ and $K_d = 10$. The results for this case are also very satisfactory as can be seen in Figs 11 and 12.

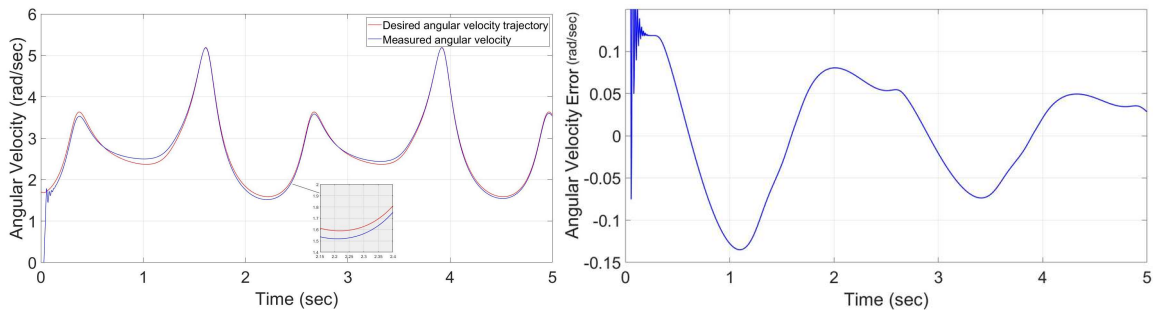


Fig. 11. a) Comparison of desired and calculated crank speeds and b) crank speed error of Model-2 mechanism for $V_C^{des} = 0.1 \text{ m/sec}$

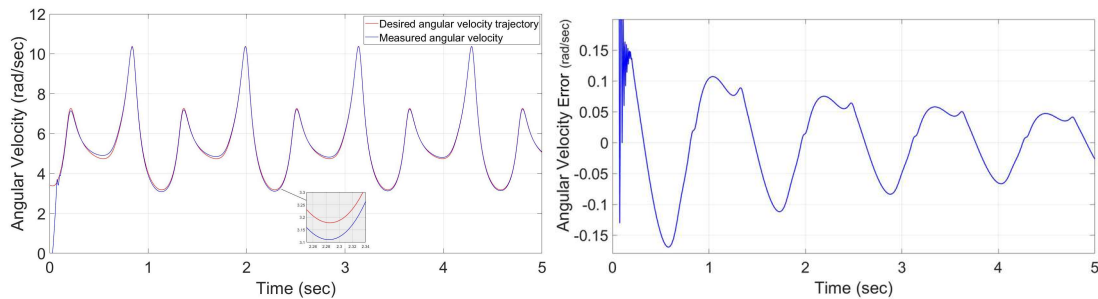


Fig. 12. a) Comparison of desired and calculated crank speeds and b) crank speed error of Model-2 mechanism for $V_C^{des} = 0.2 \text{ m/sec}$

5. Experimental Study

For the experimental study Model 1 and Model 2 mechanisms, are manufactured where moving parts links 2-4 are produced by laser cutting from steel sheet with thickness of 5 mm and fixed part link 1 is produced by 3D printing from PLA filament. For Model-2, the link 3 is manufactured thicker. A 12 V DC motor with a gear box and optical encoder, whose parameters are given in Table 2, is used to drive the crank. ATMEGA 328, 8 bit- 16 MHz microchip were used to control the system. The mechanism is controlled by the microcontroller at a frequency of approximately 200 Hz. The experimental system is shown in Fig. 13. It should be noted that 1 kHz PWM signal is generated for the motor driver and a low-pass filter on the encoder output was used to eliminate the noise.

For the experimental study, both Model-1 and Model-2 mechanisms are run for the cases constant coupler point velocities $V_C^{des} = 0.1$ and $V_C^{des} = 0.2 \text{ m/sec}$. PID control parameters are estimated using the trial-and-

error method as $K_p = 8, K_i = 12, K_d = 20$ for Model 1 and $K_p = 13, K_i = 50, K_d = 32$ for Model 2. The results for both mechanisms are given in Figs 14-17. As can be seen in the Figs, the measured crank speed agrees with desired crank speed trajectory but some noise. For these cases the trajectory errors are under 0.6 rad/sec.

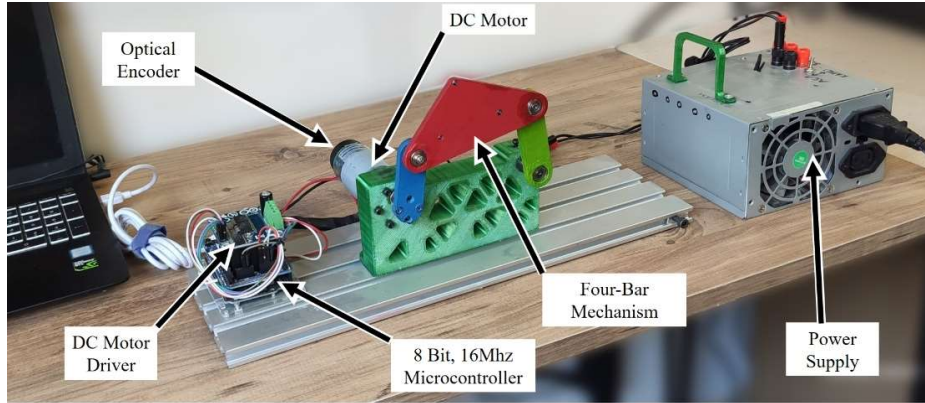


Fig. 13. Experimental system

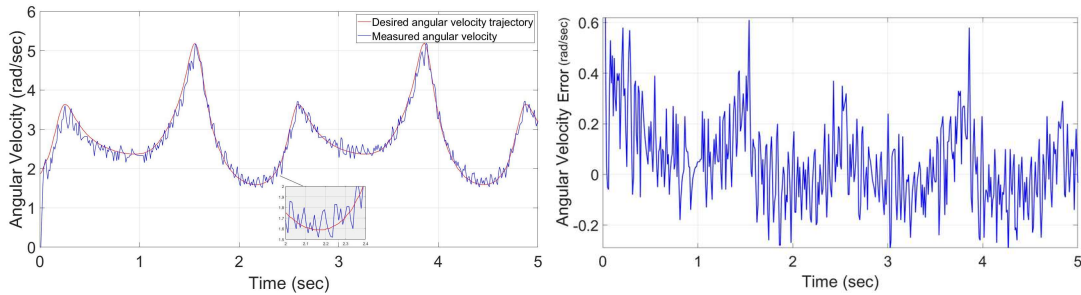


Fig. 14. a) Comparison of desired and measured crank speeds and b) crank speed error of Model-1 mechanism for $V_C^{des} = 0.1 \text{ m/sec}$

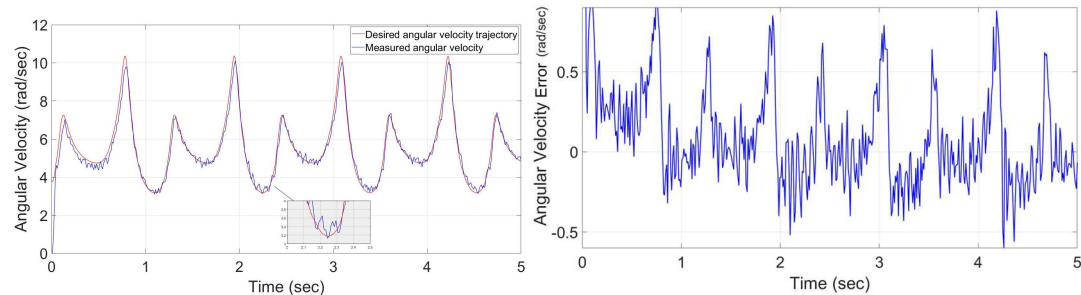


Fig. 15. a) Comparison of desired and measured crank speeds and b) crank speed error of Model-1 mechanism for $V_C^{des} = 0.2 \text{ m/sec}$

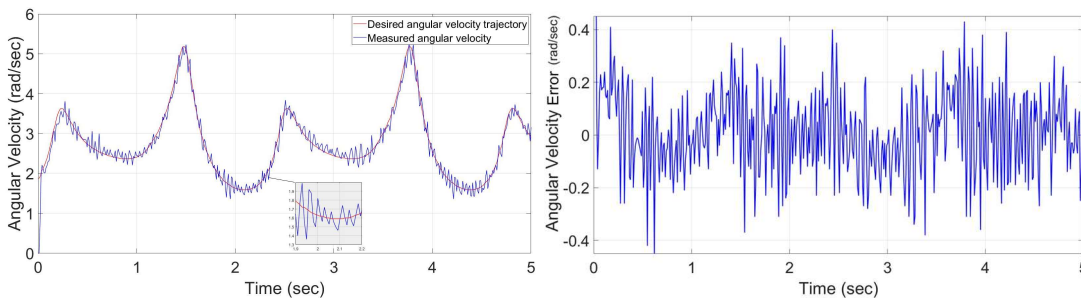


Fig. 16. a) Comparison of desired and measured crank speeds and b) crank speed error of Model-2 mechanism for $V_C^{des} = 0.1 \text{ m/sec}$

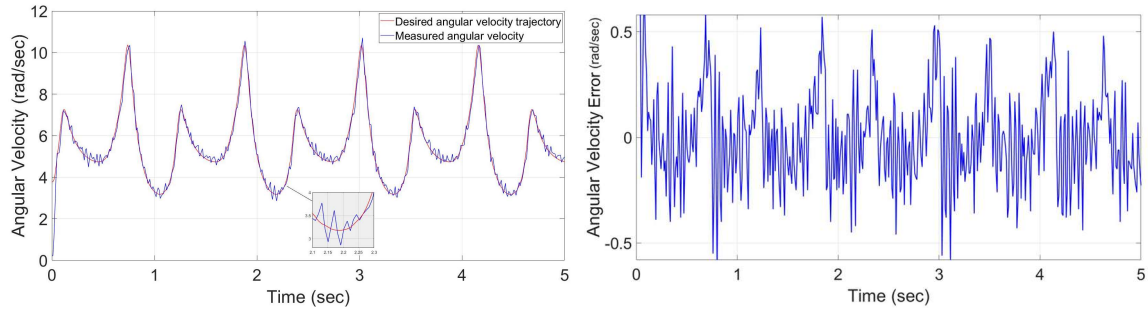


Fig. 17. a) Comparison of desired and measured crank speeds and b) crank speed error of Model-2 mechanism for $V_c^{des} = 0.2 \text{ m/sec}$

5.1. Comparison of numerical and experimental results

In this section, the desired coupler point velocities obtained from the numerical simulation and the experimental studies are compared. The results are given in Figs 18-21. It can be seen in all of the Figs, the coupler point velocities determined by the numerical simulation oscillate around the desired value of which and they continue to decrease during the time. A similar situation also exists in the experimental cases but there are noise and sudden ups and downs. Approximate maximum deviations from desired velocity values for all cases are given in Table 3.

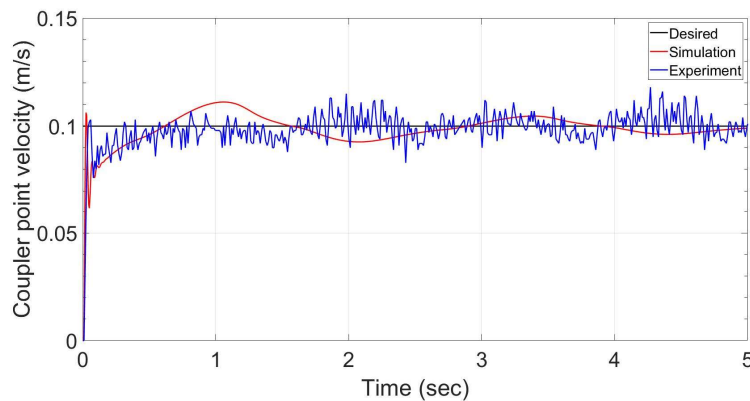


Fig. 18. Comparison of the coupler point velocities: desired, numerical simulation and experimental case for $V_c^{des} = 0.1 \text{ m/s}$ (Model 1)

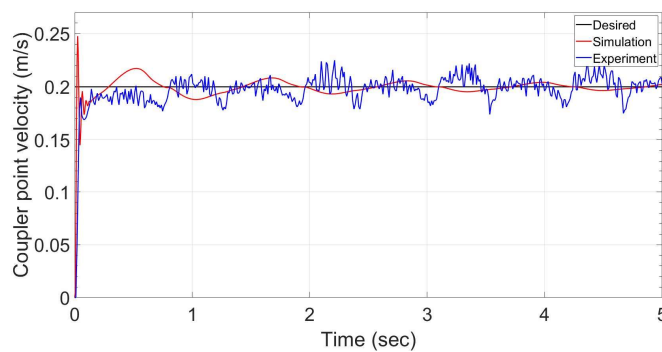


Fig. 19. Comparison of the coupler point velocities: desired, numerical simulation and experimental case for $V_c^{des} = 0.2 \text{ m/s}$ (Model 1)

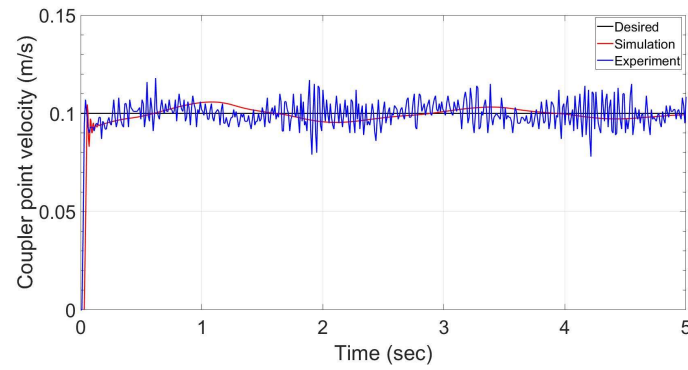


Fig. 20. Comparison of the coupler point velocities: desired, numerical simulation and experimental case for $V_c^{des} = 0.1 \text{ m/s}$ (Model 2)

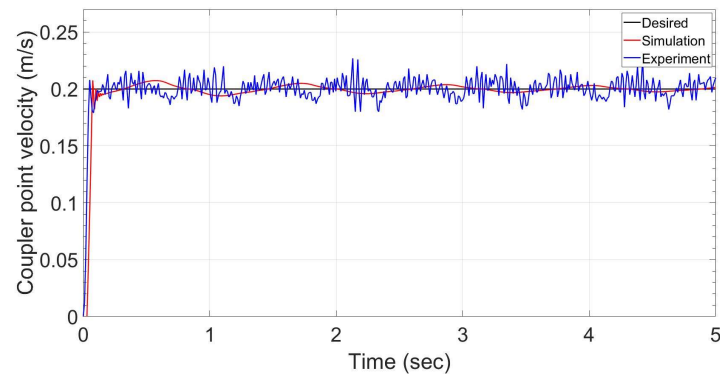


Fig. 21. Comparison of the coupler point velocities: desired, numerical simulation and experimental case for $V_c^{des} = 0.2 \text{ m/s}$ (Model 2)

Table 3. The maximum deviations for numerical and experimental case studies

Mechanism	Desired Velocity	Maximum Deviation (m/s)	
		Simulation	Experimental
Model 1	0.1	0.01	0.020
	0.2	0.01	0.025
Model 2	0.1	0.01	0.025
	0.2	0.01	0.025

In Table 3 and Figs. 18 through 21, it can be seen that the deviations in both the numerical and experimental case studies are acceptable. These minor deviations do not significantly impact the overall system performance or reliability. The deviations in the experimental case studies are bigger than that of the numerical simulations. However, the coupler point velocity approaches to the desired value as time progress in the numerical simulations while it goes up and down about reference value in the experimental case. This is an expected result. Because the sampling rate of the experimental system is lower than that of the numerical simulation due to frequency of the microprocessor used in the system. On the other hand, the mechanical issues such as looseness and manufacturing tolerances affect the experimental results. It is no doubt that the mechanical system works perfectly in the numerical simulation but it cannot fully represent the real mechanical structure. Nevertheless, the rise time is 0.07 sec and the settling time is 1.5 sec for all cases. As a result, it can be said that the desired velocity is achieved in both the numerical and experimental studies.

The numerical and experimental results are also compared for the desired velocities 0.1, 0.2, 0.3 and 0.4 m/sec in Fig. 22 for Model-1 and Model-2 mechanisms. It is seen that the deviations become larger as the desired velocity increases.

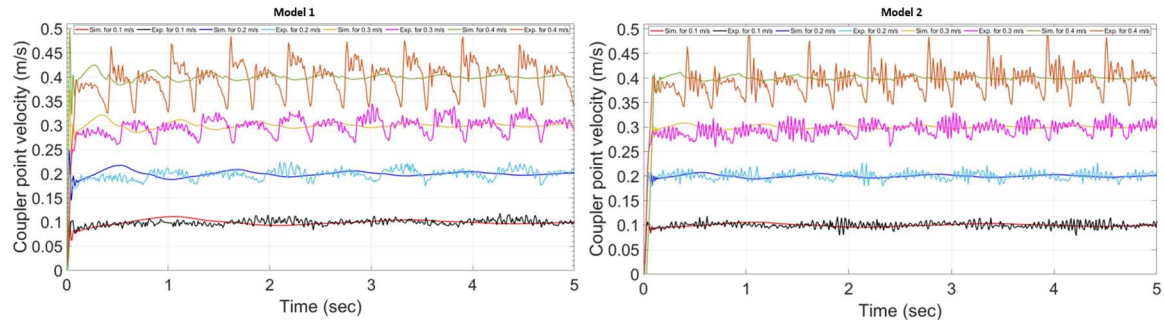


Fig. 22. Comparison of the coupler point velocity for different values: a) Model-1 b) Model-2

6. Conclusion and Discussion

The numerical simulations and the experimental case studies are made in order to show the efficiency of the method. Different constant coupler point velocity are considered in the case studies. However, the effect of the mass properties of the link 3 is investigated. It is shown that the constant coupler velocity could be achieved by the variable crank speed. The coupler point velocity approaches to the desired value as time progress in the numerical simulations. But there are sudden ups and downs about reference value in the experimental case. This is due to sampling rate of the microprocessor and the motor encoder, and some mechanical issues. As a result, MSM can provide analysis of the mechatronic systems without deriving the complex mathematical model as long as the parameters of the system are set accurately.

The experimental results demonstrate that for industrial applications requiring a stable speed, the system can maintain a speed of up to 0.2 m/s with oscillations around 0.025 m/s. This finding suggests that a low-cost system, designed to handle specified loads, could be effectively implemented for applications within this speed range. At target speeds of 0.3 m/s and 0.4 m/s, however, the system experiences increased fluctuations of about 0.04 m/s and 0.1 m/s along the trajectory, respectively. This knowledge allows for a well informed system selection, acknowledging that at higher speeds, speed stability may be compromised. Therefore, the system configuration can be chosen based on the allowable oscillation range, ensuring a balance between cost-effectiveness and performance requirements.

Conflict of Interest Statement

The authors declare that there is no conflict of interest.

References

- [1] E. Söylemez, *Mechanisms*, MMO Middle East Technical University publication number 64, 1985.
- [2] J. Tao and J.P Sadler, "Constant speed control of a motor driven mechanism system," *Mechanisms and Machine Theory*, vol. 30, no. 5, pp. 737-748, 1995. doi: 10.1016/0094-114X(94)00072-S
- [3] Ö. Gündoğdu and K. Erentürk, "Fuzzy Control of a dc motor driven four-bar mechanism," *Mechatronic*, Cilt:15, s:423-438, 2005. doi: 10.1016/j.mechatronics.2004.10.004
- [4] G. Şevkat ve S. Telli, "Elektrik Motoru İle Tahrik Edilen Dört Çubuk Mekanizmasının Kayan Kip Hız Kontrolü," *Uludağ Üniversitesi Mühendislik-Mimarlık Dergisi*, Cilt:13, No:2, s: 15-26, 2008. doi: 10.17482/uujfe.96125
- [5] O. Çakar and A.K.Tanyildizi, "Application of moving sliding mode control for a DC motor driven four-bar mechanism," *Advances in Mechanical Engineering*, vol.10, no. 3, pp. 1–13, 2018. doi: 10.1177/1687814018762184
- [6] M. Salah, A. Al-Jarrah, E. Tatlicioglu et al. "Robust Backstepping Control for a Four-Bar Linkage Mechanism Driven by a DC Motor," *J Intell Robot Syst*, vol. 94, pp. 327–338, 2019. doi: 10.1007/s10846-018-0811-y
- [7] G. O Koca, Z. H Akpolat and M. Özdemir, "Type-2 fuzzy sliding mode control of a four-bar mechanism," *Int J Model Simul*, vol. 31, pp. 60–68, 2011. doi: 10.2316/Journal.205.2011.1.205-5335

- [8] A. Al-Jarrah, M. Salah, K.S. Banihani, et al. "Applications of various control schemes on a four-bar linkage mechanism driven by a geared DC motor," *WSEAS Trans Syst Contr*, vol. 10, pp. 584–597, 2015. <https://api.semanticscholar.org/CorpusID:11080447>
- [9] C.F. Chang, "Synthesis of adjustable four-bar mechanisms generating circular arcs with specified tangential velocities," *Mechanism and Machine Theory*, vol. 36, no. 3, pp. 387-395, 2001. doi: 10.1016/S0094-114X(00)00049-5
- [10] H. S. Yan and R. C. Soong, "Kinematic and dynamic design of four-bar linkages by links counterweighing with variable input speed," *Mechanism and Machine Theory*, vol. 36, no. 9, pp. 1051-1071, 2001. doi: 10.1016/S0094-114X(01)00032-5
- [11] R. Peón-Escalante, M. Flota-Bañuelos, L. J. Ricalde, C. Acosta, G. S. Perales, "On the coupler point velocity control of variable input speed servo-controlled four-bar mechanism," *Advances in Mechanical Engineering*, vol. 8, no. 11, pp. 1–9, 2016. doi: 10.1177/1687814016678356
- [12] M. Flota-Bañuelos, R. Peón-Escalante, L. J. Ricalde, B. J. Cruz, R. Quintal-Palomo, J. Medina, "Vision-based control for trajectory tracking of four-bar linkage," *J Braz. Soc. Mech. Sci. Eng*, vol. 43, no. 324, pp. 1–11, May, 2021. doi: 10.1007/s40430-021-03043-z
- [13] R. Peón-Escalante, M. Flota-Bañuelos, R. Quintal-Palomo, L.J. Ricalde, F. Peñuñuri, B. Cruz Jiménez and J. Avilés Viñas, "Neural Network Based Control of Four-Bar Mechanism with Variable Input Velocity," *Mathematics*, vol. 11, no.2148, pp. 1-17, 2023. doi: 10.3390/math11092148
- [14] O. Denizhan and M. S. Chew, "Linkage mechanism optimization and sensitivity analysis of an automotive engine hood," *International Journal of Automotive Science and Technology*, vol. 2, no. 1, pp. 7-16, 2018. doi: 10.30939/ijastech..364438
- [15] Matlab, 2021,(n.d.).<https://www.mathworks.com/products/simmechanics.html>. [Accessed: Feb. 1, 2025].
- [16] H. Hülako and O. Yakut, "Control of Three-Axis Manipulator Placed on Heavy-Duty Pentapod Robot," *Simul. Model Pract. Theory*, vol. 108, no. May 2020, 2021. doi: 10.1016/j.simpat.2020.102264

This is an open access article under the CC-BY license



GAZİ

JOURNAL OF ENGINEERING SCIENCES

Predicting of Credit Card Customer Churn Using Machine Learning Methods

M. Hanefi Calp^{a*}

Submitted: 18.10.2024 Revised: 09.01.2025 Accepted: 24.01.2025 doi:10.30855/gmbd.070525N02

ABSTRACT

Keywords: Credit Card, Customer Churn, Card Cancellation, Machine Learning, Prediction

^{a*} Ankara Hacı Bayram Veli University,
Faculty of Economics and Administrative
Science,
Dept. of Management Information
Systems
06500 - Ankara, Türkiye
Orcid: 0000-0001-7991-438X
e mail: hanefi.calp@hbv.edu.tr

*Corresponding author:
hanefi.calp@hbv.edu.tr

Today, customers can give up using credit cards for various reasons, and this situation has negative consequences for banks. Therefore, it is necessary to predict potential customers who will cancel their credit cards in advance and to turn these cancellations in favor of the bank and thus to regain the customers. This situation is also very important in terms of monitoring customer churn and preventing such churn. In this context, a model is proposed using machine learning methods to detect the card cancellation status of customers using credit cards and thus predict customer churn. A dataset obtained from the Kaggle platform was utilized to create the model. This dataset contains credit card data belonging to a total of 10127 customers. Although there were 23 features in the dataset, 2 features were deleted without being included in the model because they did not affect the results. As a result, a total of 21 different variables were used, 20 inputs and 1 output. The models were created using Artificial Neural Networks, Logistic Regression, Support Vector Machines, K-Nearest Neighbor, Decision Tree, Random Forest, Ada Boost, and Gradient Boosting machine learning algorithms. As a result, it was seen that the model with the highest performance was Gradient Boosting with a rate of 98.70%, and the model with the lowest performance was Support Vector Machines with a rate of 67.9%. All these results clearly show that Credit Card Customer Churn can be effectively predicted by machine learning methods.

Kredi Kartı Müşteri Kaybının Makine Öğrenmesi Yöntemleri Kullanılarak Tahmin Edilmesi

ÖZ

Günümüzde müşteriler muhtelif sebeplerle kredi kartı kullanımlarından vazgeçebilmekte ve bu durum bankalar açısından olumsuz sonuçlar doğurmaktadır. Dolayısıyla, kredi kartı iptali yapacak muhtemel müşteriler önceden tahmin edilerek sözkonusu iptallerin banka lehine çevrilmesi ve böylece müşterilerin geri kazanılması gerekmektedir. Bu durum, müşteri kaybının takibi ve sözkonusu kaybın önlenmesi açısından da oldukça önem arz etmektedir. Bu bağlamda, çalışmada kredi kartı kullanan müşterilerin kart iptal durumlarını tespit etmek ve dolayısıyla müşteri kaybını tahmin etmek için makine öğrenmesi yöntemleri kullanılarak bir model önerilmiştir. Modelin oluşturulması için Kaggle platformundan elde edilen bir verisetinden yararlanılmıştır. Bu veri setinde toplam 10127 müşteriye ait kredi kartı verisi bulunmaktadır. Veri setinde 23 özellik olmasına rağmen 2 özelliğin sonuçlara etkisi olmadığından modele dahil edilmeden silinmiştir. Sonuç olarak 20 girdi, 1 çıktı olmak üzere toplamda 21 farklı değişken kullanılmıştır. Modeller; Yapay Sinir Ağları, Lojistik Regresyon, Destek Vektör Makineleri, K-En Yakın Komşu, Karar Ağacı, Rastgele Orman, Ada Boost ve Gradient Boosting makine öğrenmesi algoritmaları kullanılarak oluşturulmuştur. Sonuç olarak, en yüksek performansı gösteren modelin %98.70'lik bir oranla Gradient Boosting, en düşük performansın ise %67.9'luk bir oranla Destek Vektör Makineleri modeli olduğu görülmüştür. Elde edilen tüm bu sonuçlar, Kredi Kartı Müşteri Kaybının makine öğrenmesi yöntemleriyle etkili bir şekilde tahmin edilebileceğini açıkça göstermektedir.

Anahtar Kelimeler: Kredi Kartı, Müşteri Kaybı, Kart İptali, Makine Öğrenmesi, Tahmin

1. Introduction

A highly dynamic and competitive market has emerged with the existence of a large number of service providers such as banks worldwide [1]. These banks have become reliable places for the storage of money and similar valuable metals. With the increase in competition, the most important thing for banks is the customer. Because customers are very important for banks to survive in difficult market conditions. What is important here is customer loyalty. Because banks make high profits by keeping customers in their organization for a long time, therefore, banks should keep customer churn to a minimum [2]. Harvard Business Review stated that companies can make a profit between 25% and 85% with 5% deviation in the number of customers [3]. In this context, customer churn basically means customers giving up on preferring the company due to competition [4].

Customer churn can be defined as a customer giving up or not preferring a bank. The increase in customer churn rates is inversely proportional to the rate of campaigns and satisfactory services that banks carry out compared to each other. In other words, the more customer satisfaction there is, the less churn there is. In this process, access to technological facilities, low transaction fees, staff quality and competence, advertisements, proximity in terms of location and similar services are also very effective [5,6]. Churn is the transfer of a customer to another bank or the complete abandonment of the bank, thus decreasing the bank's profit. It is very important for banks to predict this situation before a customer switches to another bank [7].

In today's competitive environment, banks should know their customers well and be honest with them in order to provide faster and more effective service to their customers, to reach all of their customers, and therefore not to lose customers. With the development of technology, banks record and use the data they obtain. It is important to analyze this data, which develops and grows every day. Banks use many technologies for data analysis. Thanks to these technologies, they can analyze the data in question effectively, quickly, and statistically reliably [3]. With the analysis of data, banks can take some campaigns or actions by predicting many problems in advance. These analyses prevent possible customer churn or regain customers who have left the bank [8].

This entire process is only possible with current and new technologies such as machine learning. Machine learning is a subset of artificial intelligence and is a mathematical model established to help the computer learn the model or subject without direct guidance. A high-performance machine learning model can provide effective resource management or savings. Machine learning models are trained based on given examples and automate the task given to them by detecting certain patterns. Unlike traditional methods, it produces results by giving input and output in the process of solving any problem [9,10].

Machine learning actually works with trial-and-error logic and allows programs to make predictions. Machine learning algorithms can be used in almost every field from health to tourism, from sports to education. There are different types such as supervised, unsupervised, and reinforced [11]. When the literature is scanned, it is seen that different methods are used to predict the losses that will occur in bank customers. In the literature, machine learning algorithms such as Support Vector Machines (SVM), K-Nearest Neighbors (KNN), Artificial Neural Network (ANN), Logistic Regression (LR), Decision Trees (DT), and Random Forest (RF) are mostly used for this prediction [12-16].

Therefore, in this context, the aim of the study is to predict customer churn (credit card cancellation cases) with an up-to-date and effective approach such as machine learning methods, thus offering a new approach to the problem of customers quitting credit card use and providing a proactive perspective for the future. The second part of the study includes all the details of the material and method. The third part includes experimental findings and discussion, and the fourth part includes information on the results and recommendations obtained from the study.

2. Material and Methods

This section includes all the details of the study, including the dataset, dataset preprocessing, model selection, model creation, and findings from model performance. In the study, the card cancellation status of credit card customers and thus customer churn were estimated using machine learning methods. For this purpose, a total of 8 different methods were used, including Ada Boost, RF, ANN, KNN, LR, DT, SVM, and Gradient Boosting (GBoosting). Before moving on to the models, information about the dataset was provided.

2.1. Dataset

The data set was obtained from the address 'Credit Card Customer Dataset' [17] and contains 10127 data and consists of 23 attributes. Two attributes that were not seen to directly affect the results were deleted and reduced to 21 (20 Inputs, 1 Output). Info Gain, Gain Ratio, Gini, ANOVA, Chi2, ReliefF, and FCBF (Fast Correlation Based Filter) were used to determine the extracted attributes (Figure 1).

	#	Info. gain	Gain ratio	Gini	ANOVA	χ^2	ReliefF	FCBF	
1	N Total_Trans_Ct	0.117	0.059	0.040	NA	1165.960	0.090	0.097	
2	N Total_Revolving_Bal	0.081	0.041	0.033	NA	544.972	0.078	0.066	
3	N Total_Trans_Amt	0.077	0.038	0.023	NA	335.959	0.071	0.000	
4	N Total_Ct_Chng_Q4_Q1	0.075	0.038	0.032	NA	688.376	0.009	0.060	
5	N Avg_Utilization_Ratio	0.066	0.033	0.028	NA	541.112	0.045	0.000	
6	N Months_Inactive_12_mon	0.027	0.015	0.009	NA	190.317	0.021	0.022	
7	N Contacts_Count_12_mon	0.026	0.013	0.009	NA	219.283	0.019	0.020	
8	N Total_Relationship_Count	0.019	0.010	0.007	NA	195.035	0.039	0.000	
9	N Total_Amt_Chng_Q4_Q1	0.013	0.007	0.005	NA	57.527	0.008	0.000	
10	N Avg_Open_To_Buy	0.013	0.006	0.005	NA	11.070	0.010	0.000	
11	N Credit_Limit	0.003	0.002	0.001	NA	20.585	0.011	0.000	
12	N CLIENTNUM	0.003	0.001	0.001	NA	30.128	0.004	0.002	
13	C Gender	2	0.001	0.001	0.000	NA	7.443	0.012	0.000
14	C Income_Category	6	0.001	0.000	0.000	NA	9.431	0.056	0.000
15	C Education_Level	7	0.001	0.000	0.000	NA	0.339	0.096	0.000
16	N Customer_Age		0.001	0.000	0.000	NA	3.202	0.016	0.000
17	N Dependent_count		0.001	0.000	0.000	NA	3.851	0.012	0.000
18	C Marital_Status	4	0.000	0.000	0.000	NA	1.303	0.054	0.000
19	N Months_on_book		0.000	0.000	0.000	NA	1.479	0.003	0.000
20	C Card_Category	4	0.000	0.000	0.000	NA	0.986	0.002	0.000

Figure 1. Scores of input and output variables

The attributes in the dataset are as follows: Client_Num (Client Number), Customer_Age (Customer's Age in Years), Gender (Demographic variable - M=Male, F=Female), Dependent_Count (Number of Dependents), Education_Level (Educational Qualification of the account holder), Marital_Status (Married, Single, Divorced, Unknown), Income_Category (Annual Income Category of the account holder), Card_Category (Type of Card), Months_on_Book (Period of relationship with bank), Total_Relationship_Count (Total no. of products held by the customer), Months_Inactive_12_mon (No. of months inactive in the last 12 months), Contacts_Count_12_mon (No. of Contacts in the last 12 months), Credit_Limit (Credit Limit on the Credit Card), Total_Revolving_Bal (Total Revolving Balance on the Credit Card), Avg_Open_To_Buy (Open to Buy Credit Line (Average of last 12 months)), Total_Amt_Chng_Q4_Q1 (Change in Transaction Amount (Q4 over Q1)), Total_Trans_Amt (Total Transaction Amount (Last 12 months)), Total_Trans_Ct (Total Transaction Count (Last 12 months)), Total_Ct_Chng_Q4_Q1 (Change in Transaction Count (Q4 over Q1)), Avg_Utilization_Ratio (Average Card Utilization Ratio), and Attrition_Flag (Internal event (customer activity) variable - if the account is closed then 1 else 0). The features, types, and value ranges found in the dataset are given in Table 1.

Table 1. Dataset features

INPUT

Number Value	Feature	Type	Range
1	Client_num	Numerical	No Limit
2	Customer_Age	Numeric	0-150
3	Gender	Categorical	Female, Male
4	Dependent_count	Numeric	0-50
5	Education_Level	Categorical	College, Doctorate, Graduate, High School, Post-Graduate, Uneducated, Unknown
6	Marital_Status	Categorical	Divorced, Married, Single, Unknown
7	Income_Category	Categorical	\$40k-\$60k, \$60k-\$80k, \$80k-\$120k, \$120k+, Less than \$40k, Unknown
8	Card_Category	Categorical	Blue, Gold, Platinum, Silver
9	Months_on_book	Numeric	No range
10	Total_Relationship_Count	Numeric	No limit
11	Months_Inactive_12_mon	Numeric	No limit
12	Contacts_Count_12_mon	Numeric	No limit
13	Credit_Limit	Numeric	No limit
14	Total_Revolving_Bal	Numeric	No limit
15	Avg_Open_To_Buy	Numeric	No limit
16	Total_Amt_Chng_Q4_Q1	Numeric	No limit
17	Total_Trans_Amt	Numeric	No limit
18	Total_Trans_Ct	Numeric	No limit
19	Total_Ct_Chng_Q4_Q1	Numeric	No limit
20	Avg_Utilization_Ratio	Numeric	No Limit

OUTPUT (Target)

Number Value	Feature	Type	Range
1	Attrition_Flag (Customer Activity)	Categorical	Customer Churn Existing Customer

2.2. Data preprocessing

During the preprocessing phase of the data set, two different columns indicating the change in the number of transactions and the type of change in the number of transactions were ignored and not included in the model. Repeating rows or inconsistent data in the data were revised. The first column contains classification data for customer activity (customer churn). The other columns contain the number of customers, customer age, gender, number of dependents, education level, marital status, income category, card category, months (duration of relationship with the bank), credit limit, total number of relationships, number of inactive months in the last 12 months, number of people in the last 12 months, revolving balance on the credit card, credit limit open for purchase (average of the last 12 months), total transaction amount (12 months), total number of transactions (12 months) and average card usage rate. Therefore, "Customer Churn" was estimated using the data in all these columns in the study. A sample section from the data set after preprocessing is given in Table 2.

Table 2. A Sample section from the dataset

CN	CA	G	DC	EL	MS	IC	CC	MB	TRC	MI_12_mon	CC_12_mon	CL	TRB	AOB	TAC_Q4_Q1	TTA	TTC	TCC_Q4_Q1	AUR	AF
709188108	45	M	2	Graduate	Single	\$60K - \$80K	Silver	33	4	2	2	34516	1529	32987	0.609	13940	105	0.81	0.044	Existing Customer
719106783	52	M	1	High School	Single	\$80K - \$120K	Blue	41	4	1	4	4103	1972	2131	0.665	16344	118	0.788	0.481	Existing Customer
713437008	40	F	3	Graduate	Married	Unknown	Blue	25	1	2	3	6888	1878	5010	1059	9038	64	0.829	0.273	Customer Churn
719574033	38	M	1	High School	Single	\$60K - \$80K	Blue	28	2	2	2	21906	0	21906	0.696	15349	119	0.7	0	Existing Customer
710005683	56	M	2	College	Single	\$80K - \$120K	Blue	46	3	3	5	12540	1696	10844	0.799	16518	115	0.716	0.135	Existing Customer
801036033	31	M	0	High School	Single	\$40K - \$60K	Blue	25	3	2	3	4493	1388	3105	0.795	17744	104	0.763	0.309	Existing Customer
716644008	55	M	3	Graduate	Single	\$120K +	Silver	36	4	3	4	34516	0	34516	1007	9931	70	0.75	0	Customer Churn
718372458	42	M	2	Graduate	Unknown	\$40K - \$60K	Blue	30	3	2	5	3735	1723	2012	0.595	14501	92	0.84	0.461	Existing Customer
720608658	33	F	1	Uneducated	Single	Less than \$40K	Blue	36	5	3	3	8398	1875	6523	0.727	16706	123	0.757	0.223	Existing Customer
717185658	51	M	1	High School	Married	\$80K - \$120K	Blue	36	4	3	4	22754	0	22754	0.799	8531	77	0.791	0	Customer Churn
715474083	51	M	3	Graduate	Single	\$60K - \$80K	Silver	36	3	2	2	29663	1743	27920	0.667	14638	93	0.722	0.059	Existing Customer
709646433	59	F	1	High School	Married	Less than \$40K	Blue	50	1	4	3	5043	743	4300	0.805	10170	66	0.784	0.147	Customer Churn
717494358	58	F	0	Graduate	Single	Less than \$40K	Blue	48	2	2	5	4299	1334	2965	0.66	15068	123	0.685	0.31	Existing Customer
713924283	61	M	0	Graduate	Single	\$60K - \$80K	Blue	54	2	1	4	11859	1644	10215	0.866	8930	79	0.837	0.139	Customer Churn
714471183	47	M	4	Graduate	Divorced	\$80K - \$120K	Blue	39	4	3	4	17504	476	17028	0.892	10468	66	0.737	0.027	Customer Churn
780613758	47	M	5	High School	Single	Less than \$40K	Blue	35	4	3	5	4165	0	4165	0.813	17093	111	0.82	0	Existing Customer
718225683	56	M	1	Graduate	Single	\$80K - \$120K	Silver	49	5	2	2	34516	1091	33425	0.64	15274	108	0.714	0.032	Existing Customer
710734308	49	M	1	Graduate	Single	\$60K - \$80K	Blue	40	6	3	3	6481	1569	4912	0.692	15937	119	0.803	0.242	Existing Customer
708564858	33	M	2	College	Married	\$120K +	Gold	20	2	1	4	34516	0	34516	1004	9338	73	0.622	0	Customer Churn
713733633	27	M	0	High School	Divorced	\$60K - \$80K	Blue	36	2	3	2	13303	2517	10786	0.929	10219	85	0.809	0.189	Customer Churn
712210458	38	M	1	Uneducated	Single	\$40K - \$60K	Blue	36	2	3	2	5639	1558	4081	0.614	16628	109	0.946	0.276	Existing Customer
714109308	46	M	5	College	Single	\$80K - \$120K	Blue	36	1	2	3	13187	2241	10946	0.689	15354	112	0.931	0.17	Existing Customer
712503408	57	M	2	Graduate	Married	\$80K - \$120K	Blue	40	6	3	4	17925	1909	16016	0.712	17498	111	0.82	0.106	Existing Customer
716893683	55	F	3	Uneducated	Single	Unknown	Blue	47	4	3	3	14657	2517	12140	0.166	6009	53	0.514	0.172	Customer Churn
710841183	54	M	1	High School	Single	\$60K - \$80K	Blue	34	5	2	0	13940	2109	11831	0.66	15577	114	0.754	0.151	Existing Customer
713899383	56	F	1	Graduate	Single	Less than \$40K	Blue	50	4	1	4	3688	606	3082	0.57	14596	120	0.791	0.164	Existing Customer

CN: Client_Num, CA: Customer_Age, G: Gender, DC: Dependent_Count, EL: Education_Level, MS: Marital_Status, IC: Income_Category, CC: Card_Category, MB:Months_on_Book, TRC: Total_Relationship_Count, MI_12_mon: Months_Inactive_12_mon, CC_12_mon: Contacts_Count_12_mon, CL: Credit_Limit, TRB:Total_Revolving_Bal, AOB: Avg_Open_To_Buy, TAC_Q4_Q1: Total_Amt_Chng_Q4_Q1, TTA:Total_Trans_Amt, TTC: Total_Trans_Ct, TCC_Q4_Q1: Total_Ct_Chng_Q4_Q1, AUR: Avg_Utilization_Ratio, AF: Attrition_Flag

As seen in Table 2, the first column is determined as the output (target). The remaining 20 columns constitute the study's inputs.

2.3. Model infrastructure

The models used in the study to classify credit card customer churn are Logistic Regression, Artificial Neural Network, K-Nearest Neighbor (one neighbor), K-Nearest Neighbor 2 (two neighbors), K-Nearest Neighbor 3 (three neighbors), Decision Tree, Random Forest, Support Vector Machines, Ada Boost, and Gradient Boosting. Brief explanations of these models are given in this section.

2.3.1. Random forest (RF)

RF is an algorithm that uses randomization to create many decision trees. This algorithm aims to obtain more accurate and reliable results by training multiple decision trees and combining their predictions. Each tree is trained on a randomly selected subset of features, and then the predictions of these trees are combined. The output of these trees is collected into a single output using averaging for classification or regression problems [18,19].

2.3.2. Support vector machine (SVM)

SVM is a powerful supervised learning algorithm used for classification and regression analysis. It is effective in high-dimensional spaces and is versatile due to the variety of kernel functions that can be used. SVM is known for its ability to handle outliers and is suitable for scenarios with a large number of features compared to the number of samples [20,21].

2.3.3. Decision tree (DT)

DT is a method of analyzing a dataset using a tree structure that represents a series of decisions in the dataset. A decision tree consists of many nodes and the edges connecting these nodes. Each node corresponds to a feature or decision. Starting from the first node, it branches according to the value of a feature in the dataset. Decision trees stand out with their understandability and interpretability. In addition, thanks to their ability to handle complexity in the dataset, they can be used in various tasks such as classification and regression [22,23].

2.3.4. Adaptive Boosting (AdaBoost)

AdaBoost is a machine learning algorithm that combines strong learners to form an ensemble. This algorithm uses an adaptive method to improve the performance of weak learners. The basic principles of AdaBoost are Weak Learners, Weights and Error Focus, Ensemble Building, and Boosting [24,25].

2.3.5. Gradient boosting (GBoost)

GBoost is an ensemble method that combines weak learners to form a strong model. This method uses gradient descent to eliminate the weaknesses of the model. The basic principles of GBoost are Weak Learners, Error Focus, Gradient Descent, and Boosting. GBoost is often used effectively in regression and classification problems. This method is known for its ability to create complex and high-performance models [26].

2.3.6. Logistic regression (LR)

LR is a parametric model used for binary classification. It estimates the probability that a given input belongs to a given category. It is relatively fast and efficient, which makes it a good starting point for classification tasks. However, it may not perform well in complex relationships in the data [27].

2.3.7. Artificial neural network (ANN)

An ANN is a model inspired by biological neural networks and is known for its ability to learn complex

relationships. ANNs have a structure consisting of layers of interconnected neurons. Each neuron receives input values, multiplies them with weights, subjects them to an activation function, and transmits the output to other neurons. In this way, the network gains the ability to learn complex relationships in the dataset [28-30].

2.3.8. K-nearest neighbor (KNN)

It is one of the machine learning methods and is a supervised learning algorithm with effective, parameter-free learning. This algorithm is used in classification and regression problems. Its basic logic is to determine the class of a data point by considering its KNNs. The KNN model works according to the proximity principle by considering the nearest neighbors in the feature space of the data to be classified [31]. The Euclidean distance between the training samples and the test sample is used to predict the label of the test sample [32].

2.4. Creating models

First, the inputs and outputs of the study were determined to create the models. Then, the steps of loading the dataset, preprocessing steps, creating the models, performance evaluation, and visualization of the results were carried out respectively. First, the machine learning methods to be used and the basic features to be used for each were determined. After the dataset was loaded into the system, the data were examined and possible data-cleaning processes were carried out at this stage. Finally, the models were created and the results and the graphs of the created models were obtained. In the preprocessing process of the data, two variables were deleted without being included in the model since it was seen that they did not affect the results much. Then, the data were checked again. While evaluating the model results, the data were normalized to obtain more reliable data, and the general results were answered.

2.4.1. Inputs and outputs

Inputs; number of customers, customer activity (current customer-lost customer), customer age, gender, number of dependents, education level, marital status, income category, card category, months (duration of relationship with the bank), credit limit, total number of relationships, number of inactive months in the last 12 months, number of people in the last 12 months, revolving balance on the credit card, credit limit open for purchase (average of the last 12 months), total transaction amount (12 months), total number of transactions (12 months), change in transaction amount (from 4th quarter to 1st quarter), change in number of transactions (from 4th quarter to 1st quarter) and average card usage rate.

The output is Customer Churn and Existing Customer, which are in two categories.

2.4.2. General structure of the study

In the process of creating the models, first of all, the available data was divided into two parts 80% training and 20% test. Then, training and test performances were measured for each model and the most appropriate model was decided. The general structure of the study including all models is given in Figure 2.

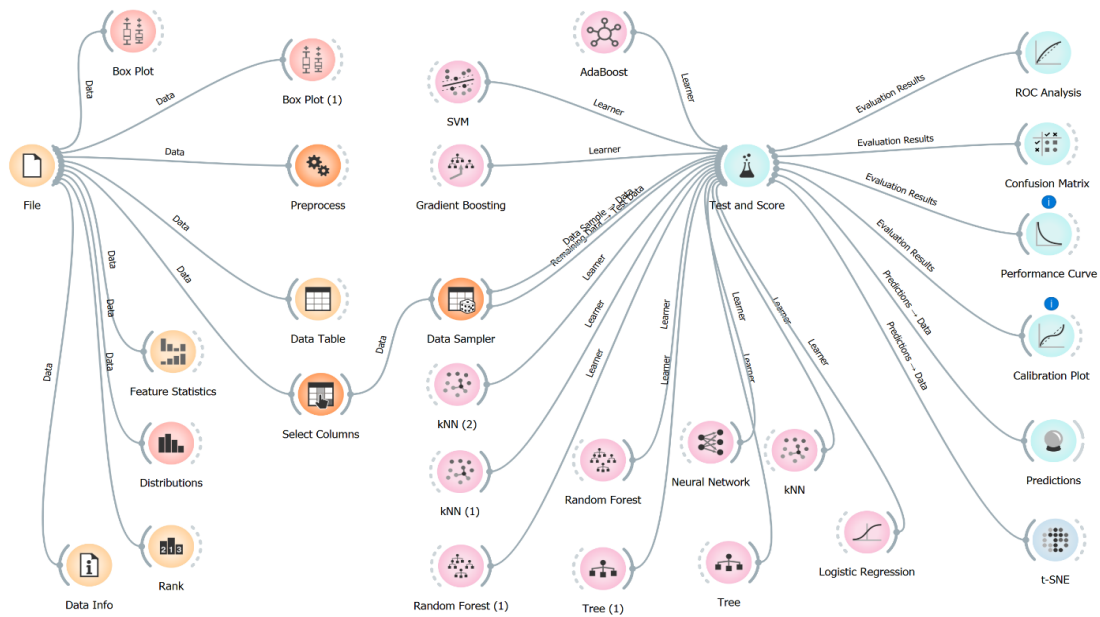


Figure 2. The general structure of the study

When Figure 2 is examined, in the first section, the file named File containing the dataset was obtained and then it was subjected to a preprocessing process to create the models. After the dataset was prepared, exploratory data analysis was performed using tools such as tables, graphics, feature statistics, and distribution.

In the second section, the dataset was integrated into the models (AdaBoost, GBoost, SVM, RF, LR, DT (1 and 2 leaves), ANN and KNN (1, 2 and 3 neighbors) in light of the previously determined features. Then, using the Test and Score tool, the test results/outputs of the models were obtained under six headings in total, namely ROC analysis, Confusion Matrix, Performance Curve, Relationship Graph, t-SNE and Prediction.

3. Experimental Findings and Discussion

This section includes the evaluation of the performance of the created models and a detailed analysis of the results obtained.

3.1. Performance of models

ROC Analysis, Confusion Matrix, Scatter Plots, Accuracy Value (AUC), Sensitivity, Specificity, and F1 score values to evaluate the performance in the study were taken into consideration. In this context, visualization tools such as ROC analysis, confusion matrix, recall-precision, and scatter plots were used. ROC analysis is used to evaluate the sensitivity and specificity of classification models. The larger the area under the ROC curve (AUC), the higher the performance of the model. AUC Value, the size of the area under the ROC curve, is a measure of the classification performance of the model. If the AUC value takes a value between 0-1 and approaches 0.5, the classification performance of the model is no different from random selection. An AUC value approaching 1 indicates that the model has high sensitivity and low false positive rates and that the classification performance increases. Sensitivity and Specificity, ROC curve shows the balance between sensitivity and specificity. Ideally, the closer the curve is to the upper left corner, the better the model performs. The ROC curve also shows the relationship between sensitivity and specificity values in the test. A steep curve indicates a model that provides high sensitivity and specificity [33,34]. The confusion matrix is a matrix that shows the classification performance of the model in more detail. The confusion matrix shows how the model predicts positive (separated) and negative (non-separated) classes. High TP and TN values indicate the overall correct classification ability of the model. FP and FN values represent incorrect classifications [35,36]. The scatter plot provides the opportunity to visually examine the distribution of data points belonging to different classes. Recall expresses the ratio of correctly predicted positive values to all true positive class values. Precision is the ratio of correctly predicted positive class values to all positively predicted class values [37].

First of all, the general performances of the models used in the study were evaluated. Here, the type of kernel

function used for SVM was determined as RBF. The numbers 1, 2 and 3 specified for KNN indicate the number of neighbors used. Regularization type Ridge (L2) and C value were determined as 1 for LR. For ANN, the number of neurons in the hidden layer was determined as 100, the activation function was determined as Adam, the ReLu learning optimization algorithm, and the maximum iteration number as 200. The number of trees was determined as 10 for RF. For DT, the number of leaves was taken as 2 and the maximum tree depth was taken as 1000, and it was decided to stop when majority reached 95. For AdaBoost, the number of predictors was taken as 50, the classification algorithm was SAMME.R, the Regression loss function was taken as Linear, and the learning rate was taken as 1. Finally, for the GBoost model, the number of trees was determined as 100, the learning rate was 0.1, and the individual tree depth limit was determined as 3.

When the overall accuracy performances of the models created using these features are examined, it is seen that the values of 86.8% for the LR model, 94.2% for ANN, 70.5% for SVM, 95.6% for RF, 96.0% for GBoost, 93.2% for AdaBoost, 87.2% for KNN (1), 88.4% for KNN (3), 88.7% for KNN (5) and 92.5% for DT are obtained. In light of this information, the AUC values of the models in the study were between 67.9% and 98.7%. When the findings obtained from the models are examined in general, it can be said that the models exhibit a classification performance that can be considered good to a large extent.

3.1.1. Gradient boosting model

As seen in the Confusion Matrix created for GBoost (Figure 3), 91.7% (1078) of those who are actually Customers were predicted correctly, while 3.2% (224) were predicted incorrectly. In addition, 96.8% (6703) of those who are actually Existing Customers were predicted correctly, while 8.3% (97) were predicted incorrectly.

		Predicted		Σ
		Customer Churn	Existing Customer	
Actual	Customer Churn	91.7 %	3.2 %	1302
	Existing Customer	8.3 %	96.8 %	6800
Σ		1175	6927	8102

Figure 3. Confusion Matrix - GBoost

When we look at the ROC curves for Customer Churn and Existing Customer in Figure 4, we observe high sensitivity and specificity in terms of classification success with the size of the area under the curves. In addition, in Figure 5, the recall and precision graphs also reveal the high success of the model. While the area under the curve for the Customer Churn is 0.652, it is obtained as 0.997 for the Existing Customer.

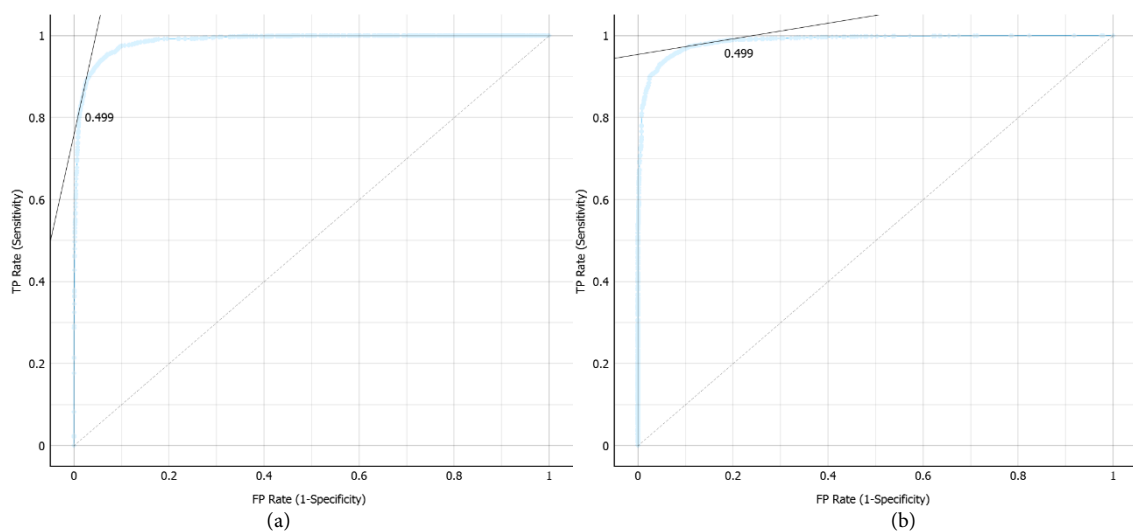


Figure 4. ROC analysis- GBoost a) Customer churn, b) Existing customer

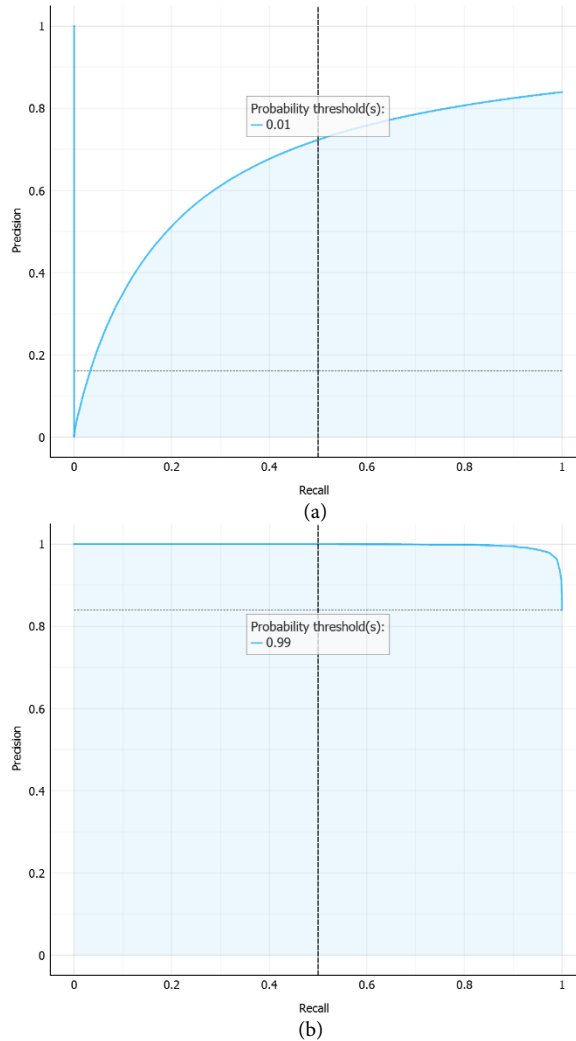


Figure 5. Performance curve (precision-recall) – Gboost a) Customer churn, b) Existing customer

3.1.2. AdaBoost model

As seen in the Confusion Matrix created for the AdaBoost algorithm (Figure 6), 79.8% (1021) of those who are actually Customer Churns were predicted correctly, while 4.1% (283-1) were predicted incorrectly. In addition, 95.9% (6541) of those who are actually Existing Customers were predicted correctly, while 20.2% (259) were predicted incorrectly.

		Predicted		Σ
		Customer Churn	Existing Customer	
Actual	Customer Churn	79.8 %	4.1 %	1302
	Existing Customer	20.2 %	95.9 %	6800
Σ		1280	6822	8102

Figure 6. Confusion matrix – AdaBoost

When we look at the ROC curves for Customer Churn and Existing Customer in Figure 7, it cannot be said that the size of the area under the curves shows a good success in terms of classification success. In addition, in Figure 8, the recall and precision graphs also reveal the success of the model. While the area under the curve for the Customer Churn is 0.24, it is obtained as 0.998 for the Existing Customer.

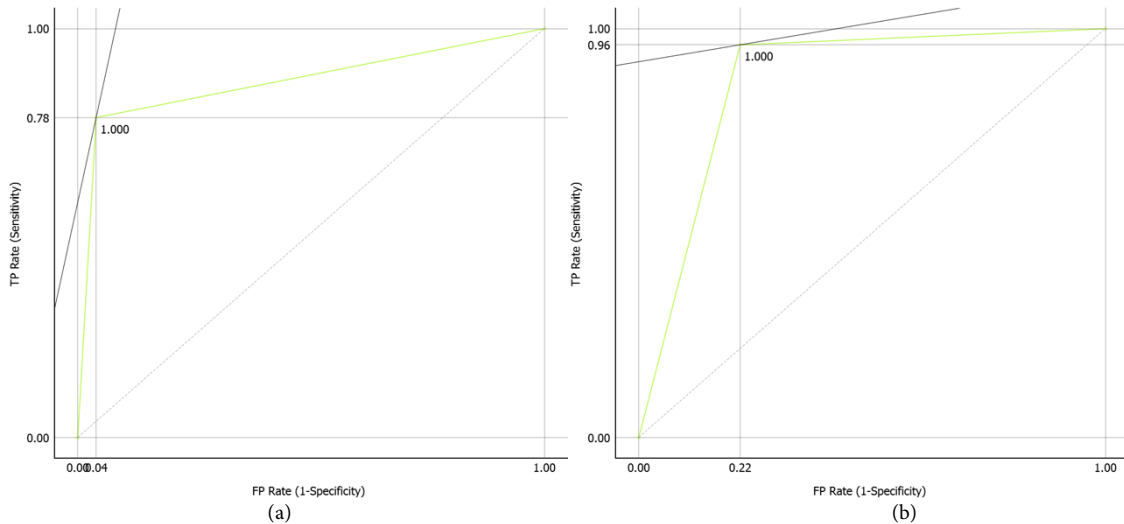


Figure 7. ROC analysis- AdaBoost a) Customer churn, b) Existing customer

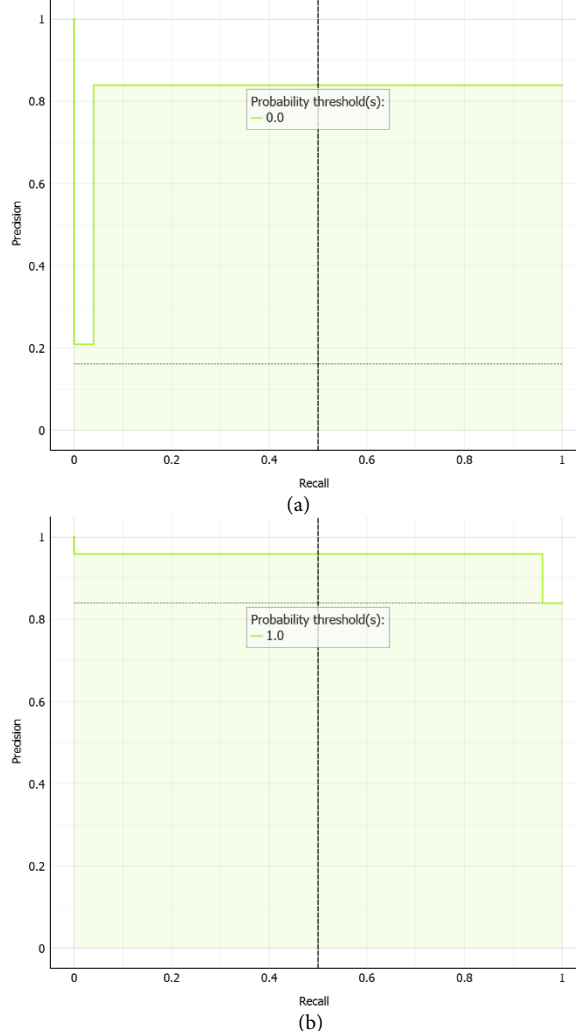


Figure 8. Performance curve (Precision-Recall) – AdaBoost a) Customer churn, b) Existing customer

3.1.3. Random forest

As seen in the Confusion Matrix created for the RF algorithm (Figure 9), 89.6% (1065) of those who are actually Customer Churns were predicted correctly and 3.4% (237) were predicted incorrectly. In addition, 96.6% (6676) of those who are actually Existing Customers were predicted correctly and 10.4% (124) were predicted incorrectly.

		Predicted		Σ
		Customer Churn	Existing Customer	
Actual	Customer Churn	89.6 %	3.4 %	1302
	Existing Customer	10.4 %	96.6 %	6800
Σ		1189	6913	8102

Figure 9. Confusion matrix – Random forest

When we look at the ROC curves for Customer Churn and Existing Customer in Figure 10, the size of the area under the curves shows high sensitivity and specificity in terms of classification success. In addition, in Figure 11, the recall and precision graphs also reveal the success of the model. While the area under the curve for Customer Churn is 0.636, it is obtained as 0.626 for Existing Customer.

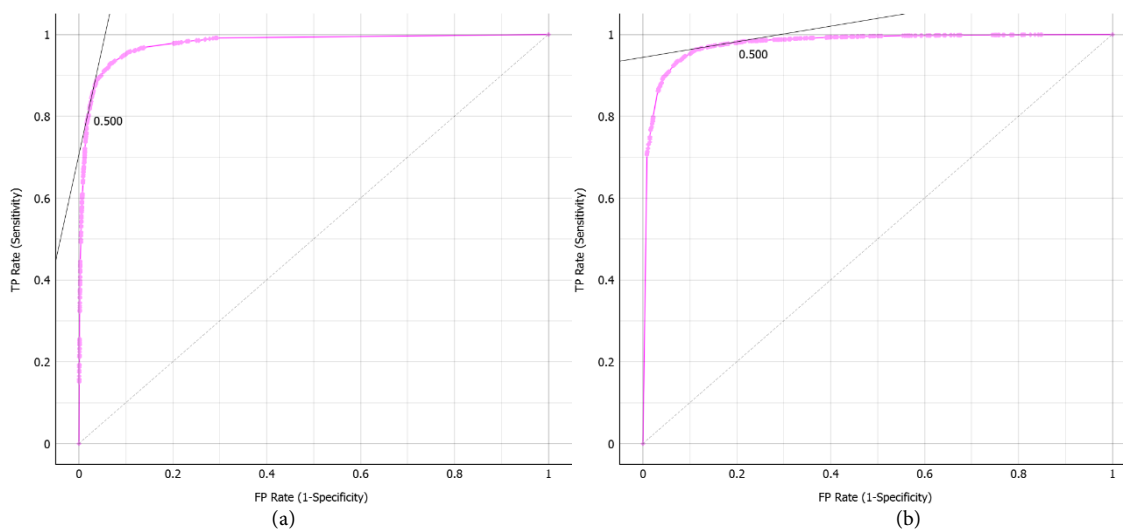


Figure 10. ROC analysis- Random forest a) Customer churn, b) Existing customer

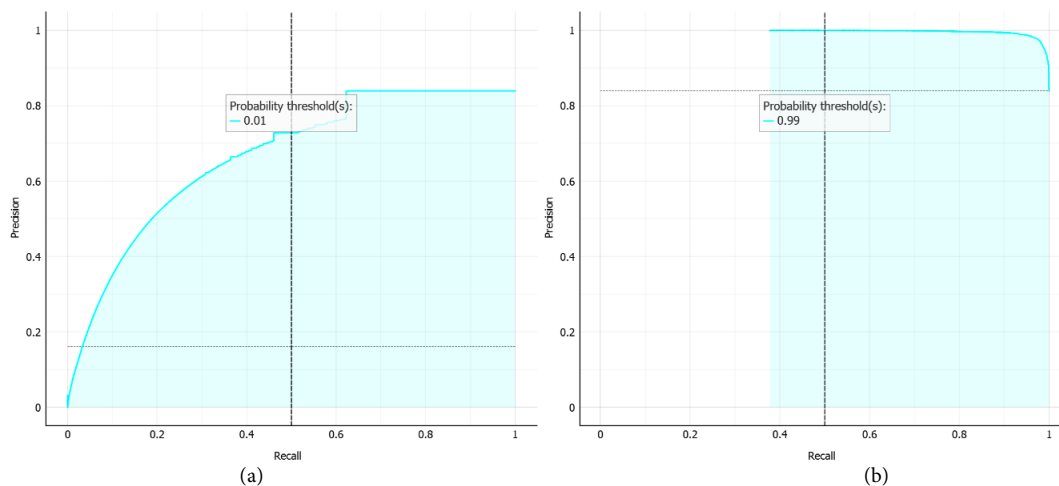


Figure 11. Performance curve (Precision-Recall) – Random forest a) Customer churn, b) Existing customer

3.1.4. Artificial neural network model

As seen in the Confusion Matrix created for the ANN algorithm (Figure 12), 82.3% (984) of those who are actually Customer Churns were correctly predicted, while 4.6% (318) were incorrectly predicted. In addition, 95.4% (6588) of those who are actually Existing Customers were correctly predicted, while 17.7% (212) were incorrectly predicted.

		Predicted		Σ
		Customer Churn	Existing Customer	
Actual	Customer Churn	82.3 %	4.6 %	1302
	Existing Customer	17.7 %	95.4 %	6800
Σ		1196	6906	8102

Figure 12. Confusion matrix – Neural network

When we look at the ROC curves for Customer Churn and Existing Customer in Figure 13, the size of the area under the curves shows high sensitivity and specificity in terms of classification success. In addition, in Figure 14, the recall and precision graphs also reveal the high success of the model. While the area under the curve for Customer Churn is 0.654, it is obtained as 0.995 for Existing Customer.

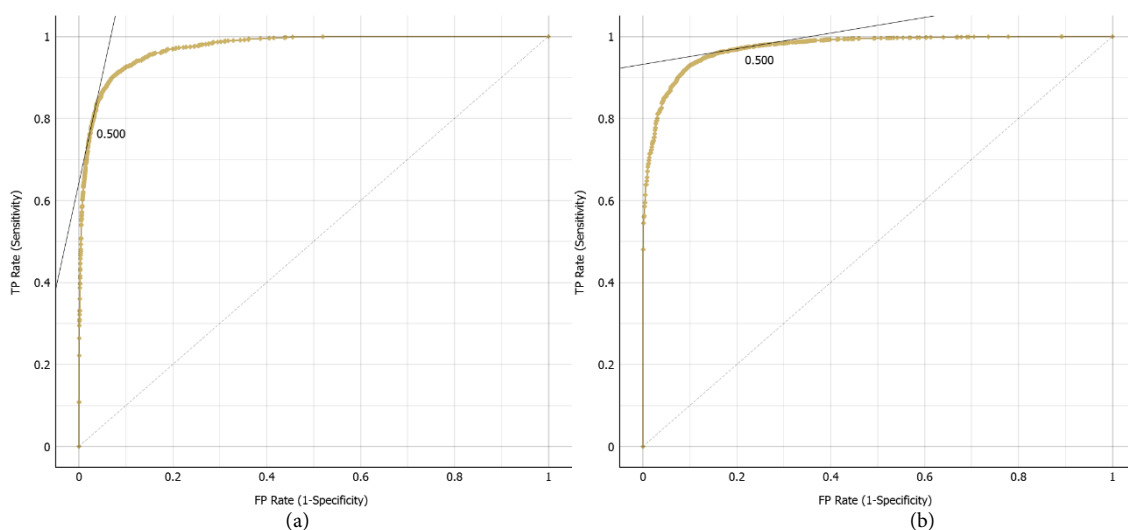


Figure 13. ROC analysis- Neural network a) Customer churn, b) Existing customer

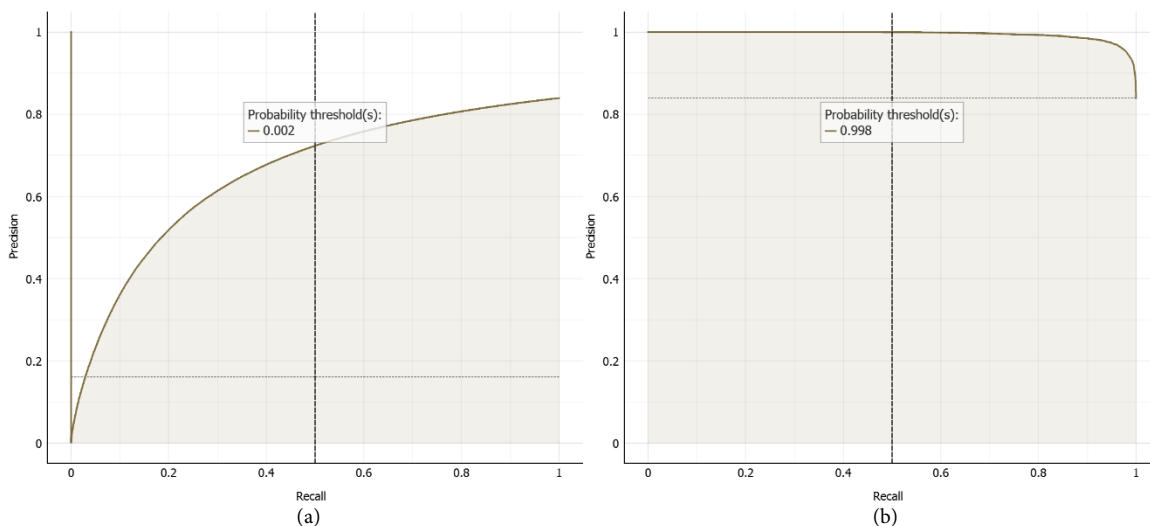


Figure 14. Performance curve (Precision-Recall) – Neural network a) Customer churn, b) Existing customer

This section includes a comparison of the general performance curves of the four models. In these graphs, the ratio of true positive data samples was analyzed according to the threshold of the classifier or the number of samples classified as positive. Although the results were close to each other, the best result was obtained from the Gradient Boosting and AdaBoost models.

3.2. Cumulative gains curve and t-SNE

In the study, the Cumulative Gains Curve and t-SNE distribution graph were also examined. The Cumulative Gains Curve shows the support, which is the ratio of true positive samples to current customers and the fraction of positively predicted samples to customer churn, assuming that the samples are sequential. According to the probability of the model being positive for Customer Churn, the larger the area between the curve and the baseline (dashed diagonal line), the better the model is. It can be said that the model created in the study is meaningful. Here, since the model is looked at for lost customers, we see that it remains below the line in the Performance Curve analysis. This table can be looked at again by multiplying the data in the data collection for customer churn.

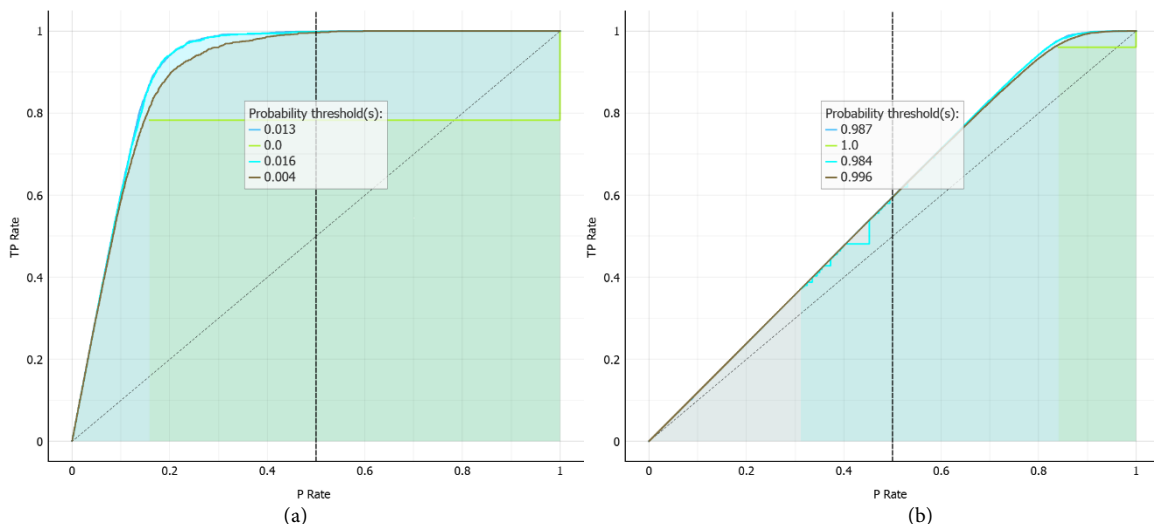


Figure 15. Cumulative gains curve a) Customer churn, b) Existing customer

Finally, a visualization is created using t-distributed stochastic neighbor embedding with t-SNE. The aim here is to reduce one dimension by mapping points into two-dimensional space according to their probability distributions. It accepts a data table or distance matrix as input.

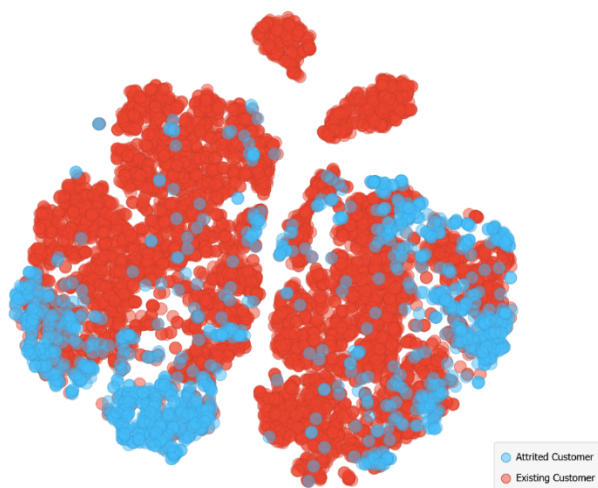


Figure 16. T- distributed stochastic neighbor embedding (t-SNE)

As seen in Figure 16, the distribution of the number of Customer Churns and Existing Customers generated by considering the distances between data points is shown. The graph clearly shows the distribution pattern of the two customer categories. There are clusters with a higher density of existing customers (red) in some regions and a higher density of customers who left (blue) in other regions. There are also areas where the two categories overlap significantly. The graph shows the regions where customers are more likely to be Churned or Existing. Identifying these regions can help understand the characteristics or behaviors that cause customer churn or customer retention. This shows that although there is some overlap, there are clear areas that can be targeted with specific strategies to reduce churn or increase retention.

As a result, the prediction performance results of the ANN, RF, SVM, KNN, DT, AdaBoost, LR, and GBoost models are given in Table 3 for comparison.

Table 3. Findings from all models

Model	AUC	CA	F1	Precision	Recall	MCC
GB	98,7	96,1	96	96	96,1	94,9
RF (1)	98,5	95,6	95,6	95,5	95,6	83,4
RF	97,7	95,1	95	95	95,1	81,3
ANN	97,3	94,3	94,2	94,2	94,3	78,3
LR	88,7	88,2	86,8	87,1	88,2	49,4
KNN (5)	88,3	89,1	88,7	88,5	89,1	57,1
AdaBoost	87,2	93,2	95,4	97,3	92,7	74,6
KNN (3)	85,5	88,8	88,4	88,2	88,8	56
DT	81,3	92,8	92,5	92,5	92,8	71,9
KNN (1)	75,7	87,3	87,2	87,1	87,3	52,3
SVM	67,9	66,3	70,5	79,1	66,3	19,5

When Table 3 is examined, it is clearly seen that the highest performance is GBoost; the lowest performance is obtained with the SVM model, and the other models produce results with similar and different values. At this stage, the results obtained from the models were compared with the experimental results in the literature. In Table 4, some of the studies in the literature related to customer churn prediction and summary information about the proposed study are given in the last line of the table. Models have been developed using various data mining and machine learning methods in these studies. Some of these and their details are summarized below:

The studies given in Table 4 show that various machine learning and data mining techniques have been successfully applied for customer churn prediction in different sectors. In particular, the highest success rate (99.67%) was obtained in study number 3, and in the table in general, it is seen that a success rate of over 95% was obtained in studies number 3 and 10. At this point, very little data was used in study number 3, which showed the highest performance. This situation also brings to mind that the model memorizes. In addition, studies number 14 and 15 also have high rates (around 95%).

The most striking study in the table is study number 2 with a very low success rate (68%). The reason for the low success in this study may be the use of the Naïve Bayes algorithm, which is not fully suitable for the study. In addition, the fact that the data number was too large (50000) and could not be included in the preprocessing/cleaning process can also be shown as a reason. As a result, a high success rate of 98.70% was obtained in the proposed study. Although this rate is not the highest, there is approximately 1 point difference between it and 99.67% (study number 3).

Table 4. Comparison of the models created in the study with the literature

No	Author(s)	Industry	Methods Used	Number of Data	Dataset Properties	Results	Performance
1	Keramati et al. (2014) [38]	Telecommunications	Decision Tree, Artificial Neural Networks, K-Nearest Neighbor, Support Vector Machines	3150	Data from a telecommunications company in Iran	Mixed methodology achieved high accuracy. Additionally, a new methodology for extracting influential features in the dataset was introduced and tested.	95%
2	Nath (2014) [39]	Telecommunications	Naive Bayes	50000	Geographic and demographic data, call details, service quality, package features	Customer churn analysis was conducted using the Naive Bayes method. A framework was developed to help customers analyze their own business.	68%
3	Dahiya and Bhatia (2015) [40]	Telecommunications	Logistic Regression, Decision Trees	50, 100, 608	50, 100, and 608 features	Decision Tree model showed the best performance.	99.67%
4	Kaynar et al. (2017) [41]	Telecommunications	Support Vector Machines, Artificial Neural Networks, Naive Bayes	4667	4667 customers, 21 features	Artificial Neural Networks provided more successful results than other methods.	91.35%
5	Rautio (2019) [42]	Software	Artificial Neural Network, Support Vector Machines, Random Forest	Unspecified	Business metrics, feature usage, platform usage metrics, service quality metrics, event metrics	Support Vector Machines showed the best performance.	85%
6	Ullah et al. (2019) [43]	Telecommunications	Random Forest, J48, Naive Bayes, Logistic Regression, IBK, and LWL	64,107 and 3,333	Data from 64,107 and 3,333 customers	Random Forest model achieved the highest accuracy.	88.63%
7	Özbaş (2020) [44]	Telecommunications	OptiScorer, Python, Knime	7043	21 columns (variables) and 7043 rows (customers)	Customer churn prediction was performed using the OptiScorer engine.	82%
8	Deng et al. (2021) [45]	Banking	Catboost, LightGBM, Random Forest	10000	Banking customer data	Random Forest model achieved the best results with 91% accuracy.	91%
9	Haddadi et al. (2022) [46]	Banking	Bi-LSTM, Decision Tree, Naive Bayes, Logistic Regression	50000	Customer data from a bank in Iran	Bi-LSTM model outperformed other models.	84%
10	Peng, K., Peng, Y., and Li, W. (2023) [47]	Banking	Seven classifier models including decision trees and neural networks	10000	Bank customer data with demographic and transaction features	Achieved high prediction accuracy; emphasized the importance of model interpretability in understanding churn factors. SMOTEENN proved more effective than SMOTE and ADASYN in handling unstable banking data.	96.08%
11	Özcan, B., Kayapınar, K., and Adem, K. (2023) [48]	Banking	Random Forest, Decision Tree, Gaussian, K-Nearest Neighbor, Adaboost, Logistic Regression	10000	Composed of 12 features	Random Forest algorithm yielded the highest accuracy rate. Other algorithms' success followed in the order of K-Nearest Neighbor, Decision Tree, Adaboost, Gaussian, and Logistic Regression.	84%
12	Khattak et al. (2023) [49]	General	Composite deep learning models	7033	Large-scale customer datasets with behavioral features, 20 different features	Deep learning techniques provided superior performance in churn prediction compared to traditional machine learning models.	81%
13	Mouli et al. (2024) [50]	General	Various classification models including logistic regression and support vector machines	7043	Customer data across multiple industries	Identified the most effective classification models for churn prediction, providing insights for businesses to select appropriate techniques.	85%
14	Vu, V. H. (2024, July) [51]	Banking	Combined feature selection methods with machine learning classifiers	Unspecified	Banking customer data with various attributes	The integrated approach improved prediction accuracy, aiding in early detection of potential churners in the banking sector.	95.13%

Table 4. Comparison of the models created in the study with the literature (Contunue)

No	Author(s)	Industry	Methods Used	Number of Data	Dataset Properties	Results	Performance
15	He, C., and Ding, C. H. (2024) [52]	General	Ensemble-Fusion model combining multiple machine learning algorithms	8500	Diverse customer data with feature selection	The proposed model outperformed traditional methods in predicting churn, demonstrating higher accuracy and robustness.	95.35%
16	Calp (2025)	Banking	RF, DT, Gradient Boosting, LR, ANN, KNN, SVM, and AdaBoost	10127	21 different variables in the dataset	The highest performance was achieved with Gradient Boosting (98.70%), while the lowest performance was with Support Vector Machines (67.9%).	98.70%

4. Conclusion and Recommendations

In this study, the churn of bank customers, their departure from the bank, or card cancellations were predicted using various machine learning algorithms. The fact that machine learning is a powerful tool in every field, has started to be used, and can find solutions to important problems has been effective in its use in this study. The algorithms used include RF, DT, GBoost, LR, ANN, KNN, SVM, and AdaBoost. All machine learning methods used were compared and evaluated. According to the results obtained from the models, GBoost showed the highest level of performance with a high accuracy rate, and a good result was obtained in predicting customer churn with this algorithm. The model created with SVM ranked last in terms of performance and remained below the performance expected from the algorithm. Despite all this, it has also been observed that the models have significant accuracy rates regarding credit card customer churn. At this point, much higher performances will be achieved by reaching more customers, obtaining more data, and recording this data. At this point, both increasing customer registration and using hybrid models will positively increase the success of the model. As a result, this study clearly showed that Credit Card Customer Churn can be effectively predicted with machine learning methods. Finally, the use of powerful algorithms such as deep learning or hybrid approaches is considered in the future planning of the study. In addition, it is planned to develop an online system where business managers can make effective decisions. The system in question can be developed within the scope of an expert system or decision support system, which will have some important features such as identifying customer situations, strengthening customer satisfaction, increasing customer loyalty, and being able to track customer movements instantly.

Conflict of Interest Statement

The author declare that there is no conflict of interest.

References

- [1] D. AL-Najjar, N. Al-Rousan and H. AL-Najjar, "Machine Learning to Develop Credit Card Customer Churn Prediction," *Journal of Theoretical and Applied Electronic Commerce Research*, vol. 17, no. 4, pp. 1529–1542, 2022. doi: 10.3390/jtaer17040077
- [2] S. Kim, K. S. Shin, and K. Park, "An application of support vector machines for customer churn analysis: Credit card case," In *International Conference on Natural Computation*, Berlin, Heidelberg: Springer Berlin Heidelberg, 27 – 29 August 2005, pp. 636–647, 2005. doi: 10.1007/11539117_91
- [3] A. Keramati, H. Ghaneei and S. M. Mirmohammadi, "Developing a prediction model for customer churn from electronic banking services using data mining," *Financial Innovation*, vol. 2, no. 1, pp. 2–13, 2016. doi: 10.1186/s40854-016-0029-6
- [4] D. Nettleton, *Commercial Data Mining: Processing, Analysis and Modeling for Predictive Analytics Projects* (1st ed.). San Francisco, CA, USA: Morgan Kaufmann Publishers Inc., 2014. doi: 10.1016/C2013-0-00263-0
- [5] M. A. H. Farquad, V. Ravi and S. B. Raju, "Churn prediction using comprehensible support vector machine: An analytical CRM application," *Applied Soft Computing*, vol. 19, pp. 31–40, 2014. doi: 10.1016/j.asoc.2014.01.031
- [6] R. Hejazinia and M. Kazemi, "Prioritizing factors influencing customer churn," *Interdisciplinary Journal of Contemporary Research in Business*, vol. 5, no. 12, pp. 227–236, 2014.
- [7] E. Domingos, B. Ojeme and O. Daramola, "Experimental analysis of hyperparameters for deep learning-based churn prediction in the banking sector," *Computation*, vol. 9, no. 3, pp. 2–19, 2021. doi: 10.3390/computation9030034
- [8] S. M. S. Hosseini, A. Maleki and M. R. Gholamian, "Cluster analysis using data mining approach to develop CRM methodology to assess the customer loyalty," *Expert Systems with Applications*, vol. 37, no. 7, pp. 5259–5264, 2010. doi: 10.1016/j.eswa.2009.12.070

- [9] İ. T. Ağım, "Makine Öğrenmesi Teknikleriyle iskonto/İştira Kredilerinin Değerlendirilmesi," M.Sc. İzmir Katip Çelebi Üniversitesi Fen Bilimleri Enstitüsü, 2024.
- [10] F. Chollet, "On the measure of intelligence," arXiv preprint arXiv:1911.01547, 2019. doi: 10.48550/arXiv.1911.01547
- [11] S. Savaş and S. Buyrukoğlu, *Teori ve Uygulamada Makine Öğrenmesi*, Cilt: 1, Nobel Akademik Yayıncılık, Ed.: Savaş, S ve Buyrukoğlu, S., pp. 302, 2022.
- [12] N. Gordini and V. Veglio, "Customers churn prediction and marketing retention strategies. An application of support vector machines based on the AUC parameter-selection technique in B2B e-commerce industry," *Industrial Marketing Management*, 2016, doi: 10.1016/j.indmarman.2016.08.003
- [13] M. Haenlein, "Social interactions in customer churn decisions: The impact of relationship directionality," *International Journal of Research in Marketing*, vol. 30, no. 3, pp. 236–248, 2013. doi: 10.1016/j.ijresmar.2013.03.003
- [14] A. Tamaddoni Jahromi, S. Stakhovych and M., Ewing, "Managing B2B customer churn, retention and profitability," *Industrial Marketing Management*, vol. 43, no. 7, pp. 1258–1268, 2014. doi: 10.1016/j.indmarman.2014.06.016
- [15] C.F. Tsai and Y.H. Lu, "Customer churn prediction by hybrid neural networks," *Expert Systems with Applications*, vol. 36, no. 10, pp. 12547–12553, 2009. doi: 10.1016/j.eswa.2009.05.032
- [16] M. Fathian, Y. Hoseinpoor and B. Minaei-Bidgoli, "Offering a hybrid approach of data mining to predict the customer churn based on bagging and boosting methods," *Kybernetes*, vol. 45, no. 5, pp. 732–743, 2016. doi: 10.1108/K-07-2015-0172
- [17] Kaggle, [Online]. Available: <https://www.kaggle.com/datasets/sakshigoyal7/credit-card-customers>. [Accessed: Sept. 14, 2024].
- [18] S. J. Rigatti, "Random forest," *Journal of Insurance Medicine*, vol. 47, no. 1, pp. 31-39, 2017. doi: 10.17849/inm-47-01-31-39.1
- [19] B. Özkan, C. Parim and E. Çene, "Ülkelerin Gelişmişlik Düzeylerinin Karar Ağacı ve Rastgele Orman Yöntemleriyle Tahmin Edilmesi," *EKOIST Journal of Econometrics and Statistics*, Sayı: 38, ss. 87- 104, 2023. doi: 10.26650/ekoist.2023.38.1172190
- [20] A. Singhal, N. Kumari, P. Ghosh, Y. Singh, S. Garg, M. P. Shah, ... and D. K. Chauhan, "Optimizing cellulase production from *Aspergillus flavus* using response surface methodology and machine learning models," *Environmental Technology and Innovation*, vol. 27, no. 102805, pp. 2-15, 2022. doi: 10.1016/j.eti.2022.102805
- [21] Z. Özdemir Güler, M. A. Bakır and F. Kardiyen, "Destek vektör makinesi ile elde edilen olasılık çıktılarına dayalı yeni bir istatistiksel süreç izleme yöntemi," *Gazi Üniversitesi Mühendislik Mimarlık Fakültesi Dergisi*, vol. 39, no. 2, pp. 1099-1112, 2023, doi: 10.17341/gazimmfd.1192354
- [22] J. R. Quinlan, *C4.5: Programs for Machine Learning*. Morgan Kaufmann, San Mateo, CA, pp. 302, 1993.
- [23] Ö. Gür, "Karar ağacı destekli hile tespiti ve bir uygulama," *Alanya Akademik Bakış*, vol. 7, no. 1, pp. 511-528, 2023. doi: 10.29023/alanyaakademik.1196078
- [24] F. Bulut, "Determining Heart Attack Risk Ration Through AdaBoost," *Celal Bayar University Journal of Science*, vol. 12, no. 3, pp. 459-472, 2016. doi: 10.18466/cbayarfbe.280652
- [25] E. A. Sağbaş, "MFCC Öznitelikleri ve AdaBoost Topluluk Öğrenme Yöntemi Kullanılarak Uyku Seslerinin Sınıflandırılması," *Computer Science (IDAP-2023)*, pp. 31-36, 2023. doi: 10.53070/bbd.1347221
- [26] A. Callens, D. Morichon, S. Abadie, M. Delpy and B. Liquet, "Using Random Forest and gradient boosting trees to improve wave forecast at a specific location," *Applied Ocean Research*, vol. 104, no. 10233, 2020. doi: 10.1016/j.apor.2020.102339
- [27] E. Güvenç, M. Sakal, G. Çetin and O. Özkaraca, "Öğrencilerin Dersteki Niteliklerinin Makine Öğrenmesi Teknikleri Kullanılarak Sınıflandırılması," *Düzce Üniversitesi Bilim ve Teknoloji Dergisi*, vol. 10, no. 3, pp. 1359-1371, 2022. doi: 10.29130/dubited.1017202
- [28] H. Karamanli, T. Yalcinoz, M. A. Yalcinoz and T. Yalcinoz, "A prediction model based on artificial neural networks for the diagnosis of obstructive sleep apnea," *Sleep and Breathing*, vol. 20, pp. 509-514, 2016. doi: 10.1007/s11325-015-1218-7
- [29] M. B. Odabaşı and M. C. Toklu, "Comparative Analysis of Artificial Neural Networks and Deep Learning Algorithms for Crypto Price Forecast," *Journal of Intelligent Systems: Theory and Applications*, vol. 6, no. 2, pp. 96-107, 2023. doi: 10.38016/jista.1228629
- [30] M. H. Calp, "İşletmeler için personel yemek talep miktarının yapay sinir ağları kullanılarak tahmin edilmesi," *Politeknik Dergisi*, vol. 22, no. 3, pp. 675-686, 2019. doi: 10.2339/politeknik.444380
- [31] P. K. Syriopoulos, N. G. Kalampalikis, S. B. Kotsiantis, and M. N. Vrahatis, "kNN Classification: a review," *Ann Math Artif Intell*, pp. 1–33, Sep. 2023. doi: 10.1007/S10472-023-09882-X/METRICS
- [32] J. Zhang, Z. Bian and S. Wang, "Bayes-Decisive Linear KNN with Adaptive Nearest Neighbors" *International Journal of Intelligent Systems*, vol. 2024, no. 1, pp. 6664942, 2024. doi: 10.1155/2024/6664942
- [33] J. A. Hanley and B. J. McNeil, "A method of comparing the areas under receiver operating characteristic curves derived from the same cases," *Radiology*, vol. 148, no. 3, pp. 839-843, 1983. doi: 10.1148/radiology.148.3.6878708

- [34] K. H. Zou, A. J. O'Malley and L. Mauri, "Receiver-operating characteristic analysis for evaluating diagnostic tests and predictive models," *Circulation*, vol. 115, no. 5, pp. 654-657, 2007. doi: 10.1161/CIRCULATIONAHA.105.594929
- [35] D. M. Powers, "Evaluation: from precision, recall, and F-measure to ROC, informedness, markedness, and correlation," arXiv preprint arXiv:2010.16061, 2020. doi: 10.9735/2229-3981
- [36] N. Japkowicz and M. Shah, *Evaluating learning algorithms: a classification perspective*. Cambridge University Press, 2011. doi: 10.1017/CBO9780511921803
- [37] J. Davis and M. Goadrich, "The relationship between Precision-Recall and ROC curves," In Proceedings of the 23rd international conference on Machine learning, 25 – 29 June 2006, pp. 233-240, 2006. Doi: 10.1145/1143844.1143874
- [38] A. Keramati, R. Jafari-Marandi, M. Aliannejadi, I. Ahmadian, M. Mozaffari and U. Abbasi. "Improved churn prediction in telecommunication industry using data mining techniques", *Applied Soft Computing*, 24, pp. 994-1012, 2014. doi: 10.1016/j.asoc.2014.08.041
- [39] S. V. Nath, and R. S. Behara. "Customer churn analysis in the wireless industry: A data mining approach," In *Proceedings-annual meeting of the decision sciences institute*, vol. 561, pp. 505-510, November 2003.
- [40] K. Dahiya and S. Bhatia. "Customer churn analysis in telecom industry," In *2015 4th International Conference on Reliability, Infocom Technologies and Optimization (ICRITO) Trends and Future Directions*, 2-4 Sept. 2015, pp. 1-6. IEEE, 2015. doi: 10.1109/ICRITO.2015.7359318
- [41] O. Kaynar, M. F. Tuna, Y. Görmez and M. A. Deveci, "Makine öğrenmesi yöntemleriyle müşteri kaybı analiz," *Cumhuriyet Üniversitesi İktisadi ve İdari Bilimler Dergisi*, vol. 18, no. 1, pp. 1-14, 2017.
- [42] A. J. O. Rautio. "Churn prediction in SaaS using machine learning," (Master's thesis), 2019.
- [43] I. Ullah, B. Raza A. K. Malik, M. Imran, S. U. Islam, and S. W. Kim. "A churn prediction model using random forest: analysis of machine learning techniques for churn prediction and factor identification in telecom sector," *IEEE Access*, 7, pp. 60134-60149, 2019. doi: 10.1109/ACCESS.2019.2914999
- [44] F. S. Özbaş, Müşteri Kayıp Tahmini (Customer Churn Prediction), YBS Ansiklopedi, vol. 8, no. 1, Haziran 2020.
- [45] Y. Deng, D. Li, L. Yang, J. Tang and J. Zhao, "Analysis and prediction of bank user churn based on ensemble learning algorithm," *Proceedings of 2021 IEEE International Conference on Power Electronics, Computer Applications, ICPECA 2021*, 22-24 January 2021, pp. 288–291, 2021. doi: 10.1109/ICPECA51329.2021.9362520
- [46] S. J. Haddadi, M. O. Mohammadi, M. Bahrami, E. Khoeni, M. Beygi and M. H. Khoshkar, "Customer churn prediction in the iranian banking sector," In *2022 International Conference on Applied Artificial Intelligence (ICAPAI)*, 5-5 May 2022, pp. 1-6, IEEE, 2022. doi: 10.1109/ICAPAI55158.2022.9801574
- [47] K. Peng, Y. Peng and W. Li, "Research on customer churn prediction and model interpretability analysis," *PLOS One*, vol. 18, no. 12:e0289724, 2023. doi: 10.1371/journal.pone.0289724
- [48] B. Özcan, K. Kayapınar and K. Adem, "Gelişen Teknoloji ile Bankacılık Sektöründe Veri Analitiği: Müşteri Kaybı Tahmini İçin Makine Öğrenmesi Yaklaşımları," *Uluslararası Sivas Bilim ve Teknoloji Üniversitesi Dergisi*, vol. 2, no 1, pp. 74-84, 2023.
- [49] A. Khattak, Z. Mehak, H. Ahmad, M. U. Asghar, M. Z. Asghar and A. Khan, "Customer churn prediction using composite deep learning technique. *Scientific Reports*," vol. 13, no. 1, pp. 17294, 2023. doi: 10.1038/s41598-023-44396-w
- [50] K. C. Mouli, C. V. Raghavendran, V.Y. Bharadwaj, G. Y. Vybhavi, C. Sravani, K. M. Vafaeva ... and L. Hussein, "An analysis on classification models for customer churn prediction," *Cogent Engineering*, vol. 11, no. 1, pp. 2378877, 2024 doi: 10.1080/23311916.2024.2378877
- [51] V. H. Vu, "An Efficient Customer Churn Prediction Technique Using Combined Machine Learning in Commercial Banks," In *Operations Research Forum*, vol. 5, no. 3, pp. 66. Cham: Springer International Publishing, July, 2024. doi: 10.1007/s43069-024-00345-5
- [52] C. He and C. H. Ding. "A novel classification algorithm for customer churn prediction based on hybrid," *Ensemble-Fusion model. Scientific Reports*, vol. 14, no. 1, pp. 20179, 2024. doi: 10.1038/s41598-024-71168-x

This is an open access article under the CC-BY license



GAZİ

JOURNAL OF ENGINEERING SCIENCES

Mechanical Properties of SLJs with Graphene and MWCNT Nanoparticle-Doped Hybrid Polyurethane Adhesives on Epoxy-Based Carbon Fiber Reinforced Composite Plates

Mehmet Tongur^{a*}, Necati Ataberk^b

Submitted: 30.10.2024 Revised: 26.12.2024 Accepted: 10.02.2025 doi:10.30855/gmbd.070525N03

ABSTRACT

In this study, we investigated the mechanical effect of by weight of 0.05%, 0.1% and 0.15% Graphene Nanoplates (GNPs) and MWCNTs doped polyurethane adhesives on single lap joint of Epoxy based and Carbon Fiber Reinforced Composite (CFRP) plates. First of all, Nanocomposite adhesive was produced by adding different weight ratios of nanoparticles into polyurethane adhesive. Then, the tensile test samples were produced using these adhesives and tensile tests were performed in accordance with the ASTM D 882 standard. According to the obtained results, the additive ratios showing the best mechanical properties were determined and single lap joints (SLJ) were produced. Then, the mechanical properties of the SLJ were tested in accordance with the ASTM D1002-10 standard under a constant tensile loading ratio. The highest tensile strength was observed in the 05GR15CNT sample with an increase of 52.67% (14.58 MPa) among the tensile test specimens. On the other hand, the highest shear strength was obtained in the 10GR10CNTSLJ sample with an increase of 14.80% (15.51 MPa) for the SLJ specimens. The distribution of the nanoparticles and the morphology of the failure surfaces were analyzed by scanning electron microscopy (SEM) images.

Keywords:

Mechanical Properties,
Tensile Test,
Nano Particle Doped
Polyurethane Adhesives,
Scanning Electron Microscopy

^{a,*} Necmettin Erbakan University
Engineering and Architectural Faculty,
Mechanical Engineering Department,
Konya, Türkiye
Orcid: 0000-0002-5847-3295
E mail: mehmettongur@ahievran.edu.tr

^b Necmettin Erbakan University
Engineering and Architectural Faculty,
Mechanical Engineering Department,
Konya, Türkiye
Orcid: 0000-0002-5394-9549
E mail: nataberk@erbakan.edu.tr

^{*}Corresponding author:
mehmettongur@ahievran.edu.tr

Grafen ve MWCNT Nanoparçacık Katkılı Poliüretan Yapıştırıcı ile Birleştirilmiş Epoksi Bazlı Karbon Fiber Takviyeli Kompozit Levhaların Tek Taraflı Bindirmeli Bağlantılarının Mekanik Özellikleri

ÖZ

Bu çalışmada, epoksi esaslı karbon fiber takviyeli kompozit (CFRP) plakaların tek taraflı bindirme bağlantılarda, ağırlıkça %0.05, %0.1 ve %0.15 grafen nanoparçacık (Gr) ve çok duvarlı karbon nanotüp (ÇCKNT) katkıli poliüretan yapıştırıcıların mekanik etkisi incelenmiştir. İlk olarak, farklı ağırlık oranlarında nanoparçacıklar poliüretan yapıştırıcıya eklenerek nanokompozit yapıştırıcı üretilmiştir. Daha sonra, bu yapıştırıcılar kullanılarak çekme testi numuneleri üretilmiş ve çekme testleri ASTM D 882 standardına uygun olarak gerçekleştirilmiştir. Elde edilen sonuçlara göre en iyi mekanik özellikleri gösteren katkı oranları belirlenmiş ve tek taraflı bindirme bağlantıları (TTBB) üretilmiştir. Ardından, TTBB'nin mekanik özellikleri sabit çekme yüklemeye oranı altında ASTM D1002-10 standardına uygun olarak test edilmiştir. Çekme test numuneleri arasında en yüksek çekme dayanımı, %52.67 artışla (14.58 MPa) 05GR15CNT numunesinde gözlemlenmiştir. Öte yandan, TTBB numuneleri arasında en yüksek kayma dayanımı, %14.80 artışla (15.51 MPa) 10GR10CNTSLJ numunesinde elde edilmiştir. Nanoparçacıkların dağılımı ve hasar yüzeylerinin morfolojisi, taramalı elektron mikroskobu (SEM) görüntüleri ile analiz edilmiştir.

Anahtar Kelimeler :

Mekanik Özellikler,
Çekme Testi,
Nano Parçacık Katkılı
Poliüretan Yapıştırıcılar,
Taramalı Elektron Mikroskobu

To cite this article : M.Tongur and N. Ataberk "The Mechanical Properties of Single Lap Joints with Graphene and MWCNT Nanoparticle-doped Polyurethane Adhesive on Epoxy based Carbon Fiber Reinforced Composite Plates", Gazi Journal of Engineering Sciences, vol.11, no.1, pp. 35-47, 2025. doi:10.30855/gmbd.070525N03

1. Introduction

Adhesive is defined as a chemical bonding material applied to the surfaces of materials to bind and hold them together [1]. Adhesive bonds are preferred due to their advantages such as addressing the shortcomings of traditional joining methods, combining different materials, and providing uniform stress distribution [2]. A range of adhesive types, including polyurethane, epoxy, acrylic, silicone, and latex, are available for diverse structural applications [3]. Polyurethane adhesives (PU) are essential in numerous industries because of their versatility and superior performance attributes [4]. PU adhesives are utilized in various applications, thanks to their outstanding resistance to external factors, including as coatings, binders for efficient processes like seawater desalination, sealing components, foam in sandwich panels, adhesives for industrial purposes, and even in biomedical applications [5]. Due to their extensive range of applications, various methods have been proposed to increase the mechanical properties of structural adhesives. It has been observed that the strength of adhesive joints depends on the type and surface quality of the adherend, the application and curing techniques of the adhesive, the size of the adhesive joints, testing under different loading conditions, and environmental factors such as temperature and humidity [6]. In addition to these properties, the incorporation of nanoparticle reinforcements into adhesives has emerged as a prominent method for enhancing the strength of adhesive bonds [7]. Nanoparticles, such as aluminum oxide (Al₂O₃), silica (SiO₂), nano clay, rubber particles, carbon black, graphite, GNPs, MWCNTs, and fullerenes, are advanced materials that offer a wide range of opportunities for obtaining nanocomposite materials [8]. MWCNTs and GNPs with exceptional properties have gained considerable recognition among researchers. Numerous studies have investigated the effects of these components in detail [9]. MWCNTs have an extremely high aspect ratio and are regarded as one-dimensional nanomaterials with exceptional mechanical properties. Their unique structure and outstanding mechanical and physical properties render them advanced fillers for the development of new composite adhesives [10]. Gilad Otorgust et al. [11] developed a nanocomposite adhesive by adding MWCNTs at concentrations of 0.1 to 0.4 wt% to structural polyurethane (PU) adhesives with the aim of improving their properties. According to SLJ shear test results, the bonded shear strengths increased by up to 64% and 22%, respectively. Wernik et al [7] conducted tensile tests on dogbone specimens, tensile bond tests, double lap shear tests, and double cantilever beam fracture toughness tests to experimentally investigate the mechanical properties of MWCNT-reinforced epoxy adhesives. Experimental observations indicate that the greatest improvement in measured properties occurs at a critical carbon nanotube concentration of approximately 1.5 wt%. However, at concentrations exceeding this critical value, the properties begin to degrade, sometimes falling below the levels of pure epoxy. Ozkan et al [12] investigated the effects of nanoparticle hybridization on the shear and flexural performance of SLJs of glass fiber reinforced polymer (GFRP) composites. For this purpose, MWCNT and silica nanoparticles were incorporated into the epoxy adhesive at various concentration rates. The effects of these nanoparticles on adhesion performance under different loads were analyzed through three-point bending tests and single-lap shear tests. The maximum shear and flexural strengths were achieved with the combination of 0.5 wt.% MWCNT and 0.25 wt.% nano-silica particles, showing improvements of 45.4% and 63.2% respectively, compared to pure samples. Scanning electron microscopy (SEM) was used to examine fracture mechanisms and failure modes, revealing that nanoparticle-doped samples exhibited higher load-bearing capability, with observed failure mechanisms including crack deviation, crack pinning, pull-out and bridging. Jia et al [13] conducted an experimental study to investigate the mode I fracture resistance of epoxy construction adhesive reinforced with graphene nanoplatelets (GNPs) using double cantilever beam (DCB) samples. The study revealed that the incorporation of 0.25 wt% graphene resulted in a fivefold enhancement in mode I fracture toughness compared to the neat epoxy adhesive. However, increasing the graphene content further led to a decrease in fracture toughness due to the aggregation of graphene particles within the adhesive matrix. Research studies often use low-viscosity laminating resins to facilitate the effective mixing and uniform dispersion of nanoparticles in adhesive formulations [14]. When nanoparticle concentrations are ≤ 0.5 wt%, significant variations in adhesive performance [15], particularly in terms of mechanical strength enhancement, have been reported [16].

In complex structures, it is often necessary to join components in a way that maintains structural integrity under different loads and environmental conditions. While metals are typically joined using techniques such as riveting, bolting, gluing, brazing, and soldering, the joining methods for polymer matrix fiber-reinforced composites are predominantly limited to adhesive bonding. This highlights the essential role of adhesives in the effective assembly of these advanced composite materials [17]. Research on the mechanical strength of adhesive joints focuses on factors such as joint geometry, overlap length, adhesive thickness, material properties, and environmental conditions. In recent years, studies on the effects of nanoparticles added to polyurethane adhesives on mechanical and thermal properties have been limited. The literature shows that nanoparticles are generally used in epoxy-based adhesives, while research on polyurethane adhesives remains scarce.

Nanoparticles enhance the thermal, electrical, and mechanical properties of adhesives while also improving environmental resistance and aging performance. Therefore, it is possible to develop hybrid adhesives by incorporating nanoparticles into polyurethane adhesives. Polyurethane was preferred in this study due to its cost-effectiveness and wide range of applications, and the potential of polyurethane-based hybrid adhesives has been demonstrated.

In this study, neat and nanoparticle-added polyurethane adhesives were used to join the epoxy-based carbon fiber-reinforced composite plates. Tensile tests for dog-bone adhesive samples and SLJ tensile tests for adhesively jointed composite plates were conducted to obtain the mechanical properties. SEM analysis was performed to examine the fractured surfaces after tensile tests.

2. Materials And Method

2.1. Materials

In this study, the adhesive used is KLB 75, a two-component polyurethane-based adhesive supplied by Duratek® company. This adhesive consists of polyester-based polyols used as catalysts in suitable proportions, accounting for 80% of the components, and a curing isocyanate mixture comprising the remaining 20%. The viscosity of KLB 75 adhesive at room temperature is 1800 mPas, with a density of 1.35 ± 0.10 g/cm³. The curing time at room temperature when used in the proportions specified by the manufacturer (80% polyol by weight, 20% isocyanate) is approximately 1 to 2 hours. Graphene and MWCNT were used as nanoparticles. The MWCNTs utilized have an outer diameter ranging from 15 to 25 nm, an inner diameter between 5 and 10 nm, and lengths varying from 10 to 20 μ m. The properties of graphene include a purity of 99.5%, a diameter of 24 μ m, a specific surface area of 150 m²/g, and an elasticity modulus of 0.5 TPa. The nanoparticles were procured from Nanografi company. In this study, CFRP plates produced by Kompozitsan company were used as the adhered material. The CFRP plates consist of 8 layers and have a total thickness of 2 mm.

2.2. Preparation of nanoparticles doped polyurethane adhesive

For the purpose of adhering the composite plates, nanoparticles doped adhesives were prepared. Different ratios of nanoparticles added into the polyurethane resin were mixed using a Bandelin HD 2200 ultrasonic mixer to ensure a homogeneous distribution without compromising the structure of the polyurethane and nanoparticles to prevent overheating and maintain the stability of the polyurethane-nanoparticle mixture, the mixing was performed in a beaker containing ice water. Then the solution was subjected to degassing at room temperature under a vacuum of 0.25 bar for one hour to evacuate any entrapped air bubbles within the solution. Subsequently, a hardening agent was added at a concentration of 20% and mechanically mixed for 10 minutes to ensure uniform dispersion. Following this procedure, the nano-adhesive was prepared for application.

2.3. Preparing the surfaces of adhesive bonding samples

In the surface preparation of CFRP plates, the bonding surfaces were abraded perpendicular to the direction of tension using 240-grid SiC sandpaper. Following abrasion, the samples were sequentially rinsed with tap water and distilled water, and subsequently immersed in acetone for 10 minutes. The samples were then dried in a sterilized oven at 60°C for 20 minutes to complete the surface preparation process.

2.4. Manufacturing of dogbone and single lap joints samples

The nanoparticle-doped and pure polyurethane adhesives, produced with nanoparticle additives, were poured into metal molds prepared according to ASTM D638 [18] standards as Figure 1, following the casting process, the dogbone tensile samples were left to cure completely at room temperature for 72 hours, in accordance with the manufacturer's recommendation. At the end of this waiting period, the samples were prepared for tensile testing. The nanoparticle type, additive percentage by weight (%), and abbreviated names of the prepared samples are as shown in Table 1. Using the manufactured nano-composite adhesives, CFRP-CFRP single lap joints were produced in accordance with the dimensions specified in ASTM D1002 [19] standards (Figure 1). During the preparation of bonded joints with the adhesive, a specially designed fixture was utilized to ensure the materials remained stationary and to adjust the desired adhesive thickness. After completing this process and placing the topmost sample, the fixture was closed, and the SLJs samples was subjected to a 72-hour curing process at room temperature.

Table 1. Naming of the produced nanocomposite materials

Samples	Additive by Weight (%)	
	Graphene	MWCNT
PU	-	-
05GR	0.05	-
10GR	0.1	-
15GR	0.15	-
05CNT	-	0.05
10CNT	-	0.1
15CNT	-	0.15
05GR05CNT	0.05	0.05
05GR10CNT	0.05	0.1
05GR15CNT	0.05	0.15
10GR05CNT	0.1	0.05
10GR10CNT	0.1	0.1
10GR15CNT	0.1	0.15
15GR05CNT	0.15	0.05
15GR10CNT	0.15	0.1
15GR15CNT	0.15	0.15

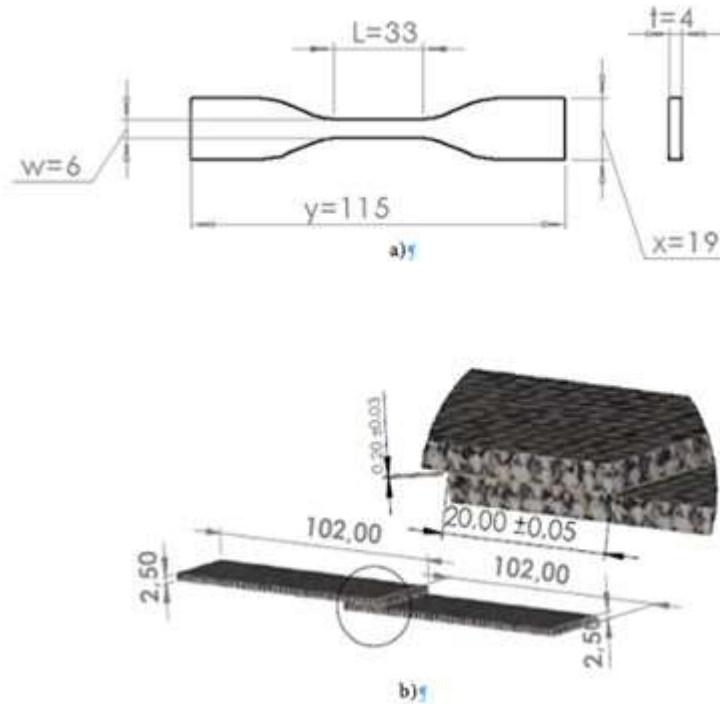


Figure 1. Schematic view of a) tensile sample, b) SLJ test sample

2.5. Characterization

Tensile tests of the dogbone samples were conducted according to ASTM D638, with the specimens loaded at a constant tensile speed of 2 mm/min until failure, while shear strength tests of composite-to-composite SLJs followed ASTM D1002 standards, with the SLJs tested at a tensile speed of 1 mm/min. Both tests were performed using a Shimadzu AGS-X tensile testing machine equipped with Trapezium-x software. An Epsilon 3560 model extensometer was employed to measure deformations in the adhesive regions of the single lap joint samples.

3. Experimental Results

3.1. Dogbone tensile tests results for nanocomposites

Tensile tests were conducted to determine the mechanical behavior of dogbone samples made from both doped and neat polyurethane adhesives, resulting in stress-strain curve (Figure 2). From these curves, the tensile strengths, maximum strains and toughness values of the nanoparticle-reinforced samples were determined. The results for tensile samples containing graphene nanoparticles at weight fractions of 0.05%, 0.10%, and 0.15% are presented in Table 2. The results for tensile samples containing MWCNT nanoparticles at weight fractions of 0.05%, 0.10%, and 0.15% are shown in Table 3. Additionally, the test results for hybrid adhesive tensile samples containing both graphene and MWCNT nanoparticles at weight fractions of 0.05%, 0.10%, and 0.15% are provided in Table 4. After the dog-bone tensile test, the tensile strength of the neat polyurethane sample was found to be 9.55 MPa. Compared to this, the maximum strain value was observed in the 05GR10CNT sample, with a 52.67% increase, reaching 14.58 MPa. The minimum strain value was recorded for the 10CNT sample at 7.57 MPa.

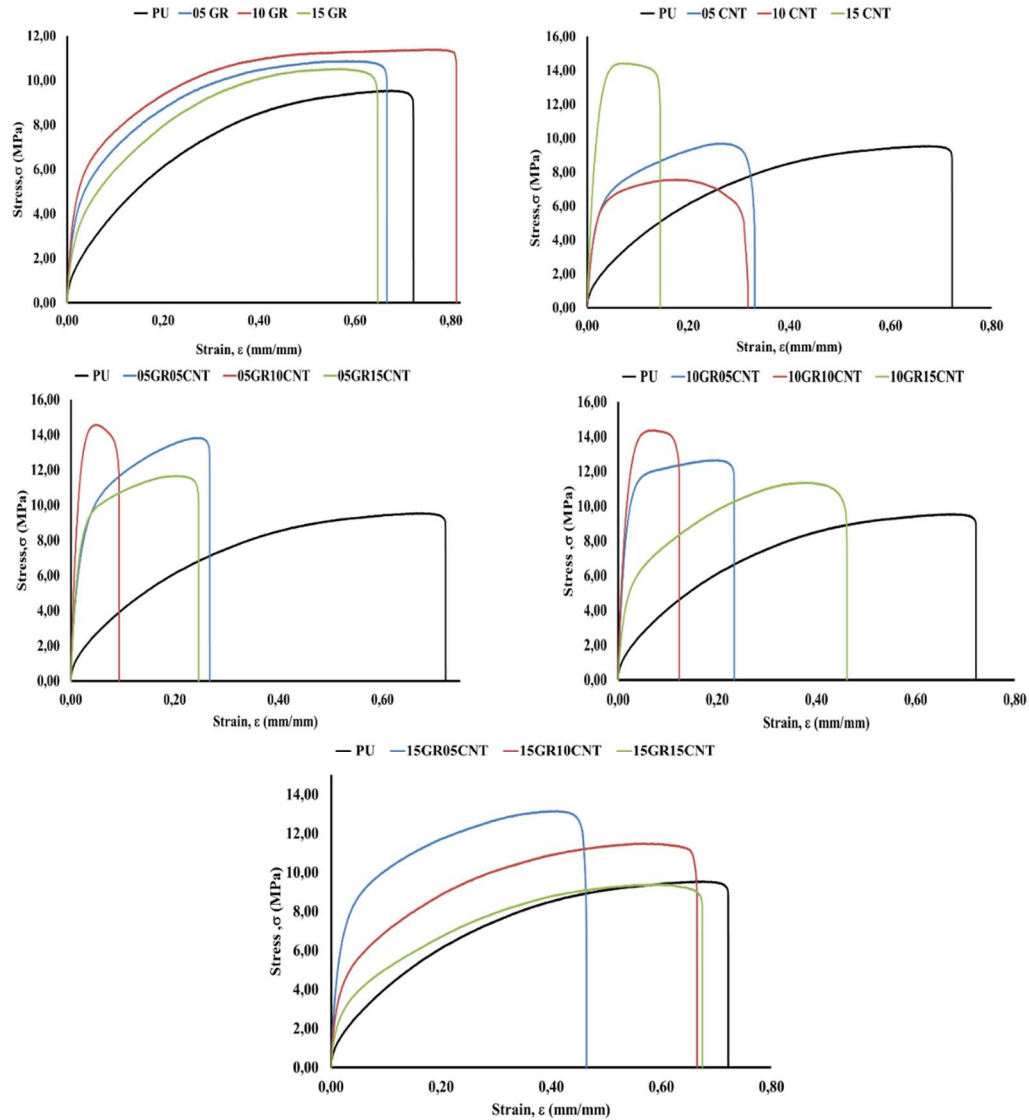


Figure 2. Stress-strain curves of pure Polyurethane adhesive and GNPs and MWCNTs nanoparticle doped adhesives

Table 2. Mechanical properties of pure polyurethane and graphene doped nanocomposites

Sample	Tensile Strength (MPa)	Maximum Strain (mm/mm)	Percentage Change (%)	Toughness (kJ/m ³)
PU	9.55±0.76	0.72±0.15	-	5.22±1.61
05GR	10.88±0.46	0.67±0.10	13.93	6.12±1.06
10GR	11.41±0.39	0.81±0.04	19.48	7.11±0.47
15GR	10.52±0.39	0.65±0.10	10.16	5.51±1.18

Table 3. Mechanical properties of polyurethane and MWCNT doped nanocomposites

Sample	Tensile Strength (MPa)	Maximum strain (mm/mm)	Percentage Change (%)	Toughness (kJ/m ³)
PU	9.55±0.76	0.72±0.15	-	5.22±1.61
05CNT	9.71±0.09	0.33±0.08	1.68	2.71±1.02
10CNT	7.57	0.31	-20.73	1.88
15CNT	14.43	0.14	51.10	2.06

Table 4. Mechanical Properties of graphene and mwcnt doped nanocomposites

Sample	Tensile Strength (MPa)	Maximum Strain (mm/mm)	Percentage Change (%)	Toughness (kJ/m ³)
PU	9.55±0.76	0.72±0.15	-	5.22±1.61
05GR05CNT	13.83±0.95	0.27±0.05	44.82	3.07±0.49
05GR10CNT	14.58±1.49	0.09±0.012	52.67	1.17±0.19
05GR15CNT	11.67±0.56	0.25±0.08	22.20	2.56±0.97
10GR05CNT	12.66±0.99	0.23±0.04	32.57	2.71±0.57
10GR10CNT	14.37±1.34	0.12±0.03	50.47	1.66±0.58
10GR15CNT	10.57±0.52	0.46±0.05	10.68	4.02±0.54
15GR05CNT	13.15±0.59	0.46±0.07	37.70	5.42±0.79
15GR10CNT	11.51±0.84	0.66±0.09	20.52	6.31±0.98
15GR15CNT	9.71±0.91	0.67±0.12	3.98	5.33±0.67

3.2. Shear tests of single lap joints

Based on the results obtained from the dogbone tensile tests, adhesives with the best mechanical properties were selected for lap shear tensile tests and the stress-strain (shear strain) curves were plotted. These curves are shown in Figure 3. The shear strengths, shear strain values, and shear modulus derived from the stress-strain curves are seen in Table 5. The results indicate that the addition of nanoparticles led to an increase in shear strengths. The maximum shear stress was achieved with the 10GR10CNTSLJ sample as 15.51 MPa, showing a 14.80% improvement compared to the unmodified PUSLJ sample. Additionally, the 10GRSLJ sample exhibited a 13.18% increase in shear stress, and the addition of 0.10 wt.% MWCNT to the 10GR10CNTSLJ sample resulted in a noticeable improvement in shear strength. This enhancement is attributed to the higher elastic modulus of MWCNTs compared to graphene nano particles, which provides better stress transfer and joint strength [20]. The highest shear strain for the maximum shear strength was observed for the 15GR05CNTSLJ sample, which has the maximum graphene nanoparticle content and the minimum MWCNT nanoparticle content.

Table 5. Mechanical properties of graphene and MWCNT doped single lap joints

Sample	Shear Strength (MPa)	Strain For Maximum Shear Stress (mm/mm)	Percentage Change (%)	Shear Modulus (GPa)
PUSLJ	13.51±0.43	1.83±0.20	-	9.32±1.83
10GRSLJ	15.29±1.16	1.43±0.32	13.18	10.06±1.4
15CNTSLJ	14.99±1.20	0.86±0.42	10.95	9.43±3.47
05GR10CNTSLJ	14.17±0.82	1.15±0.40	4.89	13.50±1.2
10GR10CNTSLJ	15.51±1.72	0.98±0.56	14.80	12.91±4.2
15GR05CNTSLJ	15.11±2.07	2.05±0.63	11.84	9.81±2.07

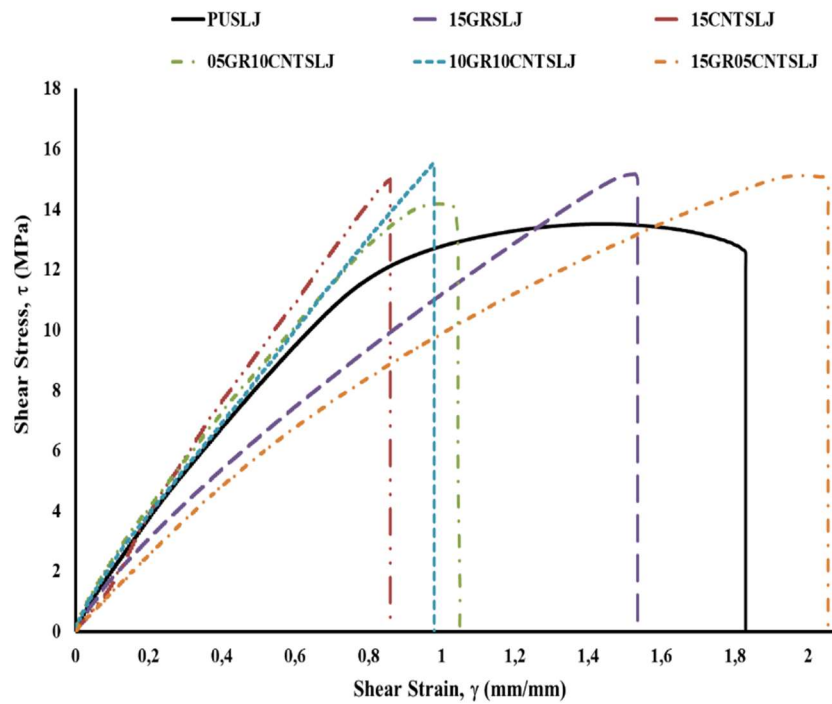


Figure 3. Shear stress- shear strain curves of single lap joints

3.3. SEM analysis of fractured surfaces of nanocomposites

After dogbone tensile and lap shear tensile tests, fracture surfaces were examined by ZEISS Evo LS 10 Scanning Electron Microscope (SEM). The fracture surfaces provide initial insights into the effects of nanoparticle additives on fracture behavior and mechanisms [21]. As shown in Figure 4a, the examination of neat polyurethane sample fracture surfaces reveals a smoother and more uniform surface, indicative of the material's weak resistance to crack initiation and propagation, characteristic of a brittle fracture process. After the tensile test, the fracture surfaces of thermosetting polymers display a mirror-like region, where cracks initially propagate slowly and then suddenly accelerate, forming a relatively smooth area. This mirror region is followed by a more pronounced rough zone with significant surface irregularities and flow lines (river pattern), which forms as the deformation rate increases, reflecting the final crack propagation [22]. Polymer-based adhesives can be considered more brittle than nanoparticle-reinforced adhesives due to the density of mirror regions, which indicates a weaker resistance to crack initiation and propagation [23]. The addition of nanoparticles to polyurethane adhesives enhances mechanical properties within the composite structure through various toughening mechanisms. These include nanoparticle rupture, crack development, bridging, shear band formation, plastic deformation, crack pinning, and crack bending [24]. SEM images of the 15GR tensile sample are presented in Figure 4b that highlights the regions of embedded graphene and matrix fracture on the fracture surface. Comparing these images reveals that the surface has a rougher texture and that the graphene effectively inhibits crack propagation [25]. In Figure 4b, the single-lap joint sample exhibits coarser fracture surfaces and features steeply inclined structures on its surface. Typically, increased surface roughness accompanies plastic deformation of the matrix, resulting in higher fracture energy expenditure. Consequently, the improved dispersion and distribution of graphene within the adhesive matrix led to enhanced shear strength and toughness values due to increased energy distribution during the fracture process. These indicators suggest cohesive damage in the adhesive region, thus confirming the high quality of the prepared composite surfaces and the produced nanocomposite adhesive [26].

SEM images of the 15CNT tensile sample are presented in Figure 4c, while SEM images of the 15CNTSLJ sample are shown in Figure 5c. The images clearly illustrate that the MWCNTs effectively arrest crack propagation across the matrix fracture surfaces through a bridging mechanism. The SEM images of the 15GR05CNT SLJ sample (Figure 5d) reveal that the addition of MWCNTs results in rougher regions on the

fracture surfaces of the adhesives compared to pure polyurethane. Significant toughness increasing observed in MWCNT-reinforced polyurethane adhesives include nanotube pull out, delamination, and bridging effects, which contribute to changes in crack propagation direction or branching[27]. In the 15GR05CNTSLJ sample (Figure 5d), the surface seems an even rougher texture due to the combined addition of graphene and MWCNTs. The nanoparticle reinforcement effectively inhibits crack propagation, thereby enhancing the toughness of the adhesive.

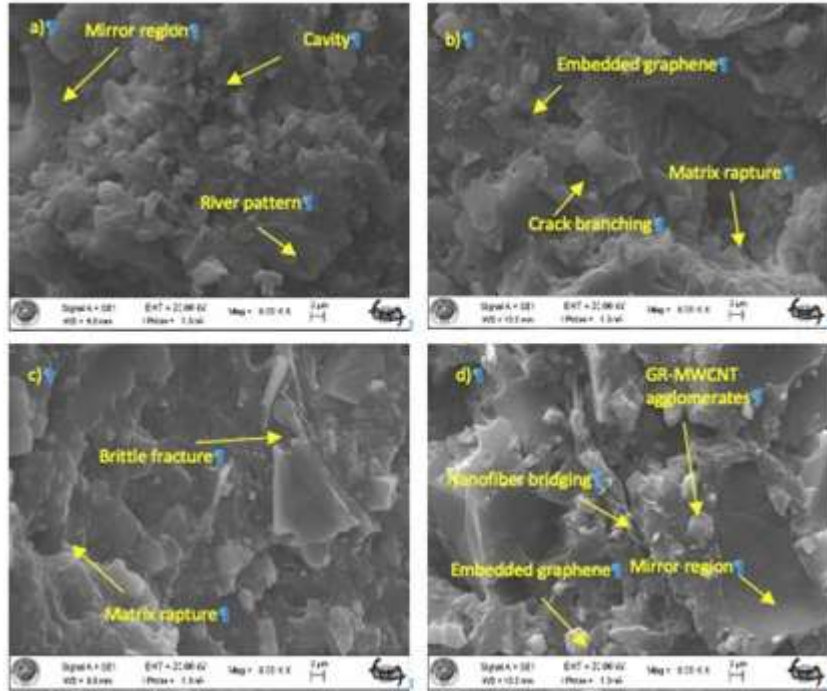


Figure 4. SEM images of nanocomposite materials' fractured surfaces of doped with MWCNT and graphene after tensile tests at 10kX magnification a) Neat polyurethane, b) 0.15% graphene doped c) 0.15%MWCNT doped, d) 0.10% graphene and 0.10%MWCNT doped

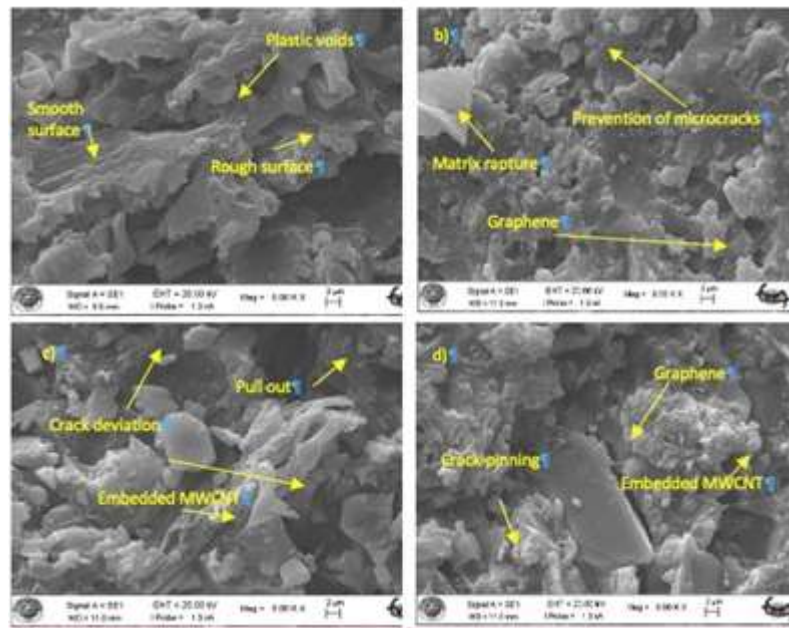


Figure 5. SEM images of nanocomposite materials' fractured surfaces of doped with MWCNT and graphene after shear tests at 10kX magnification a) Neat polyurethane, b) 0.15% graphene doped c) 0.15%MWCNT doped, d) 0.15% graphene and 0.05%MWCNT doped

3.3. Fractured surfaces of nanocomposites

Figure 6 presents the fracture surfaces of samples exhibiting the best mechanical properties resulting from shear strength tests of SLJs. There is no significant difference observed in the fracture surfaces among different nanoparticle-reinforced adhesives in terms of mechanical properties. The appearance of damaged surfaces in almost all SLJ samples is approximately the same. It is observed that the damage mechanisms of SLJ samples are cohesive failure because of adhesive remained on both fracture surfaces [28]. Examining the fracture surfaces of PUSLJ, 15GRSLJ, and 15CNTSLJ samples, no air cavities were observed. However, air cavities were observed in samples with high nanoparticle contents, such as 05GR10CNTSLJ, 10GR10CNTSLJ, and 15GR05CNTSLJ. This condition is interpreted as contributing to the reduction in mechanical properties [29].

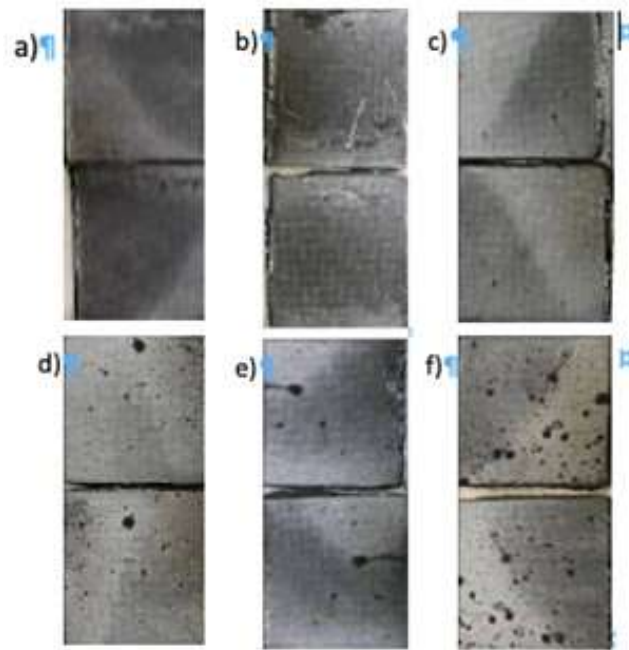


Figure 6. Macroscopic images of the broken surfaces of SLJ connections;
a) PUSLJ, b) 15GRSLJ, c) 15CNTSLJ, d) 05GR10CNTSLJ e) 10GR10CNTSLJ and f) 15GR05CNTSLJ

3. Results and Discussion

In this study, the mechanical properties of polyurethane nanocomposite adhesives, reinforced with graphene and MWCNT nanoparticles were experimentally investigated. For this purpose, SLJ and dogbone tensile samples were prepared, and their mechanical properties were examined. The major conclusions are presented as follows:

When examining the experimental results,

- It is observed that the addition of graphene nanoparticles increases the tensile strength of the samples while causing a decrease in the maximum strain values at failure. Additionally, the increasing in toughness values was observed with the increase in graphene content. If the MWCNT were added to the polyurethane adhesive, an increase in tensile strength was observed, while a decrease in unit strain values occurred. In contrast to the addition of graphene nanoparticles, the incorporation of MWCNT nanoparticles resulted in a decrease in toughness values.

- When graphene and MWCNT nanoparticles were used together as additives in dogbone tensile samples, the highest values for tensile strength, maximum strain, and toughness were achieved when the graphene content was maximum and the MWCNT content was minimum.

- Improvement in mechanical properties was observed compared to the pure polyurethane adhesive when nanoparticles were added to the polyurethane adhesive.

When examining the experimental results of composite-to-composite SLJ samples,

- An increase in shear strength was observed in all SLJs. The highest shear strength was observed in sample 10GR10CNTSLJ, where the graphene nanoparticle content was maximum and the MWCNT nanoparticle content was minimum. Upon examining the strain values at the maximum shear strength, it was observed that the maximum strain values decreased with the addition of MWCNT nanoparticles, while an increase in strain values was observed with the increase in graphene nanoparticle content.

- In SEM images, it has been determined that MWCNT nanoparticles and graphene nanoparticles halt the propagation of cracks between fracture surfaces by bridging, or causing the crack to branch. The formation of these types of damage indicates that a homogeneous mixture was achieved and that nanoparticle reinforcement, aimed at enhancing the strength and toughness of the adhesive, was successful.

Acknowledgment

This study was funded by the Scientific Research Projects Coordination Unit of Necmettin Erbakan University under project number 191319006.

Conflict of Interest Statement

The authors declare that there is no conflict of interest.

References

- [1] ASTM D907, "Standard Terminology of Adhesives," *American Society for Testing and Materials*. 2011. doi: 10.1520/D0907-12A.2
- [2] A. Y. Kanani, X. Hou, and J. Ye, "A novel dissimilar single-lap joint with interfacial stiffness improvement," *Composite Structures*, vol. 252, Nov. 2020. doi: 10.1016/J.COMPSTRUCT.2020.112741
- [3] A. J. Kinloch, "Adhesion and Adhesives," Dordrecht: Springer Netherlands, 1987. doi: 10.1007/978-94-015-7764-9
- [4] H. Dodiuk, I. Belinski, A. Dotan, and S. Kenig, "Polyurethane adhesives containing functionalized nanoclay," *Journal of Adhesion Science and Technology*, vol. 20, no. 12, pp. 1345–1355, 2006. doi: 10.1163/156856106778456573
- [5] P. Galvez, J. Abenojar, and M. A. Martinez, "Durability of steel-CFRP structural adhesive joints with polyurethane adhesives," *Composites Part B: Engineering*, vol. 165, pp. 1–9, May 2019. doi: 10.1016/j.compositesb.2018.11.097
- [6] N. Naat, Y. Boutar, S. Naïmi, S. Mezlini, and L. F. M. Da Silva, "Effect of surface texture on the mechanical performance of bonded joints: a review," *The Journal of Adhesion*, vol. 99, no. 2, pp. 166–258, Jan. 2023. doi: 10.1080/00218464.2021.2008370
- [7] J. M. Wernik and S. A. Meguid, "On the mechanical characterization of carbon nanotube reinforced epoxy adhesives," *Materials and Design*, vol. 59, pp. 19–32, 2014. doi: 10.1016/j.matdes.2014.02.034
- [8] C. Guo *et al.*, "Mechanical and thermal properties of multiwalled carbon-nanotube-reinforced Al₂O₃ nanocomposites," *Ceramics International*, 2020. doi: 10.1016/j.ceramint.2020.04.039
- [9] H. Ejaz, A. Mubashar, E. Uddin, Z. Ali, and N. Arif, "Effect of functionalised and non-functionalised GNPs addition on strength properties of high viscous epoxy adhesive and lap shear joints," *Polymer Testing*, vol. 113, p. 107680, 2022. doi: 10.1016/j.polymertesting.2022.107680
- [10] M. De Volder, S. Tawfik, R. Baughman, and A. J. Hart, "Carbon Nanotubes: Present and Future Commercial Application," *Science*, vol. 339, pp. 535–539, 2013. doi: 10.1126/science.1222453

- [11] G. Otorgust, H. Dodiuk, S. Kenig, and R. Tenne, "Important insights into polyurethane nanocomposite-adhesives; a comparative study between INT-WS2 and CNT," *European Polymer Journal*, vol. 89, pp. 281–300, Apr. 2017. doi: 10.1016/j.eurpolymj.2017.02.027
- [12] Ö. Özbek and M. Çakır, "MWCNT and Nano-silica Hybrids Effect on Mechanical and Fracture Characterization of Single Lap Joints of GFRP plates," *International Journal of Adhesion and Adhesives*, vol. 117, p. 103159, 2022. doi: 10.1016/j.ijadhadh.2022.103159
- [13] Z. Jia and G. Yuan, "Numerical study on the mechanical behavior of a polyurethane adhesive under high strain rate," *Composites Part B: Engineering*, vol. 158, pp. 131–140, 2019. doi: 10.1016/j.compositesb.2018.08.110
- [14] Z. Jia, J. Yu, Q. Liu, S. Yu, and Z. Wang, "Functionally graded adhesive joints with exceptional strength and toughness by graphene nanoplatelets reinforced epoxy adhesives," *International Journal of Adhesion and Adhesives*, vol. 125, p. 103402, Jul. 2023. doi: 10.1016/j.ijadhadh.2023.103402
- [15] H. Ejaz, A. Mubashar, E. Uddin, Z. Ali, and N. Arif, "Influence of MWCNTs on Strength Properties of High Viscous Epoxy Adhesive and Fracture Behavior of Adhesively Bonded Joints," *Theoretical and Applied Fracture Mechanics*, vol. 120, p. 103412, 2022. doi: 10.1016/j.tafmec.2022.103412
- [16] H. Ejaz, A. Mubashar, M. A. M, and S. Waqar, "Effect of GNP and MWCNT Addition on Lap Shear Strength of Adhesively Bonded Joints," in *2022 19th International Bhurban Conference on Applied Sciences and Technology (IBCAST)*, IEEE, Aug. 2022. pp. 116–121. doi: 10.1109/IBCAST54850.2022.9990107
- [17] A. Hallal, A. Elmarakbi, A. Shaito, and H. El-Hage, "Overview of Composite Materials and their Automotive Applications," *Advanced Composite Materials for Automotive Applications: Structural Integrity and Crashworthiness*, pp. 1–28, 2013. doi: 10.1002/9781118535288.CH1
- [18] ASTM D638, "Standard Test Method for Tensile Properties of Plastic," Available: <https://www.astm.org/d0638-10.html>. [Accessed: Oct. 09, 2022].
- [19] ASTM D1002-10, "Standard Test Method for Apparent Shear Strength of Single-Lap-Joint Adhesively Bonded Metal Specimens by Tension Loading (Metal-to-Metal)," in *ASTM Book of Standards*, ASTM International, 2019. pp. 1–5. doi: 10.1520/D1002-10R19
- [20] M. V. Cakir and D. Kinay, "MWCNT, nano-silica, and nano-clay additives effects on adhesion performance of dissimilar materials bonded joints," *Polymer Composites*, vol. 42, no. 11, pp. 5880–5892, Nov. 2021. doi: 10.1002/pc.26268
- [21] X. Jia, B. Liu, L. Huang, D. Hui, and X. Yang, "Numerical analysis of synergistic reinforcing effect of silica nanoparticle–MWCNT hybrid on epoxy-based composites," *Composites Part B: Engineering*, vol. 54, pp. 133–137, Nov. 2013. doi: 10.1016/j.compositesb.2013.04.002
- [22] M. S. Goyat, S. Suresh, S. Bahl, S. Halder, and P. K. Ghosh, "Thermomechanical response and toughening mechanisms of a carbon nano bead reinforced epoxy composite," *Materials Chemistry and Physics*, vol. 166, pp. 144–152, 2015. doi: 10.1016/j.matchemphys.2015.09.038
- [23] M. Rashad *et al.*, "Effect of graphene nanoplatelets (GNPs) addition on strength and ductility of magnesium-titanium alloys," *Journal of Magnesium and Alloys*, vol. 1, no. 3, pp. 242–248, 2013. doi: 10.1016/j.jma.2013.09.004
- [24] F. Ghadami, M. R. Dadfar, and M. Kazazi, "Hot-cured epoxy-nanoparticulate-filled nanocomposites: Fracture toughness behavior," *Engineering Fracture Mechanics*, vol. 162, pp. 193–200, 2016. doi: 10.1016/j.engfracmech.2016.05.016
- [25] R. Rodríguez, B. Pérez, and S. Flórez, "Effect of different nanoparticles on mechanical properties and curing behavior of thermoset polyurethane adhesives," in *Journal of Adhesion*, Taylor and Francis Inc., 2014. pp. 848–859. doi: 10.1080/00218464.2014.893509
- [26] Y. Wei, X. Jin, Q. Luo, Q. Li, and G. Sun, "Adhesively bonded joints – A review on design, manufacturing, experiments, modeling and challenges," *Composites Part B: Engineering*, vol. 276, p. 111225, May 2024. doi: 10.1016/j.compositesb.2024.111225
- [27] W.-S. Kim, I.-H. Yun, J.-J. Lee, and H.-T. Jung, "Evaluation of mechanical interlock effect on adhesion strength of polymer–metal interfaces using micro-patterned surface topography," *International Journal of Adhesion and Adhesives*, vol. 30, no. 6, pp. 408–417, Sep. 2010. doi: 10.1016/j.ijadhadh.2010.05.004
- [28] A. Nemati Giv, M. R. Ayatollahi, S. H. Ghaffari, and L. F. M. da Silva, "Effect of reinforcements at different scales on mechanical properties of epoxy adhesives and adhesive joints: a review," *The Journal of Adhesion*, vol. 94, no. 13, pp. 1082–1121, Nov. 2018. doi: 10.1080/00218464.2018.1452736

[29] R. Moriche, M. Sánchez, A. Jiménez-Suárez, S. G. Prolongo, and A. Ureña, "Strain monitoring mechanisms of sensors based on the addition of graphene nanoplatelets into an epoxy matrix," *Composites Science and Technology*, vol. 123, pp. 65–70, Feb. 2016. doi: 10.1016/j.compscitech.2015.12.002

This is an open access article under the CC-BY license



GAZİ

JOURNAL OF ENGINEERING SCIENCES

Classification of Encrypted Traffic with Machine Learning Algorithms

Nur Betül Demirel^a, Aydın Erden^b

Submitted: 04.06.2024 Revised: 09.12.2024 Accepted: 23.01.2025 doi:10.30855/gmbd.070525N04

ABSTRACT

Keywords: Machine Learning, Ensemble Learning, Encrypted Network Traffic, Network Traffic Classification, Cybersecurity

^a Marmara University,
Institute for Graduate Studies in Pure
Applied Sciences,
Dept. of Computer Engineering
34722 - İstanbul, Türkiye
Orcid: 0009-0001-9782-2507
e mail: nur.okur@tubitak.gov.tr

^b Marmara University,
Faculty of Business Administration,
Dept. of Management Information
Systems
34854 - İstanbul, Türkiye
Orcid: 0000-0002-5124-8335

*Corresponding author:
nur.okur@tubitak.gov.tr

Anahtar Kelimeler: Makine Öğrenmesi, Topluluk Öğrenmesi, Şifreli Ağ Trafik, Ağ Trafik Sınıflandırma, Siber Güvenlik

In this study, machine learning and ensemble learning methods have been developed for the classification of encrypted network traffic. Using the ISCXVPN2016 dataset, the performances of Light Gradient Boosting Machine (LGBM), k-Nearest Neighbors (KNN), Support Vector Machines (SVM), and Logistic Regression (LR) algorithms were compared. The data underwent various processes, such as feature selection, addressing class imbalances via Synthetic Minority Over-Sampling Technique (SMOTE), and hyperparameter optimization. The LGBM algorithm stood out due to its high accuracy and fast performance, providing an effective model for accurate and rapid classification of encrypted traffic. This work contributes to the development of effective solutions to detect and prevent cybersecurity threats.

Makine Öğrenmesi Algoritmaları ile Şifreli Trafik Sınıflandırılması

ÖZ

Bu çalışmada, şifreli ağ trafiğinin sınıflandırılmasına yönelik olarak makine öğrenmesi ve topluluk öğrenmesi yöntemleri geliştirilmiştir. Çalışmada, ISCXVPN2016 veri seti kullanılarak Light Gradient Boosting Machine (LGBM), k-Nearest Neighbours (KNN), Support Vector Machines (SVM) ve Logistic Regression (LR) algoritmalarının performansları karşılaştırılmıştır. Veriler özellik seçimi, Synthetic Minority Over-Sampling Technique (SMOTE) ile sınıf dengesizliklerinin giderilmesi ve hiperparametre optimizasyonu gibi süreçlerden geçirilerek analiz edilmiştir. LGBM algoritması, yüksek doğruluk ve hızlı performansı ile öne çıkmış, şifreli trafiğin doğru ve hızlı sınıflandırılması için etkin bir model sunulmuştur. Çalışma, siber güvenlik tehditlerini tespit etmek ve önlemek için etkili çözümler geliştirilmesine katkıda bulunmaktadır.

1. Giriş (Introduction)

Günümüzde internet, bilgiye erişim ve iletişimin sağlanmasında temel bir araç haline gelmiştir. Dünya genelinde milyarlarca insana, geniş bir bilgi yelpazesine anında erişebilme imkanı sunmaktadır [1]. İnternetin yaygın olarak kullanılması; sağlık, güvenlik, sanat, eğlence, teknoloji ve ticaret gibi birçok alanda önemli faydalar sağlamaktadır. Ancak, internet üzerinden kişiler ve kurumlar tarafından kişisel, finansal, askeri ve diğer birçok hassas verinin iletilmesi, sağlanan bu faydalarla birlikte güvenlik endişelerini de beraberinde getirmektedir [2]. Bu nedenle, internet üzerinden iletilen verilerin güvenliğinin sağlanması büyük önem taşımaktadır. Verilerin güvenliği sağlanmadığında, siber saldırılara ve veri ihlallerine maruz kalma riski artmaktadır [3].

Şifreleme, hassas verilerin izinsiz erişime karşı korunması amacıyla uygulanan temel güvenlik önlemlerinden biridir. Böylece iletilen verilerin gizliliği sağlanmaya çalışılır. Ancak, ağa sızmış olan saldırganlar da şifreli trafiği kullanarak saldırılar gerçekleştirebilmekte ve izlerini gizleyebilmektedirler. Bu tür saldırılara karşı önlem alabilmek için çeşitli çözümler geliştirilmiş olsa da mevcut ticari güvenlik çözümleri, şifrelenmiş trafiği deşifre etmeden analiz yapamadıkları için şifreli trafiğin sınıflandırılmasında yetersiz kalabilmektedir [4,5].

Makine öğrenmesi algoritmaları, şifreli trafiği deşifre etmeden, başka bir deyişle veri paketinin içeriğini görmeden paket sayısı, uzunluğu, boyutu, iletişim süreleri ve hedef IP adresleri gibi özellikleri kullanarak şifreli trafikteki veri paketlerini kategorize edebilmekte ve şifreli trafiği sınıflandırabilmektedir. Böylece, siber tehditlerin daha doğru ve hızlı bir şekilde tespit edilmesinde ve saldırıların önlenmesinde etkili bir araç haline gelmektedir [6].

Bu çalışmada, ağ trafiği deşifre edilmeden, ağ üzerinden gerçekleşen veri akışına ait paket sayısı, uzunluğu, boyutu, iletişim süreleri ve hedef IP adresleri gibi değişkenler makine öğrenmesi teknikleri ile analiz edilmiş ve sınıflandırılmıştır. Şifreli trafiğin sınıflandırılmasında makine öğrenmesi tekniklerinin etkinliğinin test edilebilmesi amacıyla denetimli makine öğrenmesi algoritmaları ve makine öğrenmesinin bir alt dalı olan topluluk öğrenmesi algoritmaları kullanılmıştır. Çalışmada, yüksek başarı oranına ve hızlı performansa sahip algoritmalar ile bu algoritmalar için en iyi parametrelerin tespit edilmesi hedeflenmiştir. Analizlerde, Kanada Siber Güvenlik Enstitüsü tarafından yayımlanan şifreli trafik verilerini içeren ISCXVPN2016 veri seti [7] kullanılmıştır.

Çalışmanın ana katkıları aşağıdaki gibidir:

- ISCXVPN2016 veri seti kullanılarak yapılan bu çalışmada, daha önce bir arada ele alınmamış Light Gradient-Boosting Machine (LGBM) topluluk öğrenmesi algoritması ile k-Nearest Neighbours (KNN), Support Vector Machines (SVM) ve Logistic Regression (LR) denetimli makine öğrenmesi algoritmaları, hem başarı oranı hem de hız açısından karşılaştırılmıştır.
- Önerilen modelin test edilebilmesi için, kullanılan veri setindeki tüm senaryolara ilişkin veriler analiz edilmiştir. Bu süreçte Synthetic Minority Over-Sampling Technique (SMOTE) yöntemiyle sınıf dengesizlikleri giderilmiş ve hiperparametre optimizasyonu amacıyla rastgele örneklenen hiperparametre kümeleri üzerinde çapraz doğrulama yapılarak en iyi kombinasyon belirlenmiştir.
- Hem doğruluk hem de hız bakımından diğer yöntemlere kıyasla daha yüksek performans gösteren bir LGBM topluluk öğrenmesi modeli önerilmiştir.

Makalenin devamında öncelikle ağ trafiğinin şifrelenmesi ve sınıflandırılmasına ilişkin yöntemler ele alınarak ilgili literatür incelenmiştir. Ardından kullanılan algoritmalar, üzerinde çalışılan veri seti, önerilen iki aşamalı model ve model performans metrikleri açıklanmıştır. Son bölümde elde edilen sonuçlar karşılaştırmalı analizlerle değerlendirilmiş, çalışmanın hem akademik hem de sektörel açıdan pratik katkıları ortaya konmuş ve gelecekteki çalışmalara yönelik öneriler sunularak makale sonuca bağlanmıştır.

2. Ağ Trafikinin Sınıflandırılması ve İlgili Araştırmalar (Classification of Network Traffic and Related Research)

İnternetin yaygın kullanımı, bilgiye hızlı erişim imkanı sunmanın yanı sıra sağlık, güvenlik, sanat, eğlence, teknoloji ve ticaret gibi pek çok alanda önemli avantajlar sağlamaktadır. Ancak bu avantajlarla birlikte, internet üzerinden kişisel, finansal, askeri ve diğer hassas verilerin iletilmesi, söz konusu verilerin güvenliğine ilişkin endişeleri artırmaktadır.

Bu endişelerin giderilmesi ve olası tehditlerin önlenmesi amacıyla ağ trafiğinin şifrenmesi gerekliliği doğmuştur. Ağ trafiğinin şifrenmesi, internet üzerindeki hassas bilgilerin güvenli bir şekilde aktarılmasına olanak tanımaktadır [8].

Hypertext Transfer Protocol Secure (HTTPS) protokolü ve Virtual Private Network (VPN) teknolojisi, güvenli iletişim sağlamak için sıkça kullanılan yöntemler arasındadır [9]. HTTPS protokolünde, kullanıcı ile bağlandığı sunucu arasındaki veri trafiği şifrenerek kullanıcının internet üzerinden sunulan hizmetlere güvenli biçimde erişmesi sağlanmaktadır [10]. VPN teknolojisinde ise iletişim şifreli bir tünel aracılığıyla gerçekleştirilmektedir. Veriler bu güvenli tünelden iletilirken kapsüllenerek farklı bir paket içerisine alınmakta ve şifrenmektedir [11]. Böylece kullanıcılar, internet üzerinden güvenli bir bağlantı sağlayabilmektedir.

Şifreleme yöntemleri ve protokolleri, kullanıcıların güvenliğini artırırken, saldırganların ağ üzerindeki kötü niyetli faaliyetlerini gizlemesine de olanak tanıyabilmektedir. Bu durum, kötü niyetli etkinliklerin tespitini zorlaştırmaktadır. Ayrıca, şifreli iletişim kanallarının yaygınlaşması bilgi güvenliği açısından olumlu bir gelişme olsa da, siber güvenlik uzmanlarının trafiği analiz etme ve ağdaki güvenlik tehditlerini tanımlama süreçlerini karmaşıklaştırabilmektedir. Tüm bu etkenler, şifreli trafiğin sınıflandırılmasını ağ güvenliğinin sağlanmasında önemli bir konu haline getirmektedir [12].

Ağ trafiğinin sınıflandırılmasına yönelik olarak literatürde sıkça kullanılan üç temel yöntem bulunmaktadır. Bunlar; port tabanlı sınıflandırma, içerik tabanlı sınıflandırma ve makine öğrenmesi tabanlı sınıflandırma yaklaşımlarıdır [12,13].

2.1. Port tabanlı sınıflandırma (Port-based classification)

Sınıflandırma işlemi için kullanılan en eski yöntem, internet kaynaklarının tahsisi ve düzenlenmesinden sorumlu Internet Assigned Numbers Authority (IANA) tarafından yönetilen "Service Name and Transport Protocol Port Number Registry" veritabanındaki port numaralarını sorgulamaktır. Bu veritabanı, internet hizmetlerinin adları ile bu hizmetlere tahsis edilmiş port numaralarını içermekte ve siber güvenlik uzmanlarına saldırıların tanımlanmasında bir referans kaynağı sunmaktadır [14]. Ancak saldırganlar, port sahtekarlığı, port atlama ve yanıltıcı trafik yönlendirmesi gibi hileli taktikler kullanarak bu yöntemi atlatılabilmektedir. Bu nedenle port tabanlı sınıflandırma yöntemi düşük bir güvenilirlik seviyesine sahip olarak değerlendirilmektedir [15].

2.2. İçerik tabanlı sınıflandırma (Content-based classification)

İçerik tabanlı sınıflandırma yönteminde ağ trafiğindeki veri paketlerinin içeriği ayrıntılı bir şekilde incelenerek sınıflandırma gerçekleştirilmektedir [16]. Bu yaklaşım genellikle Deep Packet Inspection (DPI) tekniklerini kullanmakta olup, trafiğin yüksek doğrulukla analiz edilmesini sağlamaktadır. Ancak DPI, imza tabanlı bir yaklaşım benimsediğinden, belirli örüntü veya imzaları tespit etmek amacıyla sürekli güncellenmesi gereken bir imza veritabanına ihtiyaç duymaktadır. Bu veritabanı güncel tutulmadığında, yeni ve değişen tehditlerin tespitinde yetersiz kalılabilmektedir. Bunun yanı sıra, içerik tabanlı sınıflandırmada derinlemesine inceleme yapılması gizlilik endişelerine neden olabilmektedir. En önemli zayıflığı ise şifrenmiş paket içeriklerini tanımlayamamasıdır [12,17].

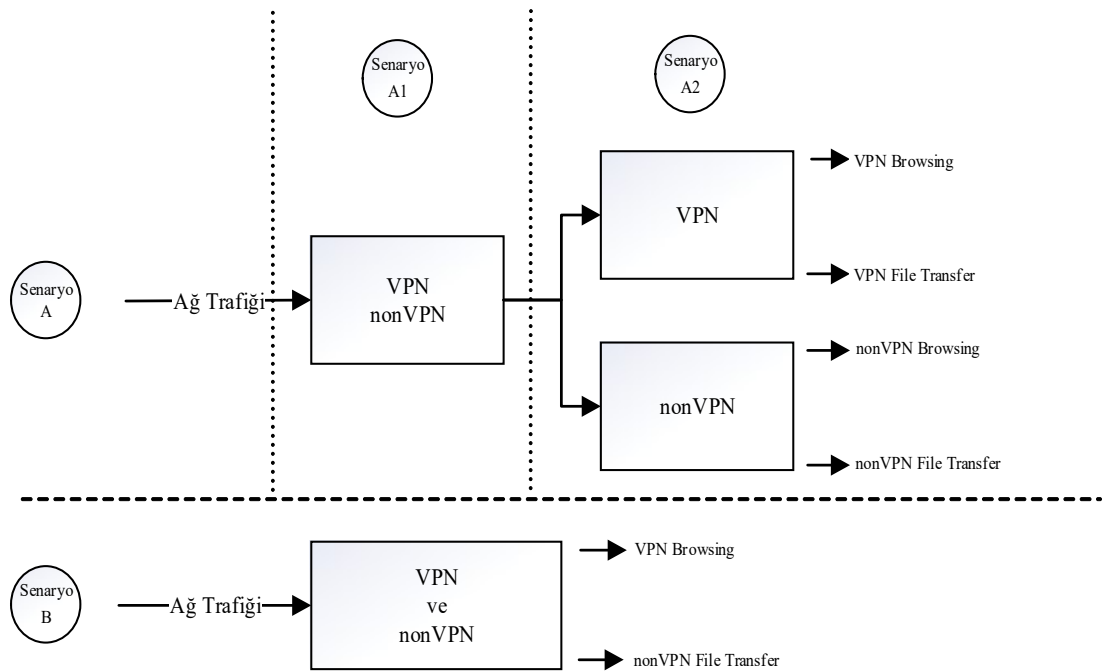
2.3. Makine öğrenmesi tabanlı sınıflandırma (Machine Learning-based classification)

Topluluk öğrenmesi ve derin öğrenme gibi çeşitli öğrenme tekniklerini de içeren bu yöntem ile, trafiğin şifreli olduğu durumlarda, ağ üzerindeki veri iletişimine ait; paket sayısı, uzunluğu, boyutu, iletişim süresi ve hedef IP adresi gibi şifrelenmemiş bazı veriler kullanılarak sınıflandırma yapılabilmektedir. Bu sayede, siber güvenlik uzmanları ağda iletilen verilere ilişkin önemli bilgilere ulaşabilmektedir [18,19]. Diğer yöntemlere göre daha esnek ve duyarlı olan bu yaklaşım, karmaşık ve değişken ağ trafiği üzerinde etkin sınıflandırma olanağı sunmaktadır. Ayrıca, büyük hacimli veri trafiği üzerinde daha yüksek performans göstermektedir [16,20].

2.4. İlgili araştırmalar (Related Research)

Şifreli ağ trafiğinin sınıflandırılması, ağ güvenliği ve trafik yönetimi açısından kritik bir araştırma alanıdır. Yapılan çalışmada şifreli trafik verilerini içeren ISCXVPN2016 veri seti kullanılmıştır. ISCXVPN2016 veri seti temel alınarak gerçekleştirilen birçok çalışma farklı makine öğrenmesi, topluluk öğrenmesi ve derin öğrenme algoritmaları kullanarak yüksek doğruluk oranlarına ulaşmayı amaçlamaktadır. Draper-Gil vd [7], ISCXVPN2016 veri setini oluşturarak şifreli ağ trafiğinin sınıflandırılması için önemli bir temel oluşturmuşlardır. Bu veri seti, 14 farklı etiketten yararlanan akış tabanlı bir sınıflandırma yaklaşımına dayanmaktadır. Gerçek internet trafik verilerinden elde edilen veri setinde, ağ trafiğinde yaygın olarak görülen Browsing, Email, Chat, Streaming, File Transfer, Voice over Internet Protocol (VoIP) ve Peer-to-Peer (P2P) olmak üzere toplam 7 sınıf bulunmaktadır. Veri setinde, HTTPS protokolüyle şifrelenmiş trafik ve VPN teknolojisiyle şifrelenmiş trafik verileri yer almakta; bu trafik türleri veri seti içerisinde sırasıyla non-VPN ve VPN olarak 2 türde kategorize edilmektedir.

Veri setinde, Şekil 1'de gösterildiği üzere Senaryo A ve Senaryo B olmak üzere iki farklı senaryo bulunmaktadır. Senaryo A'da sınıf türü ve trafik türüne göre kategorizasyon iki adımda, Senaryo B'de ise tek adımda gerçekleştirilmiştir. Her iki senaryoda da veriler, zamanla ilgili özellikler doğrultusunda akış sürelerine göre 15, 30, 60 ve 120 saniyelik veri gruplarından oluşmaktadır.



Şekil 1. Veri setinde yer alan senaryolar
(Scenarios included in the dataset)

Draper-Gil vd. [7], yukarıda ayrıntıları verilen kendi oluşturdukları ISCXVPN2016 veri setini kullanarak, C4.5 ve KNN algoritmalarıyla çalışmalar gerçekleştirmiş ve senaryoya bağlı olarak VPN ve non-VPN sınıflayıcılarında %80,9 ila %90,6 arasında değişen doğruluk oranlarına ulaşmışlardır. Bu veri seti ve çalışma, literatürde sonraki araştırmalara önemli bir rehber niteliği taşımaktadır.

Bu veri seti kullanılarak şifreli trafiğin makine öğrenmesi yöntemleriyle sınıflandırılmasına ilişkin yapılan çalışmalar incelendiğinde, senaryo bazlı karşılaştırmaların sınırlı sayıda olduğu görülmektedir. Karşılaştırılabilir sonuçlar elde etmek amacıyla, bu çalışmada genel başarı oranları yerine “senaryo” bazlı başarı oranlarını raporlayan çalışmalar [2,5,7,21,22] temel alınarak değerlendirme yapılmıştır.

Ayrıca, ilgili veri setinin yayımlanmasından bu yana ISCXVPN2016 veri seti kullanılarak şifreli trafiğin sınıflandırılmasına ilişkin yürütülen çalışmalar [2,5,7,8,15,19,21-34] incelenmiş ve bu alanda gerçekleştirilen az sayıda çalışmada [35], günümüzde hemen her alanda önemli bir kriter olan zaman unsuruna ilişkin test süresi metriğinin [36] ele alındığı görülmüştür. Test süresi, eğitilen algoritmanın test aşamasında harcadığı süreyi ifade etmektedir. Bu çalışmada kullanılan algoritmaların test süreleri de hesaplanarak karşılaştırılmıştır.

Aşağıda, kullanılan yöntemlere göre literatürde öne çıkan çalışmalar ve bulgular ele alınmıştır.

2.4.1. Makine öğrenmesi yöntemleri ile sınıflandırma (Classification with machine learning methods)

Birçok çalışma, ISCXVPN2016 veri setini kullanarak makine öğrenmesi algoritmalarının etkinliğini analiz etmiştir. Yamansavaşçılar vd. [23], farklı algoritmalar arasında en iyi sonucu %93,94 doğruluk oranıyla KNN algoritması ile elde etmişlerdir. Caicedo-Muñoz vd. [5], trafik sınıflandırması için özel bir Quality of Service (QoS) sınıflayıcı önermiş ve bu doğrultuda ISCXVPN2016 veri setinden QoS etiketli bir veri kümesi oluşturmuşlardır. Çalışmanın sonucunda, Bagging algoritması ile A2 senaryosunda %94,42, B senaryosunda ise %86,94 doğruluk oranları elde etmişlerdir. Zhang vd. [27], dengesiz şifreli trafiğin sınıflandırılması için Random Forest (RF) algoritmasını kullanarak bir şema önermişler ve bu yöntemle %93 doğruluk oranına ulaşmışlardır. Bagui vd. [24], RF ve Gradient Boosting Tree (GBT) algoritmaları ile %90 doğruluk oranı elde etmişlerdir. Zhou vd. [30] ise RF algoritması kullanarak %98 doğruluk oranına ulaşmıştır.

Literatürdeki bu çalışmalar, KNN, Bagging ve RF algoritmalarının ön planda olduğunu ve başarılı sonuçlar verdiğini göstermektedir. KNN algoritması %93,94, Bagging algoritması %94,42 ve RF algoritması %98 doğruluk oranına ulaşmıştır. Ayrıca GBT algoritması da etkili sonuçlar elde edilen bir diğer yöntem olarak öne çıkmaktadır.

2.4.2. Derin öğrenme yöntemleri ile sınıflandırma (Classification with deep learning methods)

Derin öğrenme yöntemleri, şifreli trafiğin sınıflandırılmasında kayda değer başarılar elde etmiştir. Örneğin, Guo vd. [28], Convolutional Auto Encoder (CAE) modelini kullanarak %99,87 doğruluk oranına ulaşmış; Ismailaj vd. [33] ise Convolutional Neural Network (CNN) tabanlı yaklaşımlarıyla %90 doğruluk oranı elde etmiştir. Obasi [19], Artificial Neural Network (ANN), CNN ve Long Short-Term Memory (LSTM) gibi derin öğrenme modellerini Decision Tree (DT) ve RF algoritmalarıyla karşılaştırmış ve RF ile %96 doğruluk oranına varmıştır. Bu sonuç, Bagui vd. [24] ile Zhou vd. [30] tarafından bildirilen bulgularla da örtüşerek, RF algoritmasının sınıflandırmadaki üstün başarısını ön plana çıkarmaktadır. Böylece RF, ANN, CNN ve LSTM gibi derin öğrenme modelleriyle kıyaslandığında, %96 doğruluk oranı ile yüksek bir performans sergilemektedir.

2.4.3. Hibrit ve topluluk öğrenmesi yöntemleri ile sınıflandırma (Classification with hybrid and ensemble learning methods)

Hibrit modeller ve topluluk öğrenmesi yöntemleri, birden fazla algoritmayı bir araya getirerek performansı artırmayı amaçlamaktadır. Huang vd. [8], önerdikleri hibrit bir yaklaşım ile %80 F1 skoru elde etmişlerdir. Bozkır [22] ise Extreme Gradient Boosting (XGBoost) algoritması ile %99 F1 skoru yakalayarak en yüksek sonuçlardan birini elde etmiştir. Uğurlu vd. [2], XGBoost algoritması kullanarak %93,04 doğruluk oranına ulaşmışlardır. Almomani [34], ANN, RF ve SVM algoritmalarını bir araya getirerek oluşturduğu topluluk öğrenmesi modeli ile %98 doğruluk oranı elde etmiştir.

Afuwape vd. [32], şifreli trafiği sınıflandırmak için AdaBoost, GBT, RF, Bagging Decision Tree (BDT), KNN, LR, Multi Layer Perceptron (MLP) ve Naive Bayes (NB) tekniklerini ISCXVPN2016 veri seti üzerinde kullanmışlardır. Bu çalışmada, topluluk algoritmalarının tekli algoritmalarından daha iyi performans gösterdiği sonucuna varılmış ve RF ile %93,8 doğruluk oranına ulaşılmıştır. Genel olarak, hibrit modeller daha yüksek doğruluk ve F1 skorları sağlarken, topluluk öğrenmesi yöntemleri birden fazla algoritmanın birleşimi sayesinde performansı önemli ölçüde artırmaktadır. Ayrıca, farklı tekniklerin uygulandığı çalışmalarda da topluluk algoritmalarının tekli algoritmalarından daha iyi sonuçlar verdiği gözlemlenmiştir.

2.4.4. Alternatif veri setleri ve karşılaştırmalar (Alternative datasets and comparisons)

ISCXVPN2016 verisetinin yanı sıra, bazı araştırmacılar kendi veri setlerini de kullanmışlardır. Khatouni ve Heywood [35], Gradient Descent, DT, NB, SVM ve RF algoritmalarını kendi veri setlerinde kullanarak %85 doğruluk oranına ulaşmışlardır. Ayrıca RF algoritmasının doğruluk açısından üstün olmasına rağmen, DT algoritmasının işlem hızı konusundaki avantajlarına dikkat çekmişlerdir. Majeed vd. [21], şifreli trafiğin sınıflandırılması için özellik tabanlı Horizontal Federated Learning yöntemini önermiş ve bu yöntemle %86 doğruluk oranı elde etmişlerdir.

Bunların yanı sıra, karanlık ağ (Dark Web) trafiğinin sınıflandırılması için makine öğrenmesi tabanlı yöntem kullanılarak yapılan çalışmalara da [37-40] rastlanmıştır.

Sonuç olarak literatürde yer alan araştırmalar KNN, Bagging, RF gibi makine öğrenmesi algoritmalarının yanı sıra, CNN ve CAE gibi derin öğrenme modellerinin yüksek doğruluk oranları sunduğunu göstermiştir. Hibrit ve topluluk modelleri, bu yöntemleri birleştirerek daha yüksek performans ve doğruluk sağlamıştır. Çeşitli veri setleri ve alternatif yöntemler kullanılarak yapılan çalışmalar, özellikle RF algoritmasının sınıflamada üstün başarı gösterdiğini ortaya koymuştur. Literatür taraması kapsamında değerlendirilen tüm önceki çalışmalar Tablo 1'de ayrıca özetlenmiştir.

Tablo 1. Literatür özeti (Literature Review)

Yıl	Kaynak	Veri Seti	Algoritma Türü	Algoritma Adı	Sonuç
2016	Draper-gil vd. [7]	ISCXVPN2016 (Veri setini kendileri hazırlamıştır.)	Makine öğrenmesi	C4.5 ve KNN	C4.5 ile Senaryo A1 %90,6 kesinlik Senaryo A2 %89 kesinlik Senaryo B %80,9 kesinlik
2017	Yamansavaşçılar vd. [25]	ISCXVPN2016	Makine öğrenmesi	J-48, RF, KNN ve Bayes Net	KNN ile %93,94 doğruluk
2017	Bagui vd. [24]	ISCXVPN2016	Makine öğrenmesi, Topluluk öğrenmesi	NB, SVM, KNN, LR, RF ve GBT	RF ve GBT ile %90 doğruluk
2018	Caicedo vd. [5]	ISCXVPN2016	Makine öğrenmesi, Topluluk öğrenmesi	C4.5, Bagging ve Boosting	Bagging ile Senaryo A2 %94,42 doğruluk Senaryo B %86,94 doğruluk
2020	Zhang vd. [27]	ISCXVPN2016	Makine öğrenmesi, Topluluk öğrenmesi	C4.5, KNN ve RF	RF ile 0,93 doğruluk
2020	Guo vd. [28]	ISCXVPN2016	Derin öğrenme, Makine öğrenmesi	CAE, CNN, KNN ve C4.5	CAE ile %99,87 genel doğruluk
2020	Obasi [19]	ISCXVPN2016 ve Solana Networks	Derin öğrenme, Makine öğrenmesi, Topluluk öğrenmesi	ANN, CNN, LSTM, CapsNet, DT ve RF	RF ile %96 doğruluk
2020	Zhou vd. [30]	ISCXVPN2016 ve ISCX-Tor/Non-Tor	Derin öğrenme, Makine öğrenmesi, Topluluk öğrenmesi	ANN, SVM, NB, LR ve RF	RF ile %98 doğruluk
2020	Majeed vd. [21]	ISCXVPN2016	Makine öğrenmesi	Horizontal Federated Learning yöntemi	Senaryo A %86, Senaryo B %81 doğruluk
2021	Afuwape vd. [32]	ISCXVPN2016	Makine öğrenmesi, Derin öğrenme, Topluluk öğrenmesi	KNN, LR, NB, MLP, AdaBoost, GBT, RF ve BDT	RF ile %93,80 doğruluk
2021	Uğurlu vd. [2]	ISCXVPN2016	Makine öğrenmesi, Topluluk öğrenmesi	DT, XGBoost ve RF	XGBoost ile Senaryo A1 %93,04 kesinlik Senaryo A2 %94,53 doğruluk Senaryo B %86,06 kesinlik
2021	Huang vd. [8]	ISCXVPN2016	Derin öğrenme, Makine öğrenmesi	Kendi önerdikleri hibrit yaklaşım	Önerilen yöntem ile %80 F1 Skoru
2021	Ismailaj vd. [33]	ISCXVPN2016	Derin öğrenme, Topluluk öğrenmesi	CNN ve LGBM	CNN ile %90 doğruluk
2022	Almomani [34]	ISCXVPN2016	Derin öğrenme, Makine öğrenmesi	ANN, SVM ve kendi önerdikleri yöntem	Önerilen yöntem ile %98 doğruluk
2023	Bozkır vd. [22]	ISCXVPN2016	Topluluk öğrenmesi	GBT, LGBM ve XGBoost	XGBoost ile Senaryo A ve Senaryo B %99 F1

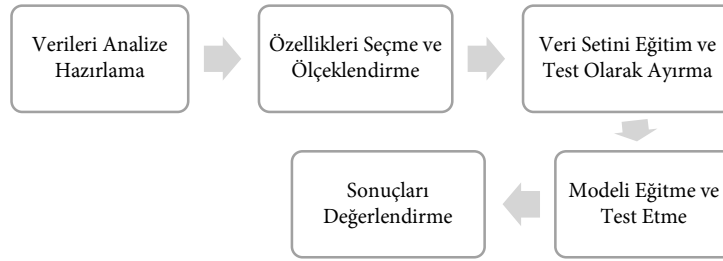
3. Materyal ve Yöntem (Materials and Methods)

Yapılan çalışmada, Drapper-Gil vd. tarafından oluşturulan ve Kanada Siber Güvenlik Enstitüsü tarafından yayımlanan kapsamlı bir etiketli veri seti olan ISCXVPN2016 kullanılmıştır [7]. Bu veri seti için KNN, SVM ve LR denetimli makine öğrenmesi algoritmalarının yanı sıra LGBM topluluk öğrenmesi algoritması ile çalışılmıştır.

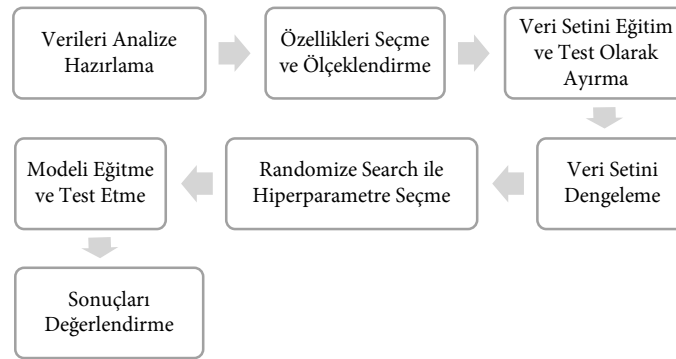
Çalışmada veriler öncelikle, eksik veri kontrolü ve sayısallaştırma yapılarak analize hazır hale getirilmiştir. Sonrasında önem derecesine göre özellik seçimi yapılmış ve her bir özellik için ölçeklendirme işlemi gerçekleştirilmiştir. Ölçeklendirme sonrası veriler, %70'i eğitim ve %30'u test verisi olacak şekilde rastgele bir şekilde bölünerek ayrılmıştır.

Çalışmanın birinci aşaması olan orijinal veri seti ile eğitim ve test, yukarıda yapılan işlemler sonrasında gerçekleştirilmiştir. İkinci aşamada ise dengesiz dağılıma sahip veri setleri SMOTE tekniği ile dengelenmiş, hiperparametrelerin rastgele örnekleri seçilerek çapraz doğrulama uygulanmış ve böylece en iyi hiperparametre kombinasyonu belirlenmiştir. Ardından bu optimize edilmiş hiperparametreler kullanılarak tekrar eğitim ve test adımları gerçekleştirilmiştir.

Çalışma kapsamında makine öğrenmesi algoritmaları ile şifreli trafiğin sınıflandırılmasında izlenen bu iki aşamanın adımları sırasıyla Şekil 2 ve Şekil 3'te gösterilmektedir.



Şekil 2. Birinci aşama araştırma metodolojisinde izlenen adımlar
(The steps followed in the research methodology of the first stage)



Şekil 3. İkinci aşama araştırma metodolojisinde izlenen adımlar
(The steps followed in the research methodology of the second stage)

Çalışmada kullanılan ISCXVPN2016 veri seti etiketli verilerden oluşmaktadır [7]. Veri setinin analize uygun hale getirilmesi için eksik veriler kontrol edilmiş ve eksik veri bulunmadığı tespit edilmiştir. Ardından, veri setinde kategorik verilerin varlığı incelenmiş ve sınıf etiketlerinin kategorik olduğu belirlenmiştir. Bu kategorik sınıf etiketleri sayısal değerlere dönüştürülmüştür (Tablo 2).

Tablo 2. Sınıf etiketlerine atanan sayısal değerler (Numerical values assigned to class labels)

Trafik Sınıfı	Atanan Değer
Browsing	0
Chat	1
File Transfer	2
Email	3
P2P	4
Streaming	5
VoIP	6
VPN-Browsing	7
VPN-Chat	8
VPN-File Transfer	9
VPN-Email	10
VPN-P2P	11
VPN-Streaming	12
VPN-VoIP	13

Makine öğrenmesi modellerinin başarı oranlarını etkilemeden çalışma performansını artırmak, hesaplama maliyetini düşürmek ve gereksiz özelliklerin etkisini azaltmak amacıyla özellik seçimi yapılmaktadır [41]. Bu çalışmada, Decision Tree Classifier kullanılarak modelde yer alan özelliklerin önem dereceleri hesaplanmıştır. Bu önem dereceleri, toplamı 1 olacak şekilde ağırlıklandırma yapılmıştır. Tüm sınıfları içeren Senaryo B-15s veri setinde, ağırlığı 0,01'in üzerinde ağırlığa sahip Tablo 3'de yer alan ilk 15 özellik seçilerek kullanılmıştır.

Tablo 3. Senaryo B 15s'ye ait özelliklerin ağırlık değerleri (The weight values of the features for Scenario B 15s)

No	Özellik Adı	Ağırlığı
1	total_biat	0,143661
2	flowBytesPerSecond	0,117527
3	duration	0,114499
4	min_flowiat	0,087023
5	total_fiat	0,065198
6	std_flowiat	0,060411
7	max_fiat	0,059739
8	max_flowiat	0,056023
9	mean_biat	0,046961
10	min_biat	0,045398
11	max_biat	0,045074
12	mean_flowiat	0,040779
13	flowPktsPerSecond	0,031403
14	min_fiat	0,020947
15	mean_fiat	0,018952
16	std_idle	0,008859
17	mean_idle	0,007039
18	max_active	0,006434
19	min_idle	0,006154
20	std_active	0,005152
21	mean_active	0,004819
22	min_active	0,004677
23	max_idle	0,003259

Sonrasında veri seti analiz edilmiş ve değerlerin farklı ölçeklere sahip olduğu görülmüştür. Örnek olarak aşağıda bulunan Tablo 4'te Senaryo B 15s'ye ait betimsel istatistik veriler paylaşılmıştır. Tablodaki veriler incelendiğinde, değişkenlerin aritmetik ortalamaları ile minimum ve maksimum değerleri arasında ciddi farklılıklar olduğu gözlemlenmiştir. Örneğin, bazı değişkenlerde maksimum değerlerin milyonlarla ifade edilmesi, diğer değişkenlerde ise oldukça düşük değerlere sahip olması, verilerde ölçek farklılıklarını ortaya koymaktadır. Bu tür dengesizlikler, özellikle makine öğrenimi modellerinde kullanılan metriklerin dengesiz çalışmasına ve model performansında sapmalara yol açabilmektedir.

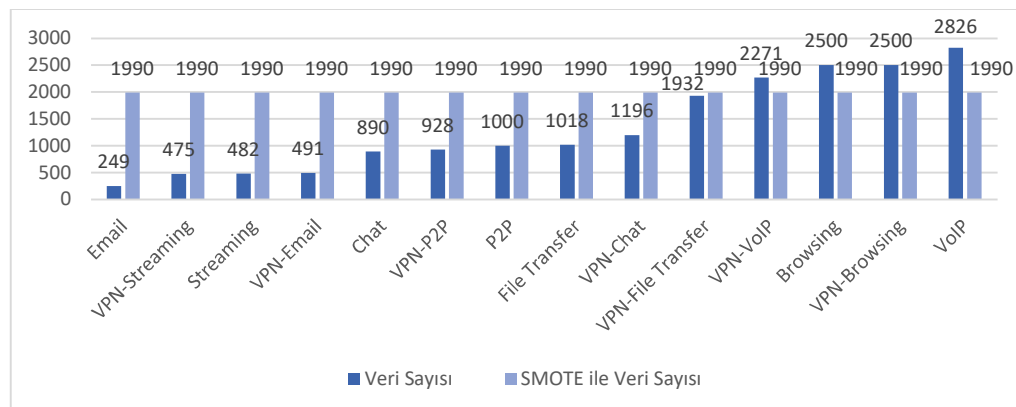
Tabloda görülen özelliklerden flowBytesPerSecond isimli olan byte/saniye, flowPktsPerSecond isimli olan paket/saniye, kalan diğer tüm veriler ise saniye cinsindedir. Hem özellikler arasındaki dengesizlikler hem de farklı cinslerde özelliklerin bir arada kullanımı verilerin normalleştirilmesi ihtiyacını ortaya çıkarmaktadır. Bu durumu dengelemek ve verileri aynı ölçek seviyesine getirmek amacıyla min-max normalizasyonu ile ölçeklendirme işlemi yapılmıştır [40].

Tablo 4. Senaryo B 15s'ye ait betimsel istatistik veriler (Descriptive statistical data for Scenario B 15s)

	Veri Sayısı	Aritmetik Ortalama	Standart Sapma	Minimum Değer	Maksimum Değer
total_biat (s)	13.130	638.875	2.362.490	1	43.002.380
flowBytesPerSecond (byte/saniye)	13.130	454.718	8.982.233	0	565.000.000
Duration (s)	13.130	9.788.733	14.807.250	0	601.405.000
min_flowiat (s)	13.130	43.427	466.325	721	18.919.900
total_fiat (s)	13.130	619.785	2.274.082	1	37.680.790
std_flowiat (s)	13.130	1.032.781	3.595.225	0	136.000.000
max_fiat (s)	13.130	1.016.790	3.328.565	0	152.000.000
max_flowiat (s)	13.130	3.852.325	14.311.790	1	601.109.700
mean_biat (s)	13.130	604.968	2.390.375	0	98.000.000
min_biat (s)	13.130	2.871.231	10.275.070	1	600.109.700
max_biat (s)	13.130	928.233	2.504.501	0	43.000.000
mean_flowiat (s)	13.130	480.361	1.475.132	0	60.700.000
flowPktsPerSecond (paket/saniye)	13.130	1.909	15.646	0	666.666
min_fiat (s)	13.130	3.306.506	10.627.500	1	303.595.700
mean_fiat (s)	13.130	8.410.637	4.509.882	0	215.000.000

$$z = \frac{x - \min(x)}{\max(x) - \min(x)} \quad (1)$$

Min-max normalizasyon ölçeklendirmesi, yukarıda yer alan formüldeki (1) gibi, bir veri setindeki bir değer minimum değere olan uzaklığının, maksimum ve minimum değerler arasındaki farka bölünmesiyle gerçekleştirilir. Bu yöntem, veri setindeki değerleri 0 ile 1 aralığına indirger. Böylece, değerler arasındaki büyük farklılıklar ortadan kaldırılarak modelin daha doğru ve dengeli sonuçlar üretmesi sağlanmaktadır. Ölçeklendirme sonrası veriler, %70'i eğitim ve %30'u test verisi olacak şekilde rastgele bölünerek ayrılmış ve çalışmanın birinci aşaması olan orijinal veri seti ile eğitim ve test gerçekleştirilmiştir. İkinci aşamada, sınıf dengesizliği bulunan A2 ve B senaryolarındaki veri setleri için dengeleme işlemi uygulanmıştır. Bu işlemde, yeniden örnekleme yöntemlerinden SMOTE kullanılmıştır. SMOTE, az sayıdaki sınıflar için sentetik örnekler oluşturarak veri setindeki dengesizliği gidermeyi amaçlamaktadır. Tüm sınıfları içeren Senaryo B-15s veri setinde, dengeleme öncesi ve sonrası veri dağılımı Şekil 4'te gösterilmiştir.



Şekil 4. Senaryo B-15s için SMOTE ile verilerin dengelemesi
(Balancing the data for Scenario B-15s using SMOTE)

Hiperparametreler, algoritmaların performansını doğrudan etkilemektedir [42]. Çalışmanın ikinci aşamasında, algoritmalar için en iyi parametre kombinasyonunu belirlemek amacıyla rastgele arama tekniği kullanılmıştır. Bu teknikte, belirlenen bir aralıktaki hiperparametre değerleri rastgele denenecek optimize edilir. Bu yaklaşım, hesaplama süresi açısından daha az zaman gerektirdiği için avantaj sağlamaktadır. Ayrıca, tüm parametrelere eşit kaynak ayırmak yerine, önemli parametrelere odaklandığından, verimli ve pratik bir

yöntemdir [43].

Kullanılan makine öğrenmesi algoritmalarının parametreleri, belirlenen aralıklar içinde rastgele arama yöntemine tabi tutulmuş ve sınıflandırma işlemi için en iyi sonuçları veren parametreler belirlenmiştir. Parametre seçimi için kullanılan aralıklar Tablo 5'te gösterilmiştir.

Tablo 5. Kullanılan hiperparametre aralıkları (The hyperparameter ranges used)

Algoritma Adı	Hiperparametre Aralıkları
KNN	'n_neighbors': [3, 5, 7, 9], 'weights': ['uniform', 'distance'], 'metric': ['euclidean', 'manhattan', 'minkowski'].
SVM	'C': [0.1, 1, 10, 100], 'gamma': ['scale', 0.1, 1, 10], 'kernel': ['linear', 'rbf', 'sigmoid'].
LR	'C': [0.0001, 0.001, 0.01, 0.1, 1, 10, 100, 1000, 10000], 'penalty': ['none', 'l1', 'l2'], 'solver': ['newton-cg', 'lbfgs', 'liblinear', 'sag', 'saga'], 'max_iter': [30, 50, 100, 200, 500, 1000, 2000, 5000].
LGBM	'num_leaves': sp_randint(6, 100), 'learning_rate': [0.01, 0.05, 0.1, 0.3, 0.5, 0.7], 'max_depth': sp_randint(3, 30), 'min_child_samples': sp_randint(100, 1000), 'subsample': [0.6, 0.7, 0.8, 0.9, 1.0], 'colsample_bytree': [0.5, 0.6, 0.7, 0.8, 0.9, 1.0], 'reg_alpha': [0, 0.1, 0.5, 1, 2, 5, 10], 'reg_lambda': [0, 0.1, 0.5, 1, 2, 5, 10], 'min_child_weight': [1e-3, 1e-2, 0.1, 0.5, 1, 5, 10], 'n_estimators': sp_randint(50, 1000).

Rastgele arama işlemi ile birlikte hiperparametre seçiminde çapraz doğrulama da yapılmıştır. Çapraz doğrulama işleminde veri setinin her bir parçası hem eğitim hem de test verisi olarak kullanılmaktadır. Böylece veri, daha verimli değerlendirilmekte ve daha güvenilir tahmin yapılmaktadır. Çapraz doğrulama veri setini k sayıda alt kümeye bölmekte ve her alt küme için modeli eğitmektedir. Bu işlem k kez tekrarlanmakta ve sonuçların ortalamaları alınarak performans değeri elde edilmektedir [44]. Bu çalışmada tüm algoritmalar için çapraz doğrulama işleminde kullanılan katman sayısı 3 olarak belirlenmiştir.

Çalışmada performans metriklerinden doğruluk, F1 skor ve test süresi dikkate alınmıştır. Performans metriklerinin hesaplanmasında, makine öğrenmesi modelinin doğru ve yanlış yaptığı sınıflandırma sayılarına ihtiyaç duyulmaktadır. Bu kapsamda gerçek ve tahmin değerlerini içeren karmaşıklık matrisi kullanılmaktadır. Karmaşıklık matrisi yapısı Tablo 6'da yer almaktadır.

Tablo 6. Karmaşıklık matrisi yapısı (The structure of the confusion matrix)

Karmaşıklık Matrisi		Tahmin	
		X ₁ (Pozitif)	X ₂ (Negatif)
Gerçek	X ₁ (Pozitif)	DP	YN
	X ₂ (Negatif)	YP	DN

Gerçekte pozitif olup pozitif sınıflandırılan Doğru Pozitif (DP), gerçekte negatif olan ama pozitif sınıflandırılan Yanlış Pozitif (YP), gerçekte negatif olup negatif sınıflandırılan Doğru Negatif (DN), gerçekte pozitif olan ama negatif sınıflandırılan ise Yanlış Negatif (YN) örnek sayısını vermektedir [45].

Doğruluk, doğru sınıflandırılan tahminlerin oranını bulmak için kullanılmakta ve aşağıda yer alan formülle (2) hesaplanmaktadır.

$$Doğruluk = \frac{DP + DN}{DP + DN + YP + YN} \quad (2)$$

Kesinlik, pozitif olarak tahmini yapılan örneklerin gerçekte ne kadarının pozitif olduğunu ölçmek için kullanılmaktadır. Aşağıda yer alan formülle (3) hesaplanmaktadır.

$$Kesinlik = \frac{DP}{DP + YP} \quad (3)$$

Duyarlılık, gerçek pozitif örneklerin ne kadarının doğru tahmin edildiğini ölçmek için kullanılmaktadır. Aşağıda yer alan formülle (4) hesaplanmaktadır.

$$Duyarlılık = \frac{DP}{DP + YN} \quad (4)$$

F1 skor (F1-score), hassasiyet ve duyarlılığın harmonik ortalamasını alarak modelin ne kadar dengeli bir ölçüm sağladığını ölçmek için kullanılmakta ve aşağıdaki formülle (5) hesaplanmaktadır.

$$F1 \text{ skor} = \frac{2 * Kesinlik * Duyarlılık}{Kesinlik + Duyarlılık} \quad (5)$$

Test süresi, bir sınıflandırma sürecinde algoritmanın sınıflandırma işlemini ne kadar sürede gerçekleştirdiğini ifade etmektedir. Bu süre bir sınıflandırma algoritmasının ne kadar hızlı veya ne kadar yavaş çalıştığını belirlenmesine yardımcı olmaktadır. Algoritmaların hızı, sınıflandırma işleminde yapılan tespitin daha hızlı olabilmesini sağlayacağından daha etkin bir sınıflandırma ve kaynakların daha verimli kullanılması açısından fayda sağlayacaktır [36].

4. Bulgular ve Yorumlar (Findings and Interpretations)

Senaryo A1'de yer alan 4 adet, Senaryo A2'de yer alan 8 adet ve Senaryo B'de yer alan 4 adet zaman bazlı veri setlerinin her biri için ayrı ayrı denetimli makine öğrenmesi ve topluluk öğrenmesi algoritmaları kullanılarak çalışma yapılmıştır.

4.1. Birinci aşamada elde edilen sonuçlar (The results obtained in the first stage)

Çalışmanın bu ilk aşamasında, veri dengeleme işlemi ve hiperparametre seçimi yapılmamıştır. LGBM, KNN, SVM ve LR algoritmaları kullanılarak orijinal veri seti ile elde edilen sonuçlar Tablo 7'de gösterilmiştir. Tablo 8'de ise algoritmalar için test süreleri raporlanmıştır.

Tablo 7. Orijinal veri seti ile başarı oranları (The success rates with the original dataset)

Senaryolar	Algoritma	LGBM		KNN		SVM		LR	
		Doğruluk	F1 Skor	Doğruluk	F1 Skor	Doğruluk	F1 Skor	Doğruluk	F1 Skor
Senaryo A1 15s		0,9087*	0,9085*	0,8211*	0,8212*	0,6075	0,5924	0,5721*	0,5678*
Senaryo A1 30s		0,8924	0,8922	0,8144	0,8140	0,6078	0,5859	0,5612	0,5389
Senaryo A1 60s		0,8901	0,8912	0,7889	0,7891	0,6123	0,6108	0,5603	0,5231
Senaryo A1 120s		0,8927	0,8926	0,7935	0,7930	0,6173*	0,6125*	0,5518	0,5156
Senaryo A2 No-VPN 15s		0,9468**	0,9461**	0,8539	0,8521	0,6874**	0,6310**	0,5825	0,4790
Senaryo A2 VPN 15s		0,8999	0,8988	0,8043	0,8028	0,5752	0,5106	0,4847	0,3503
Senaryo A2 No-VPN 30s		0,9383	0,9373	0,8613**	0,8578**	0,6460	0,5791	0,5742	0,4801
Senaryo A2 VPN 30s		0,9130	0,9121	0,8311	0,8290	0,5890	0,5277	0,5050	0,3862
Senaryo A2 No-VPN 60s		0,9169	0,9166	0,8050	0,8013	0,5812	0,5262	0,5190	0,4460
Senaryo A2 VPN 60s		0,8813	0,8785	0,7967	0,7915	0,5320	0,4448	0,4786	0,3827
Senaryo A2 No-VPN 120s		0,9353	0,9341	0,8551	0,8480	0,6578	0,5767	0,6255**	0,5380**
Senaryo A2 VPN 120s		0,8728	0,8684	0,7834	0,7791	0,5811	0,4841	0,5053	0,3644
Senaryo B 15s		0,8658*	0,8657*	0,7166	0,7147	0,4394*	0,3987*	0,2601	0,1882
Senaryo B 30s		0,8576	0,8562	0,7232*	0,7286*	0,3938	0,3595	0,3219	0,2420
Senaryo B 60s		0,8335	0,8234	0,7187	0,7245	0,3767	0,3443	0,3289	0,2619
Senaryo B 120s		0,8250	0,8222	0,6754	0,6681	0,4049	0,3655	0,3354*	0,2634*

* Kalın yazılan değerler, ilgili senaryo ve algoritmada elde edilen en yüksek başarı oranlarıdır.

**Kalın ve kırmızı yazılan değerler, ilgili algoritmada tüm senaryolar içinde elde edilen en yüksek başarı oranlarıdır.

Orijinal veri seti ile

Tablo 8. Orijinal veri seti ile test süreleri (The test durations with the original dataset)

Senaryolar	Algoritma	Test Edilen Girdi Sayısı (adet)	LGBM		KNN		SVM		LR	
			Toplam Test Süresi (s)	Birim Test Süresi (s/ad)	Toplam Test Süresi (s)	Birim Test Süresi (s/ad)	Toplam Test Süresi (s)	Birim Test Süresi (s/ad)	Toplam Test Süresi (s)	Birim Test Süresi (s/ad)
Senaryo A1 15s		5.628	0,01	0,000002	0,34	0,000060	2,73	0,000485	0,04	0,000007
Senaryo A1 30s		4.397	0,01	0,000002	0,43	0,000098	2,09	0,000475	0,01	0,000002
Senaryo A1 60s		4.655	0,03	0,000006	0,56	0,000120	1,80	0,000387	0,01	0,000002
Senaryo A1 120s		3.236	0,13	0,000040	0,61	0,000189	1,13	0,000349	0,01	0,000003
Senaryo A2 No-VPN 15s		2.690	0,04	0,000015	0,25	0,000093	0,63	0,000234	0,01	0,000004
Senaryo A2 VPN 15s		2.938	0,05	0,000017	0,16	0,000054	0,96	0,000327	0,01	0,000003
Senaryo A2 No-VPN 30s		2.076	0,05	0,000024	0,09	0,000043	0,41	0,000197	0,01	0,000005
Senaryo A2 VPN 30s		2.321	0,04	0,000017	0,13	0,000056	0,59	0,000254	0,01	0,000004
Senaryo A2 No-VPN 60s		2.574	0,04	0,000016	0,09	0,000035	0,69	0,000268	0,01	0,000004
Senaryo A2 VPN 60s		2.081	0,03	0,000014	0,22	0,000106	0,46	0,000221	0,01	0,000005
Senaryo A2 No-VPN 120s		1.546	0,02	0,000013	0,07	0,000045	0,18	0,000116	0,01	0,000006
Senaryo A2 VPN 120s		1.690	0,12	0,000071	0,39	0,000231	0,33	0,000195	0,01	0,000006
Senaryo B 15s		5.704	0,17	0,000030	0,72	0,000126	6,31	0,001106	0,01	0,000002
Senaryo B 30s		4.543	0,14	0,000031	0,49	0,000108	2,97	0,000654	0,01	0,000002
Senaryo B 60s		4.825	0,12	0,000025	0,45	0,000093	2,03	0,000421	0,01	0,000002
Senaryo B 120s		3.501	0,12	0,000034	0,39	0,000111	1,62	0,000463	0,01	0,000003
Ortalama Test Süreleri			0,07	0,000022	0,33	0,000098	1,56	0,000385	0,01	0,000004

* Kalın yazılan değerler, en yüksek başarı oranı elde edilen senaryo ve algoritmadaki test süreleridir.

Orijinal veri seti ile

Tüm senaryolar göz önünde bulundurulduğunda, orijinal veri setiyle en yüksek başarı oranlarına denetimli makine öğrenmesi algoritmaları arasında KNN ile ulaşılmıştır. KNN algoritması ile elde edilen en yüksek başarı oranları, 0,8613 doğruluk ve 0,8578 F1 Skoru ile Senaryo A2 No-VPN 30s veri setinde kaydedilmiştir. Test süresi 2.076 girdi için 0,09 saniye olmuş, bu da girdi başına 0,000043 saniyede kategorizasyon yapılabildiği anlamına gelmektedir. Topluluk öğrenme algoritması LGBM’de ise ulaşılan en yüksek başarı oranları, 0,9468 doğruluk ve 0,9461 F1 Skoru ile Senaryo A2 No-VPN 15s veri setinde elde edilmiştir. Test süresi 2.690 girdi için 0,04 saniye olarak hesaplanmış ve bu, her bir girdinin 0,000015 saniyede kategorize edildiğini göstermektedir. Sonuç olarak, LGBM ile elde edilen başarı oranlarının, hem doğruluk ve F1 Skoru açısından hem de kategorizasyonun gerçekleştirilme süresinin kısalığı bakımından KNN’den daha yüksek performans gösterdiği görülmektedir.

Çalışmanın ilk aşamasında algoritmaların varsayılan parametre değerleri kullanılmıştır. KNN ve LGBM algoritmalarında kullanılan varsayılan parametre değerleri Tablo 9’da gösterilmiştir.

Tablo 9. KNN ve LGBM algoritmaları için varsayılan parametre değerleri
(The default parameter values for the KNN and LGBM algorithms)

Algoritma	Parametrenin Adı	Varsayılan Değer
KNN	n_neighbors	5
	weights	uniform
	metric	minkowski
LGBM	colsample_bytree	1.0
	learning_rate	0.1
	max_depth	-1
	min_child_samples	20
	min_child_weight	0.001
	n_estimators	100
	num_leaves	31
	reg_alpha	0.0
	reg_lambda	0.0
	subsample	1.0

Tablolar incelendiğinde hem test süreleri hem de performans metrikleri açısından öne çıkan modelin LGBM olduğu görülmektedir. LGBM, çoğu senaryoda diğer algoritmalarından daha yüksek doğruluk ve F1 skor değerlerine ulaşırken, test süresi ve birim test süresi bakımından da son derece verimli görünmektedir. KNN, performans açısından LGBM’nin gerisinde kalsa da özellikle A2 senaryolarında makul doğruluk ve F1 skor değerlerine ulaşabilmekte, ancak birim test süresi LGBM’ye kıyasla daha uzun kalmaktadır. SVM, bazı durumlarda orta düzeyde performans sunarken, test sürelerinin göreceli olarak daha yüksek olduğu ve birim test süresinin KNN ve LR’a kıyasla daha maliyetli olduğu dikkat çekmektedir. LR ise genellikle en düşük doğruluk ve F1 skoruna sahip olmakla beraber, test süresi ve birim test süresi açısından en hızlı sonuç veren yöntemdir. Sonuç olarak, yüksek performans ile düşük test süresini dengelemek isteyenler için LGBM öne çıkarken, çok hızlı ancak düşük doğruluk isteyen durumlar için LR, daha ılımlı bir dengeye gerektiği senaryolar için ise KNN veya SVM alternatif olarak değerlendirilebilir. Ayrıca, No-VPN koşullarının performansa genellikle olumlu etki yaptığı görülmektedir.

4.2. İkinci aşamada elde edilen sonuçlar (The results obtained in the second stage)

Çalışmanın ikinci aşamasında, Senaryo A1’de VPN ve No-VPN olarak yapılan ikili sınıflandırmada verilerin dengeli olduğu gözlemlenmiştir. Bu nedenle, Senaryo A1’deki zaman bazlı 4 adet veri seti için veri seti dengeleme işlemi yapılmamıştır. Ancak, Senaryo A2 ve Senaryo B’de yer alan toplam 12 adet veri setinde SMOTE kullanılarak dengeleme işlemi gerçekleştirilmiştir. Ayrıca hiperparametrelerin rastgele örnekleri seçilip çapraz doğrulama yapılarak en iyi kombinasyon belirlenmiş ve hiperparametre optimizasyonu sağlanmıştır. Yapılan optimizasyon sonrasında veriler tekrar eğitim ve teste tabi tutulmuştur. LGBM, KNN,

SVM ve LR algoritmaları kullanılarak yapılan optimizasyon sonrası elde edilen sonuçlar Tablo 10'da yer almaktadır. Dengeleme işlemi yapılmayan Senaryo A1'de yer alan 4 adet veri seti için optimizasyon sonrası en iyi hiperparametre seçimi yapıldıktan sonra elde edilen sonuçlara da aynı tabloda yer verilmiştir. Tablo 11'de ise optimizasyon sonrası algoritmalar için test süreleri raporlanmıştır.

Tablo 10. Veri setinde optimizasyon sonrası başarı oranları (The success rates after optimization on the dataset)

Senaryolar	Algoritma	LGBM		KNN		SVM		LR	
		Doğruluk	F1 Skor	Doğruluk	F1 Skor	Doğruluk	F1 Skor	Doğruluk	F1 Skor
Senaryo A1 15s		0,9135*	0,9173*	0,8277*	0,8421*	0,6167	0,6113	0,5963*	0,5877*
Senaryo A1 30s		0,8994	0,9081	0,8279	0,8289	0,6445	0,6367	0,5956	0,5874
Senaryo A1 60s		0,8915	0,9005	0,8089	0,8191	0,6323	0,6308	0,5603	0,5231
Senaryo A1 120s		0,8870	0,9015	0,8127	0,8209	0,6576*	0,6388*	0,5904	0,5802
Senaryo A2 No-VPN 15s		0,9653**	0,9459**	0,9126**	0,8591**	0,7403	0,7633	0,6646**	0,7197**
Senaryo A2 VPN 15s		0,9267	0,8989	0,8695	0,8203	0,6511	0,6411	0,5692	0,5486
Senaryo A2 No-VPN 30s		0,9468	0,9302	0,9109	0,8505	0,6427	0,6866	0,6489	0,6746
Senaryo A2 VPN 30s		0,9299	0,9076	0,8989	0,8454	0,7602**	0,7176**	0,6278	0,5735
Senaryo A2 No-VPN 60s		0,9294	0,9169	0,8675	0,8186	0,6372	0,6374	0,5537	0,6009
Senaryo A2 VPN 60s		0,9228	0,8678	0,8739	0,7999	0,6866	0,6293	0,5430	0,5044
Senaryo A2 No-VPN 120s		0,9437	0,9271	0,8993	0,8433	0,6748	0,6711	0,6171	0,6293
Senaryo A2 VPN 120s		0,9149	0,8614	0,8725	0,7972	0,6969	0,6049	0,5518	0,4746
Senaryo B 15s		0,9005*	0,8614*	0,8219	0,7334	0,5914*	0,5696*	0,3608	0,4008
Senaryo B 30s		0,8989	0,8561	0,8379*	0,7357*	0,4245	0,4234	0,3950*	0,3778*
Senaryo B 60s		0,8335	0,8234	0,8187	0,7245	0,3767	0,3443	0,3289	0,2619
Senaryo B 120s		0,8869	0,8253	0,8214	0,7140	0,4128	0,3810	0,3705	0,3281

* Kalın yazılan değerler, ilgili senaryo ve algoritmada elde edilen en yüksek başarı oranlarıdır.

**Kalın ve kırmızı yazılan değerler, ilgili algoritmada tüm senaryolar içinde elde edilen en yüksek başarı oranlarıdır.

Tablo 11. Veri setinde optimizasyon sonrası test süreleri (The test durations after optimization on the dataset)

Senaryo	Algoritma	Test Edilen Girdi Sayısı (adet)	LGBM		KNN		SVM		LR	
			Test Süresi (s)	Birim Test Süresi (s/ad)	Test Süresi (s)	Birim Test Süresi (s/ad)	Test Süresi (s)	Birim Test Süresi (s/ad)	Test Süresi (s)	Birim Test Süresi (s/ad)
Senaryo A1 15s		5.628	0,06	0,000011	0,43	0,000076	2,56	0,000455	0,01	0,000002
Senaryo A1 30s		4.397	0,10	0,000023	0,31	0,000071	1,82	0,000414	0,01	0,000002
Senaryo A1 60s		4.655	0,25	0,000054	0,44	0,000095	1,30	0,000279	0,01	0,000002
Senaryo A1 120s		3.236	0,34	0,000105	0,60	0,000185	0,96	0,000297	0,01	0,000003
Senaryo A2 No-VPN 15s		2.690	0,27	0,000100	1,50	0,000558	3,45	0,001283	0,01	0,000004
Senaryo A2 VPN 15s		2.938	0,93	0,000317	0,17	0,000058	1,79	0,000609	0,01	0,000003
Senaryo A2 No-VPN 30s		2.076	0,03	0,000014	0,10	0,000048	1,45	0,000698	0,01	0,000005
Senaryo A2 VPN 30s		2.321	0,04	0,000017	0,15	0,000065	1,31	0,000564	0,01	0,000004
Senaryo A2 No-VPN 60s		2.574	0,03	0,000012	0,11	0,000043	2,94	0,001142	0,01	0,000004
Senaryo A2 VPN 60s		2.081	0,03	0,000014	0,14	0,000067	1,31	0,000630	0,01	0,000005
Senaryo A2 No-VPN 120s		1.546	0,02	0,000013	0,06	0,000039	0,74	0,000479	0,01	0,000006
Senaryo A2 VPN 120s		1.690	0,11	0,000065	0,45	0,000266	1,10	0,000651	0,01	0,000006
Senaryo B 15s		5.704	0,16	0,000028	1,46	0,000256	12,75	0,002235	0,01	0,000002
Senaryo B 30s		4.543	0,64	0,000141	0,65	0,000143	7,70	0,001695	0,01	0,000002
Senaryo B 60s		4.825	0,23	0,000048	0,60	0,000124	6,50	0,001347	0,01	0,000002
Senaryo B 120s		3.501	0,79	0,000226	0,54	0,000154	6,00	0,001714	0,01	0,000003
Ortalama Test Süreleri			0,25	0,000074	0,48	0,000140	3,35	0,000906	0,01	0,000003

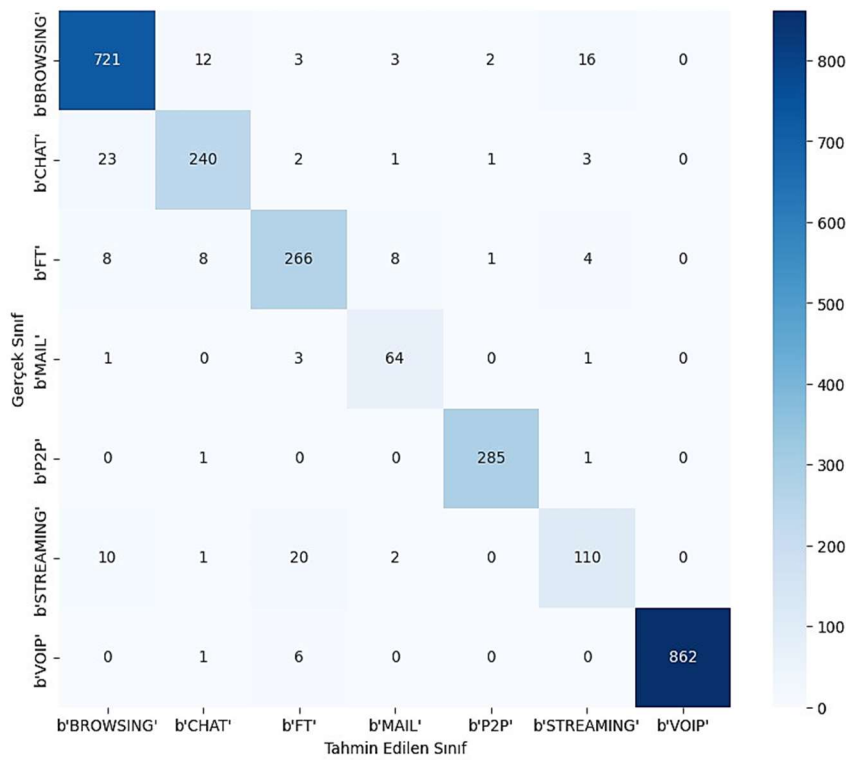
* Kalın yazılan değerler, en yüksek başarı oranı elde edilen senaryo ve algoritmadaki test süreleridir.

Tüm senaryolarda optimizasyon sonrasında en yüksek başarı oranlarına denetimli makine öğrenmesi algoritmaları arasında KNN ile ulaşılmıştır. KNN algoritmasında elde edilen en yüksek başarı oranları, Senaryo A2 No-VPN 15s veri setinde 0,9126 doğruluk ve 0,8591 F1 skor olarak gerçekleşmiştir. Bu veri setinde 2.690 girdi için test süresi 1,5 saniye sürmüştür, bu da her bir girdinin ortalama 0,000558 saniyede kategorize edilebildiğini göstermektedir.

Topluluk öğrenmesi algoritmalarından LGBM’de ise en yüksek başarı oranlarına, yine Senaryo A2 No-VPN 15s veri setinde 0,9653 doğruluk ve 0,9459 F1 skor ile ulaşılmıştır. Ayrıca LGBM, her bir girdiyi ortalama 0,0001 saniyede kategorize edebilmiştir.

Sonuç olarak LGBM’nin hem doğruluk ve F1 skor değerleri hem de kategorizasyon süresinin kısıtlılığı bakımından KNN’den daha etkin olduğu görülmektedir.

Senaryo A2 No-VPN 15s veri seti ile LGBM algoritması kullanılarak elde edilen en başarılı sonuç için Şekil 5’deki karmaşıklık matrisine göre yapılan analizde, sınıf türlerini tahmin etmedeki en belirgin hatanın Chat ile Browsing sınıfları arasında olduğu görülmektedir. Bu durum, Chat sınıfına ait örneklerin Browsing olarak ya da Browsing sınıfına ait örneklerin Chat sınıfı olarak tahmin edildiğini göstermektedir.



Şekil 5. LGBM algoritması ile Senaryo A2 No-VPN 15s veri seti karmaşıklık matrisi
(The confusion matrix for the Scenario A2 No-VPN 15s dataset with the LGBM algorithm)

KNN ve LGBM algoritmalarına ait parametre optimizasyonu sonrasında elde edilen en iyi parametreler Tablo 12’de sunulmaktadır.

Tablo 12. KNN ve LGBM algoritmaları için en iyi parametre değerleri
(The best parameter values for the KNN and LGBM algorithms)

Algoritma	Parametrenin Adı	Hiperparametre Aralıkları	En İyi Değer
KNN	n_neighbors	[3, 5, 7, 9]	7
	weights	['uniform', 'distance']	distance
	metric	['euclidean', 'manhattan', 'minkowski']	manhattan
LGBM	colsample_bytree	[0.5, 0.6, 0.7, 0.8, 0.9, 1.0]	0.8
	learning_rate	[0.01, 0.05, 0.1, 0.3, 0.5, 0.7]	0.5
	max_depth	sp_randint(3, 30)	13
	min_child_samples	sp_randint(100, 1000)	257
	min_child_weight	[1e-3, 1e-2, 0.1, 0.5, 1, 5, 10]	0.01
	n_estimators	sp_randint(50, 1000)	604
	num_leaves	sp_randint(6, 100)	18
	reg_alpha	[0, 0.1, 0.5, 1, 2, 5, 10]	0
	reg_lambda	[0, 0.1, 0.5, 1, 2, 5, 10]	1
	subsample	[0.6, 0.7, 0.8, 0.9, 1.0]	0.9

Çalışmanın her iki aşamasında da algoritmaların test süreleri incelendiğinde, senaryolardaki en düşük toplam test sürelerinin genellikle LGBM ve LR algoritmalarında elde edildiği, buna karşılık KNN ve özellikle SVM'nin daha yüksek test sürelerine sahip olduğu görülmektedir. Birim test süresi değerlendirildiğinde LR, çoğunlukla her bir giriş başına en düşük süreyi sunarken (yaklaşık 2 ila 7 mikro saniye), LGBM de bu açıdan rekabetçi sonuçlar ortaya koymaktadır. KNN ve SVM ise hem toplam hem de birim başına test süresi anlamında diğer iki algoritmaya kıyasla daha uzun test süreleriyle dikkat çekmektedir. Özellikle SVM'nin birim test başına milisaniyeye yaklaşan veya geçen süreleri (0,000279 s/ad ve üzerine çıkan değerler) onu hız açısından dezavantajlı hale getirirken, LR ve LGBM test koşullarında en hızlı tepki verebilen modeller olarak öne çıkmıştır. Bu veriler genel olarak, test süresinin kritik olduğu hallerde LR ve LGBM'nin tercih edilebileceğine, KNN ve SVM'nin ise daha uzun işlem süresi gerektirdiğine işaret etmektedir.

5. Sonuçlar ve Tartışma (Results and Discussion)

Bu çalışmada, siber güvenlik uzmanlarının ağ üzerindeki tehditleri tespit etme ve saldırıları önleme yeteneklerinin artırılarak sistemlerin daha güvenli hale getirilmesi amaçlanmıştır. Bu sınıflandırma sayesinde, siber güvenlik uzmanları belirledikleri politikalar doğrultusunda, örneğin yetkisiz erişim olarak etiketlenmiş istenmeyen ağ trafiğini tespit edip engelleyebileceklerdir. Çalışma kapsamında, ağ trafiğinde yaygın olarak kullanılan sınıfları içeren ve gerçek internet trafiğinden elde edilen ISCXVPN2016 veri seti kullanılmıştır.

Bu veri seti için denetimli makine öğrenmesi algoritmalarından KNN, SVM ve LR ile topluluk öğrenmesi algoritmalarından LGBM algoritması kullanılmıştır. Kullanılan algoritmalar için öncelikle orijinal veri seti ile eğitim ve test gerçekleştirilmiştir. Daha sonra, dengesiz dağılımlı veri setleri SMOTE ile dengelenip, rastgele arama ve çapraz doğrulama yöntemleri ile parametre optimizasyonu yapılarak tekrar eğitim ve test gerçekleştirilmiştir. Optimizasyon sonucunda başarı oranlarının arttığı görülmüştür.

Bu çalışmada, optimizasyon sonrası LGBM algoritması ile elde edilen en başarılı sonuçlar ile literatürde yer alan diğer araştırmacıların geliştirdiği algoritmaların başarı oranlarının karşılaştırması Tablo 13'te sunulmuştur.

Tablo 13. Literatür karşılaştırması (Literature comparison)

Senaryo	Yazar(lar)	Algoritma	Doğruluk	F1 Skor	Kesinlik
A1	Draper-gil vd. [8]	C4.5	-	-	90,60%
	Majeed vd. [38]	Federated Learning	86%	-	-
	Uğurlu vd. [2]	XGBoost	93,04%	-	-
	Bozkır vd. [22]	XGBoost	-	99%	-
	Kendi çalışmamız	LGBM	91,35%	91,73%	91,99%
A2	Draper-gil vd. [8]	C4.5	-	-	89%
	Caicedo vd. [6]	Bagging	94,42%	-	-
	Majeed vd. [38]	Federated Learning	86%	-	-
	Uğurlu vd. [2]	XGBoost	94,53%	-	-
	Bozkır vd. [22]	XGBoost	-	99%	-
Kendi çalışmamız	LGBM	96,53%	94,59%	94,86%	
B	Draper-gil vd. [8]	C4.5	-	-	80,90%
	Caicedo vd. [6]	Bagging	86,94%	-	-
	Majeed vd. [38]	Federated Learning	81%	-	-
	Uğurlu vd. [2]	XGBoost	86,06%	-	-
	Bozkır vd. [22]	XGBoost	-	99%	-
Kendi çalışmamız	LGBM	90,05%	86,14%	86,83%	

Senaryo A1’de en yüksek başarı oranları 15s veri setinde elde edilmiş olup doğruluk %91,35, F1 Skor %91,73 ve kesinlik %91,99’dur. Draper-gil vd. [7] ve Majeed vd. [21] tarafından yapılan çalışmalara göre daha yüksek başarı oranlarına ulaşıldığı görülmüştür. Ancak Uğurlu vd. [2] ve Bozkır vd. [22] tarafından yapılan çalışmalardan daha az başarı elde edilmiştir. Senaryo A2’de en yüksek başarı oranları 15s veri setinde elde edilmiş olup doğruluk %96,53, F1 Skor %94,59 ve kesinlik %94,86’dır. Senaryo B’de en yüksek başarı oranları da yine 15s veri setinde elde edilmiş olup doğruluk %90,05, F1 Skor %86,14 ve kesinlik %86,83’dır. Her iki senaryoda da Draper-gil vd. [7], Caicedo vd. [5], Majeed vd. [21] ve Uğurlu vd. [2] tarafından yapılan çalışmalara göre daha yüksek başarı oranlarına ulaşıldığı görülmüştür. Ancak Bozkır vd. [22] tarafından yapılan çalışmadan daha az başarı elde edilmiştir.

Şifreli ağ trafiğinin sınıflandırılmasına ilişkin bu çalışmada, başarı oranlarının yanı sıra günümüzde hemen her alanda önemli bir kriter haline gelen test süresi de ölçülmüştür. Optimize edilmiş koşullarda, LGBM topluluk öğrenmesi algoritmasının ortalama girdi kategorizasyon süresi 0,000074 saniye olarak hesaplanırken, KNN makine öğrenmesi algoritmasının ortalama kategorizasyon süresi 0,00014 saniye olarak belirlenmiştir. Bu değerlere göre LGBM algoritması, KNN’ye kıyasla girdi kategorizasyonunda daha hızlı çalışmaktadır. Elde edilen bulgular, Khatouni ve Heywood [35] tarafından yapılan çalışmanın aksine, şifreli trafiğin sınıflandırılmasında topluluk öğrenmesi algoritmasının makine öğrenmesi algoritmasına oranla daha yüksek bir hız sağlayabileceğini ortaya koymaktadır.

Yapılan çalışmada hem doğruluk hem de hız açısından yüksek performanslı bir LGBM topluluk öğrenmesi modeli geliştirilmiştir. Şifreli trafiğin sınıflandırılmasına odaklanan bu yaklaşım, mevcut tehdit tespit ve engelleme sistemlerinin iyileştirilmesini ve güçlendirilmesini mümkün kılmaktadır. Önerilen model, şifreli trafiği daha doğru ve hızlı biçimde sınıflandırırken, yeni nesil güvenlik duvarları veya ağ izleme sistemleriyle entegre edilerek daha etkin ve uyarlanabilir bir güvenlik yapısı oluşturulabilir. Gelecekte, farklı veri kaynaklarının kullanımıyla daha kapsamlı ve güvenilir sınıflandırma modellerinin geliştirilmesi, modelin hızını artıracak yeni yöntemlerin tasarlanması ve veri bütünlüğünü korumak amacıyla zaman damgası entegrasyonunun sağlanması öngörülmektedir. Bu alanda sürdürülen çalışmalar ilerledikçe, modellere daha yüksek güvenilirlik düzeyleri kazandırılacak ve böylece sistemler daha güvenli bir hale getirilebilecektir.

Çıkar Çatışması Beyanı (Conflict of Interest Statement)

Yazarlar tarafından herhangi bir çıkar çatışması bildirilmemiştir.

Kaynaklar (References)

- [1] B. M. Leiner, R. E. Kahn, J. Postel, and L. Kleinrock, "A brief history of the internet," *ACM SIGCOMM Computer Communication Review*, vol. 39, no. 5, pp. 22-31, Oct. 2009. doi: 10.1145/1629607.1629613
- [2] M. Uğurlu, İ. A. Doğru, and R. S. Arslan, "A new classification method for encrypted internet traffic using machine learning," *Turkish Journal of Electrical Engineering and Computer Sciences*, vol. 25, no. 9, pp. 2450-2468, 2021. doi: 10.3906/ELK-2011-31
- [3] E. Cengiz and M. Gök, "Reinforcement learning applications in cyber security: A Review," *Sakarya University Journal of Science*, vol. 27, no. 2, pp. 481-503, Apr. 2023. doi: 10.16984/saufenbilder.1237742
- [4] M. K. Pehlivanoglu, R. Atay, and D. E. Odabaş, "İki seviyeli hibrit makine öğrenmesi yöntemi ile saldırı tespiti," *Gazi Journal of Engineering Sciences*, vol. 5, no. 3, pp. 258-272, Dec. 2019. doi: 10.30855/gmbd.2019.03.07
- [5] J. A. Caicedo-Muñoz, A. L. Espino, J. C. Corrales, and A. Rendón, "QoS-classifier for VPN and Non-VPN traffic based on time-related features," *Computer Networks*, vol. 144, pp. 271-279, Oct. 2018. doi: 10.1016/j.comnet.2018.08.008
- [6] M. Uğurlu, "Şifrelenmiş internet trafiğinin makine öğrenmesi yaklaşımı ile sınıflandırılması," Yüksek Lisans Tezi, Gazi Üniversitesi, Fen Bilimleri Enstitüsü, Ankara, 2020
- [7] G. Drapper-Gil, A. H. Lashkari, M. S. I. Mamun, and A. A. Ghorbani, "Characterization of encrypted and VPN traffic using time-related features," ICISSP 2016 - Proceedings of the 2nd International Conference on Information Systems Security and Privacy, 19-21 Şubat 2016, Roma, İtalya, SciTePress, pp. 407-414. doi: 10.5220/0005740704070414
- [8] Y. F. Huang, C. B. Lin, C. M. Chung, and C. M. Chen, "Research on QoS classification of network encrypted traffic behavior based on machine learning," *Electronics (Switzerland)*, vol. 10, no. 12, Jun. 2021. doi: 10.3390/electronics10121376
- [9] S. Frankel (NIST), P. Hoffman (Virtual Private Network Consortium), A. Orebaugh (BAH), R. Park (BAH), "NIST SP 800-113 Guide to SSL VPNs." [Online]. Available: <https://csrc.nist.gov/pubs/sp/800/113/final> [Accessed: Mar. 24, 2024].
- [10] N. H. Nguyen, *SSL/TLS interception challenge from the shadow to the light*, SANS Institute, 2019.
- [11] S. Frankel, P. Hoffman, A. Orebaugh, and R. Park, "NIST-“Guide to SSL VPNs,” Recommendations of the National Institute of Standards and Technology. [Online]. Available: <https://nvlpubs.nist.gov/nistpubs/Legacy/SP/nistspecialpublication800-113.pdf> [Accessed: Mar. 21, 2024].
- [12] Cisco, "Chapter: Traffic Classification," www.cisco.com. [Online]. Available: https://www.cisco.com/c/en/us/td/docs/nsite/enterprise/wan/wan_optimization/wan_opt_sg/chap05.html. [Accessed: Mar. 7, 2024].
- [13] R. T. Elmaghraby, N. M. Abdel Aziem, M. A. Sobh, and A. M. Bahaa-Eldin, "Encrypted network traffic classification based on machine learning," *Ain Shams Engineering Journal*, vol. 15, no. 2, 2023. doi: 10.1016/j.asej.2023.102361
- [14] Internet Assigned Numbers Authority, "Service name and transport protocol port number registry," www.iana.org. [Online]. Available: <https://www.iana.org/assignments/service-names-port-numbers/service-names-port-numbers.xhtml>. [Accessed: Mar. 19, 2024].
- [15] D. T. Ergönül and O. Demir, "Real-time encrypted traffic classification with deep learning," *Sakarya University Journal of Science*, vol. 26, no. 2, pp. 313-332, Apr. 2022. doi: 10.16984/saufenbilder.1026502
- [16] A. Azab, M. Khasawneh, S. Alrabaee, K. K. Choo, and M. Sarsour, "Network traffic classification: Techniques, Datasets, and Challenges," *Digital Communications and Networks. KeAi Communications Co.*, Sep. 2022. doi: 10.1016/j.dcan.2022.09.009
- [17] V. A. Muliukha, L. U. Laboshin, and A. Lukashin, "Analysis and classification of encrypted network traffic using machine learning," XXIII International Conference on Soft Computing and Measurements, 27-29 May. 2020, Saint Petersburg, Russia, pp. 194-197. doi: 10.1109/SCM50615.2020.9198811
- [18] A. Lichy, O. Bader, R. Dubin, A. Dvir, and C. Hajaj, "When an RF beats a CNN and GRU, together-a comparison of deep learning and classical machine learning approaches for encrypted malware traffic classification," Jun. 2022. [Online]. Available: <http://arxiv.org/abs/2206.08004>
- [19] T. C. Obasi, "Encrypted network traffic classification using ensemble learning techniques," Ph.D. dissertation, Carleton University, Ottawa, Ontario, Canada, 2020. doi: 10.22215/etd/2020-14171

- [20] G. Abbas, U. Farooq, P. Singh, S. S. Khurana, and P. Singh, "Feature engineering and ensemble learning-based classification of VPN and Non-VPN based network traffic over temporal features," *SN Comput Science*, vol. 4, Sep. 2023. doi: 10.1007/s42979-023-01944-5
- [21] U. Majeed, L. U. Khan, and C. Seon Hong, "Cross-silo horizontal federated learning for flow-based time-related-features oriented traffic classification," APNOMS 2020 - 2020 21st Asia-Pacific Network Operations and Management Symposium: Towards Service and Networking Intelligence for Humanity, 23-25 Eylül 2020, Daegu, Güney Kore, pp. 389-392. doi: 10.23919/APNOMS50412.2020.9236971
- [22] R. Bozkır, "Şifreli ağ trafiğinin içerik açısından sınıflandırılması," Yüksek Lisans Tezi, Bursa Uludağ Üniversitesi, Fen Bilimleri Enstitüsü, Bursa, 2022.
- [23] B. Yamansavascilar, M. A. Guvensan, A. G. Yavuz, and M. E. Karsligil, "Application identification via network traffic classification," 2017 International Conference on Computing, Networking and Communications, 26-29 Ocak 2017, Santa Clara, CA, ABD, pp. 843-848. doi: 10.1109/ICCNC.2017.7876241.
- [24] S. Bagui, X. Fang, E. Kalimantan, S. C. Bagui, and J. Sheehan, "Comparison of machine-learning algorithms for classification of VPN network traffic flow using time-related features," *Journal of Cyber Security Technology*, vol. 1, no. 2, pp. 108-126, Apr. 2017. doi: 10.1080/23742917.2017.1321891.
- [25] M. Lotfollahi, M. Jafari Siavoshani, R. Shirali Hossein Zade, and M. Saberian, "Deep packet: A Novel Approach for Encrypted Traffic Classification using Deep Learning," *Soft Comput*, vol. 24, no. 3, pp. 1999-2012, Feb. 2019. doi: 10.1007/s00500-019-04030-2
- [26] T. Shapira and Y. Shavitt, "Encrypted internet traffic classification is as easy as image recognition," IEEE INFOCOM 2019 - IEEE Conference on Computer Communications Workshops, 29 Nisan - 2 Mayıs 2019, Paris, France, pp. 680-687. doi: 10.1109/INFCOMW.2019.8845315.
- [27] F. Zhang, T. Shang, and J. Liu, "Imbalanced encrypted traffic classification scheme using random forest," 2020 International Conferences, Rhodes, Greece, pp. 837-842, 2020. doi: 10.1109/iThings-GreenCom-CPSCoM-SmartData-Cybermatics50389.2020.00142
- [28] L. Guo, Q. Wu, S. Liu, M. Duan, H. Li, and J. Sun, "Deep learning-based real-time VPN encrypted traffic identification methods," *Journal of Real-Time Image Processing 17*, Springer, pp. 103-114, Feb. 2020. doi: 10.1007/s11554-019-00930-6
- [29] J. Cheng, R. He, E. Yuepeng, Y. Wu, J. You, and T. Li, "Real-time encrypted traffic classification via lightweight neural networks," 2020 IEEE Global Communications Conference, GLOBECOM 2020 - Proceedings, Institute of Electrical and Electronics Engineers Inc., 7-11 Aralık 2020, Taipei, Tayvan, pp. 1-6. doi: 10.1109/GLOBECOM42002.2020.9322309
- [30] K. Zhou, W. Wang, C. Wu, and T. Hu, "Practical evaluation of encrypted traffic classification based on a combined method of entropy estimation and neural networks," *ETRI Journal*, vol. 42, no. 3, pp. 311-323, Jun. 2020. doi: 10.4218/etrij.2019-0190
- [31] Z. Bu, B. Zhou, P. Cheng, K. Zhang, and Z. H. Ling, "Encrypted network traffic classification using deep and parallel network-in-network models," *IEEE Access*, vol. 8, pp. 132950-132959, 2020. doi: 10.1109/ACCESS.2020.3010637
- [32] A. A. Afuwape, Y. Xu, J. H. Anajemba, and G. Srivastava, "Performance evaluation of secured network traffic classification using a machine learning approach," *Comput. Stand. Interfaces*, vol. 78, Oct. 2021. doi: 10.1016/j.csi.2021.103545
- [33] K. Ismailaj, M. Camelo, and S. Latré, "When deep learning may not be the right tool for traffic classification," in Proc. of the 2021 IFIP/IEEE International Symposium on Integrated Network Management (IM), May 2021, Bordeaux, France, pp. 884-889. Available: IEEE Xplore, <https://ieeexplore.ieee.org/abstract/document/9463927>
- [34] A. Almomani, "Classification of virtual private networks encrypted traffic using ensemble learning algorithms," *Egyptian Informatics Journal*, vol. 23, no. 4, pp. 57-68, Dec. 2022. doi: 10.1016/j.eij.2022.06.006
- [35] A. S. Khatouni and N. Z. Heywood, "Integrating machine learning with off-the-shelf traffic flow features for HTTP/HTTPS traffic classification," 2019 IEEE Symposium on Computers and Communications (ISCC), 29 Haziran - 3 Temmuz 2019, Barç., Spain, pp. 1-7. doi: 10.1109/ISCC47284.2019.8969578
- [36] A. Aydın, "Topluluk öğrenmesi kullanılarak zararlı alan adlarının sınıflandırılması," Yüksek Lisans Tezi, Marmara Üniversitesi, Fen Bilimleri Enstitüsü, İstanbul, 2023.
- [37] K. Eker, A. G. Eker, D. Mandal, M. Pehlivanoglu, and N. Duru, "Makine öğrenmesi yaklaşımları ile ağ trafik sınıflandırılması," 7th International Conference on Computer Science and Engineering, UBMK 2022, 14-16 Eylül 2022, Diyarbakır, Türkiye, pp. 393-397. doi: 10.1109/UBMK55850.2022.9919497
- [38] Y. Alaca, "Siber güvenlikte CIC-Darknet2020 veri seti kullanarak VPN/NoVPN ve Tor/NoTor sınıflandırması: Basit ve Karmaşık Modellerin Kullanımı," *Fırat Üniversitesi Müh. Bilimleri Dergisi*, vol. 35, no. 2, pp. 569-579 Jul. 2023. doi: 10.35234/fumbd.1291388

- [39] M. Uğurlu, İ. A. Doğru, and R. S. Arslan, "Detection and classification of darknet traffic using machine learning methods," *Journal of the Faculty of Engineering and Architecture of Gazi University*, vol. 38, no. 3, pp. 1737–1746, 2023. doi: 10.17341/gazimmfd.1023147
- [40] E. G. İlğün, Y. Sönmez, and M. Dener, "DarkWEB traffic detection and classification using machine learning method," *Gazi Journal of Engineering Sciences*, vol. 9, no. 4, pp. 126-140, 2023. doi: 10.30855/gmbd.0705S13
- [41] A. Zheng and A. Casari, "Feature engineering for machine learning: Principles and Techniques for Data Scientists," Chapter 2- Feature Selection, Almanya: O'Reilly Media. 2018.
- [42] L. Yang and A. Shami, "On hyperparameter optimization of machine learning algorithms: Theory and Practice," *Neurocomputing*, vol. 415, pp. 295-316, Nov. 2020. doi: 10.1016/j.neucom.2020.07.061
- [43] J. Bergstra and Y. Bengio, "Random search for hyper-parameter optimization," 2012. [Online]. Available: <http://scikit-learn.sourceforge.net>. [Accessed: March 05, 2024].
- [44] C. Schaffer, "Selecting a classification method by cross-validation," *Mach Learn* 13, 135-143, 1993. doi: 10.1007/BF00993106
- [45] X. Deng, Q. Liu, Y. Deng, and S. Mahadevan, "An improved method to construct basic probability assignment based on the confusion matrix for classification problem," *InfSci (NY)*, vol. 340–341, pp. 250-261, May 2016. doi: 10.1016/j.ins.2016.01.033

This is an open access article under the CC-BY license



GAZİ

JOURNAL OF ENGINEERING SCIENCES

Optimal Location and Sizing of Distributed Generation Using Artificial Bee Colony and JAYA Algorithms

Salih Ermiş^{a*}, Oğuz Taşdemir^b

Submitted: 30.12.2024 Revised: 30.01.2025 Accepted: 03.02.2025 doi:10.30855/gmbd.070525N05

ABSTRACT

Keywords: Distributed Generation (DG), Optimal Placement, Artificial Bee Colony (ABC), JAYA Algorithm, Power Loss Reduction

^{a*} Kırşehir Ahi Evran University,
Faculty of Engineering and Architecture,
Dept. of Electrical and Electronics
Engineering
40100 - Kırşehir, Türkiye
Orcid: 0000-0002-1053-9160
e mail:sermis@ahievran.edu.tr

^b Kırşehir Ahi Evran University,
Faculty of Engineering and Architecture,
Dept. of Electrical and Electronics
Engineering
40100 - Kırşehir, Türkiye
Orcid: 0000-0003-1782-0024
e mail:oguz.tasdemir@ahievran.edu.tr

*Corresponding author:
sermis@ahievran.edu.tr

The rapid increase in energy demand, environmental concerns, and the necessity for efficient utilization of energy resources highlight the importance of distributed generation (DG) systems. Optimal positioning and sizing of DG units play a critical role in reducing power losses, improving voltage profiles, and increasing system reliability. This study evaluates the performance of the Artificial Bee Colony (ABC) and JAYA algorithms for solving the optimal DG location and sizing problem on an IEEE 33-bus distribution system. The results show that the JAYA algorithm provides superior performance in reducing power losses, achieving a 73.00% reduction in active power loss and a 68.77% reduction in reactive power loss in the DG3 scenario. The minimum bus voltage improved from 0.902 p.u. (base case) to 0.979 p.u. with the JAYA algorithm. The ABC algorithm, on the other hand, was more effective in improving the voltage profile, reaching 0.969 p.u. in the DG3 scenario. Moreover, the JAYA algorithm achieved a faster convergence rate and lower computational time compared to the ABC algorithm. These findings indicate that a hybrid approach combining both algorithms may lead to further improvements in DG optimization. This study aims to contribute to the effective planning and implementation of distributed generation units in modern power systems.

Yapay Arı Kolonisi ve JAYA Algoritmaları Kullanarak Dağıtık Üretimin Optimal Yerleşimi ve Boyutlandırılması

ÖZ

Enerji talebindeki hızlı artış, çevresel kaygılar ve enerji kaynaklarının verimli kullanılması gerekliliği, dağıtık üretim (DG) sistemlerinin önemini vurgulamaktadır. DG ünitelerinin optimum konumlandırılması ve boyutlandırılması, güç kayıplarının azaltılmasında, gerilim profillerinin iyileştirilmesinde ve sistem güvenilirliğinin artırılmasında kritik bir rol oynamaktadır. Bu çalışma, bir IEEE 33-bus dağıtım sisteminde optimum DG konumu ve boyutlandırma problemini çözmek için Yapay Arı Kolonisi (ABC) ve JAYA algoritmalarının performansını değerlendirmektedir. Sonuçlar, JAYA algoritmasının güç kayıplarını azaltmada üstün performans sağladığını ve DG3 senaryosunda aktif güç kaybında %73,00 ve reaktif güç kaybında %68,77 azalma elde ettiğini göstermektedir. Minimum bara gerilimi JAYA algoritması ile 0,902 p.u.'dan (baz durum) 0,979 p.u.'ya yükselmiştir. ABC algoritması ise gerilim profilini iyileştirmede daha etkili olmuş ve DG3 senaryosunda 0,969 p.u. değerine ulaşmıştır. Ayrıca, JAYA algoritması ABC algoritmasına kıyasla daha hızlı bir yakınsama oranı ve daha düşük hesaplama süresi elde etmiştir. Bu bulgular, her iki algoritmayı birleştiren hibrit bir yaklaşımın DG optimizasyonunda daha fazla iyileştirmeye yol açabileceğini göstermektedir. Bu çalışma, modern güç sistemlerinde dağıtık üretim birimlerinin etkin bir şekilde planlanmasına ve uygulanmasına katkıda bulunmayı amaçlamaktadır.

Anahtar Kelimeler: Dağıtık Üretim (DG), Optimal Yerleşim, Yapay Arı Kolonisi (ABC), JAYA Algoritması, Güç Kaybı Azaltma

1. Introduction

Today, increasing energy demand, environmental concerns, and the need for efficient use of energy resources have necessitated the adoption of innovative approaches in energy generation and distribution systems. In this context, DG has emerged as an important solution that aims to shift energy generation from centralized systems to smaller and more localized energy sources. DG systems can be defined as small-scale power generation within the distribution system [1]. Distributed generation systems have the potential to reduce energy losses and improve system reliability and efficiency [2-4]. However, the effective integration of these systems requires correct siting and sizing decisions [5]. Improper placement and sizing of DGs can lead to excessive power losses, voltage ripples, and increased costs [6].

The optimal placement and sizing of DGs require balancing multiple objectives such as reducing energy generation costs, minimizing power losses, improving voltage profiles, and enhancing system reliability. To maximize the benefits of DGs, single/multi-objective target functions should be established. Therefore, such multi-objective optimization problems necessitate the use of robust and flexible optimization methods [7-9]. When determining these objective functions, the constraints and limitations must be well-defined to ensure maximum system benefit.

DG systems are flexible in utilizing renewable energy sources such as solar, wind, hydro, biomass, and geothermal, as well as conventional energy sources like gas turbines, microturbines, fuel cells, and internal combustion engines [10]. For efficient allocation of DGs in distribution networks, minimization of power losses is very important. Various optimization techniques are also used to minimize power loss. Genetic Algorithm (GA) [11], Artificial Neural Networks (ANN) [12], Particle Swarm Optimization (PSO) [13] have been widely used to achieve this goal. Moreover, determining the optimal location of the DGs is a critical issue that needs careful consideration, and various methods have been proposed to address it. In the literature, continuous power flow (CPF) analysis has been used to calculate the sensitivity of each bus and determine the optimal DG placement [14]. Weak Bus Sensitivity Index (WBSI) is proposed using CPF to identify suitable locations for DG integration [15]. Moreover, PSO and GA are used to determine the optimal size and location of DGs [16]. Voltage Sensitivity Index (VSI) is used to identify the weakest bus in the system [17]. Furthermore, the optimal allocation and sizing of DGs in distribution networks are performed to minimize power losses and improve voltage stability. Three VSI and PSO are used in this process: Direct Voltage Stability Index (DVSI), Fast Voltage Stability Index (FVSI), and Line Quality Factor (LQF) [18].

In the IEEE 69-bus distribution system, studies aimed at optimizing the allocation and sizing of DGs to reduce total active power losses and improve the voltage stability index have been presented using PSO and Bat Algorithm (BA) [19]. The Grey Wolf Optimizer (GWO), Whale Optimization Algorithm (WOA), and PSO have been applied to the IEEE 33-bus and IEEE 69-bus test systems to reduce power losses and improve voltage profiles [20]. Moreover, a hybrid model based on PSO and Chaotic Frog Leaping Algorithm (PSO-CFL) has been proposed to minimize power losses and enhance voltage profile quality. This study developed a PSO-CFL based algorithm to determine the optimal DG location and size, analyzing its performance on IEEE 33-bus and IEEE 69-bus radial distribution systems [21]. Additionally, optimization techniques such as Biogeography-Based Optimization (BBO), GWO, Salp Swarm Algorithm (SSA), WOA, and Moth Flame Optimization (MFO) have been proposed to solve the sizing and allocation problems of DGs in the IEEE 33-bus, IEEE 69-bus, and other distribution systems while reducing energy losses [22]. To find the optimal size and location of different types of DGs and optimally reconfigure the grid, continuous and binary PSO algorithms (CBPSO) have been recommended. These methods have been applied to the IEEE 33-bus and IEEE 69-bus distribution networks to reduce power losses and improve voltage profiles [23].

In the IEEE 33-bus distribution network, GA, Harmony Search Algorithm (HSA), and improved HSA have been proposed to determine optimal DG locations and improve voltage profiles [24]. Furthermore, a new methodology is applied to minimize power losses through optimal reconfiguration and placement of DGs in

IEEE 33-bus and IEEE 69-bus test radial distribution systems. Three optimization algorithms, PSO, GA, and Blue Whale Optimization (BWO) were used to achieve these objectives [25]. The optimal dimensioning and placement of distributed generators in the 7-33-71 bus power systems have been achieved by the application of a high convergence optimization algorithm [26]. The artificial rabbit optimization technique was employed in radial distribution systems to enhance the voltage stability index, facilitating the calculation of optimal locations and sizes of DGs [27]. To determine the optimum DG allocation in IEEE 14-30 bus systems, Garra Rufa optimization was used to reduce active power loss and increase the voltage index, thus realizing location and size allocation [28]. Finally, a fine-tuned PSO-based approach is proposed to optimize the placement and sizing of various types of DGs in IEEE 33-bus, IEEE 69-bus, and real-world radial distribution networks in Malaysia [29].

The location and size of DGs must be carefully considered when assessing the installation, cost, and impact of a distribution system. Incorrect selection of DG location and size can cause more harm than benefit, leading to significant power losses and instability in the distribution network. That is, incorrect location and size can lead to significant power losses and instability in the distribution network. In distribution systems, power flows from the grid supply point to the load. This can result in large power losses.

This study aims to address the problem of optimal placement and sizing of distributed generation (DG) systems by evaluating the performance of the Artificial Bee Colony (ABC) and JAYA algorithms. The main objectives of the study are to minimize power losses, improve voltage profiles, and enhance system reliability. The analyses conducted on the IEEE 33-bus distribution system compare both algorithms in terms of convergence speed, power loss reduction, voltage improvement capability, and computation time. The obtained results indicate that the JAYA algorithm achieves faster convergence and more effective reduction of active/reactive power losses. On the other hand, the ABC algorithm proves to be more successful in improving voltage profiles. This study aims to contribute to the efficient planning and implementation of distributed generation units in modern power systems.

The manuscript is organized as follows: Section 2 defines the mathematical formulation and objective functions for the optimal placement and sizing problem of DGs. Section 3 introduces the proposed algorithms. Analysis results, comparisons, and literature discussions are presented in Section 4. Finally, Section 5 concludes the study.

2. Formulation of The Problem

To determine the optimum location and size of DGs in distribution systems, the objective functions of minimizing active power losses and reducing voltage deviation are determined within various constraints and limitations.

2.1. Power loss minimization

To minimize the total power loss in distribution systems, it is formulated as in Eq. 1.

$$f_1(x) = P_{Loss} = \sum_{i=1}^N R_i |I_i|^2 \quad (1)$$

Where, $f_1(x)$ is the power loss objective function, N is the number of buses, R_i is the resistance of bus i . and I_i is the current of bus i .

2.2. Voltage deviation

To minimize the voltage deviation value in distribution systems, it is formulated as in Eq. 2.

$$f_2(x) = VD = \sum_{i=1}^N |V_i - 1| \quad (2)$$

Where, $f_2(x)$ is the voltage deviation objective function, V_i is the voltage at bus i .

2.3. Objective function

The objective function for the optimum location and size of DGs in the distribution system, which is the sum of the power loss reduction and voltage deviation value, is given in Eq. 3.

$$f(x) = \omega f_1(x) + (1 - \omega) f_2(x) \quad (3)$$

Here, $f(x)$ is the objective function for the optimal location and size, ω is chosen as the weight factor. The weighting factor is determined according to the needs of the system and can be adjusted by the operator. For example, if the power loss in a distribution system is high, the value of ω can be kept high. If voltage fluctuations are a major problem, ω can be selected at low values. In this way, system performance is optimized by producing solutions suitable for different network conditions and operating strategies.

2.3.1. Equality constraints

The equality constraints are based on the balance principle. The power flow equations corresponding to both the active and reactive power balance equations are defined mathematically as Eqs. 4 and 5:

$$P_{Gi} - P_{Di} - V_i \sum_{j=1}^N V_j [G_{ij} \cos(\delta_i - \delta_j) + B_{ij} \sin(\delta_i - \delta_j)] = 0 \quad (4)$$

$$Q_{Gi} - Q_{Di} - V_i \sum_{j=1}^N V_j [G_{ij} \sin(\delta_i - \delta_j) + B_{ij} \cos(\delta_i - \delta_j)] = 0 \quad (5)$$

Here, P_{Gi} is the active power produced by the generators at bus i . P_{Di} , the active power demand at bus i . Q_{Gi} is the reactive power produced by the generators at bus i . Q_{Di} , the active power demand at bus i . G_{ij} and B_{ij} are the conductance and susceptance values of the transmission line between the i . and j . buses.

2.3.2. Inequality constraints

The voltage value of each busbar must be maintained within the limits in Eq. 6. In the study, V_{min} and V_{max} values are taken as 0.95 and 1.05 p.u, respectively.

$$V_{min} \leq V \leq V_{max} \quad (6)$$

The maximum operating limits of the DGs are defined in Eq. 7.

$$P_i \leq P_i^{max} \quad (7)$$

Here, P_i^{max} is the maximum operating limit of the DGs. In the study, P_i^{max} is chosen as 5 MW.

3. Optimization Algorithms

3.1. Artificial bee colony algorithm (ABC)

The ABC algorithm [30] is an optimization method inspired by the foraging behavior of honeybees, developed to solve complex optimization problems. Figure 1 visually illustrates the foraging process of bees. Bees are generally categorized into three main groups: worker bees, onlooker bees, and scout bees. Worker bees are primarily tasked with searching for abundant food sources, functioning as onlooker bees during this process.

After gathering information from high-quality food sources, worker bees perform a waggle dance to guide other bees to the optimal food source. Subsequently, scout bees combine the information received from onlooker bees with the probabilities of nectar sources to select a new food source, then initiate a search in a new area, similar to onlooker bees. If the newly found food source offers a better solution, it replaces the current solution. This cycle continues throughout the solution process until the best solution is identified based on fitness value or error rate [31].

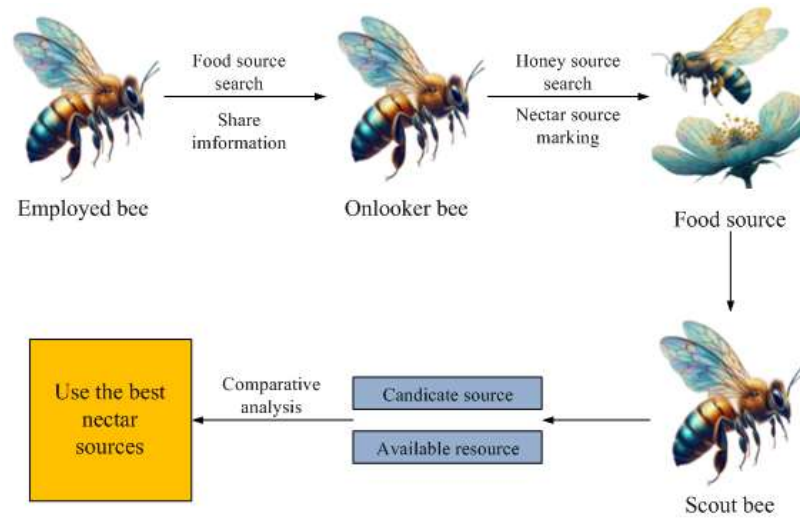


Figure 1. Food foraging and information sharing process of bees

The pseudo-code sequence of the ABC algorithm used for optimal location and sizing of DGs is given below.

ABC_ALGORITHM()

1. Load IEEE 33-bus system data
2. Initialize candidate solutions randomly (each solution represents DG location and capacity)
3. Define colony size and number of iterations
- FOR
- iteration = 1 TO Maximum_Iterations DO
- # Employed Bees Phase
- FOR i = 1 TO Number_of_Food_Sources DO
4. Select a random neighbor solution (between i and k)
5. Generate a new DG location and capacity:
 $New_Solution = Current_Solution + \varphi * (Current_Solution - Neighbor_Solution)$
6. Evaluate the fitness of the new solution:
 $f_new = CALCULATE_OBJECTIVE_FUNCTION(New_Solution)$
7. If f_new is better, update the current solution
8. Otherwise, increase the abandonment counter
- ENDFOR
- # Onlooker Bees Phase
9. Compute selection probabilities based on solution fitness
10. Select a solution randomly and generate a new solution
11. Evaluate the new solution's fitness and update if it is better
- # Scout Bees Phase
12. Replace abandoned solutions with new random ones
13. Update the best solution and record iteration progress
- ENDFOR
14. Return the optimal DG locations and capacities

(1) Worker Bees; this process consists of two main stages. The first stage, the initialization phase, accepts each food source as a feasible solution and randomly initializes the parameters of this solution. Each feasible

solution is then evaluated by substituting its parameters into the objective function, and the resulting function values are assessed using the fitness function, defined as Eq. 8:

$$fitness = \begin{cases} 1/(1 + f_i), & f_i \geq 0 \\ 1 + abs(f_i), & f_i < 0 \end{cases} \quad (8)$$

Here, f_i represents the function value for each feasible solution.

The second sub-stage involves a crossover mutation where the j . dimension of each feasible solution is modified using a randomly generated neighbor solution in the j . dimension. This is expressed by Eq. 9:

$$V_{ij} = x_{ij} + \varphi_{ij}(x_{ij} - x_{kj}) \quad (9)$$

Here, V_{ij} represents the valid solution obtained after the crossover mutation. x_{ij} represents the j . dimension solution of the i . valid solution, while x_{kj} represents the j . dimension solution of the k . valid solution, which is the neighbor of the i . solution. φ_{ij} is a random number. After the crossover-mutation stage, the fitness value will be calculated according to Eq. 8. This value will be compared with the initial fitness value in the initial stage, and if the post-mutation value is better, the parameters of the valid solution will be updated with the post-mutation parameters.

(2) Onlooker Bees; onlooker bees evaluate all information returned by worker bees and select a set of solutions from this information. The probability of selecting a solution (p_i) is calculated using Eq. 10:

$$p_i = \frac{fitness_i}{\sum_{i=1}^{SN} fitness_i} \quad (10)$$

Here, $fitness_i$ represents the fitness value of each feasible solution. SN denotes the number of feasible solutions, which equals the number of available food sources. At this stage, a random number between 0 and 1 is compared with the probability of each solution. If the random number is smaller, it is used as a criterion to determine whether the corresponding food source improves the objective function. If the improvement is insignificant or the random number exceeds the probability value, the crossover mutation process is performed as per Eq. 9.

(3) Scout Bees; if a feasible solution does not converge within a specified number of crossover mutations, it is considered invalid, and a new solution is randomly generated for recalculation.

3.1. JAYA algorithm

The JAYA algorithm, proposed by Rao (2016), is a population-based global optimization method [32]. The fundamental principle of the algorithm is that each solution should consistently move towards the optimal solution within a population while simultaneously moving away from inferior solutions. A key advantage of this algorithm is its simplicity, as it relies solely on a single equation without requiring parameter adjustments to find the optimal solution [33]. In conclusion, the JAYA algorithm is considered more intuitive and distinct compared to other metaheuristic algorithms [34]. The position update equation of the JAYA algorithm is expressed in Eq. 11 [35].

$$X'_{k,j} = X_{k,j} + r_1 \times (Best_j - |X_{k,j}|) - r_2 \times (worst_j - |X_{k,j}|) \quad (11)$$

In the equation given above, $k = 1, 2, \dots, N$ is the index of the candidate solution, $j = 1, 2, \dots, D$ is the relevant dimension of the problem, $Best_j$ is the best solution for the population, $worst_j$ is the worst solution in the population. r_1 and r_2 represent a random value generated between [0,1]. The pseudo-code sequence of the JAYA algorithm used for optimal location and sizing of DGs is given below.

JAYA_ALGORITHM()

1. Load IEEE 33-bus system data
2. Initialize population randomly (each solution represents DG location and capacity)
3. Define number of particles and number of iterations
- FOR iteration = 1 TO Maximum_Iterations DO
 4. Identify the best and worst solutions in the population
 - FOR i = 1 TO Population_Size DO
 5. Generate two random factors (r1, r2)
 6. Compute the new solution using:

$$\text{New_Solution} = \text{Current_Solution} + r1 * (\text{Best_Solution} - \text{Current_Solution}) - r2 * (\text{Current_Solution} - \text{Worst_Solution})$$
 7. Evaluate the fitness of the new solution:

$$f_{\text{new}} = \text{CALCULATE_OBJECTIVE_FUNCTION}(\text{New_Solution})$$
 8. If f_{new} is better, update the current solution
 - ENDFOR
 9. Update the best solution and record iteration progress
- ENDFOR
10. Return the optimal DG locations and capacities

4. Simulations and Results

In this study, the analysis of optimal sizing and placement of DG was carried out using the IEEE 33-bus distribution system. The ABC and JAYA algorithms were employed to perform these analyses. The total active power of the IEEE 33-bus power system was taken as 3.72 MW, and the total reactive power was taken as 2.3 MVar [36]. The single-line diagram of the IEEE 33-bus system is shown in Figure 2. All analyses were conducted on a PC with an Intel Core(TM) i7-2620 2.7GHz processor and 8 GB RAM (64-bit) using MATLAB R2017b.

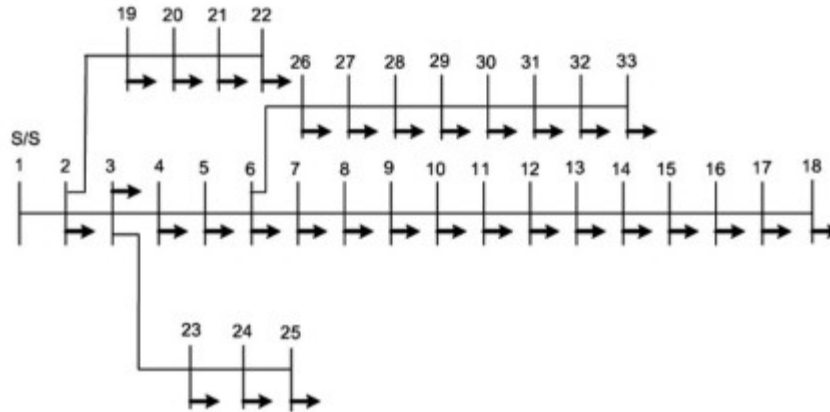


Figure 2. Single-line diagram of the IEEE 33-bus distribution network

The objective functions of the IEEE 33-bus power system were to minimize active power losses and reduce voltage deviations to achieve optimal DG sizing and placement. The ABC and JAYA algorithms were utilized to determine the optimal size and location based on these objective functions. Analyses were conducted for three cases based on the number of DGs:

- Sizing and placement of a single DG (DG1)
- Sizing and placement of two DGs (DG2)
- Sizing and placement of three DGs (DG3)

In the base case without DGs, total active and reactive power losses and bus voltage values were calculated

using the Newton-Raphson power flow method. The values obtained for the base case were then compared in detail with those obtained for DG1, DG2, and DG3 cases using the ABC and JAYA algorithms.

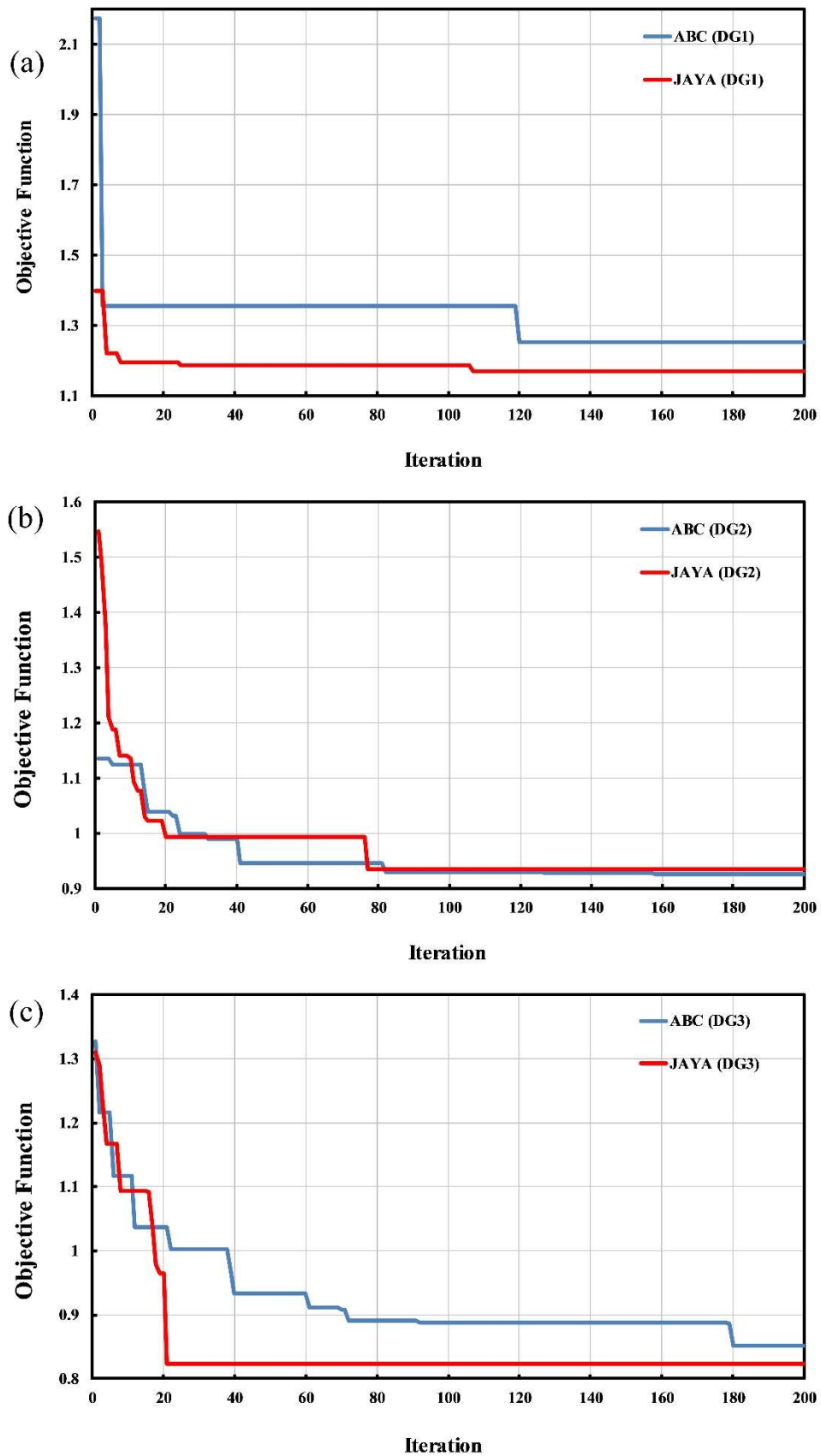


Figure 3. Convergence graphs of the algorithms based on objective functions (a) DG1, (b) DG2, (c) DG3

Figure 3 presents the convergence graphs of ABC and JAYA algorithms for three cases. Both algorithms were run for 200 iterations to determine the optimum size and location of DGs concerning their objective functions. As shown in Figure 3, the JAYA algorithm showed faster convergence than the ABC algorithm in all three cases. JAYA algorithm achieved 4.26%, 16.46%, and 24.32% lower objective function values compared to ABC in DG1, DG2, and DG3 cases, respectively. When more DG units were placed, the objective function decreased to lower values and the system became more efficient.

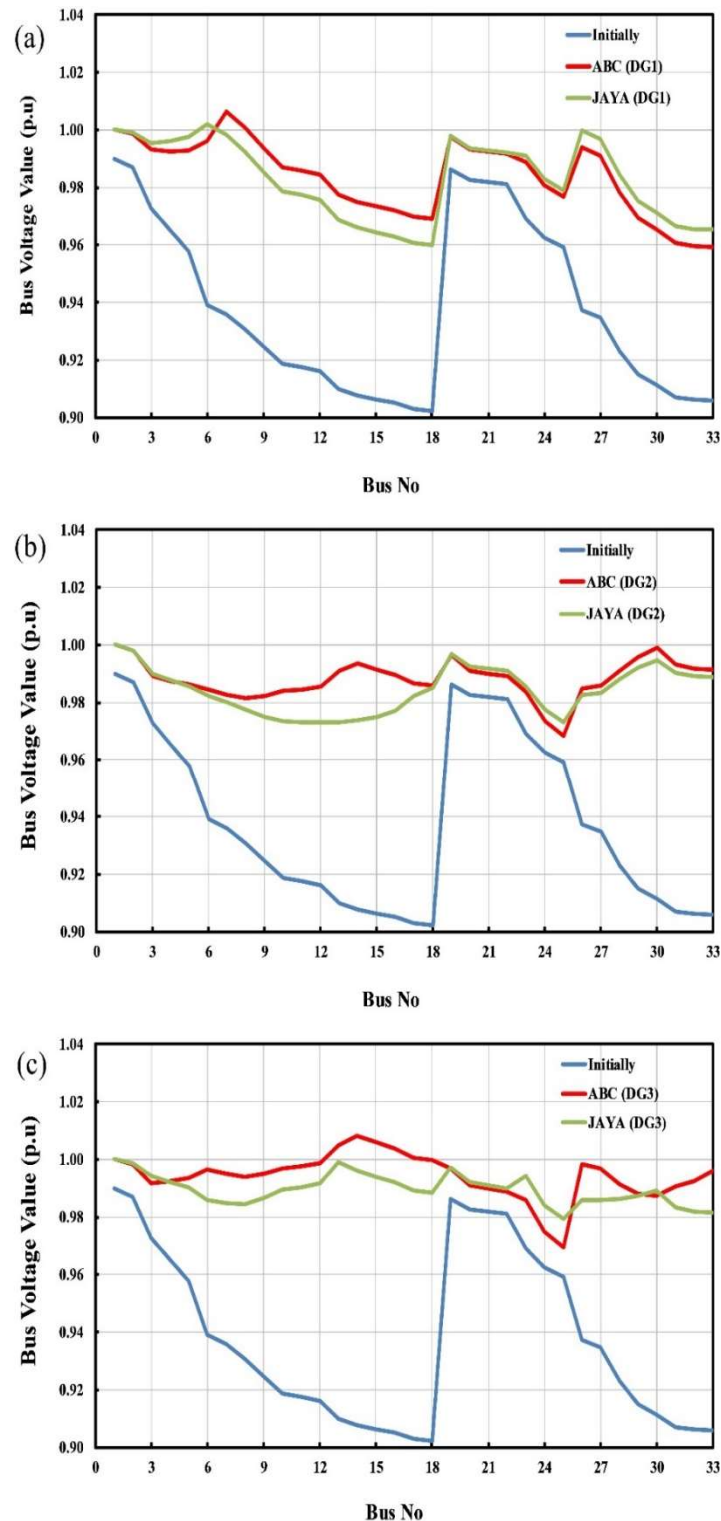


Figure 4. Voltage profiles of the algorithms (a) DG1, (b) DG2, (c) DG3

Figure 4 shows the bus voltage profiles for the base case, DG1, DG2, and DG3 scenarios calculated using the ABC and JAYA algorithms. The results indicate that both algorithms successfully maintained the bus voltage values within the specified limits of 0.95–1.1 p.u. In terms of voltage profile improvement, the ABC algorithm is more successful compared to the JAYA algorithm. However, it has been observed that as the number of DGs in the power system increases, the improvement in bus voltage values also increases.

As seen in Figure 4 and Table 1, the lowest bus voltage in the base case was calculated as 0.902 p.u. (Bus 18). With the ABC algorithm, this value increased to 0.959 p.u. in the DG1 scenario, 0.968 p.u. in the DG2 scenario, and 0.969 p.u. in the DG3 scenario. In the JAYA algorithm, the lowest voltage values were calculated as 0.956 p.u., 0.973 p.u., and 0.979 p.u., respectively. The highest improvement was achieved with the JAYA algorithm in the DG3 scenario, reaching a value of 0.979 p.u.

With the reduction in voltage deviations, a more balanced voltage profile has been established in the system. In particular, the ABC algorithm has been more effective in providing a more homogeneous improvement in low-voltage buses, while the JAYA algorithm has been more effective in raising the minimum voltage level. This situation offers a significant advantage in terms of increasing system stability and improving energy quality.

Table 1. Analysis results for the IEEE 33-bus power system under DG1, DG2, and DG3 scenarios

Analysis	Without DG	DG1		DG2		DG3	
	Initially	ABC	JAYA	ABC	JAYA	ABC	JAYA
Active Power Loss (KW)	0.207	0.094	0.090	0.079	0.066	0.074	0.056
Reactive Power Loss (KVA _r)	0.138	0.076	0.071	0.057	0.047	0.058	0.043
Active Power Reduction (%)		54.33	56.48	61.55	67.92	64.24	73.00
Reactive Power Reduction (%)		45.21	48.36	58.98	66.03	58.30	68.77
DG1 Size (MW) and Location		3.235, 7	3.768, 6	1.367, 14	1.931, 30	1.215, 33	1.557, 23
DG2 Size (MW) and Location				2.271, 30	2.485, 18	1.489, 14	1.542, 13
DG3 Size (MW) and Location						2.097, 26	1.817, 30
Minimum Voltage (p.u.) and Location	0.902, 18	0.959, 33	0.956, 18	0.968, 25	0.973, 12	0.969, 25	0.979, 25
VD (p.u.)	2.047	0.548	0.570	0.392	0.521	0.237	0.344
Time (sn)		664.9	241.6	1261.6	842.6	1942.7	570.7

As shown in Table 1, the inclusion of DGs reduced both active and reactive power losses compared to the base case. The JAYA algorithm achieved greater reductions in active and reactive power losses in all cases compared to the ABC algorithm. For the DG1 case, the JAYA algorithm reduced active and reactive power losses by 56.48% and 48.36%, respectively. For the DG3 case, these reductions were 73.00% and 68.77%, respectively. These results indicate that increasing the number of DGs decreases power losses. Regarding computation time, the JAYA algorithm outperformed the ABC algorithm.

Table 2. Comparison of ABC and JAYA algorithms with other methods

Algorithm	DG1			DG2			DG3		
	Location (Bus No)	DG Size (MW)	Active Power Loss (MW)	Location (Bus No)	DG Size (MW)	Active Power Loss (MW)	Location (Bus No)	DG Size (MW)	Active Power Loss (MW)
ABC	7	3.2350	0.0944	14	1.3670	0.0795	33	1.2150	0.0739
				30	2.2710		14	1.4890	
							26	2.0970	
JAYA	6	3.7680	0.0900	30	1.9310	0.0663	23	1.5570	0.0558
				18	2.4850		13	1.5420	
							30	1.8170	
ABC [37]	6	2.5775	0.1050	6	1.9707	0.0899	6	1.7569	0.0792
				15	0.5757		15	0.5757	
							25	0.7826	
PSO-CFA [38]	6	2.5752	0.1039	14	0.7876	0.0962	10	1.0491	0.0760
				29	1.2487		25	0.8786	
							33	0.8049	
ACO-ABC [39]	6	2.5753	0.1039	13	0.8464	0.0859	14	0.7547	0.0714
				30	1.1588		24	1.0999	
							30	1.0714	
PSO [40]	6	3.1335	0.1102	6	3.1335	0.1057	6	2.1642	0.0828
				16	0.3651		16	0.3651	
							25	0.7386	

Table 2 presents the comparison of the developed ABC and JAYA algorithms on IEEE 33 busbar power systems in the literature in terms of the location, size of the DG, and the total active power losses on the system according to the cases of DG1, DG2, and DG3. It is seen that the developed algorithms give better results in terms of reducing active power losses compared to other algorithms studied in the literature.

5. Conclusion

In this study, the problem of optimal location and sizing of DG systems is analyzed using ABC and JAYA algorithms. The optimization process is focused on the objectives of minimizing active power losses and reducing voltage deviations. Simulations performed on an IEEE 33-bus power system showed that both algorithms effectively optimize the specified objective functions. The results show that the JAYA algorithm exhibits superior performance in reducing active and reactive power losses due to its faster convergence. On the other hand, the ABC algorithm is found to be more effective in terms of improving voltage profiles. Moreover, increasing the number of distributed generation units significantly reduced system losses and improved voltage stability for both algorithms. The results of the study support the applicability of the JAYA algorithm in large-scale distribution systems due to its simple structure and fast computability. On the other hand, the ABC algorithm is found to provide an effective solution in terms of voltage profile improvement. Accordingly, it is considered that a hybrid approach combining both algorithms can achieve superior results. The proposed optimization methods provide important contributions to the effective planning and implementation of DG systems within the scope of engineering and academic research. Future studies can focus on the development of optimization processes for different test systems and the integration of renewable energy sources.

Conflict of Interest Statement

The authors declare that there is no conflict of interest

References

- [1] T. Ackermann, G. Andersson, and L. Söder, "Distributed generation: a definition," *Electric power systems research*, vol. 57, no. 3, pp. 195-204, 2001. doi:10.1016/S0378-7796(01)00101-8
- [2] T. Zhou and B. François, "Energy management and power control of a hybrid active wind generator for distributed power generation and grid integration," *IEEE transactions on industrial electronics*, vol. 58, no. 1, pp. 95-104, 2010. doi: 10.1109/TIE.2010.2046580
- [3] Y. A.-R. I. Mohamed and E. F. El-Saadany, "A control scheme for PWM voltage-source distributed-generation inverters for fast load-voltage regulation and effective mitigation of unbalanced voltage disturbances," *IEEE Transactions on Industrial Electronics*, vol. 55, no. 5, pp. 2072-2084, 2008. doi: 10.1109/TIE.2008.917057
- [4] F. Blaabjerg, R. Teodorescu, M. Liserre, and A. V. Timbus, "Overview of control and grid synchronization for distributed power generation systems," *IEEE Transactions on industrial electronics*, vol. 53, no. 5, pp. 1398-1409, 2006. doi: 10.1109/TIE.2006.881997
- [5] N. Acharya, P. Mahat, and N. Mithulananthan, "An analytical approach for DG allocation in primary distribution network," *International Journal of Electrical Power & Energy Systems*, vol. 28, no. 10, pp. 669-678, 2006. doi: 10.1016/j.ijepes.2006.02.013
- [6] D. Prakash and C. Lakshminarayana, "Multiple DG placements in radial distribution system for multi objectives using Whale Optimization Algorithm," *Alexandria engineering journal*, vol. 57, no. 4, pp. 2797-2806, 2018. doi: 10.1016/j.aej.2017.11.003
- [7] De León-Aldaco, S. E., Calleja, H., & Alquicira, J. A. "Metaheuristic optimization methods applied to power converters: A review," *IEEE Transactions on Power Electronics*, vol. 30, no. 12, pp. 6791-6803, 2015. doi: 10.1109/TPEL.2015.2397311
- [8] O. S. Nduka and B. C. Pal, "Quantitative evaluation of actual loss reduction benefits of a renewable heavy DG distribution network," *IEEE Transactions on Sustainable Energy*, vol. 9, no. 3, pp. 1384-1396, 2017. doi: 10.1109/TSSTE.2017.2776610
- [9] M. P. HA, P. D. Huy, and V. K. Ramachandaramurthy, "A review of the optimal allocation of distributed generation: Objectives, constraints, methods, and algorithms," *Renewable and Sustainable Energy Reviews*, vol. 75, pp. 293-312, 2017. doi: 10.1016/j.rser.2016.10.071
- [10] V. H. Méndez et al., "Impact of distributed generation on distribution investment deferral," *International Journal of Electrical Power & Energy Systems*, vol. 28, no. 4, pp. 244-252, 2006. doi: 10.1016/j.ijepes.2005.11.016
- [11] Ayodele, T. R., Ogunjuyigbe, A. S. O., & Akinola, O. O. "Optimal location, sizing, and appropriate technology selection of distributed generators for minimizing power loss using genetic algorithm," *Journal of Renewable Energy*, vol. 2015 no. 1, 832917, pp. 1-9, 2015. doi:10.1155/2015/832917
- [12] F. S. Abu-Mouti and M. El-Hawary, "Optimal distributed generation allocation and sizing in distribution systems via artificial bee colony algorithm," *IEEE transactions on power delivery*, vol. 26, no. 4, pp. 2090-2101, 2011. doi: 10.1109/TPWRD.2011.2158246
- [13] M. AlRashidi and M. AlHajri, "Optimal planning of multiple distributed generation sources in distribution networks: A new approach," *Energy conversion and management*, vol. 52, no. 11, pp. 3301-3308, 2011. doi: 10.1016/j.enconman.2011.06.001
- [14] A. Arief, M. B. Nappu, S. M. Rachman, and M. Darusman, "Optimal photovoltaic placement at the southern sulawesi power system for stability improvement," in *2017 4th International Conference on Information Technology, Computer, and Electrical Engineering (ICITACEE)*, 18-19 October 2017, Semarang, Indonesia: IEEE, pp. 87-92. doi: 10.1109/ICITACEE.2017.8257681
- [15] M. K. Abd, S. J. Cheng, and H. S. Sun, "Optimal placement and optimal mix of RDGs for improving voltage stability and maximum loadability using PSAT," in *2016 IEEE 11th Conference on Industrial Electronics and Applications (ICIEA)*, 05-07 June 2016, Hefei, China: IEEE, pp. 1574-1578. doi: 10.1109/ICIEA.2016.7603836
- [16] I. Khenissi, R. Sellami, M. A. Fakhfakh, and R. Neji, "Power loss minimization using optimal placement and sizing of photovoltaic distributed generation under daily load consumption profile with PSO and GA algorithms," *Journal of Control, Automation and Electrical Systems*, vol. 32, no. 5, pp. 1317-1331, 2021. doi: 10.1007/s40313-021-00744-7
- [17] M. Haque, "Use of local information to determine the distance to voltage collapse," *International Journal of Emerging Electric Power Systems*, vol. 9, no. 2, 2008. doi: 10.2202/1553-779X.1911

- [18] A. Öner and A. Abur, "Voltage stability based placement of distributed generation against extreme events," *Electric Power Systems Research*, vol. 189, p. 106713, 2020. doi: 10.1016/j.epsr.2020.106713
- [19] R. Prakash and B. Sujatha, "Optimal placement and sizing of DG for power loss minimization and VSI improvement using bat algorithm," in *2016 National Power Systems Conference (NPSC)*, 19-21 December 2016, Bhubaneswar, India: IEEE, pp. 1-6. doi: 10.1109/NPSC.2016.7858964
- [20] B. M'hamdi, M. Tegar, and B. Tahar, "Optimal DG unit placement and sizing in radial distribution network for power loss minimization and voltage stability enhancement," *Periodica polytechnica Electrical engineering and computer science*, vol. 64, no. 2, pp. 157-169, 2020. doi: 10.3311/PPee.15057
- [21] A. S. Hassan, Y. Sun, and Z. Wang, "Multi-objective for optimal placement and sizing DG units in reducing loss of power and enhancing voltage profile using BPSO-SLFA," *Energy Reports*, vol. 6, pp. 1581-1589, 2020. doi: 10.1016/j.egy.2020.06.013
- [22] A. Pal, A. K. Chakraborty, and A. R. Bhowmik, "Optimal placement and sizing of DG considering power and energy loss minimization in distribution system," *International Journal on Electrical Engineering and Informatics*, vol. 12, no. 3, pp. 624-653, 2020. doi: 10.15676/ijeei.2020.12.3.12
- [23] S. Essallah and A. Khedher, "Optimization of distribution system operation by network reconfiguration and DG integration using MPSO algorithm," *Renewable Energy Focus*, vol. 34, pp. 37-46, 2020. doi: 10.1016/j.ref.2020.04.002
- [24] A. P. Sirat, H. Mehdipourpicha, N. Zendejdel, and H. Mozafari, "Sizing and allocation of distributed energy resources for loss reduction using heuristic algorithms," in *2020 IEEE power and energy conference at Illinois (PECI)*, 27-28 February 2020, Champaign, IL, USA, IEEE, pp. 1-6. doi: 10.1109/PECI48348.2020.9064636
- [25] R. Vempalle and P. Dhal, "Loss minimization by reconfiguration along with distributed generator placement at radial distribution system with hybrid optimization techniques," *Technology and Economics of Smart Grids and Sustainable Energy*, vol. 5, no. 1, p. 18, 2020. doi: 10.1007/s40866-020-00088-2
- [26] R. A. Lone, S. Javed Iqbal, and A. S. Anees, "Optimal location and sizing of distributed generation for distribution systems: an improved analytical technique," *International Journal of Green Energy*, vol. 21, no. 3, pp. 682-700, 2024. doi: 10.1080/15435075.2023.2207638
- [27] R. K. Sharma and B. K. Naick, "A Novel Artificial Rabbits Optimization Algorithm for Optimal Location and Sizing of Multiple Distributed Generation in Radial Distribution Systems," *Arabian Journal for Science and Engineering*, vol. 49, no. 5, pp. 6981-7012, 2024. doi: 10.1007/s13369-023-08559-1
- [28] R. K. Chillab, A. S. Jaber, M. B. Smida, and A. Sakly, "Optimal DG location and sizing to minimize losses and improve voltage profile using Garra Rufa optimization," *Sustainability*, vol. 15, no. 2, p. 1156, 2023. doi: 10.3390/su15021156
- [29] E. Karunarathne, J. Pasupuleti, J. Ekanayake, and D. Almeida, "Network loss reduction and voltage improvement by optimal placement and sizing of distributed generators with active and reactive power injection using fine-tuned PSO," *Indonesian Journal of Electrical Engineering and Computer Science*, vol. 21, no. 2, pp. 647-656, 2021. doi: 10.11591/ijeecs.v21.i2.pp647-656
- [30] D. Karaboga and B. Basturk, "A powerful and efficient algorithm for numerical function optimization: artificial bee colony (ABC) algorithm," *Journal of global optimization*, vol. 39, pp. 459-471, 2007. doi: 10.1007/s10898-007-9149-x
- [31] K. Taheri, M. Hasanipanah, S. B. Golzar, and M. Z. A. Majid, "A hybrid artificial bee colony algorithm-artificial neural network for forecasting the blast-produced ground vibration," *Engineering with Computers*, vol. 33, pp. 689-700, 2017. doi: 10.1007/s00366-016-0497-3
- [32] Rao, R. V., & Saroj, A. "A self-adaptive multi-population based Jaya algorithm for engineering optimization," *Swarm and Evolutionary computation*, vol. 37, pp. 1-26, 2017. doi: 10.1016/j.swevo.2017.04.008
- [33] R. Buddala and S. S. Mahapatra, "Improved teaching-learning-based and JAYA optimization algorithms for solving flexible flow shop scheduling problems," *Journal of Industrial Engineering International*, vol. 14, pp. 555-570, 2018. doi: 10.1007/s40092-017-0244-4
- [34] Rao, R. "Jaya: A simple and new optimization algorithm for solving constrained and unconstrained optimization problems," *International Journal of Industrial Engineering Computations*, vol. 7, no. 1, pp. 19-34, 2016. doi: 10.5267/j.ijiec.2015.8.004
- [35] E. Irmak, M. Yeşilbudak, and O. Taşdemir, "Enhanced PV Power Prediction Considering PM10 Parameter by Hybrid JAYA-ANN Model," *Electric Power Components and Systems*, vol. 52, no. 11, pp. 1998-2007, 2024. doi: 10.1080/15325008.2024.2322668
- [36] J. Mendoza, M. Lopez, C. Coello Coello, and E. Lopez, "Microgenetic multiobjective reconfiguration algorithm considering power losses and reliability indices for medium voltage distribution network," *IET Generation, Transmission & Distribution*, vol. 3, no. 9, pp.

825-840, 2009. doi: 10.1049/iet-gtd.2009.0009

[37] M. P. Lalitha, N. S. Reddy, and V. V. Reddy, "Optimal DG placement for maximum loss reduction in radial distribution system using ABC algorithm," *International journal of reviews in computing*, vol. 3, no. 1, pp. 44-52, 2010.

[38] K. D. Mistry and R. Roy, "Enhancement of loading capacity of distribution system through distributed generator placement considering techno-economic benefits with load growth," *International Journal of Electrical Power & Energy Systems*, vol. 54, pp. 505-515, 2014. doi: 10.1016/j.ijepes.2013.07.032

[39] M. Kefayat, A. L. Ara, and S. N. Niaki, "A hybrid of ant colony optimization and artificial bee colony algorithm for probabilistic optimal placement and sizing of distributed energy resources," *Energy Conversion and Management*, vol. 92, pp. 149-161, 2015. doi: 10.1016/j.enconman.2014.12.037

[40] W. Haider, S. J. U. Hassan, A. Mehdi, A. Hussain, G. O. M. Adjayeng, and C.-H. Kim, "Voltage profile enhancement and loss minimization using optimal placement and sizing of distributed generation in reconfigured network," *Machines*, vol. 9, no. 1, p. 20, 2021. doi: 10.3390/machines9010020

This is an open access article under the CC-BY license



The Energy Analysis for Net Zero Energy Building Using Hourly Analysis Program: A Case Study of a Residential Building In Baghdad

Lara Raad Jawad Al-Shammari ^a, Mutlu Tekir ^{*b}

Submitted: 11.10.2024 Revised : 27.12.2024 Accepted: 03.01.2025 doi:10.30855/gmbd.070525N06

ABSTRACT

Keywords: Net zero energy building, insulation, coating, thermal load, hourly analysis program

^a Karabuk University,
Engineering Faculty,
Dept. of Mechanical Engineering
78000 - Karabuk, Türkiye
Orcid: 0000-0002-0352-207X

^{b,*} Karabuk University,
Engineering Faculty,
Dept. of Biomedical Engineering
78000 - Karabuk, Türkiye
Orcid: 0000-0003-2289-7034
e mail: mutlutekir@karabuk.edu.tr

*Corresponding author:
mutlutekir@karabuk.edu.tr

This study addresses the critical challenge of reducing energy consumption in residential buildings, particularly in extreme climates like Baghdad, where thermal loads are substantial during summer and winter. Conventional construction methods often fall short in achieving energy efficiency, necessitating innovative approaches. This work evaluates alternative solutions such as exterior insulation, reflective coatings, and renewable energy systems. The study highlights a novel perspective by integrating advanced simulations using HAP and TRACE 700 to analyze thermal performance and validate findings. Key results demonstrate the pivotal role of insulation in achieving energy efficiency: cooling loads in a living room decreased from 6.8 kW to 3 kW, while heating loads reduced from 3.3 kW to 1.6 kW with insulation. The choice of reflective coatings further influenced thermal loads, though to a lesser degree. Solar energy integration proved vital in balancing the Variable Refrigerant Flow (VRF) system's energy demands, requiring 5.94 kW in summer and 3.66 kW in winter. A variance of 5% between simulation tools confirmed the reliability of the results. This research provides actionable insights into sustainable building practices, emphasizing the transformative potential of insulation and renewable energy in reducing carbon footprints and achieving net-zero energy goals.

Hourly Analysis Program Kullanarak Net Sıfır Enerji Binası İçin Enerji Analizi: Bağdat'ta Bir Konut Binası Üzerine Bir Vaka Çalışması

ÖZ

Bu çalışma, yaz ve kış aylarında termal yüklerin yüksek olduğu Bağdat gibi ekstrem iklimlerde enerji tüketimini azaltma konusundaki kritik zorlukları ele almaktadır. Geleneksel inşaat yöntemleri enerji verimliliğini sağlama konusunda yetersiz kalmakta, bu nedenle yenilikçi yaklaşımlar gerekmektedir. Bu çalışma, dış cephe yalıtımı, yansıtıcı kaplamalar ve yenilenebilir enerji sistemleri gibi alternatif çözümleri değerlendirmektedir. Ayrıca, gelişmiş simülasyon tekniklerini (HAP ve TRACE 700) kullanarak termal performansı analiz eden ve bulguları doğrulayan yeni bir perspektif sunmaktadır. Ana bulgular, enerji verimliliği sağlama konusunda yalıtımın kilit rolünü ortaya koymaktadır: oturma odasında yalıtım ile soğutma yükleri 6,8 kW'tan 3 kW'a, ısıtma yükleri ise 3,3 kW'tan 1,6 kW'a düşmüştür. Yansıtıcı kaplama tercihleri de termal yükleri etkilemiş, ancak daha az ölçüde. Yenilenebilir enerji entegrasyonu, Değişken Soğutucu Akışkan (VRF) sisteminin enerji talebini dengelemede hayati bir rol oynamış ve yazın 5,94 kW, kışın ise 3,66 kW enerji ihtiyacı belirlenmiştir. Simülasyon araçları arasında %5'lik bir fark, sonuçların güvenilirliğini doğrulamıştır. Bu araştırma, sürdürülebilir bina uygulamaları konusunda uygulanabilir bilgiler sunmakta ve yalıtım ile yenilenebilir enerjinin karbon ayak izini azaltma ve net sıfır enerji hedeflerine ulaşma konusundaki dönüştürücü potansiyelini vurgulamaktadır.

Anahtar Kelimeler: Net sıfır enerji binası, yalıtım, kaplama, ısı yükü, hourly analysis program

1. Introduction

In 2021, emissions from heating buildings accounted for 80% of all direct CO₂ emissions in the building industry. However, heating-related CO₂ emissions have only increased by 1.5% since 2010. To achieve net-zero goals, the rate of improvement in energy efficiency must accelerate, with the CO₂ intensity of heated homes needing to decrease by nearly 10% per year until 2030. Heating and cooling systems are critical components of modern construction, designed to maintain indoor comfort in various climates. Understanding the basics of these systems is essential for sustainable construction methods. Heating systems include forced air, boilers, heat pumps, hybrid heating, ductless mini-splits, radiant heating, and baseboard heaters [1].

Air conditioning is vital for cooling and dehumidifying large buildings and homes. Split systems, with separate evaporator and condenser units, as well as variable refrigerant flow (VRF) systems, offer flexibility and convenience. Chilled water systems generate cold water for cooling, while evaporative cooling systems use water evaporation to cool air [2]. Radiant cooling systems cool building surfaces using water, and passive cooling systems harness outdoor air to cool interior spaces. Zero-energy buildings (ZEBs) aim to balance energy consumption with renewable energy generation, using solar panels, wind turbines, and geothermal systems. These buildings rely on advanced insulation, efficient lighting, and smart technologies to optimize energy use. Additionally, passive design strategies, sustainable materials, and landscaping contribute to reducing the environmental impact of NZEBs [3].

1.1. Zero energy buildings

A net-zero energy building (NZEB) is designed to produce as much energy as it consumes annually, minimizing environmental impact and maximizing energy efficiency [4]. Key features of NZEBs include energy-efficient design, integration of renewable energy sources, advanced energy monitoring and management systems, passive design strategies, and energy storage solutions. Achieving net-zero energy requires a holistic approach, encompassing every aspect of building design, construction, and operation [5].

ZEBs play a crucial role in reducing the environmental impact of the built environment and combating climate change. However, many people, even in developed countries, face challenges due to a lack of electricity and adequate housing. To meet their energy needs, ZEBs rely on on-site energy generation through microgeneration technologies such as solar power, wind turbines, biomass, sewage gas, waste heat, and other renewable sources [6].

On the other hand, challenges such as financial constraints, workmanship errors, and insulation not providing the expected efficiency can undermine the intended energy savings of ZEBs in the real field. These issues can lead to financial losses, costly repairs, and operational inefficiencies, preventing buildings from achieving their intended net-zero status [7-8].

The Home Energy Rating System (HERS) is a standardized method used in the United States to assess the energy efficiency of homes and predict future energy use [9]. The U.S. Department of Energy recommends conducting a HERS assessment, which provides recommendations for cost-effective energy improvements and estimates anticipated energy savings [10].

Building environmentally friendly homes requires careful planning and design. Buildings should be well-insulated and airtight to minimize energy consumption. Although the upfront cost of electric heating and cooling systems can be high, they offer a more sustainable alternative in the long run as the energy grid shifts towards renewable sources. Energy analysis is critical for evaluating efficiency, environmental impact, and cost-effectiveness. Buildings should be appropriately sized, monitored, and equipped with advanced control systems and variable speed drives to optimize performance [11]. Heating systems can be further optimized

by reducing energy consumption, evaluating energy sources, and integrating renewable energy technologies. Regular maintenance, programmable thermostats, and heat recovery systems also help reduce energy use and improve overall efficiency. As the global energy system transitions toward renewables, using electricity for heating becomes the only sustainable option [12].

In regions with high heating demands, meeting energy needs through renewable sources becomes more difficult, especially since solar energy is scarce during the heating season. As a result, a significant portion of heating energy in densely populated areas still comes directly or indirectly from fossil fuels. The European Union has estimated that around 2000 TWh of seasonal energy storage would be required to meet winter heating demands if reliance on fossil fuels is reduced [13,14]. Germany alone would need around 40 TWh of seasonal storage [15]. Zero-energy buildings can help address these challenges by reducing the need for additional infrastructure and offering energy solutions that are less reliant on conventional heating systems [16].

Greenhouse gas emissions from electricity and heating are often reported together, making it difficult to isolate the contribution from heating alone. However, estimates suggest that heating and electricity together account for about 45% of emissions, far exceeding emissions from transportation, which contribute around 28% [17]. Approximately half of these emissions come from homes, businesses, schools, and other public and private buildings.

According to research conducted in 2014, around 70% of energy consumption in the residential sector is derived from fossil fuels. Central heating systems, such as forced steam boilers and hot water or air furnaces with radiators, typically rely on fossil fuels like natural gas [18].

1.2. Building envelopes

Overall Thermal Transfer Value (OTTV) is a metric that quantifies the average rate of heat transfer into a building through its envelope, encompassing walls, windows, and roofs. It serves as an index for comparing thermal performance of buildings, with lower OTTV values indicating better energy efficiency. Envelope Thermal Transfer Value (ETTV) is a similar measure, focusing specifically on the heat transfer through the building's envelope, excluding the roof. Both OTTV and ETTV are utilized in building codes and standards to regulate and enhance the energy efficiency of structures. Systematic Evaluation on Energy and Thermal Performance (EETP) is a comprehensive assessment approach that evaluates a building's energy consumption and thermal characteristics. While OTTV and ETTV concentrate on the building envelope's thermal properties, EETP encompasses a broader analysis, including factors like mechanical systems, occupancy patterns, and overall energy usage. This holistic evaluation aids in identifying areas for improvement to achieve optimal energy efficiency and occupant comfort [19-20].

Building envelope design takes local weather patterns into consideration, evaluating thermal effectiveness using indices like Overall Thermal Transfer Value (OTTV), systematic evaluation on energy and thermal performance (EETP), and Envelope Thermal Transfer Value (ETTV) for subtropical and hot summer/cold winter zones. Chua et al. [21] emphasize a bioclimatic approach that focuses on passive design tailored to different climate zones, minimizing heating and cooling energy consumption through four energy-efficient building envelope measures. They found 4% reduction in cooling energy consumption in Singapore according to their analyses.

Daouas et al. [22] evaluates the optimum insulation thickness, energy savings, and payback period for external walls in Tunisia's climate, considering both heating and cooling demands. Using the Complex Finite Fourier Transform (CFFT) method and life-cycle cost analysis, the results highlight that wall orientation significantly impacts energy savings, with the south-facing wall being the most economical, achieving 71.33% energy savings. They also highlight that insulation is more effective in colder regions for heating-dominated

buildings and less effective in warmer climates. However, over-insulation may lead to increased cooling needs and energy consumption. The optimal insulation thickness is typically determined through cost and energy efficiency analyses. Many designers and researchers employ thermal mass strategies to reduce interior temperatures during the day, with recent studies focusing on sensitivity analysis. Integrating nighttime ventilation with thermal mass optimizes energy conservation [23]. Artmann et al. [24] propose a design method for moderate or cold climates of Central, Eastern and Northern Europe that prevents excessive summer heating and reduces the cooling load, thus potentially mitigating the effects of climate change on the indoor environment.

Tian et al. [25] propose balancing daylight and solar apertures in and glazing design, incorporating generalized energy rating systems for sustainable building development. Boixo et al. [26] found that greening rooftops in Andalusia, Spain, could save 295 MWh of power annually, though limited roof space may hinder the deployment of renewable energy systems. Biggest savings are achieved in mild climates with up to 48%, and savings of flat dark roof of old buildings are greater.

1.3. Renewable energy and other technologies

Despite advanced energy reduction strategies, buildings still require energy for daily operations, which in Zero-Emission Buildings (ZEBs) is provided by sustainable energy technologies. These include both on-site and off-site solutions. Cheng et al. [27] describe a hybrid photovoltaic thermal system that improves photovoltaic (PV) efficiency by using a thermoelectric cooling module to lower the temperature of solar cells, thus generating both thermal and electrical energy. Strzalka et al. [28] suggest that integrating photovoltaic systems into the grid can generate on-site electricity, reducing CO₂ emissions and lessening reliance on fossil fuels. This approach enhances the use of renewable energy in urban areas and produce 35% of total electricity consumption. Foley et al. [29] indicate that wind and solar energy can complement each other, enabling the construction of hybrid PV-wind power systems, which provide superior energy performance.

1.4. Building insulation

Buildings account for approximately 40% of total energy consumption in the UK, prompting significant efforts to reduce energy use and greenhouse gas emissions through energy-efficient retrofitting. Recent studies emphasize the importance of enhancing building envelopes with advanced materials like aerogel [30], insulation plaster [31], bamboo fibre reinforced briquettes [32], hollow bricks [33] for optimal thermal performance, demonstrated by substantial reductions in heat loss coefficients and thermal bridging effects in retrofitted structures.

Azkorra et al. [34] point to the benefits of insulation, which reduces energy consumption and improves thermal comfort. Green walls, in particular, are promising for enhancing urban quality of life and reducing noise, though their sound insulation capabilities require further study. In Malaysia, increased electricity usage led researchers to assess the long-term environmental impact of various insulation materials. Shekarchian et al. [35] found that 2.2 cm of fiberglass-urethane insulation provides cost savings and reduces annual CO₂ emissions by 16.4 kg/m², with renewable power plants and the phasing out of thermal coal also contributing. Dombayci [36] highlights the importance of insulation in Denizli, Turkey's third climatic region, where heating is required for five months each year. The study explored the environmental benefits of optimal insulation thickness using coal as fuel and expanded polystyrene as an insulating material, showing that optimal insulation reduced energy usage by 46.6% and CO₂ and SO₂ emissions by 41.53%. Bolattürk [37] examined the optimal insulation thickness for Turkey's coldest cities (Erzurum, Kars, and Erzincan), using a life-cycle cost-benefit analysis. In Erzurum, the optimal insulation thickness can result in savings of up to \$12.11/m² of wall area. Insulation continues to gain popularity due to its significant impact on the environment and high energy costs.

This focus on insulation methods is further supported by studies exploring the application of advanced thermal superinsulation (TSI) materials such as aerogels (ABs) and vacuum insulated panels (VIPs). While ABs provide exceptional thermal performance with minimal thickness, their internal application is limited by space constraints, making external insulation more advantageous for avoiding space reduction and protecting building elements from corrosion. Thermal bridges can be mitigated by combining VIPs with materials like expanded polystyrene (EPS), enabling heat loss reductions of up to 90%. However, the high cost of these materials, such as silica aerogel, poses a challenge, despite projections showing the annual market budget for silica aerogel surpassing \$10 billion by 2027. Future research will focus on eco-friendly solutions and integrating TSI materials with conventional building components to enhance energy efficiency and reduce costs. Insulation continues to gain popularity due to its significant impact on the environment and high energy costs [38-39].

1.5. Energy-efficient building design

The European Union's energy strategy mandates that new buildings achieve "nearly zero" energy consumption by 2020. Achieving these goals requires research into cost-effective technologies that reduce energy usage without compromising daylight availability or thermal comfort. One such technology is vacuum glazing, which offers a high level of thermal insulation while maintaining good optical transmittance. This makes it an ideal solution for reducing heat loss without sacrificing natural daylight, contributing to both energy efficiency and indoor comfort. Vacuum glazing has become a promising solution in building design due to its impressive thermal insulation properties and ability to transmit visible light, making it an ideal choice for reducing energy consumption while maintaining natural daylight. A comprehensive review of vacuum glazing technology by Cuce and Cuce [40] highlights its evolution and future prospects, covering both experimental and theoretical studies. It has been found that vacuum glazing can achieve a reduced overall heat transfer coefficient of up to 0.20 W/m²K when integrated with low-emissivity coatings. This contributes to significant reductions in energy consumption and greenhouse gas emissions. Additionally, vacuum glazing products are assessed in terms of several performance parameters, such as visible light transmittance and solar heat gain coefficient, which further demonstrate their potential as an energy-efficient solution. In terms of retrofit solutions, thin film coatings, known for their control over solar radiation and visible light, show promise when applied to glazed areas. When combined with vacuum glazing, these technologies can optimize window performance, enhancing thermal insulation while maximizing natural light intake [41]. Recent studies have emphasized the importance of accurate U-value assessments for window systems, noting that thermal bridges and edge effects can impact the actual performance of glazing products. Therefore, vacuum glazing combined with advanced thin film technologies represents a valuable approach to enhancing building energy efficiency and reducing environmental impact [42].

While windows provide natural light, they can also contribute to discomfort and heat loss. Ghisi et al. [43] and Suvorova et al. [44] examined the influence of factors such as orientation, window size, and room geometry on energy consumption for lighting, cooling, and heating in offices across various climate zones in USA. Ghisi et al. [43] developed a method for estimating energy savings by integrating daylight into lighting systems, using the Ideal Window Area concept. Their research, conducted in Leeds and Florianopolis, showed potential energy savings of 10.8% to 44.0% for 5000 lux of exterior illumination. Lee et al. [45] investigated the impact of window-to-wall ratios, orientation, U-values, g-values, and optical transmittance on optimizing window designs in offices across five of Asia's most common climate regions Manila, Taipei, Shanghai, Seoul and Sapporo. Loutzenhiser et al. [46] suggest strategies to reduce the window-to-wall ratio while maximizing daylight in buildings. They recommend using low-emissivity glass and gas-filled cavities to reduce heat gain while still maximizing daylight. However, these strategies may not be as effective in cooling-dominated buildings with high interior heat loads. The energy-saving potential of daylighting is particularly notable in cooling-dominated structures. Motuziene et al. [47] focused on window-to-wall ratios, window orientation, and glazing types to evaluate energy usage in office buildings in Lithuania's cool climate. They found that the most energy efficient window-to-wall ratios (WWR) for the south, east and west oriented façade are 20%.

Persson et al. [48] found that in Sweden's passive homes, the size of windows no longer plays a major role in reducing heating energy demand, emphasizing that cooling need in summer is the primary concern in well-insulated homes.

Recent interest has resurfaced in the indoor thermal environment and the potential non-visual benefits of natural daylight in residential buildings, as highlighted by Mardaljevic et al. [49]. Paridari et al. [50] describe "Active Houses," which are designed to optimize natural lighting and provide pleasant views while maintaining low energy usage and a favorable indoor temperature without negatively affecting the environment. As part of the Model Home 2020 project, Alliance et al. [51] designed "Home for Life" in Denmark to maximize livability, using passive solar and ventilation cooling strategies such as natural cross-ventilation and roof windows to maintain a favorable indoor thermal environment. Foldbjerg et al. [52] found that these solar control strategies effectively maintain comfortable indoor conditions while minimizing energy consumption.

This study addresses the gap in understanding the combined effects of insulation, reflective coatings, and renewable energy systems on achieving net-zero energy in extreme climates like Baghdad. Utilizing advanced simulation tools (HAP and TRACE 700), the research provides reliable insights into cost-effective strategies for reducing heating and cooling loads in residential buildings. By integrating passive and active energy measures, the study offers a holistic approach to minimizing energy consumption and environmental impact. While reliant on simulation data, it sets a foundation for future validation and serves as a blueprint for sustainable building practices in similar climates.

2. Problem Description and Governing Equations

This study addresses the energy efficiency and optimization challenges in achieving a net-zero energy building in the specific context of a residential building in Baghdad (Figure 1), where climate conditions result in substantial thermal loads, particularly during summer. The primary focus is on evaluating the impact of exterior insulation and paint layers on the thermal performance of the building. The overall aim is to reduce the building's heating and cooling demands through passive and active energy solutions, including the integration of solar energy systems and optimized building design.

Baghdad's hot summers and relatively cold winters result in high energy consumption for cooling and heating. The problem becomes more critical when considering the urban population growth and the increasing demand for energy in the region. Traditional energy sources lead to high carbon emissions, contributing to environmental degradation and climate change. Thus, transitioning to net-zero energy buildings (NZEB) can help reduce dependency on fossil fuels, lower energy costs, and mitigate environmental impact.

This study uses a combination of passive measures (e.g., improved insulation, energy-efficient coatings) and renewable energy integration to optimize the building's energy profile. Advanced software simulations, including the Hourly Analysis Program (HAP) and TRACE 700, were used to analyze various scenarios, comparing insulation effectiveness, paint reflectivity, and the performance of solar energy systems. The results of this analysis could provide a roadmap for the future design of energy-efficient buildings in similar climates.



Figure 1. Building in Baghdad (case study) [53]

2.1. The Hourly Analysis Program (HAP)

The Iraqi refrigeration blog is an online platform for professionals and stakeholders in the refrigeration, cooling, and Heating, Ventilation, and Air Conditioning (HVAC) systems industry in Iraq. It provides a comprehensive resource on refrigeration technology, energy efficiency, sustainability, regulations, and best practices. The blog aims to foster a deeper understanding of the intricacies involved in designing, installing, operating, and maintaining refrigeration and cooling systems across various sectors. It bridges the gap between theory and practice in the refrigeration industry, facilitating continuous learning and professional development. The blog contributes to improved system design, enhanced energy efficiency, and the advancement of the refrigeration sector in Iraq. The Carrier's Hourly Analysis Program (HAP) is a computer tool that assists engineers in designing HVAC systems for commercial buildings. It estimates design loads, determines airflow rates, sizes cooling and heating coils, air circulation fans, and chillers and boilers (Figure 2).

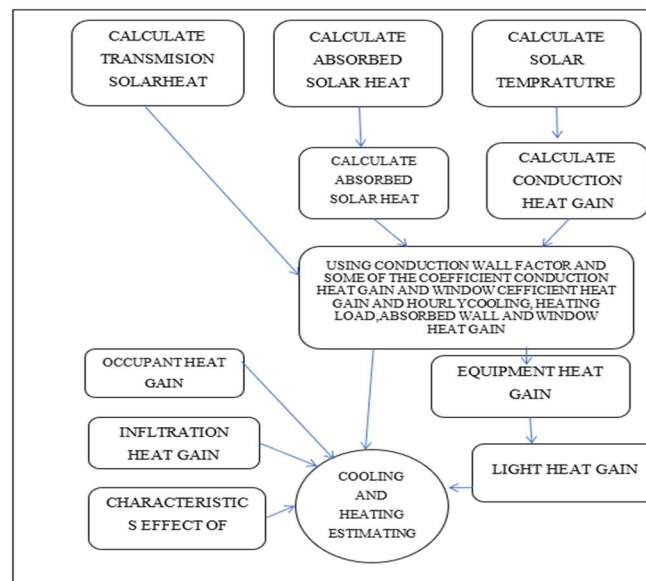


Figure 2. Flow chart HAP software

2.2. Hourly thermal load analysis and transfer function

The purpose of calculating load is to determine peak heating and cooling loads which used to size and select equipment and these calculations dependent on:

- Room conditions
- Occupancy
- Building construction
- Location

Factors Effecting Human Comfort

- Temperature
- Humidity
- Air speed

General Practice Comfort Limits [54]

- Air temperature maintained between (20°C–26°C)
- Summer: (23°C–26°C) 50% RH Max 60% RH
- Winter: (20°C–23°C) Min 35% RH
- (3°C) maximum head-to-foot temperature gradient
- Air Speed in occupied zone: 50 fpm (0.254 m/s) cooling, 30 fpm (0.15 m/s) heating

Heating Load– Heat Loss

Envelope Heat Loss

1. Walls
2. Floor
3. Windows
4. Roof

Heating Load Equation

$$q_{\text{wall}} = q_{\text{window}} = q_{\text{roof}} = \text{Area} \cdot U \cdot \Delta T \quad (1)$$

$$q_{\text{floor}} = \text{Perimeter} \cdot F \cdot \Delta T \quad (2)$$

$$q_{\text{total}} = q_{\text{wall}} + q_{\text{window}} + q_{\text{roof}} + q_{\text{floor}} \quad (3)$$

$$q = \text{Load}$$

Unit : BTU /h (Watts)

U = U -value as calculated based on material properties

Unit: BTU/(h·ft²·°F) {W/(m²·°C)}

Fp = Heat loss coefficient of slab floor construction

Unit: BTU/(h·ft²·°F) {W/(m²·°C)}

ΔT = Temperature difference between indoors and outdoors

Determined using ASHRAE published weather tables [52].

Cooling Heat Gain

Internal Heat Gain

1. People
2. Equipment
3. Lights

Envelope Heat Gain

Conductive

1. Walls
2. Floor
3. Windows
4. Roof

Solar

1. Windows

Cooling Load Equations

$$q_{\text{wall}} = U \cdot A \cdot CLTD_{\text{wall}} \quad (4)$$

$CLTD_{\text{wall}}$ depends on: construction (mass), orientation, latitude, time, Δt

$$q_{\text{roof}} = U \cdot A \cdot CLTD_{\text{roof}} \quad (5)$$

$CLTD_{\text{roof}}$ depends on: construction (mass), time, Δt

$$q_{\text{window_cond}} = U \cdot A \cdot CLTD_{\text{window}} \quad (6)$$

$CLTD_{\text{window_cond}}$ depends on: construction, time, Δt

$$q_{\text{window_solar}} = U \cdot SC \cdot SHGF \quad (7)$$

$SHGF$: Solar heat gain factor

$SHGF$ depends on: orientation, time

$$q_{\text{light}} = 3.412 W \cdot F_{\text{ul}} \cdot F_{\text{sa}} \cdot N \quad (8)$$

W = wattage

F_{ul} = lighting use factor (ratio of wattage in use)

F_{sa} = lighting allowance factor (ballast + lamp)

N = number of light

$$q_{\text{total}} = q_{\text{envelope}} + q_{\text{people}} + q_{\text{equipment}} + q_{\text{light}} \quad (9)$$

(q_{people} , $q_{\text{equipment}}$) depends on number of people and equipment [52].

3. Results and Discussion

3.1. Validation with Trane Traces 700 software

HAP and TRACE 700 are essential tools in building energy analysis and HVAC engineering. They help engineers evaluate the energy efficiency of HVAC systems and their impact on energy usage. Both programs simulate and examine HVAC systems on an hourly basis, allowing for understanding of system functions over time. They also assist in sizing HVAC equipment for comfort and efficiency. HAP and TRACE 700 can calculate heating and cooling loads for a building using variables like environment, building orientation, insulation, and occupancy. They can determine if a building meets local building rules, American Society of Heating, Refrigerating and Air-Conditioning Engineers (ASHRAE) Standard 90.1, LEED, and other energy codes and standards. Engineers can create energy models of buildings using HAP and TRACE 700, which can be used to compare different design options and energy-saving strategies. Both programs offer customizable options, allowing users to specify HVAC system configurations and operational schedules suited to their project needs. They can also determine how energy-saving solutions, such as variable-speed drives, high-efficiency machinery, and control methods, affect a building's energy usage and operating expenses. The choice between HAP and TRACE 700 depends on factors like user preference, project needs, and software familiarity within an engineering organization. Engineers and designers can choose the tool that best suits

their individual requirements and project goals.

In a validation process, HAP was compared with Trane TRACE 700 software, a similar tool used for energy analysis and load calculations (Table 1-2) in building HVAC systems. The validation involved simulating a building with light paint and insulation using both programs, applying the same parameters. The results showed a difference of less than 5% between the two software tools, a margin considered acceptable for engineering purposes. This confirms that both HAP and Trane TRACE 700 provide reliable and consistent results for such analyses.

Table 1. Terminal unit sizing data – cooling

Zone name	Cooling coil load (kW)		Sensible coil load (kW)		Zone (L/(s.m ²))	
	(HAP)	(Trace 700)	(HAP)	(Trace 700)	(HAP)	(Trace 700)
Reception	3.1	3.0	2.8	2.7	7.3	7.0
Living room	3.0	2.9	2.8	2.7	13.9	13.3
Kitchen	2.6	2.5	2.4	2.3	9.9	9.5
Bed room	2.1	2.0	2.0	1.9	7.5	7.2
Bed room 1	1.6	1.5	1.5	1.4	8.6	8.3
Bed room 2	2.2	2.1	2.0	1.9	8.0	7.6
Master bed room	3.0	2.9	2.8	2.7	8.3	8.0

Table 2. Terminal unit sizing data - heating, fan, ventilation

Zone Name	Heating coil load (kW)		Fan design airflow (L/s)		OA vent design air flow (L/s)	
	(HAP)	(Trace 700)	(HAP)	(Trace 700)	(HAP)	(Trace 700)
Reception	1.9	1.8	188.0	180.5	23.0	22.1
Living room	1.6	1.5	208.0	199.7	20.0	19.2
Kitchen	1.5	1.4	176.0	169.0	14.0	13.4
Bed room	1.3	1.2	143.0	137.3	11.0	10.6
Bed room 1	1.1	1.1	112.0	107.5	6.0	5.8
Bed room 2	1.3	1.2	151.0	145.0	11.0	10.6
Master bed room	2.0	1.9	212.0	203.5	13.0	12.5

3.2. Cooling load

The Heating, Ventilation, and Air Conditioning (HVAC) program is crucial in designing an HVAC system. It estimates the cooling load, which is the amount of heat energy needed to maintain a comfortable temperature in a building. Accurate calculations help in selecting and sizing HVAC equipment, reducing energy usage and costs. HAP data also aids in designing environmentally responsible HVAC systems, reducing greenhouse gas emissions. Engineers and designers use HAP-generated data to select the right cooling equipment, system type, capacity, and energy sources. HAP also helps in predicting long-term maintenance and operational expenses, ensuring the system remains affordable over its life. The HAP program's cooling load calculations enable architects and engineers to create thermally comfortable, environmentally friendly, and sustainable spaces.

Figure 3. shows the comparison between the insulation states or not in the light paint. Where it is noted that the value of the cooling load is reduced to half in the case of insulation, and this indicates its usefulness in using it to reduce the cooling load. In the living room, the value of the cooling load when isolated was 3 kW, but with the absence of the insulation, it rises to 6.8 kW, and this difference is vast and can be benefited It is to improve cooling loads.

Figure 4. shows the effect of the presence of insulation with no insulation on the cooling load using dark paint. The results prove once again the effectiveness of using insulators in reducing the cooling load. In the same living room, the value of the cooling load in the case of insulation was 3 kW, but with the absence of the cooling load, it rises to 7 kW, which is a big difference.

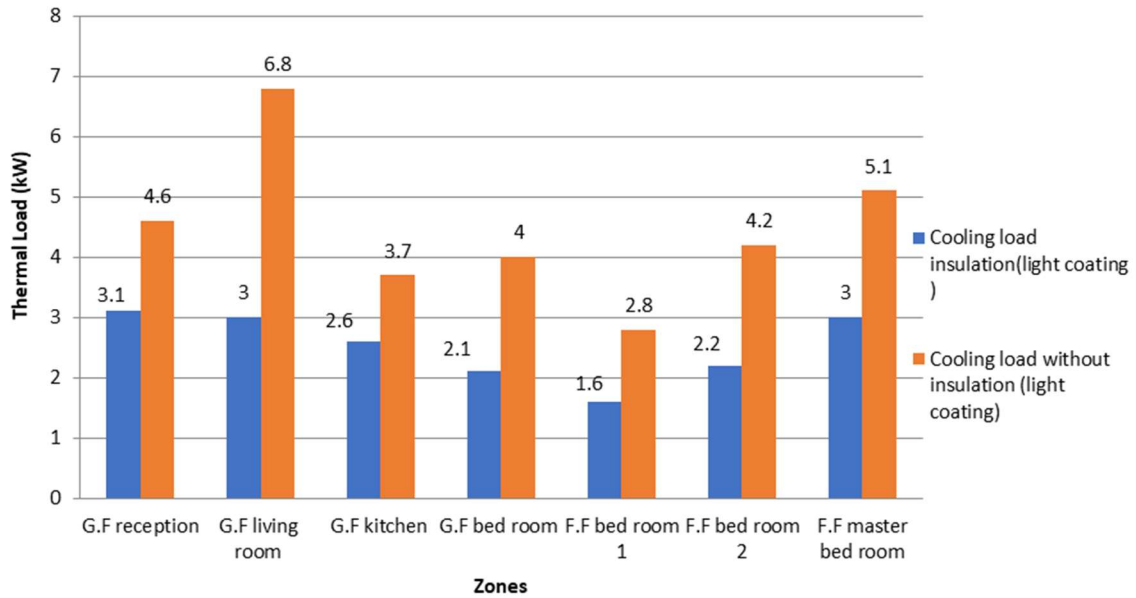


Figure 3. Cooling load insulation vs. cooling load without insulation (light coating)

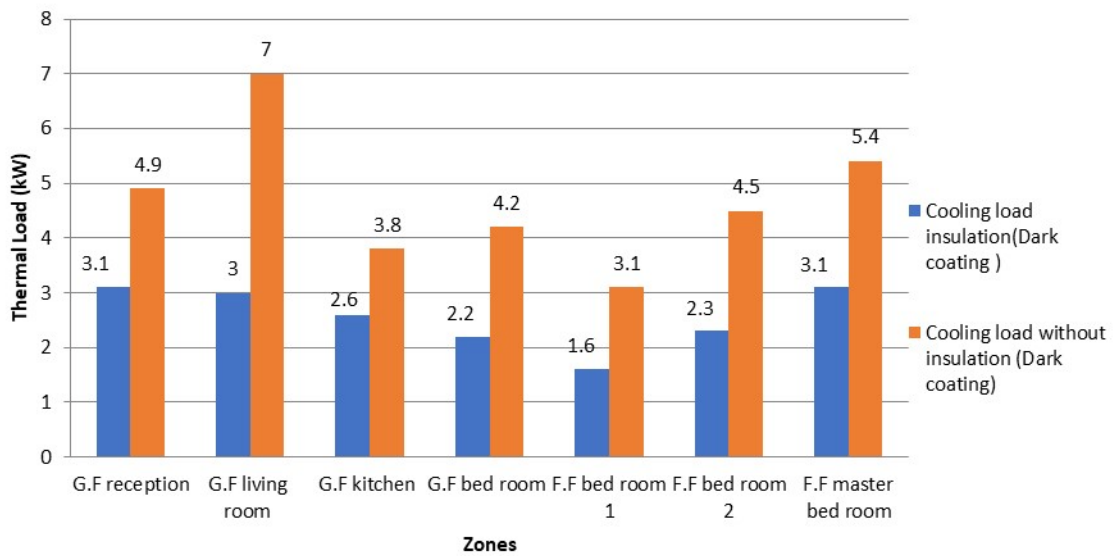


Figure 4. Cooling load with insulation vs. cooling load without insulation (dark coating)

The presence of windows and windows during the used building was many, and therefore the coating areas are few in Figure 1., as the difference between the light and dark coatings decreases, and this is what is noticeable in Figure 5., which shows the difference between the cooling load in the presence of light and dark coatings with an insulating coating, as the difference is non-existent in the living room and its value 3 kW for each floor. The difference increases in the master bedroom, so the value of the cooling load reached 3.1 kW during the dark coating and 3 kW in the light coating.

Figure 6. shows the same concept with regard to the effect of the paint, but in this case, with the absence of an insulator, the effect of changing the paint increased. The difference between the two types of paint in the cooling load reached the largest value in the master bedroom, as it was 5.4 kW in the dark paint and 5.1 kW in the light paint.

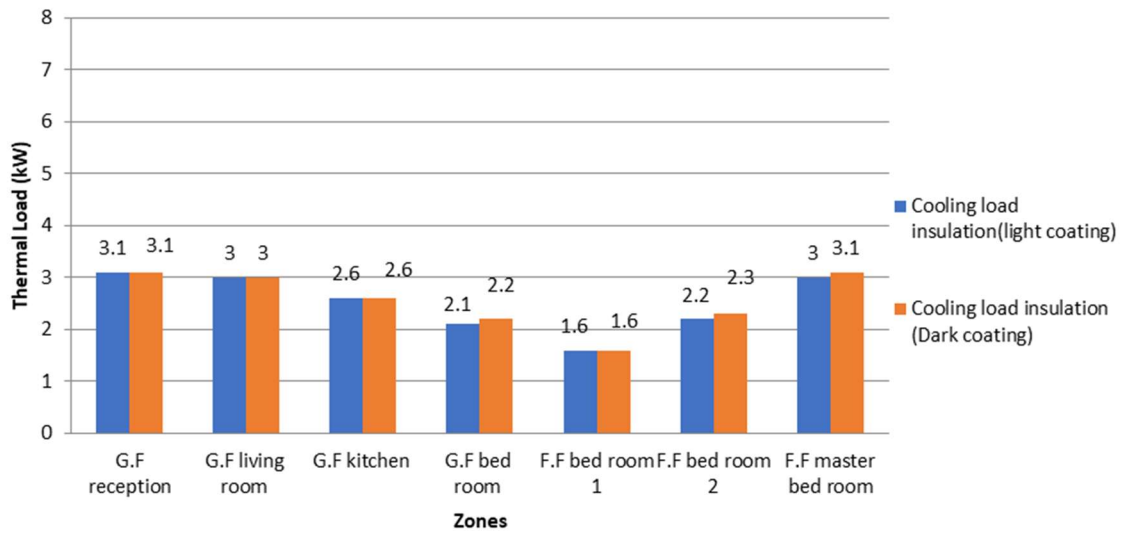


Figure 5. Cooling load insulation (light coating vs. dark coating)

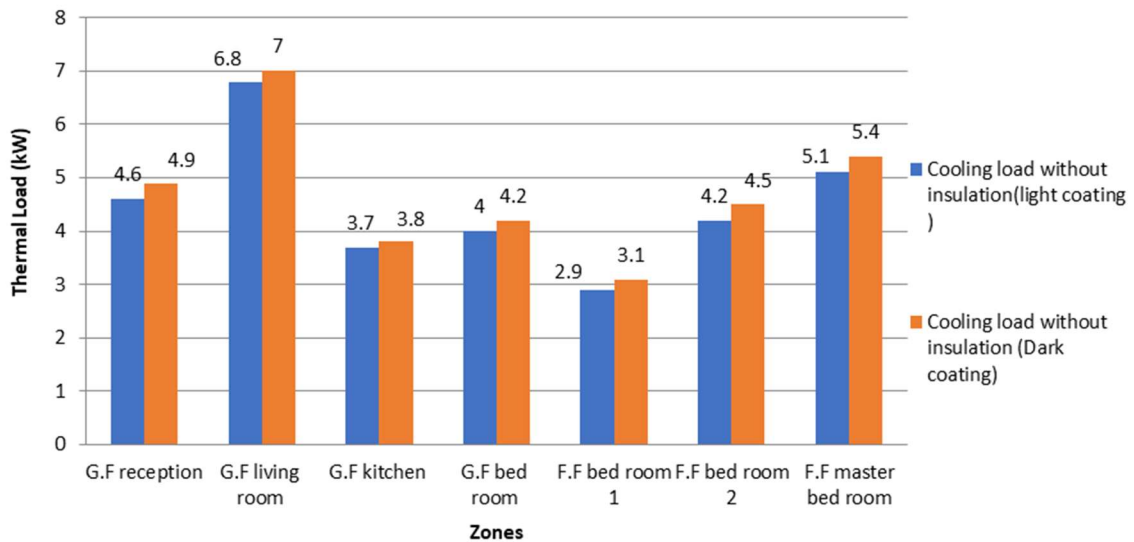


Figure 6. Cooling load without insulation (light coating vs. dark coating)

3.3. Heating load

The heating load of a structure is the thermal energy needed to maintain a building's interior temperature during cold or winter weather. It is crucial in designing and sizing heating systems, as it determines the capacity and effectiveness of heating equipment. The building's insulation, layout, and activities contribute to the heating load. Higher passenger density and heat-generating activities can increase the load. The building's ventilation needs, air leaks, and passive solar heating can also affect the load. The heating load is influenced by occupants' desired indoor temperature, and efficient heating system design aims to satisfy the load while avoiding equipment oversizing.

Figure 7. shows a comparison between cases of insulation or not in light coatings. Where it is noted that the value of the heating load decreases to half in the case of insulation, and this indicates the benefit of using it in reducing the heating load. In the living room, the value of the heating load when isolated was 1.6 kW, but with the absence of the insulation it rises to 3.4 kW, and this difference is vast and can be used to improve heating loads.

Figure 8. shows the effect of the presence of insulation with no insulation on the heating load using dark paint. The results prove once again the effectiveness of using insulators in reducing the heating load. In the same living room, the value of the heating load in the case of insulation was 1.6 kW, but with the absence of the Heating load, it rises to 3.3 kW, which is a big difference.

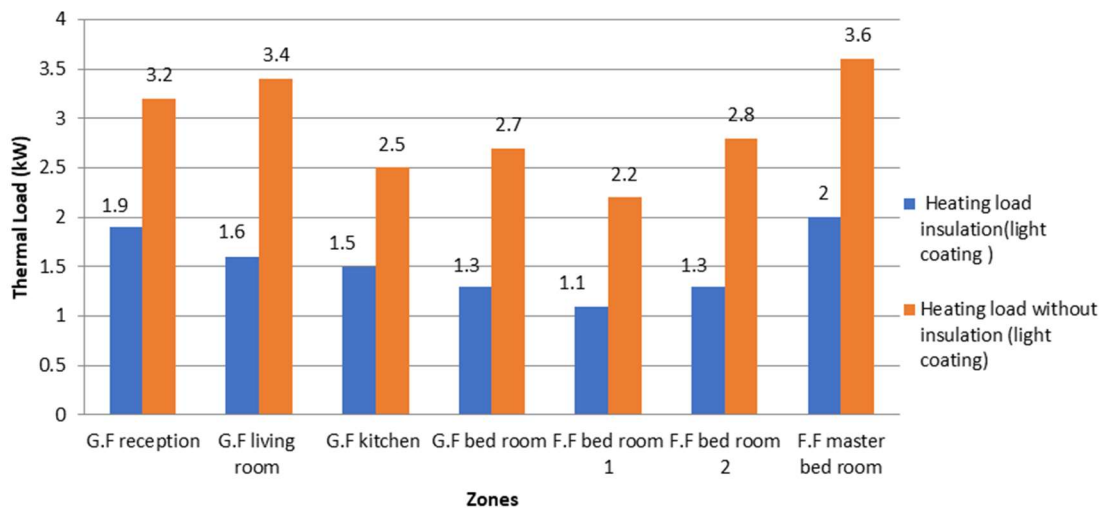


Figure 7. Heating load insulation vs. heating load without insulation (light coating)

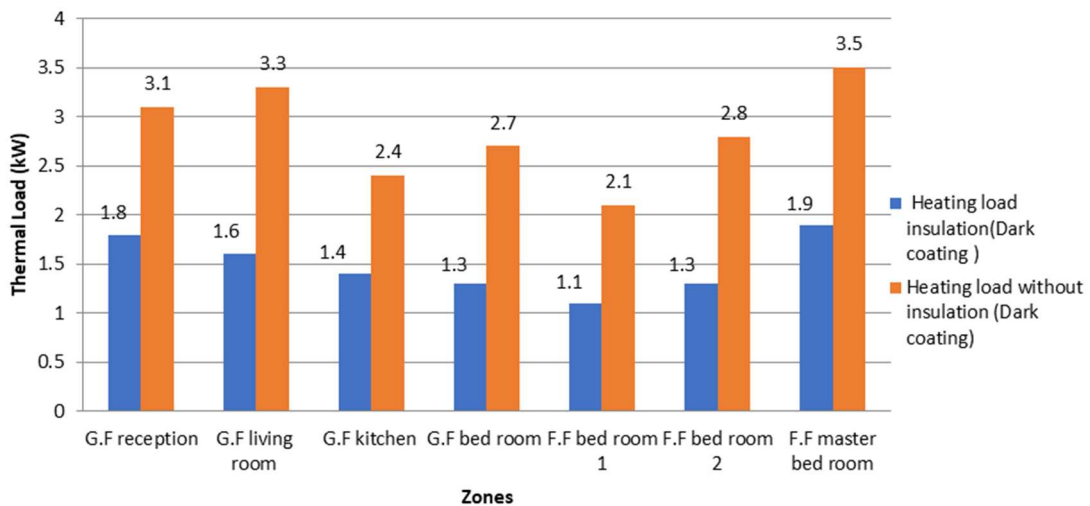


Figure 8. Heating load insulation vs. heating load without insulation (dark coating)

Figure 9. shows an improvement in reducing the heating load for rooms painted with dark insulated paint compared to rooms painted with light insulated paint, due to the presence of more areas painted with dark paint than windows. Where an improvement is noticed in reducing the heating load in relation to the master bedroom 2, where the heating load in the insulated dark coating is 1.9 kW, while the heating load in the light coating is 2 kW.

Figure 10. shows the same concept with regard to the effect of the paint, but in this case, with the absence of an insulator, the effect of changing the paint increased. The difference between the two types of paint in the heating load reached the largest value in the master bedroom, as it was 3.5 kW in the dark paint and 3.6 kW in the dark paint. light paint.

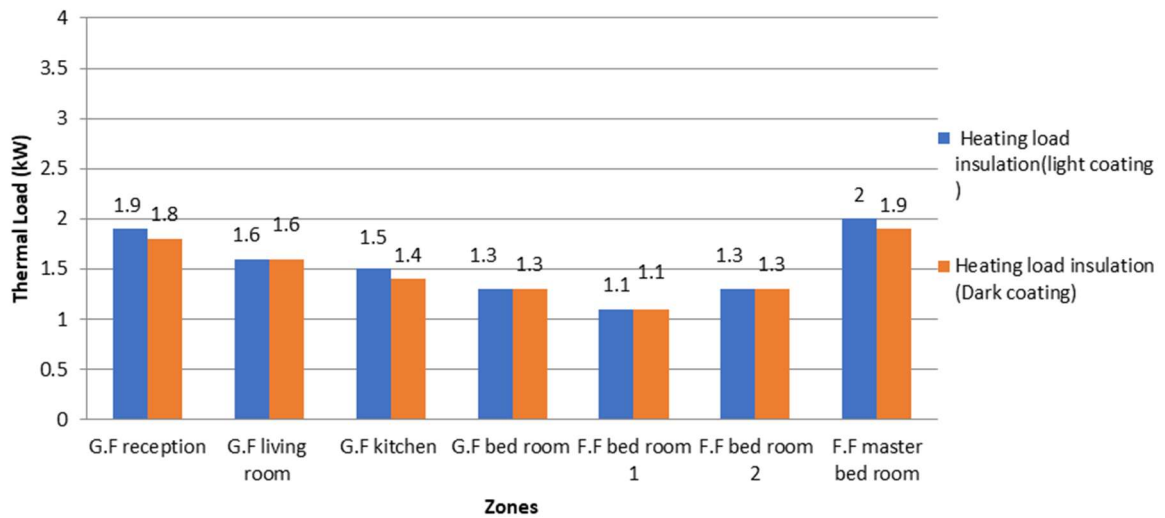


Figure 9. Heating load with insulation (light coating vs. dark coating)

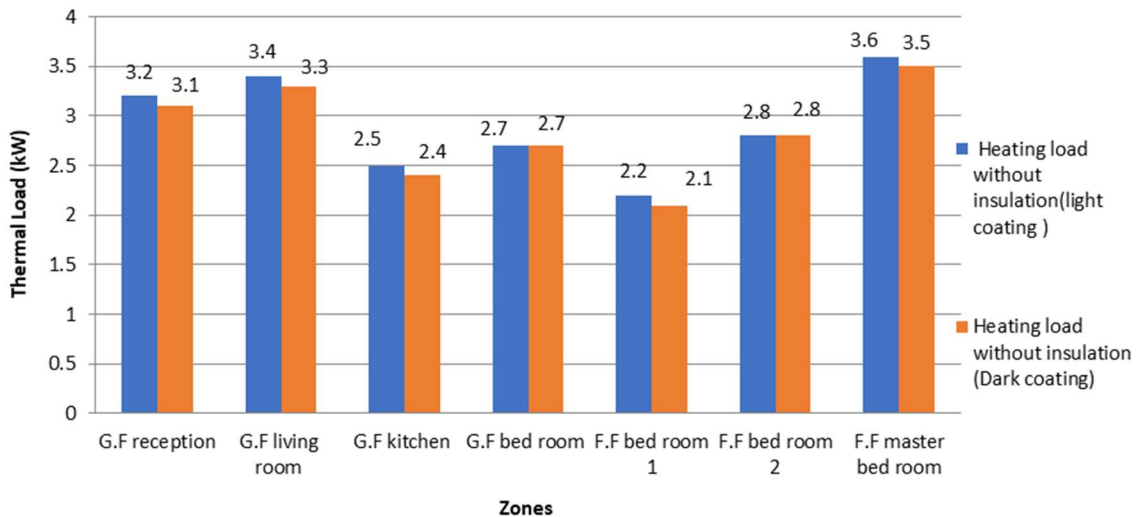


Figure 10. Heating load without insulation (light coating vs. dark coating)

3.4. Total heating and cooling loads for each case

After the process of studying thermal loads during different seasons and knowing the amount of energy required to obtain an integrated system that achieves zero energy, work has been done on a solar panel system that feeds three phases capable of operating cooling and heating systems 24 hours a day. Where the electrical model was designed by the Simulink program, the solar panel system was simulated and the voltage was obtained to feed the systems used as in Figure 11.

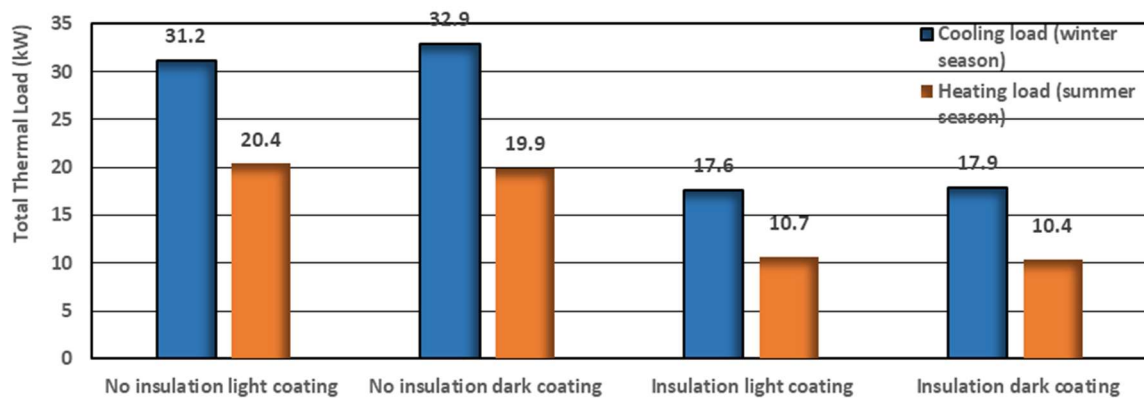


Figure 11. Total heating and cooling load (light coating vs. dark coating)

3.5. Zero energy calculation

The Variable Refrigerant Flow (VRF) system's efficiency depends on factors such as insulation, exterior coating, and local climate. Insulation reduces the amount of electricity needed for heating and cooling, while exterior coatings absorb more solar heat. Local climate, humidity, building size, and design also impact the load. Internal heat gain is influenced by heat-generating activities and the number of people inside the structure. The tenants' indoor temperature also affects energy consumption. Proper maintenance, including cleaning filters and coils, is necessary to keep the VRF system running efficiently. Energy modeling or consulting a qualified HVAC engineer can help assess energy requirements accurately. In conclusion, a VRF system's energy requirements for insulation and light coating depend on various factors, including climate and building design (Table 3).

Figure 12 clears the actual need for electrical capacity for (cooling and heating load) in summer and winter seasons for each case, The figure shows that the electrical power required for the insulated cases is much less than the no insulated cases, while the electrical power for the light and dark coating for the two cases (insulating and no insulating) is equal due to the close cooling and heating capacities for the light and dark coating cases therefore the selection of VRF system be similar for light and dark coating for two cases insulating and no insulating.

Table 3. The amount of electrical energy calculated for the devices in the case of light coating with insulation for cooling load (summer season) and heating load (winter)

Coating Color	Insulation	Season	(kW)	FF bed room 1	FF bed room 2	FF master bed room	GF bed room	GF kitchen	GF living room	GF reception	Power input (W)	
Light	With	Winter	Room load	1,10	1,30	2,00	1,30	1,50	1,60	1,90	3660	
			Heating capacity	1,80	1,80	2,50	1,80	1,80	1,80	2,50		
		Summer	Room load	1,6	2,2	3,0	2,1	2,6	3,0	3,1		5940
			Cooling capacity	1,6	2,2	3,6	2,2	2,8	3,6	3,6		
Light	With out	Winter	Room load	1,10	1,30	1,90	1,30	1,40	1,60	1,80	3660	
			Heating capacity	1,80	1,80	2,50	1,80	1,80	1,80	2,50		
		Summer	Room load	1,60	2,30	3,00	2,20	2,60	3,00	3,10		5940
			Cooling capacity	1,60	2,20	3,60	2,20	2,80	3,60	3,60		
Dark	With	Winter	Room load	2,10	2,80	3,50	2,70	2,40	3,30	3,10	5900	
			Heating capacity	2,50	3,20	4,00	3,20	2,50	4,00	3,20		
		Summer	Room load	3,1	4,5	5,4	4,2	3,8	7,0	4,9		9300
			Cooling capacity	3,6	4,5	5,6	4,5	4,5	7,1	5,6		
Dark	With out	Winter	Room load	2,20	2,80	3,60	2,70	2,50	3,40	3,20	5900	
			Heating capacity	2,50	3,20	4,00	3,20	2,50	4,00	3,20		
		Summer	Room load	2,90	4,20	5,10	4,00	3,70	6,80	4,60		9300
			Cooling capacity	3,60	4,50	5,60	4,50	4,50	7,10	5,60		

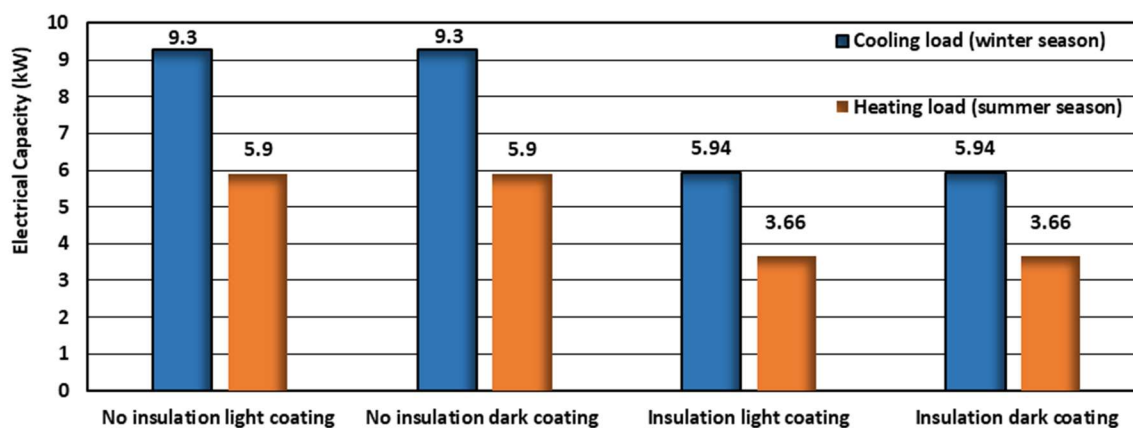


Figure 12. Electrical capacity for (cooling and heating load) in summer and winter seasons

3.6. Supplying cooling and heating systems by solar panels

After the process of studying thermal loads during different seasons and knowing the amount of energy required to obtain an integrated system that achieves zero energy, work has been done on a solar panel system that feeds three phases capable of operating cooling and heating systems 24 hours a day. Where the electrical

model was designed by the Simulink program, the solar panel system was simulated and the voltage was obtained to feed the systems.

In order to obtain an amount of capacity that can be used for processing and storing in batteries, it is necessary to use twice the solar panels for the energy required for the purpose of supplying cooling and heating systems over a 24-hour period. The values of the energy extracted from the solar panels during the summer were approximately 12 kW, but in the winter, they reached 8.3 kW as in Figure 13.

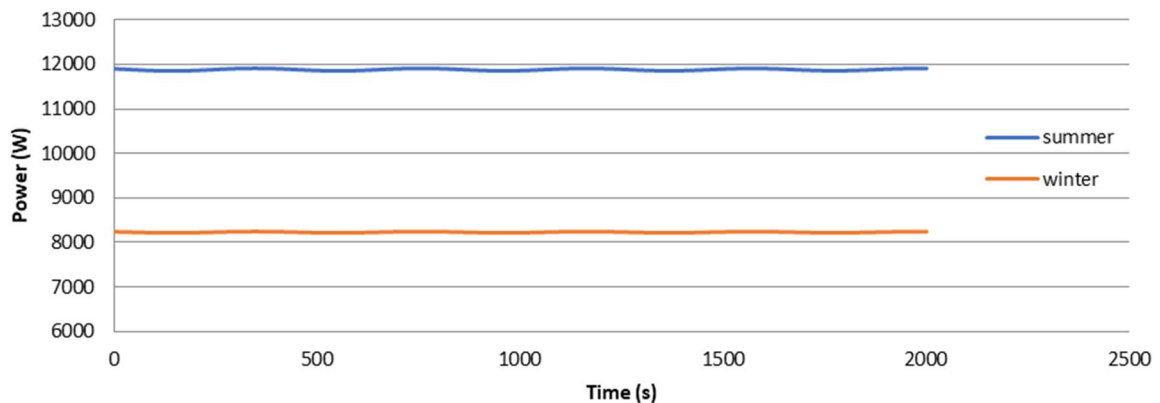


Figure 13. The output power of solar panel system

4. Conclusion

This study evaluates the combined impact of insulation, reflective coatings, and renewable energy integration on achieving net-zero energy goals for residential buildings in extreme climates. The results highlight significant improvements in energy efficiency through these measures.

- Insulation reduced cooling loads by approximately 56% in the living room (from 6.8 kW to 3.0 kW) and heating loads by 53% (from 3.4 kW to 1.6 kW).
- For dark coatings, cooling loads increased slightly compared to light coatings, but the effect was minimal. In the master bedroom, the cooling load increased by 3.3% (from 3.0 kW to 3.1 kW) when insulated and by 5.9% (from 5.1 kW to 5.4 kW) when not insulated.
- Heating loads showed a reduction of 5% in the master bedroom for dark coatings compared to light coatings when insulated (from 2.0 kW to 1.9 kW).
- Solar panels generated sufficient energy to power the VRF system, producing 12 kW in summer and 8.3 kW in winter, exceeding the VRF system's requirements of 5.94 kW (summer) and 3.66 kW (winter), with surplus energy stored for later use.
- Validation results showed a less than 5% variance between HAP and TRACE 700 simulation tools, confirming the reliability of findings.

In line with the growing importance of energy efficiency in extreme climates, other studies conducted in Iraq also emphasize the need for sustainable building practices.

- For example, a study focused on the design of sustainable models for residential buildings in North Iraq addresses the significant impact of local climate, building design, and occupant behavior on energy use. It found that residential buildings in North Iraq account for approximately 69% of the total electricity consumed, emphasizing the importance of energy-saving measures. The study utilized mixed research methods and simulations to develop a sustainable model, showing potential energy savings of up to 50% through improved designs and occupancy behavior adjustments [55].
- Additionally, research aimed at providing energy-efficient housing guidelines for architects in Iraq highlights the potential to achieve up to 50% energy reduction in housing units. This study, based on computer simulations of a reference building in Baghdad, identified cost-effective solutions for improving energy efficiency while considering local materials and budgets. The results indicate that

substantial energy savings can be achieved within a reasonable payback period, with some measures providing immediate benefits [56].

The findings of this study offer valuable insights into practical applications that can be implemented in residential buildings to enhance energy efficiency. Homeowners and builders can significantly reduce energy consumption by these strategies not only contribute to environmental sustainability but also provide actionable pathways toward achieving net-zero energy goals in everyday living spaces.

- Insulation remains a cost-effective solution for retrofitting existing buildings, significantly lowering heating and cooling demands and ensuring occupant comfort.
- Solar energy systems demonstrate practical viability, offering a sustainable alternative to traditional energy sources in regions with high solar potential.
- This research provides actionable insights into sustainable building practices, emphasizing the transformative potential of integrating insulation, reflective coatings, and renewable energy systems to achieve net-zero energy goals.

As the demand for sustainable building practices continues to grow, strategic integration of new technologies will play a crucial role in shaping the future of energy-efficient homes.

- Research into advanced insulation materials, coatings, and renewable systems tailored to different climates can further enhance energy efficiency.
- Integrating hybrid photovoltaic-thermal systems or battery storage can improve energy balance and autonomy for residential buildings.
- Policy recommendations could include the widespread adoption of these techniques in urban planning to achieve sustainable, energy-efficient housing.

Acknowledgment

This article is derived from the thesis with the same title, completed at Karabuk University under the supervision of Assist. Prof. Dr. Mutlu Tekir.

Conflict of Interest Statement

The authors declare that there is no conflict of interest.

References

- [1] N. Zhou, L. Price, D. Yande, J. Creyts, N. Khanna, D. Fridley, H. Lu, W. Feng, X. Liu, and A. Hasanbeigi, "A roadmap for China to peak carbon dioxide emissions and achieve a 20% share of non-fossil fuels in primary energy by 2030," *Applied Energy*, vol. 239, pp. 793–819, April 2019. doi: 10.1016/j.apenergy.2019.01.154
- [2] P. Nejat, F. Jomehzadeh, M. M. Taheri, M. Gohari, and M. Z. A. Majid, "A global review of energy consumption, CO2 emissions and policy in the residential sector (with an overview of the top ten CO2 emitting countries)," *Renewable And Sustainable Energy Reviews*, vol. 43, pp. 843–862, March 2015. doi: 10.1016/j.rser.2014.11.066
- [3] K. Lebling, M. Ge, K. Levin, R. Waite, J. Friedrich, C. Elliott, C. Chan, K. Ross, F. Stolle, and N. Harris, "State of climate action: assessing progress toward 2030 and 2050," *World Resource Institute (WRI)*, ClimateWorks Foundation, Nov. 2020. [Online]. Available: <https://www.wri.org/research/state-climate-action-assessing-progress-toward-2030-and-2050>. [Accessed: Feb. 21, 2024]
- [4] J. Burke, R. Byrnes, and S. Fankhauser, "How to price carbon to reach net-zero emissions in the UK," *Policy Report*, London School Of Economics, London, 2019. [Online]. Available: https://www.lse.ac.uk/GranthamInstitute/wp-content/uploads/2019/05/GRI_POLICY-REPORT_How-to-price-carbon-to-reach-net-zero-emissions-in-the-UK.pdf. [Accessed: Feb. 21, 2024]
- [5] V. Pandiyarajan, M. C. Pandian, E. Malan, R. Velraj, and R. V. Seeniraj, "Experimental investigation on heat recovery from diesel engine exhaust using finned shell and tube heat exchanger and thermal storage system," *Applied Energy*, vol. 88, no. 1, pp. 77–87, Jan. 2011. doi: 10.1016/j.apenergy.2010.07.023

- [6] I. Staffell, D. Brett, N. Brandon, and A. Hawkes, "A review of domestic heat pumps," *Energy & Environmental Science*, vol. 5, no. 11, pp. 9291–9306, Sept. 2012. doi: 10.1039/C2EE22653G
- [7] E. Alvur, M. Anaç, P. M. Cuce, and E. Cuce, "The Potential and Challenges of Bim in Enhancing Energy Efficiency in Existing Buildings: A Comprehensive Review," *Sustainable and Clean Buildings*, vol. 1, no. 1, pp. 42-65, 2024. [Online]. Available: <https://ojs.wiserpub.com/index.php/scb/article/view/4988>. [Accessed: Dec. 23, 2024]
- [8] M. Alzara, A. M. Yosri, A. Alruwaili, E. Cuce, S. M. Eldin, and A. Ehab. "Dynamo script and a BIM-based process for measuring embodied carbon in buildings during the design phase," *International Journal of Low-Carbon Technologies*, vol. 18, pp 943-955, June 2023. doi: 10.1093/ijlct/ctad053
- [9] J. Amann, A. Wilson, and K. Ackerly, *Consumer Guide to Home Energy Savings: Save Money, Save the Earth*, 10th Edition, New Society Publishers, Nov. 2012.
- [10] C. Liaukus, "Energy efficiency measures to incorporate into remodeling projects," *National Renewable Energy Lab.(NREL)*, Golden, CO (United States), Dec. 2014. [Online]. Available: <https://www.nrel.gov/docs/fy15osti/63154.pdf>. [Accessed: Feb. 22, 2024]
- [11] D. A. Jump, I. S. Walker, and M. P. Modera, "Field Measurements of Efficiency and Duct Effectiveness in Residential Forced Air Distributions Systems," *American Council for an Energy-Efficient Economy*, 1996. [Online]. Available: https://www.aceee.org/files/proceedings/1996/data/papers/SS96_Panel1_Paper15.pdf. [Accessed: Feb. 22, 2024]
- [12] M. Deng, P. Li, M. Shan, and X. Yang, "Optimizing supply airflow and its distribution between primary and secondary air in a forced-draft biomass pellet stove," *Environmental Research*, vol. 184, pp. 109301, May 2020. doi: 10.1016/j.envres.2020.109301
- [13] Z. Liao, and A. L. Dexter, "The potential for energy saving in heating systems through improving boiler controls," *Energy And Buildings*, vol. 36, no. 3, pp. 261–271, March 2004. doi: 10.1016/j.enbuild.2003.12.006
- [14] G. Martinopoulos, K. T. Papakostas, and A. M. Papadopoulos, "A comparative review of heating systems in EU countries, based on efficiency and fuel cost," *Renewable And Sustainable Energy Reviews*, vol. 90, pp. 687–699, July 2018. doi: 10.1016/j.rser.2018.03.060
- [15] S. D. Watson, K. J. Lomas, and R. A. Buswell, "Decarbonising domestic heating: What is the peak GB demand?," *Energy Policy*, vol. 126, pp. 533–544, March 2019. doi: 10.1016/j.enpol.2018.11.001
- [16] V. Pais-Magalhães, V. Moutinho, and M. Robaina, "Is an ageing population impacting energy use in the European Union? Drivers, lifestyles, and consumption patterns of elderly households," *Energy Research & Social Science*, vol. 85, pp. 102443, March 2022. doi: 10.1016/j.erss.2021.102443
- [17] H. W. Sinn, "Buffering volatility: A study on the limits of Germany's energy revolution," *European Economic Review*, vol. 99, pp. 130–150, Oct. 2017. doi: 10.1016/j.eurocorev.2017.05.007
- [18] L. Aelenei, D. Aelenei, H. Gonçalves, R. Lollini, E. Musall, A. Scognamiglio, E. Cubi, and M. Noguchi, "Design issues for net zero-energy buildings," *Open House International*, vol. 38, no. 3, pp. 7-14, Sept. 2013. doi: 10.1108/OHI-03-2013-B0002
- [17] D. MacKay, *Sustainable Energy-without the Hot Air*, UIT Cambridge, 2009.
- [18] J. W. Lee, B. Hawkins, D. M. Day, and D. C. Reicosky, "Sustainability: the capacity of smokeless biomass pyrolysis for energy production, global carbon capture and sequestration," *Energy & Environmental Science*, vol. 3, no. 11, pp. 1695–1705, July 2010. doi: 10.1039/C004561F
- [19] H. I. Onovwiona, and V. I. Ugursal, "Residential cogeneration systems: review of the current technology," *Renewable And Sustainable Energy Reviews*, vol. 10, no. 5, pp. 389–431, Oct. 2006. doi: 10.1016/j.rser.2004.07.005
- [20] A. J. Perea-Moreno, M. Á. Perea-Moreno, Q. Hernandez-Escobedo, and F. Manzano-Agugliaro, "Towards forest sustainability in Mediterranean countries using biomass as fuel for heating," *Journal Of Cleaner Production*, vol. 156, pp. 624–634, July 2017. doi: 10.1016/j.jclepro.2017.04.091
- [21] K. J. Chua, and S. K. Chou, "Energy performance of residential buildings in Singapore," *Energy*, vol. 35, no. 2, pp. 667–678, Feb. 2010. doi: 10.1016/j.energy.2009.10.039
- [22] N. Daouas, "A study on optimum insulation thickness in walls and energy savings in Tunisian buildings based on analytical calculation of cooling and heating transmission loads," *Applied Energy*, vol. 88, no. 1, pp. 156–164, Jan. 2011. doi: 10.1016/j.apenergy.2010.07.030
- [23] B. Givoni, "Effectiveness of mass and night ventilation in lowering the indoor daytime temperatures. Part I: 1993 experimental periods," *Energy And Buildings*, vol. 28, no. 1, pp. 25–32, Aug. 1998. doi: 10.1016/S0378-7788(97)00056-X

- [24] N. Artmann, H. Manz, and P. Heiselberg, "Climatic potential for passive cooling of buildings by night-time ventilation in Europe," *Applied Energy*, vol. 84, no. 2, pp. 187–201, Feb. 2007. doi: 10.1016/j.apenergy.2006.05.004
- [25] C. Tian, T. Chen, H. Yang, and T. Chung, "A generalized window energy rating system for typical office buildings," *Solar Energy*, vol. 84, no. 7, pp. 1232–1243, July 2010. doi: 10.1016/j.solener.2010.03.030
- [26] S. Boixo, M. Diaz-Vicente, A. Colmenar, and M. A. Castro, "Potential energy savings from cool roofs in Spain and Andalusia," *Energy*, vol. 38, no. 1, pp. 425–438, Feb. 2012. doi: 10.1016/j.energy.2011.11.009
- [27] T. C. Cheng, C. H. Cheng, Z. Z. Huang, and G. C. Liao, "Development of an energy-saving module via combination of solar cells and thermoelectric coolers for green building applications," *Energy*, vol. 36, no. 1, pp. 133–140, Jan. 2011. doi: 10.1016/j.energy.2010.10.061
- [28] A. Strzalka, N. Alam, E. Duminil, V. Coors, and U. Eicker, "Large scale integration of photovoltaics in cities," *Applied Energy*, vol. 93, pp. 413–421, May 2012. doi: 10.1016/j.apenergy.2011.12.033
- [29] A. M. Foley, P. G. Leahy, A. Marvuglia, and E. J. McKeogh, "Current methods and advances in forecasting of wind power generation," *Renewable Energy*, vol. 37, no. 1, pp. 1–8, Jan. 2012. doi: 10.1016/j.renene.2011.05.033
- [30] E. Cuce, P. M. Cuce, C. Wood, M. Gillott, and S. Riffat, "Experimental Investigation of Internal Aerogel Insulation Towards Low/Zero Carbon Buildings: A Comprehensive Thermal Analysis for a UK Building," *Sustainable and Clean Buildings*, vol. 1, no.1., pp. 1-22, Feb. 2024. [Online]. Available: <https://ojs.wiserpub.com/index.php/scb/article/view/4072>. [Accessed: Dec. 23, 2024]
- [31] E. Cuce, P. M. Cuce, E. Alvur, Y. N. Yilmaz, S. Saboor, I. Ustabas, E. Linul, and M. Asif, "Experimental performance assessment of a novel insulation plaster as an energy-efficient retrofit solution for external walls: A key building material towards low/zero carbon buildings," *Case Studies in Thermal Engineering*, vol. 49, pp. 103350, Sept. 2023. doi: 10.1016/j.csite.2023.103350
- [32] P. M. Cuce, E. Alvur, E. Cuce, S. Alshahrani, C. Prakash, H. Tan, and I. Ustabas, "Unlocking energy efficiency: Experimental investigation of bamboo fibre reinforced briquettes as sustainable solution with enhanced thermal resistance," *Case Studies in Thermal Engineering*, vol. 60, pp. 104680, Aug. 2024. doi: 10.1016/j.csite.2024.104680
- [33] P. M. Cuce, E. Cuce, and K. Sudhakar, "A systematic review of thermal insulation performance of hollow bricks as a function of hollow geometry," *International Journal of Ambient Energy*, vol. 43, no. 1, pp. 4406-4415, 2022. doi: 10.1080/01430750.2021.1907619
- [34] Z. Azkorra, G. Pérez, J. Coma, L. F. Cabeza, S. Bures, J. E. Álvaro, A. Erkoreka, and M. Urrestarazu, "Evaluation of green walls as a passive acoustic insulation system for buildings," *Applied Acoustics*, vol. 89, pp. 46–56, March 2015. doi: 10.1016/j.apacoust.2014.09.010
- [35] M. Shekarchian, M. Moghavvemi, B. Rismanchi, T. M. I. Mahlia, and T. Olofsson, "The cost benefit analysis and potential emission reduction evaluation of applying wall insulation for buildings in Malaysia," *Renewable And Sustainable Energy Reviews*, vol. 16, no. 7, pp. 4708–4718, Sept. 2012. doi: 10.1016/j.rser.2012.04.045
- [36] Ö. A. Dombayci, "The environmental impact of optimum insulation thickness for external walls of buildings," *Building And Environment*, vol. 42, no. 11, pp. 3855–3859, Nov. 2007. doi: 10.1016/j.buildenv.2006.10.054
- [37] A. Bolattürk, "Optimum insulation thicknesses for building walls with respect to cooling and heating degree-hours in the warmest zone of Turkey," *Building And Environment*, vol. 43, no. 6, pp. 1055–1064, June 2008. doi: 10.1016/j.buildenv.2007.02.014
- [38] S. Christopher, M. P. Vikram, C. Bakli, A. K. Thakur, Y. Ma, Z. Ma, H. Xu, P. M. Cuce, E. Cuce, and P. Singh, "Renewable energy potential towards attainment of net-zero energy buildings status—a critical review," *Journal of Cleaner Production*, vol. 405, pp. 136942, June 2023. doi: 10.1016/j.jclepro.2023.136942
- [39] P. M. Cüce, E. Cüce, and E. Alvur, "Internal or external thermal superinsulation towards low/zero carbon buildings: A critical report," *Gazi Mühendislik Bilimleri Dergisi*, vol. 9, no. 3, pp. 435-442, Dec. 2023. doi: 10.30855/gmbd.07050777
- [40] E. Cuce and P. M. Cuce, "Vacuum glazing for highly insulating windows: Recent developments and future prospects," *Renewable and Sustainable Energy Reviews*, vol. 54, pp. 1345-1357, Feb. 2016. doi: 10.1016/j.rser.2015.10.134
- [41] E. Cuce, P. M. Cuce, and S. Riffat, "Thin film coated windows towards low/zero carbon buildings: Adaptive control of solar, thermal, and optical parameters," *Sustainable Energy Technologies and Assessments*, vol. 46, pp. 101257, Aug. 2021. doi: 10.1016/j.seta.2021.101257
- [42] E. Cuce, "Accurate and reliable U-value assessment of argon-filled double glazed windows: A numerical and experimental investigation," *Energy and Buildings*, vol. 171, pp. 100-106, July 2018. doi: 10.1016/j.enbuild.2018.04.036

- [43] E. Ghisi and J. A. Tinker, "An ideal window area concept for energy efficient integration of daylight and artificial light in buildings," *Building And Environment*, vol. 40, no. 1, pp. 51–61, Jan. 2005. doi: 10.1016/j.buildenv.2004.04.004
- [44] I. Susorova, M. Tabibzadeh, A. Rahman, H. L. Clack, and M. Elnimeiri, "The effect of geometry factors on fenestration energy performance and energy savings in office buildings," *Energy And Buildings*, vol. 57, pp. 6–13, Feb. 2013. doi: 10.1016/j.enbuild.2012.10.035
- [45] J. W. Lee, H. J. Jung, J. Y. Park, J. B. Lee, and Y. Yoon, "Optimization of building window system in Asian regions by analyzing solar heat gain and daylighting elements," *Renewable Energy*, vol. 50, pp. 522–531, Feb. 2013. doi: 10.1016/j.renene.2012.07.029
- [46] P. G. Loutzenhiser, G. M. Maxwell, and H. Manz, "An empirical validation of the daylighting algorithms and associated interactions in building energy simulation programs using various shading devices and windows," *Energy*, vol. 32, no. 10, pp. 1855–1870, Oct. 2007. doi: 10.1016/j.energy.2007.02.005
- [47] V. Motuziene and E. S. Juodis, "Simulation based complex energy assessment of office building fenestration," *Journal Of Civil Engineering And Management*, vol. 16, no. 3, pp. 345–351, Sept. 2010. doi: 10.3846/jcem.2010.39
- [48] M. L. Persson, A. Roos, and M. Wall, "Influence of window size on the energy balance of low energy houses," *Energy And Buildings*, vol. 38, no. 3, pp. 181–188, March 2006. doi: 10.1016/j.enbuild.2005.05.006
- [49] J. Mardaljevic, M. Andersen, N. Roy, and J. Christoffersen, "A framework for predicting the non-visual effects of daylight–Part II: The simulation model," *Lighting Research & Technology*, vol. 46, no. 4, pp. 388–406, Aug. 2014. doi: 10.1177/1477153513491873
- [50] K. Paridari, A. Parisio, H. Sandberg, and K. H. Johansson, "Energy and CO₂ efficient scheduling of smart appliances in active houses equipped with batteries," *IEEE International Conference on Automation Science and Engineering, CASE 2014*, New Taipei, Taiwan, Aug. 18–22, 2014, S.L. Chen, C.C. Lan, J. Li, D. Popa, Eds. New Jersey: IEEE Xplore, 2014, pp. 632–639. doi: 10.1109/CoASE.2014.6899394
- [51] A. H. Alliance, "Active House–The Specifications for Residential Buildings," *activehouse.info*. Brussels: Active House Alliance, Jan. 31, 2013. [Online]. Available: https://www.activehouse.info/wp-content/uploads/2020/01/Guidelines_ActiveHouse_III_2020_Spreads.pdf. [Accessed: Dec. 25, 2024]
- [52] P. Foldbjerg and T. Asmussen, "Using ventilative cooling and solar shading to achieve good thermal environment in a Danish Active House," *rehva.eu*. The REHVA European HVAC Journal, vol. 50, no. 3, pp. 36–42, March 2013. [Online]. Available: <https://www.rehva.eu/rehva-journal/chapter/using-ventilative-cooling-and-solar-shading-to-achieve-good-thermal-environment-in-a-danish-active-house>. [Accessed: Feb. 23, 2024]
- [53] "Baghdad Boulevard Project," [Online]. Available: <https://g.co/kgs/Ct8WJpJ>. [Accessed: Oct. 1, 2024]
- [54] M. S. Kam, "25.5 deg C and human comfort," *emsd.gov.hk*. Report energy and efficiency office, the government of Hong Kong special administrative region, 2004. [Online]. Available: https://www.emsd.gov.hk/filemanager/conferencepaper/en/upload/22/HKIE_Environment_Annual_Seminar_Paper_25.5_deg_C_and_Human_Comfort.pdf. [Accessed: Dec. 23, 2024]
- [55] M. Aldoski, D. Haji, and H. Sevinc, "A Sustainable Residential Building Model in North Iraq by Considering Occupant Behaviour, Sociocultural Needs, and the Impact on Energy Use," *Sustainability*, vol. 16, no. 9, pp. 3651, April 2024. doi: 10.3390/su16093651
- [56] U. Dietrich, S. Rashid, and W. Willkomm, "Guidelines for Low-Cost, Energy-Efficient House in Iraq," *Journal of Civil Engineering and Architecture*, vol. 8, no. 12, pp. 1473–1481, Dec. 2014. doi: 10.17265/1934-7359/2014.12.001

This is an open access article under the CC-BY license



GAZİ

JOURNAL OF ENGINEERING SCIENCES

Comparative Performance Analysis of Transit Search Optimization and Particle Swarm Optimization for Overcurrent Relay Coordination in Radial System

İbrahim Arslanoğlu^a, Fatih Mehmet Nuroğlu^b, İsmail Hakkı Altaş^c

Submitted: 02.12.2024 Revised: 05.03.2025 Accepted: 17.03.2025 doi:10.30855/gmbd.070525N07

ABSTRACT

Keywords: Overcurrent relay coordination, Particle swarm optimization (PSO), Transit Search Optimization (TSO), ETAP

^a Karadeniz Technical University, Faculty of Engineering, Department of Electrical and Electronics Engineering 61080- Trabzon, Türkiye
Orcid: 0000-0002-8213-8278
e mail: ibrahimarslanoglu@ktu.edu.tr

^b Karadeniz Technical University, Faculty of Engineering, Department of Electrical and Electronics Engineering 61080- Trabzon, Türkiye
Orcid: 0000-0003-2530-8901
e mail: fmn@ktu.edu.tr

^c Ostim Technical University, Faculty of Engineering, Department of Electrical and Electronics Engineering 06374- Ankara, Türkiye
Orcid: 0000-0001-9298-4091
e mail: ismailhakkialtas@ostimteknik.edu.tr

^{*}Corresponding author: ibrahimarslanoglu@ktu.edu.tr

Anahtar Kelimeler: Aşırı akım röle koordinasyonu, Parçacık sürüsü optimizasyonu (PSO), Geçiş Arama Optimizasyonu (TSO), ETAP

Protection systems are crucial for ensuring the continuity and reliability of power systems. Simulating the power system before its implementation helps improve protection strategies. This study examines the coordination of non-directional overcurrent relays in a three-bus power system modeled in the ETAP software. A three-phase short-circuit fault was applied, and load flow analysis, short-circuit analysis, and relay coordination graphs were generated. To minimize relay operating times, the widely used Particle Swarm Optimization (PSO) algorithm and the Transit Search Optimization (TSO) algorithm, which was applied to relay coordination for the first time, were utilized. The results indicate that TSO significantly reduced the total relay operating time compared to both PSO and the calculated values. The total operating time, initially 1.428 ms, was reduced by 19.82% to 1.145 ms using PSO, and further reduced by 46.43% to 0.765 ms using TSO. Additionally, a direct comparison of PSO and TSO revealed that TSO achieved a 33.19% greater reduction in relay operating time than PSO. These findings suggest that TSO may serve as a more effective optimization method for relay coordination compared to PSO.

Radyal Sistemde Aşırı Akım Rölesi Koordinasyonu için Geçiş Arama Optimizasyonu ve Parçacık Sürüsü Optimizasyonunun Karşılaştırmalı Performans Analizi

ÖZ

Koruma sistemleri, güç sistemlerinin sürekliliğini ve güvenilirliğini sağlamak için kritik öneme sahiptir. Güç sisteminin tesisinden önce simüle edilmesi, koruma stratejilerini iyileştirmeye yardımcı olur. Bu çalışmada, ETAP programında oluşturulan üç baralı bir güç sisteminde yönsüz aşırı akım rölelerinin koordinasyonu incelenmiştir. Üç faz kısa devre arızası uygulanarak yük akışı, kısa devre analizi ve röle koordinasyon grafikleri oluşturulmuştur. Rölelerin çalışma sürelerini en aza indirmek için, yaygın olarak kullanılan Parçacık Sürü Optimizasyonu (PSO) algoritması ile röle koordinasyonunda ilk kez uygulanan Transit Arama Optimizasyonu (TSO) algoritması kullanılmıştır. Elde edilen sonuçlara göre, TSO hem PSO'ya hem de hesaplanan değerlere kıyasla rölelerin toplam çalışma süresini önemli ölçüde azaltmıştır. Hesaplanan toplam süre 1.428 ms olup, PSO ile %19.82 oranında azaltılarak 1.145 ms'ye, TSO ile %46.43 oranında azaltılarak 0.765 ms'ye düşürülmüştür. Ayrıca, PSO ve TSO karşılaştırıldığında, TSO PSO'ya göre röle çalışma süresini %33.19 daha fazla azaltmıştır. Bu bulgular, röle koordinasyonunda TSO'nun PSO'ya kıyasla daha etkin bir optimizasyon yöntemi olabileceğini göstermektedir.

1. Introduction

The demand for electrical energy is steadily increasing. Therefore, the reliability of the power system and the continuity of energy supply are crucial at all stages, from generation to consumption. Ensuring reliability and continuity is heavily reliant on designing protection systems that align with operational conditions.

To prevent equipment damage and ensure stable operation during fault conditions, protective systems are essential in distribution networks. Faults often cause significant fluctuations in current levels within short-circuited areas. Devices like fuses and overcurrent relays react to these variations to safeguard the system. In radial distribution networks, non-directional overcurrent relays are widely preferred because they offer a cost-effective, straightforward, and dependable protection solution [1,2].

In power system design, operational safety must be prioritized under all conditions by accounting for worst-case scenarios and selecting appropriate equipment. Faults in the system are inevitable, leading to high fault currents that, if not promptly detected and cleared, can cause equipment damage and system instability. Protection systems are integral to ensuring reliable operation, minimizing outage durations, and maximizing power delivery efficiency within the distribution network [1].

Power systems are engineered to prevent harm to people, equipment, and property. This design is based on criteria such as speed, reliability, selectivity, cost-effectiveness, and ease of operation [3,4]. Protection equipment in power systems includes relays, which perform calculations using current and voltage data from measuring instruments; circuit breakers, which operate according to relay commands in the event of a fault; current and voltage transformers, which supply data to the relays; and auxiliary communication equipment.

The primary goal of protection in power systems is to maintain operation within specified voltage and current limits, isolate faulted sections during malfunctions, and prevent damage to equipment and harm to personnel. Due to the complexity of power systems, it is essential to model and simulate them in a virtual environment. This enables a comprehensive analysis of system behavior and facilitates the implementation of protection strategies for potential fault scenarios. As the number of overcurrent relays increases, coordinating their operation has become a major challenge, further complicated by various system constraints. Optimization techniques have proven effective in managing these challenges, significantly enhancing operational efficiency.

When examining the literature, numerous studies have focused on minimizing the total operating time of relays through overcurrent relay coordination in radial networks. In one study [5], relay coordination was performed using ETAP software, while in [6], the impact of integrating a solar power plant into a 13-bus test system on relay coordination was analyzed and resolved using ETAP. Additionally, in [7], an adaptive modified firefly algorithm (AMFA) was employed for relay coordination using both MATLAB and ETAP software. In [8], the time multiplier setting required for relay coordination was optimized using the Two-Phase Simplex and Particle Swarm Optimization (PSO) algorithms. These studies highlight the effectiveness of ETAP software in power system modeling and relay coordination analysis, demonstrating its capability to simulate fault scenarios and optimize protection settings with high accuracy.

Several studies have examined various optimization techniques to improve overcurrent relay coordination. In [9], a genetic algorithm was applied with a proposed objective function to optimize relay settings for radial and parallel feeders, effectively mitigating miscoordination between primary and backup relays. In [10], the Time Dial Setting (TDS) of overcurrent relays was optimized using the Cuckoo Search Algorithm (CSA) and compared with the Firefly Algorithm (FA), with ETAP simulations confirmed that CSA delivered superior and more reliable relay coordination. In [11], the Bozkurt Optimization Algorithm (BOA) was successfully applied to the IEEE 8-Bus test system, with a comprehensive performance analysis demonstrating its effectiveness. Furthermore, the study in [12] tackled the overcurrent relay coordination problem at the Hasançelebi transformer center using four different algorithms and found that the Whale Optimization Algorithm (WOA) delivered the fastest solutions.

These studies emphasize the effectiveness of metaheuristic optimization algorithms in enhancing the coordination of overcurrent relays. By employing advanced computational techniques, significant

improvements in relay response time and overall protection system reliability can be achieved, thereby increasing the efficiency and robustness of power system protection.

In [13], the Path-Finder Algorithm (PFA) and Neural Network Algorithm (NNA) were applied for the first time to solve the overcurrent relay coordination problem. A performance analysis was conducted using three test cases with objective functions for both directional and non-directional relays. Research in [14] applied PSO to solve the overcurrent relay coordination problem. Similarly, the study in [15] applied PSO and the Crow Search Algorithm (CSA) to coordinate directional and non-directional relays in power system protection. Lastly, in [16], the Fidan Developmental Algorithm (FGA) and League Championship Algorithm (LCA) were employed for overcurrent relay coordination, yielding effective results. These studies highlight the diversity and effectiveness of metaheuristic approaches in addressing relay coordination challenges.

This study focuses on optimizing overcurrent relay coordination in power systems using both traditional and novel metaheuristic algorithms. A three-busbar power system model was simulated in the ETAP software, where load flow, short circuit analyses, and relay coordination graphs were developed. Particle Swarm Optimization (PSO) and the newly introduced Transit Search Optimization (TSO) Algorithm were applied to minimize relay operating times. The results demonstrated that the TSO algorithm outperformed PSO by significantly reducing total relay operating times, highlighting its potential as an effective optimization method for relay coordination.

The rest of this paper is organized as follows; Overcurrent relay coordination formulation for distribution networks, parameters of radial network and information about different optimization algorithms are given in Section II. Section III presents information about the application of the algorithms on sample test systems and a comparative analysis with other algorithms. Conclusions are discussed in Section IV.

2. Material and Method

2.1. Overcurrent protection

This section is prepared in accordance with the following IEEE standards: IEEE Guide for Protective Relay Applications to Distribution Lines (IEEE Std C37.230™-2020), IEEE Guide for Protective Relay Applications to Transmission Lines (IEEE Std C37.113™-2015), and IEEE Recommended Practice for System Grounding of Industrial and Commercial Power Systems (IEEE Std 3003.1-2019).

When a fault occurs in a power system, the fault current exceeds the current flowing under normal operating conditions. To protect the system, overcurrent relays are connected to the equipment. When the nominal current level is exceeded, an opening signal is sent to the breaker to prevent damage. The relationship between the current through the overcurrent relay and its operating current is expressed as the current–time (operating) characteristic. Based on this characteristic, relays can be configured to operate in either definite-time or inverse-time mode. Typically, inverse-time mode is used for phase-to-phase faults, while definite-time mode is preferred for phase-to-ground faults. Figure 1 illustrates the definite-time operating characteristic of an overcurrent relay. In definite-time mode, if the fault current exceeds the relay's set current ($I >$) threshold, the relay will trip after a specific delay ($t >$). However, regardless of the current level, the relay's opening time remains constant until the instantaneous trip ($I >>$) setting is reached. Once the instantaneous trip threshold ($I >>$) is reached, the relay activates immediately.

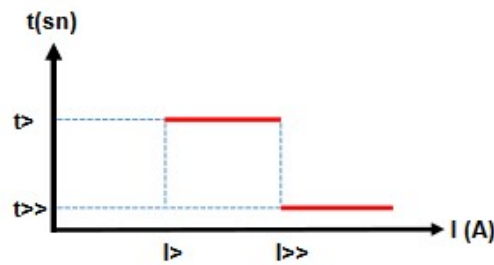


Figure 1. Definite-time operation characteristic

Figure 2 shows the inverse-time operation curve of the overcurrent relay. In inverse-time mode, when the set current threshold is exceeded, the relay's operating time decreases as the current level increases. This allows for quicker isolation of higher fault currents. Current-time curves depend on standard specifications, and Table 1 provides the coefficients for different inverse-time characteristics [3,17].

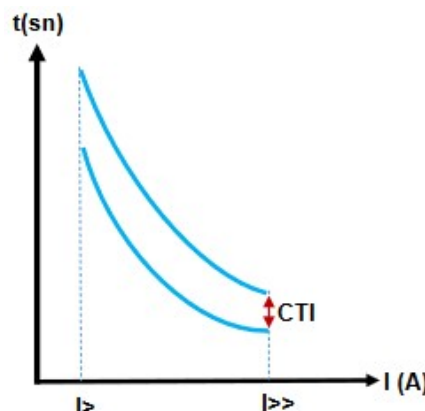


Figure 2. Inverse time operation characteristic

Table 1. Constants of curve types for the ANSI/ IEEE relay

Curve Type	Standard	A	B	P
Moderately Inverse	ANSI/IEEE	0.05	0.114	0.02
Very Inverse	ANSI/IEEE	19.61	0.491	2.00
Extremely Inverse	ANSI/IEEE	28.20	0.122	2.00

2.2. Selectivity and relay coordination

In a radial system, when multiple relays detect the same fault, the relay farthest from the source responds first, while the relay closer to the source operates later. This process is known as selectivity or selective operation. Configuring relays for selective operation is referred to as relay coordination. Figure 3 illustrates a simple radial distribution system, including a grid, transformer, line, three circuit breakers (CB1, CB2, CB3), three current transformers (CT1, CT2, CT3), three overcurrent relays (R1, R2, R3), and a load. When a fault occurs at point F, all three relays detect it. Since relay R3 is closest to the fault, it should ideally send a trip signal to circuit breaker CB3, isolating the fault at the third busbar to maintain power continuity for the rest of the system. If relay R3 fails to send a trip signal, relay R2 should then send a trip signal to breaker CB2. If relay R2 also fails, relay R1 would then operate, sending a trip signal to CB1 to isolate the faulty section from the system. A coordination time interval exists between the operating times of these relays; when calculating CTI, factors such as relay operating time, breaker operating time, and mechanical delays are also considered.

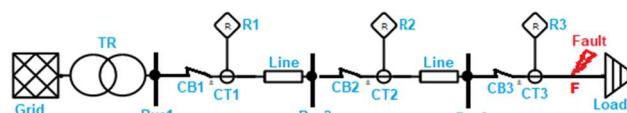


Figure 3. Radial distribution system relay coordination

2.3. Radial grid parameters

Table 2 presents the parameters of the radial grid. For phase-to-phase faults, the grid's overcurrent relays are coordinated using the standard inverse-time curve. As shown in Equation (1), generating this curve requires the pickup current (I_{Pickup}) and time dial setting (TDS) values. By optimizing these two parameters, the total operating time of the relays can be minimized [9,18,19].

Table 2. Grid parameters

Component	Teknik Özellikler
U1	Rated kV = 33 X/R= 15 10 MVA
T1	33/ 6 kV X/R= 10 %Z=8
Line	<u>Cable 1:</u> 10 km, XLPE CU 120 mm ² <u>Cable 2:</u> 5 km, XLPE CU 95 mm ² <u>Cable 3:</u> 3 km, XLPE CU 70 mm ²
Current Transformer	CT1, CT3, CT4: 300/1
Transformer	CT2: 1200/1
Circuit Breaker	CB1: 36 Kv 0.05 sec CB2, CB2, CB3: 7.2 Kv 0.05 sec
Relay	R1, R2, R3, R4: Typical overcurrent relay <u>Lump 1:</u> 2 MVA, 6 kV, (%80 Motor, %20 Static)
Load	<u>Lump 2:</u> 1 MVA, 6 kV, (%80 Motor, %20 Static) <u>Lump 3:</u> 2 MVA, 6 kV, (%80 Motor, %20 Static)

In order to perform the optimization process, the objective function is required. The objective function (OF) used in overcurrent relay coordination is presented in Equation (1).

$$OF = \sum_1^n T_{i,k} \cdot W_{i,k} \quad (1)$$

where n denotes total number of relays in the system, and W_i represents the weight coefficient. The weight coefficient is set to 1 because the probability of failure across different feeders in the network is equal, and the feeder distances are generally similar [3, 20, 21].

$$T_{i,k} = TDS_i \cdot x \frac{A}{\left(\frac{I_F}{I_{Pickup}}\right)^P - 1} + B \quad (2)$$

$T_{i,k}$ for phase fault at point k i it represents the operating time of the relay. This value is calculated by Equation (2). where; TDS_i i time setting of the relay; I_F the magnitude value of the fault current measured from the current relay; I_{Pickup} the set threshold current value of the overcurrent relay; the indices A , B and P refer to the constant coefficients given in Table 1, which vary depending on the overcurrent relay characteristic.

2.4. Constraints

There are some restrictions when performing overcurrent relay coordination. For example, in the inverse time curve given in figure 4, I_F operating time of the primary relay for fault current $T_{(i,k)p}$ and the operating time of the backup relay $T_{(i,k)b}$ can be determined as follows. The coordination constraint between the relays is given in equation (3). In addition, TDS setting constraints, I_{Pickup} setting constraints

and operating time interval constraints are also needed. These constraints are given in Equation (4)-(6) respectively [2,17].

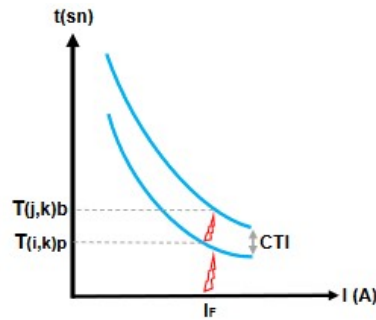


Figure 4. Inverse time curve

$$T_{(i,k)b} - T_{(j,k)p} \geq CTI \quad (3)$$

$$TDS_{(i)\min} \leq TDS_{(i)} \leq TDS_{(i)\max} \quad (4)$$

$$I_{Pickup_{(i)\min}} \leq I_{Pickup_{(i)}} \leq I_{Pickup_{(i)\max}} \quad (5)$$

$$TDS_{(i)\min} \leq TDS_{(i)} \leq TDS_{(i)\max} \quad (6)$$

2.5. Particle Swarm Optimization (PSO)

It is an algorithm developed based on the fact that the movements of certain animals moving in herds to find food influence other individuals. Each individual searching for a solution is called a particle, and the collection of these particles is known as a swarm. The basic outline of Particle Swarm Optimization (PSO) is as follows [22,23]:

Step 1: Initialize the population of particles

Step 2: Evaluate the objective function

Step 3: Update the particle solutions

Step 4: Check the stopping criteria

Step 5: Determine the optimal TDS value and I_{Pickup} based on these values, calculate the objective function

In this study, TDS and I_{Pickup} were determined according to Equation (7)-(9).

$$P_i^{k+1} = P_i^k + v_i^{k+1} \quad (7)$$

where, P_i^k represents the initial position of the particle; $k, k + 1$ represents the iteration number. Then, the velocity value (v) is updated to the position P_i^{k+1} .

$$v_i^{k+1} = w.v_i^k + c_1.rnd_1.(pbest_i - p_i^k) + c_2.rnd_2.(gbest - p_i^k) \quad (8)$$

where, $pbest$ represents the best solution of the i th particle; $gbest$ represents the best position of the swarm; c_1 and c_2 represent the weight coefficients; w represents the weight function; and rnd_1 and rnd_2 represent the random number generators that produce values between 0 and 1.

$$v_{\max} = \frac{u_b}{l_b} \quad (9)$$

where, the speed value V_{\max} is limited by the upper limit u_b and the lower limit l_b . The parameters of the PSO algorithm used in this study are presented in Table 3.

Table 3. PSO algorithm parameters

Number of Population	Number of iterations	C_1	C_2
20	60	2	2

2.5. Transit Search Optimization (TSO)

The Transit Search Optimization (TSO) algorithm is a novel astrophysics-inspired metaheuristic optimization technique. It is based on the "transit method" used in exoplanet discovery, where periodic reductions in a star's brightness indicate the presence of a transiting planet. TSO adapts this principle to solve optimization problems by balancing exploration and exploitation to find the optimal global solution. The TSO implementation is divided into five phases: galaxy, transit, planet, neighbor, and exploitation. Figure 5 represent the details of the TSO. [24,25].

TSO is particularly effective in handling complex and large-scale optimization problems where classical methods struggle. It has a wide range of applications in engineering, artificial intelligence, energy systems, and machine learning.

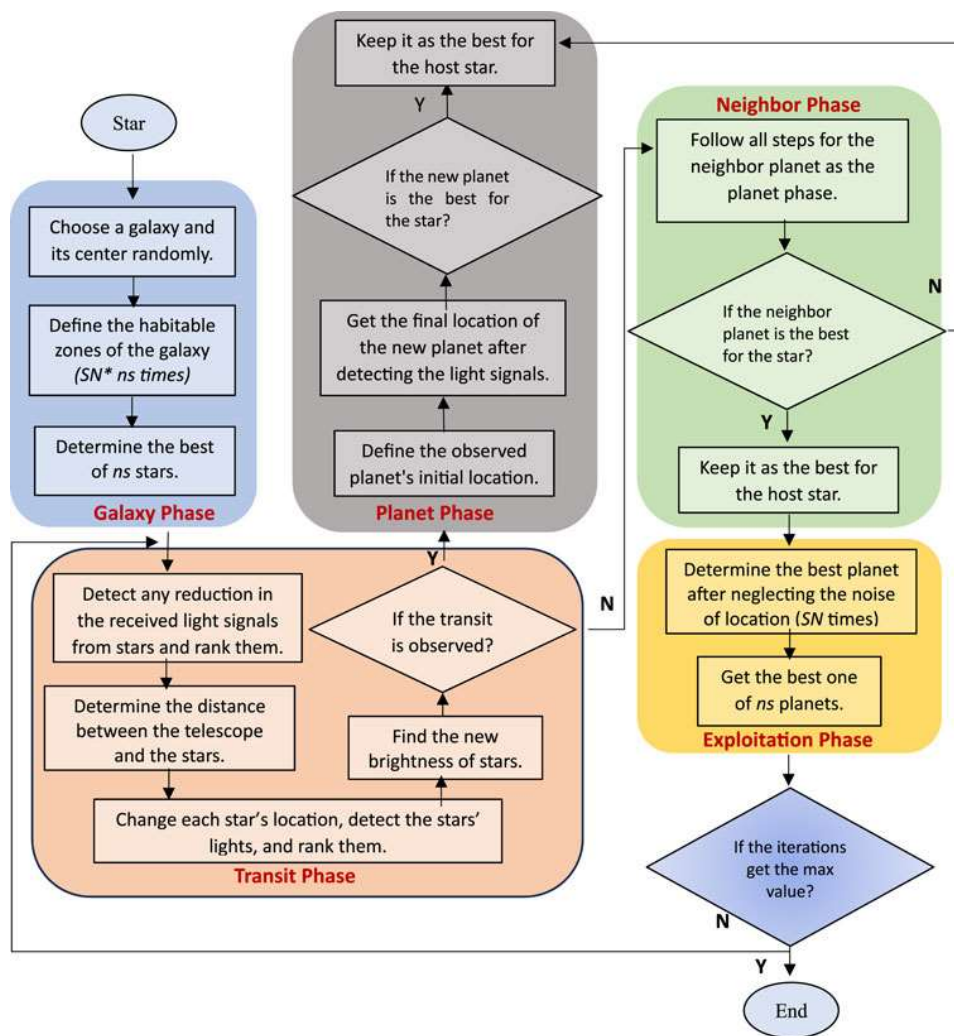


Figure 5. Flowchart of TSO algorithm

2.5.1. Fundamental steps of the TSO algorithm:

a. Galaxy Phase:

The algorithm begins by selecting a random galaxy center in the search space. The habitable zones within the galaxy are identified. Subsequently, the most promising regions with the highest potential are chosen for the next phase. The optimal locations for stellar systems, denoted as L_s (regions highly likely to host life), are illustrated in Figure 6. The locations of these regions are determined using Equations (10)-(12) as follows:

$$L_{R,I} = L_{Galaxy} + D - Noise \quad I = 1, \dots, (n_s \times SN) \tag{10}$$

$$D = \begin{cases} c_1 L_{Galaxy} - L_r & \text{if } z = 1 \text{ (Negative)} \\ c_1 L_{Galaxy} + L_r & \text{if } z = 1 \text{ (Positive)} \end{cases} \tag{11}$$

$$Noise = (c_2)^3 L_r \tag{12}$$

n_s : Number of host stars

SN :Signal-to-noise ratio

$L_{R,I}$: The fitness of the stellar system

L_R : The initial locations for the best regions of the stellar systems

L_{Galaxy} : The random location for the center region of the galaxy

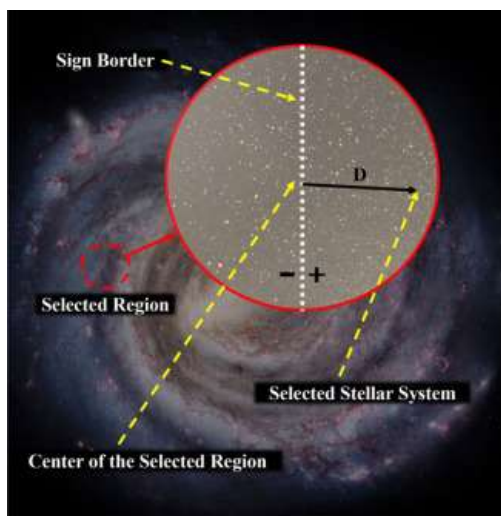


Figure 6. The selection process of the stellar systems by TSO

b. Transit phase:

The luminosity of stars is analyzed to detect potential transits. A decrease in the received light indicates the presence of a planet, allowing its location to be determined. If no transit is detected, the algorithm explores the best neighboring solutions. This phase is represented using Equations (13), (14) as follows:

$$L_i = \frac{R_i / ns}{(d_i)^2} \quad i = 1, \dots, ns \quad R_i \in 1, \dots, ns \tag{13}$$

$$d_i = \sqrt{(L_s - L_t)^2} \tag{14}$$

L_i : The luminosity and R_i , the rank of the star i are represented

d_i : The distance between the telescope and the star i .

L_t : The telescope's position (random)

c. Planet phase:

Planets corresponding to detected transits are identified, and their positions are refined by calculating distances from both the host star and the observer. Figure 7 shows a planet transiting between the star and the telescope. Figure 8 illustrates that, to account for the planet's orbital position in the TSO, three zones are defined and influenced by the application of the zone parameter (z) during the planet phase. This phase is represented using Equations (15)-(18) as shown below:

$$L_z = (C8LT + RL LS) / 2i = 1, \dots, ns \ \& \ C8 \ (random) = 0 \ or \ 1$$

L_z : The initial location of the identified planet

$$L_{m,j} = L_z + C9Lr \text{ if } z(random) = 1 \ j = 1, \dots, SNC9(random) = -1 \ or \ 1 \ \text{Aphelion region} \tag{15}$$

$$L_{m,j} = L_z + c9Lr \text{ if } z(random) = 2 \ j = 1, \dots, SNC9(random) = -1 \ or \ 1 \ \text{Perihelion region} \tag{16}$$

$$L_{m,j} = L_z + c_{10}L_r \text{ if } z(\text{random}) = 3 \text{ } j = 1, \dots, SN \text{ } C_9(\text{random}) = -1 \text{ or } 1 \text{ Neutral region} \tag{17}$$

$$L_p = \frac{\sum_{j=1}^{SN} L_{m,j}}{SN} \tag{18}$$

L_p : The detected planet's final location

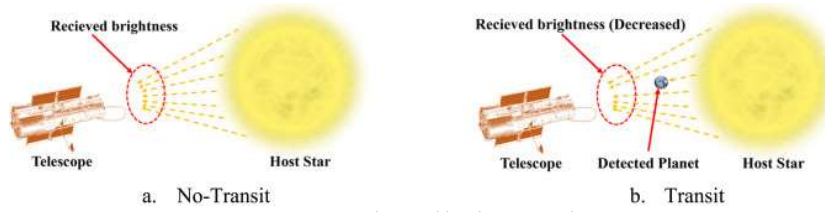


Figure 7. Transit observed by the space telescope

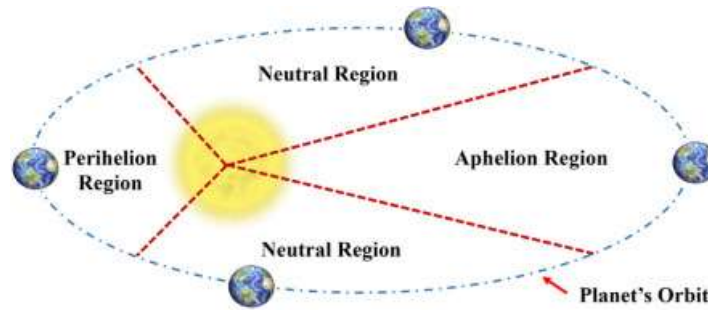


Figure 8. A planet's orbit around a star and the corresponding zones in the algorithm.

d. Neighbore phase:

If no transit is observed, the algorithm examines nearby candidate solutions surrounding the previously detected best solution. If a superior solution is identified, it replaces the previous one.

e. Exploitation phase:

The properties of detected planets (such as density, atmospheric composition, and habitability conditions) are assessed. Additional information is integrated to further refine planetary characteristics. The optimal overall solution is determined, thereby concluding the optimization process. This phase is represented using Equations (19)-(22) as follows:

$$LE, j = C_{16} L_p + C_{15}K, \text{ if } C_k = 1 \text{ (State 1)} \tag{19}$$

$$LE, j = C_{16} L_p + C_{15}K, \text{ if } C_k = 2 \text{ (State 2)} \tag{20}$$

$$LE, j = L_p + C_{15}K, \text{ if } C_k = 3 \text{ (State 3)} \tag{21}$$

$$LE, j = L_p + C_{15}K, \text{ if } C_k = 4 \text{ (State 4)} \tag{22}$$

C15 (a random number) = [0,2]; C16 (a random number) = [0,1]; $K = (C17)^p$ Lr, C17 (a random vector) = [0,1]; P (a random power) = [1, ..., SN]. LE: represents the characteristics of the planet

The phases of the proposed algorithm, along with their definitions and details, have been presented. To more clearly illustrate the implementation process of the TSO, a general pseudocode is provided in Algorithm 1 [24].

Algorithm 1. General pseudocode of the TSO algorithm

```

Inputs:
  Number of host stars  $n_s$ ; Signal-to-noise ratio  $SN$ ; The number of iterations  $n_{it}$ 
Outputs:
  Location of the best planet ever  $L_B$  and its corresponded fitness  $f_B$ 
Initialization:
  The initial location of the galaxy
do Galaxy phase using Algorithm 1
Return the Best Stars,  $L_S$ 
While (Stopping condition is not met) do
  do Transit Phase using Algorithm 2
    for  $i = 1:n_s$ 
      if transit is detected
        do Planet Phase using Algorithm 3
      else
        do Neighbor Phase using Algorithm 4
      end
    end
  Return  $L_{P,i}$  and its corresponded fitness ( $f_{P,i}$ ) for each star
  do Exploitation Phase using Algorithm 5
  Return  $L_P$  and its corresponded fitness ( $f_{P,i}$ ) for each star
end
Return  $L_B$  and its corresponded fitness ( $f_B$ )

```

3. Modeling and Analysis of The Grid

A radial grid model was developed using the ETAP software environment, incorporating the parameters specified in Table 2. The relay coordination curve was generated by performing load flow and short circuit analyses, combined with calculations based on outcomes derived from both the Particle Swarm Optimization (PSO) and Transit Search Optimization (TSO) algorithms.

Figure 9 presents the load flow analysis results, while Figure 10 illustrates the short circuit analysis. Figure 11 depicts the selectivity and relay coordination, and Figure 12 shows the calculated relay coordination curve. Figure 13 highlights the overcurrent relay coordination achieved using the PSO algorithm, whereas Figure 14 highlights the overcurrent relay coordination utilizing the TSO algorithm. Figure 15 presents the optimal objective function value obtained with both PSO and TSO. Additionally, Table 4 summarizes the relay isolation times for the three-phase fault and the total isolation time of the relays.

Table 4. Operating times of relays

	I_{FAULT} (kA)	Calculated Relay Time ms	PSO Relay Time ms	TSO Relay Time ms
R1	0.262	863	665	367
R2	1.405	381	359	236
R3	1.812	120	66	88
R4	2.179	64	55	74
Total Time		1.428	1.145	765

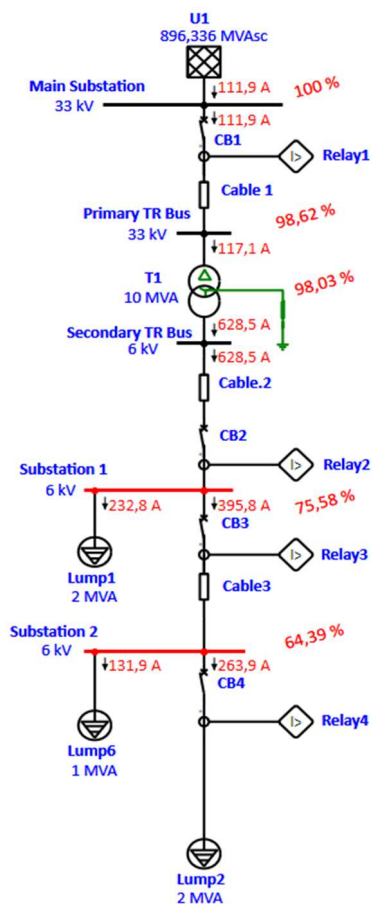


Figure 9. Load flow analysis

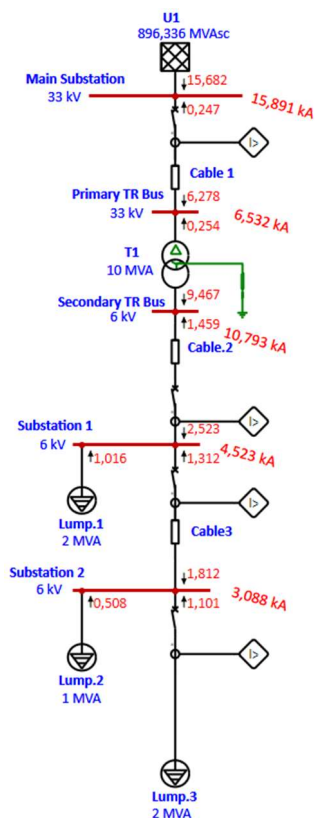


Figure 10. Short circuit analysis

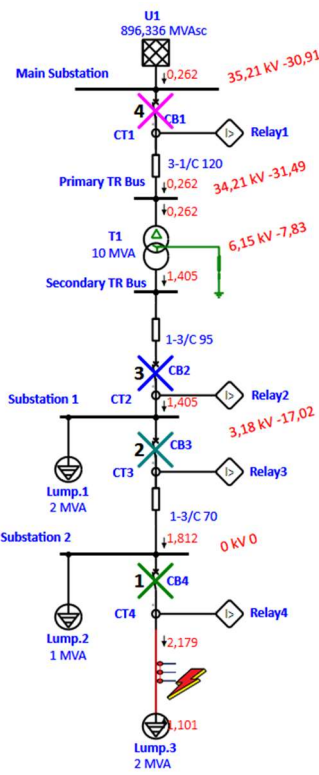


Figure 11. Selectivity and relay coordination

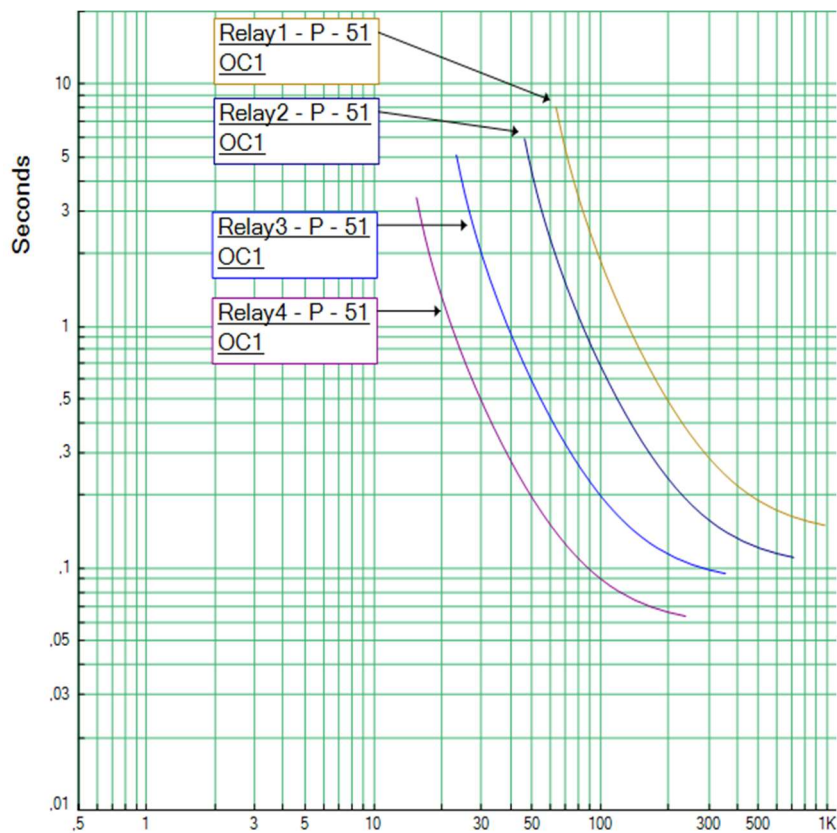


Figure 12. Calculated relay coordination

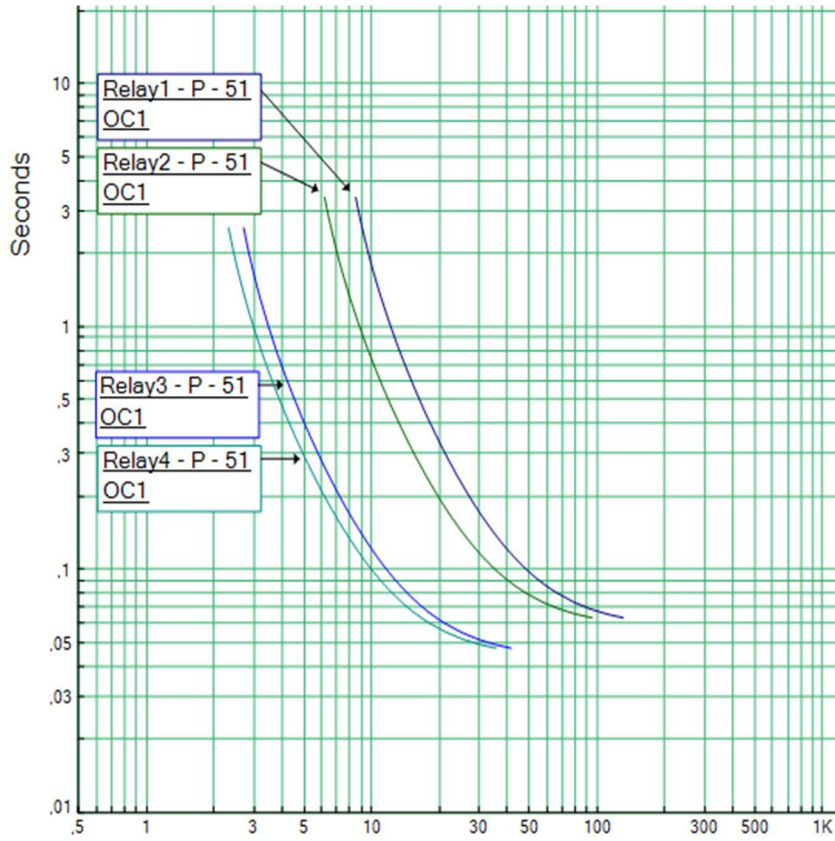


Figure 13. Overcurrent relay coordination using PSO algorithm

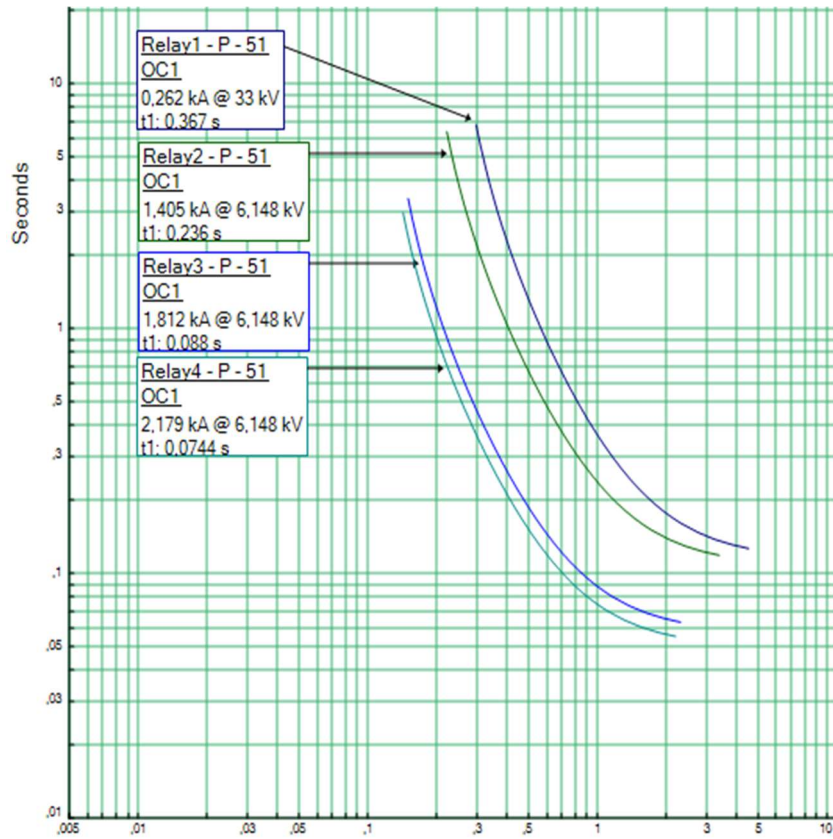


Figure 14. Overcurrent relay coordination using TSO algorithm

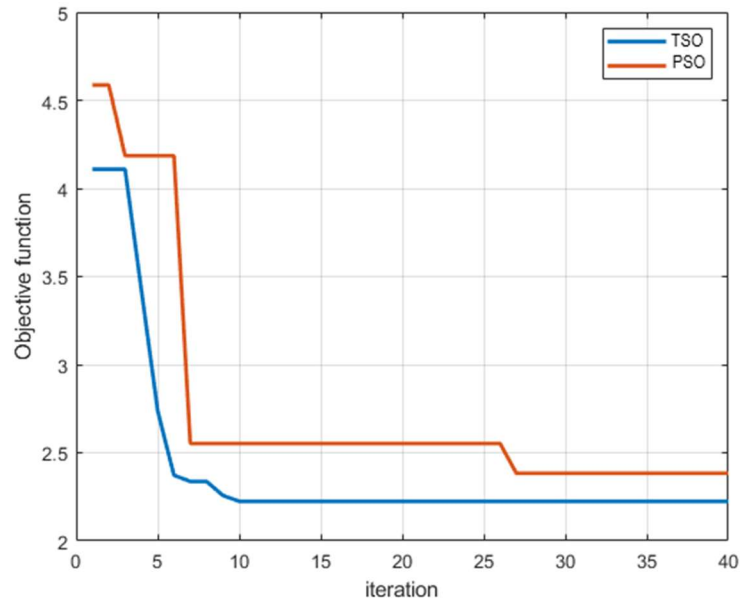


Figure 15. Best value of the objective function with PSO and TSO

4. Conclusion

This study aimed to optimize overcurrent relay coordination to enhance protection reliability and reduce the total operating time in power systems. A three-busbar power system model was developed in ETAP, where load flow analysis, short-circuit analysis, and relay coordination evaluations were performed in accordance with industry standards and regulatory requirements. An efficient and reliable protection scheme is critical for minimizing the adverse effects of faults on system stability and equipment longevity.

To achieve this, two metaheuristic algorithms (PSO, TSO) were employed to optimize relay settings. The initial total operating time of the relays was calculated as 1.428 milliseconds, which was significantly reduced through optimization. With the PSO algorithm, this value improved to 1.145 milliseconds, yielding a 19.81% reduction in total relay operating time. The newly implemented TSO algorithm provided even better results, achieving further reductions and reaching a total operating time of 0.765 milliseconds, representing a 46.42% improvement compared to the initial value. Additionally, TSO outperformed PSO by reducing the relay operating time by 33.19%. These results underscore the capability of advanced metaheuristic techniques in minimizing fault clearance times, thereby enhancing system resilience and operational efficiency.

The findings indicate that metaheuristic algorithms can play a vital role in optimizing relay settings, enabling adaptive, fast, and reliable protection schemes in complex power networks. In particular, the first-time application of the TSO algorithm in relay coordination has shown promising results, suggesting its potential as an alternative to traditional methods. Given the increasing complexity of power systems with distributed generation and dynamic network configurations, future studies should explore hybrid optimization approaches and real-time adaptive relay coordination techniques. Furthermore, additional investigations using larger test systems and incorporating renewable energy sources could evaluate the adaptability of these algorithms under varying fault conditions.

In conclusion, this study contributes to the ongoing research on overcurrent relay coordination by providing a comparative analysis of both established and novel optimization techniques. The successful implementation of TSO, along with its superior performance over PSO, highlights the importance of exploring new computational intelligence methods to improve protection system efficiency. Future research may extend this work by integrating other metaheuristic approaches, such as artificial neural networks and hybrid optimization frameworks, to further enhance relay coordination and overall system protection reliability.

Conflict of Interest Statement

The authors declare that there is no conflict of interest

References

- [1] A. J. Shendi, L. Mohammadian, R. Ghanizadeh, J. Pouladi, and J. Beiza, "Optimal synchronization of overcurrent relays in active distribution networks using a hybrid genetic-differential optimization algorithm," *Electrical Engineering*, vol. 1, pp. 1-16, 2025. doi:10.1007/s00202-024-02919-2
- [2] G. Muñoz-Arango, J. Mora-Flórez, and S. Pérez-Londoño, "Optimal data-driven adaptive overcurrent relay coordination for active distribution networks," *Electric Power Systems Research*, vol. 228, p. 110078, 2024. doi:10.1016/j.epsr.2023.110078
- [3] M. B. Atsever and M. H. Hocaoglu, "Optimal overcurrent relay coordination in distribution networks using finder algorithm," 2023.
- [4] F. M. Nuroglu and A. B. Arsoy, "Central coordination relay for distribution systems with distributed generation," *Turkish Journal of Electrical Engineering & Computer Sciences*, vol. 23, 2015. doi:10.3906/elk-1302-80
- [5] S. Shaikh, S. Shaikh, A. M. Soomar, and S. H. H. Shah, "Coordination of protective relays in the substation," *International Journal of Power Electronics and Drive Systems (IJPEDS)*, vol. 14, no. 3, pp. 1471-1478, 2023. doi:10.11591/ijpeds.v14.i3.pp1471-1478
- [6] M. T. Turan, Y. Ateş, and E. Gökulp, "Enerji Dağıtım Sistemlerinde Güneş Enerji Santrali Entegrasyonu ve Rôle Koordinasyonu," *EMO Bilimsel Dergi*, vol. 8, no. 1, pp. 63-69, 2018.
- [7] O. Seng, M. Pujiantara, A. Priyadi, and V. R. Mahindara, "Enhancement of Overcurrent Relay Coordination in Modern Industrial Distribution System Using Adaptive Modified Firefly Algorithm," in *2023 International Seminar on Intelligent Technology and Its Applications (ISITIA)*, July 2023, pp. 534-539. IEEE. doi: 10.1109/ISITIA59021.2023.10221107
- [8] N. Banerjee, R. D. Narayanasamy, and O. G. Swathika, "Optimal coordination of overcurrent relays using two phase simplex method and particle swarm optimization algorithm," in *2017 International Conference on Power and Embedded Drive Control (ICPEDC)*, March 2017, pp. 118-121. IEEE. doi: 10.1109/ICPEDC.2017.8081071
- [9] C. Jangid, S. Godwal, S. Chatterjee, and A. Nimje, "Optimum Overcurrent Relays Coordination of Radial and Parallel Distribution Systems," in *2024 IEEE Students Conference on Engineering and Systems (SCES)*, June 2024, pp. 1-6. IEEE. doi: 10.1109/SCES61914.2024.10652374
- [10] R. A. Pratiwi, M. Pujiantara, and A. Priyadi, "Optimization of Time Dial Setting Overcurrent Relay Using Cuckoo Search Algorithm Considering Inrush Current and Motor Starting," in *2024 11th International Conference on Information Technology, Computer, and Electrical Engineering (ICITACEE)*, August 2024, pp. 128-133. IEEE. doi: 10.1109/ICITACEE62763.2024.10762774
- [11] M. B. Atsever and M. H. Hocaoglu, "Aşırı Akım Rôle Koordinasyonu için Bozkurt Algoritmasının Kapsamlı Performans Analizi," *Türk Mühendislik Araştırma ve Eğitimi Dergisi*, vol. 1, no. 2, pp. 52-61, 2022.
- [12] Ö. Özgüner and E. Seyyarer, "Aşırı Akım Rôle Optimizasyonunda Optimizasyon Algoritmalarının Karşılaştırmalı Analizi," *Türk Doğa ve Fen Dergisi*, vol. 12, no. 4, pp. 25-32, 2023. doi: 10.46810/tdfd.1311104
- [13] M. B. Atsever, O. Karacasu, and M. H. Hocaoglu, "Performance Analysis of Different Optimization Algorithms on Overcurrent Relay Coordination Problem in Distribution Systems," in *2021 11th Smart Grid Conference (SGC)*, December 2021, pp. 1-6. IEEE. doi:10.1109/SGC54087.2021.9664218
- [14] M. Kheshti, B. S. Tekpeti, and X. Kang, "The optimal coordination of over-current relay protection in radial network based on particle swarm optimization," in *2016 IEEE PES Asia-Pacific Power and Energy Engineering Conference (APPEEC)*, October 2016, pp. 604-608. IEEE. doi: 10.1109/APPEEC.2016.7779575
- [15] O. Akdağ and C. Yeroğlu, "Güç sistemlerinde aşırı akım koruma koordinasyon modelinin oluşturulması, benzetimi ve optimizasyonu," *Erzincan University Journal of Science and Technology*, vol. 12, no. 1, pp. 202-214, 2019. doi: 10.18185/erzifbed.441911
- [16] E. Seyyarer, C. Hark, F. Ayata, T. Uçkan, and A. Karcı, "Fidan Gelişim ve Lig Şampiyonluk Algoritmaları Kullanarak Aşırı-Akım Rôlelerin Optimum Koordinasyonu," *Computer Science*, vol. 3, no. 2, pp. 1-14, 2018.
- [17] M. B. Atsever and M. H. Hocaoglu, "Mitigation of sympathy trips in highly cabled non-effectively earthed radial distribution systems via MINLP," *Electric Power Systems Research*, vol. 220, p. 109377, 2023. doi: 10.1016/j.epsr.2023.109377

- [18] S. Ashraf, I. Evkay, U. S. Selamogullari, M. Baysal, and O. Hasan, "Performance analysis of the dual-setting directional overcurrent relays-based protection considering the impact of curve types and fault location," *Electric Power Components and Systems*, vol. 51, no. 7, pp. 706-723, 2023. doi: 10.1080/15325008.2023.2182840
- [19] A. Korashy, S. Kamel, A. R. Youssef, and F. Jurado, "Modified water cycle algorithm for optimal direction overcurrent relays coordination," *Applied Soft Computing*, vol. 74, pp. 10-25, 2019. doi: 10.1016/j.asoc.2018.10.020
- [20] Y. Ates, A. R. Boynuegri, M. Uzunoglu, A. Nadar, R. Yumurtacı, O. Erdinc, and J. P. Catalão, "Adaptive protection scheme for a distribution system considering grid-connected and islanded modes of operation," *Energies*, vol. 9, no. 5, p. 378, 2016. doi: 10.3390/en9050378
- [21] Y. Ates, M. Uzunoglu, A. Karakas, A. R. Boynuegri, A. Nadar, and B. Dag, "Implementation of adaptive relay coordination in distribution systems including distributed generation," *Journal of Cleaner Production*, vol. 112, pp. 2697-2705, 2016. doi: 10.1016/j.jclepro.2015.10.066
- [22] İ. Arslanoğlu and İ. H. Altaş, "Modeling and analysis of a Radial Grid with Etap Program: Load Flow, Short Circuit Calculations and Relay Coordination with PSO Algorithm," in *ICENTE-24*, Konya, Turkey, 2024, pp. 89.
- [23] D. Saha, R. Nidhi, B. K. S. Roy, and M. Mukherjee, "Performance comparison of PSO, HGSO, and DE optimization techniques for computation of directional overcurrent relay coordination in power systems," *Engineering Review*, pp. 69-86, 2024.
- [24] M. Mirrashid and H. Naderpour, "Transit search: An optimization algorithm based on exoplanet exploration," *Results in Control and Optimization*, vol. 7, p. 100127, 2022. doi: 10.1016/j.rico.2022.100127
- [25] M. S. Amin, M. A. Attia, A. K. Khamees, S. F. Mekhamer, H. Kotb, K. M. AboRas, and A. Yousef, "Development of AVR controller performance using exponential distribution and transit search optimization techniques," *Frontiers in Energy Research*, vol. 12, p. 1356978, 2024. doi: 10.3389/fenrg.2024.1356978

This is an open access article under the CC-BY license



GAZİ

JOURNAL OF ENGINEERING SCIENCES

Application of Nanoparticle-Doped MOF Composite-Embedded Mixed Matrix Membranes in Carbon Capture

Özge Östürk Sömek^{a*}

Submitted: 03.12.2024 Revised: 13.02.2025 Accepted: 17.03.2025 doi: 10.30855/gmbd.070525N08

ABSTRACT

Keywords: Greenhouse gases, CO₂, carbon capturing, MOF, membrane

^{a*} Sinop University,
Engineering and Architecture Faculty,
Dept. of Environmental Engineering
57000 - Sinop, Türkiye
Orcid: 0000-0002-1082-7728
e mail: osomek@sinop.edu.tr

*Corresponding author:
osomek@sinop.edu.tr

Carbon dioxide (CO₂) is released into the atmosphere from both natural sources and human activities. In Türkiye, the largest source of CO₂ emissions from human activities is the energy sector, accounting for 85.4% of total CO₂ emissions in 2020. Over the past 30 years, CO₂ emissions have increased by 173%, making up 86% of total greenhouse gas emissions. This highlights the need for economically viable CO₂ capture technologies. Carbon capture methods are classified into pre-combustion, post-combustion, oxyfuel combustion, and direct air capture. Among these, post-combustion CO₂ capture has been widely studied in recent years. This method involves the separation, capture, and storage of CO₂ from flue gas after combustion. Common techniques include cryogenic separation, selective membranes, electrochemical separation, physical and chemical absorption, and adsorption. Among these, membrane-based CO₂ separation stands out, emphasizing the need for membranes with high CO₂ selectivity and permeability. MOFs are promising candidates due to their high porosity and CO₂ capture capacity. The development of mixed matrix membranes incorporating nanoparticle-doped MOFs into conventional membranes will enhance CO₂ selectivity in gas mixtures. This approach will enable the production of cost-effective, thermally and water-stable membranes with high CO₂ selectivity.

Karbon Yakalamada Nanoparçacık Katkılanmış MOF Kompozit Gömülü Karma Matris Membranların Uygulanması

ÖZ

Karbondioksit (CO₂), hem doğal kaynaklardan hem de insan faaliyetlerinden atmosfere salınmaktadır. Türkiye’de insan faaliyetlerinden kaynaklanan en büyük CO₂ emisyon kaynağı enerji sektörüdür ve 2020 yılında toplam CO₂ emisyonlarının %85,4’ünü oluşturmuştur. Son 30 yılda CO₂ emisyonları %173 artarak, toplam sera gazı emisyonlarının %86’sını meydana getirmiştir. Bu durum, ekonomik açıdan uygulanabilir CO₂ yakalama teknolojilerine olan ihtiyacı göstermektedir. Karbon yakalama yöntemleri; ön yanma, yanma sonrası, oksijenli yanma ve doğrudan havadan yakalama olarak sınıflandırılmaktadır. Son yıllarda, özellikle baca gazından CO₂’nin ayrılması, yakalanması ve depolanmasını içeren yanma sonrası yöntemleri daha fazla araştırılmıştır. En yaygın yöntemler, kriyojenik ayırma, seçici membranlar, elektrokimyasal ayırma, sıvı çözücülerle fiziksel/kimyasal absorpsiyon ve katılar üzerinde adsorpsiyondur. Bunlar arasında membran bazlı CO₂ ayırma öne çıkmakta olup, yüksek CO₂ seçiciliği ve geçirgenliği olan yeni membranlara ihtiyaç duyulmaktadır. MOF, yüksek gözeneklilikleri ve CO₂ tutma kapasitesi ile bu ihtiyacı karşılayabilecek aday malzemelerdir. Nanoparçacık katkılı MOF’lerin geleneksel membranlara katıldığı karışık matris membranlar geliştirilmesi, gaz karışımlarından CO₂ seçiciliğini artıracaktır. Bu yaklaşım, ısıya ve suya dayanıklı, yüksek CO₂ seçiciliğine sahip daha ekonomik membranların üretilmesini sağlayacaktır.

Anahtar Kelimeler: Sera gazları,
CO₂, karbon yakalama, MOF,
membran

1. Introduction

Global CO₂ emissions have surged rapidly in recent years, driven by industrialization and increasing energy demand. As energy consumption rises with population growth, urbanization, and economic expansion, reliance on fossil fuels persists to meet this demand [1]. CO₂ released into the atmosphere from fossil fuel combustion is recognized as one of the major factors of climate change. Climate change threatens the natural balance with effects such as growing global temperatures, sea level increments, and extreme weather events [2,3]. This situation makes reducing CO₂ emissions an urgent priority for a sustainable future.

The distribution of global CO₂ emissions plays a critical role in carbon management strategies. Figure 1 illustrates the total CO₂ emissions and CO₂ emissions per capita across various regions from 2000 to 2023. In the left graph, China's CO₂ emissions show a continuous upward trend, surpassing 12 Gt CO₂ by 2023, indicating that it emits more than other regions. India's emissions are also increasing, although at a lower level. Meanwhile, the European Union, Japan, and the United States exhibit relatively stable or declining emission levels at the same time. In the right graph, the United States has the highest CO₂ emissions per capita, though this value has been on a downward trend since 2000. Japan and the European Union also show similar decreasing trends in per capita emissions. While China's per capita emissions have been rising, they remain lower than those of industrialized nations like the United States. India, on the other hand, has the lowest per capita emissions. Overall, industrialized regions (such as the US, Japan, and the EU) show a decline in per capita emissions, whereas developing countries (particularly China and India) exhibit an increase. This reflects the impact of factors such as industrialization, population expansion, and economic development on CO₂ emissions [4].

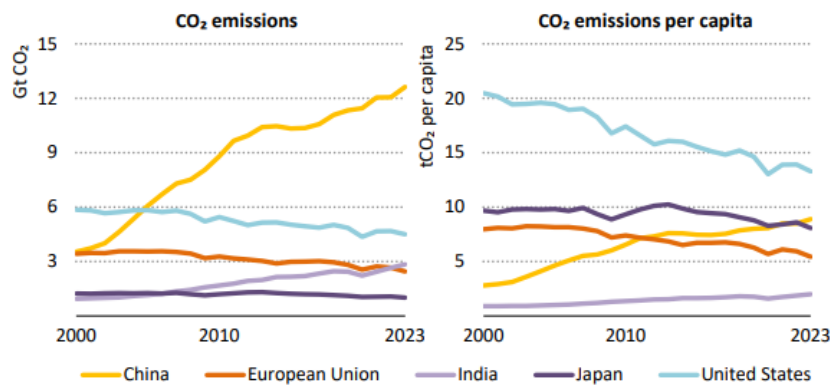


Figure 1. CO₂ total and CO₂ per capita by region [4].

Various strategies and technologies are being developed to reduce global CO₂ emissions. Strategies such as shifting to clean energy sources, optimizing energy efficiency, and utilizing renewable energy significantly contribute to reducing the carbon footprint. Additionally, energy-efficient technologies help lower carbon emissions by enabling less energy consumption in production processes [5]. However, despite these efforts, production processes in carbon-intensive sectors and the use of fossil fuels continue to generate high amounts of emissions. While there is a trend toward clean energy in electricity generation, this transition is insufficient to meet the entire demand, leading to a rise in fossil fuel use to bridge the production gap. The International Energy Agency's (IEA) 2023 CO₂ emissions report supports this situation, noting that emissions from energy generation enhanced by 900 Mt between 2019 and 2023; however, without eco-friendly energy solutions like solar, wind, nuclear, heat pumps, and electric vehicles, this increase would have been approximately three times higher [4]. Therefore, it is understood that clean energy technologies have limited the growth of CO₂ emissions. Yet, the current situation remains inadequate to achieve the net-zero emissions target, indicating that only limited improvement has been possible. In this context, solutions that go beyond existing technologies are needed to achieve more effective results.

At this point, carbon capture and storage (CCS) technologies stand out as a significant solution, directly targeting emissions in carbon-intensive sectors [6]. Carbon capture technologies have the potential to prevent CO₂ emissions originating from coal and gas power plants and industrial sites by capturing CO₂ before it reaches the atmosphere. Specifically, advanced materials such as metal-organic frameworks (MOFs) supported by nanoparticle-enriched mixed matrix membrane (MMM) systems offer a promising solution

because of their selective capability to separate and capture CO₂ molecules [7,8]. These innovative carbon capture technologies can capture CO₂ released from carbon-intensive production facilities, reducing environmental impacts and helping achieve carbon reduction goals.

This study aims to reveal the current status in this field by examining the potential of nanoparticle-doped MOF composite-embedded mixed matrix membranes in carbon capture. In this review, the structural characteristics, performance, and advantages of these next-generation membranes used in carbon capture technologies will first be discussed. Subsequently, application examples in the current literature and successful outcomes will be evaluated. Finally, the areas requiring improvement and upcoming development possibilities necessary for the widespread industrial application of these technologies will be discussed. This study intends to further insight into innovative technology with the potential to provide sustainable solutions for enhancing efficiency in carbon capture and achieving carbon reduction goals.

2. CO₂ Emissions, Sources, and Sinks

The escalation of CO₂ emissions has emerged as a pressing global challenge, primarily driven by anthropogenic activities and natural phenomena. The steady increase in CO₂ concentrations in the atmosphere is linked to significant alterations in climate patterns, resulting in severe ecological and socio-economic repercussions. A thorough comprehension of the origins and sinks of CO₂ is imperative for formulating targeted strategies aimed at curbing emissions and fostering sustainability. As industries expand and populations grow, the need to identify and address the specific contributors to carbon emissions becomes increasingly vital in the effort to tackle climate change.

In the study conducted by Liu et al. (2023), global carbon emissions for the year 2022 were analyzed in detail. Figure 2 clearly shows which sectors the emissions originate from and the annual emission trends of these sectors. When examining the sectoral distribution, it is evident that major sectors such as energy production, transportation, and industry provide significant emissions. Particularly, energy production accounts for a large portion of total emissions, playing a critical role in shaping climate policies. The transportation sector is also a significant source of emissions; this sector is directly related to the use of fossil fuels, and thus there is a need to accelerate the transition to alternative energy sources. The industrial sector produces significant emissions due to the energy and raw materials used in production processes. The study also addresses the changes in emissions from these sectors over time. For example, it notes that emissions experienced a temporary decline during the COVID-19 pandemic, but rapidly increased in 2021, approaching pre-pandemic levels. These sector-specific analyses guide policymakers on where more effort is needed to reduce emissions. The data in Fig. 2 also reflects seasonal fluctuations in emissions. For instance, it is observed that emissions rise in winter due to increased energy consumption, while this trend reverses in summer. This situation highlights how emissions are affected by seasonal changes in energy demand [9]. Deforestation and land use changes contribute approximately 10% of global CO₂ emissions. The alteration of forests for agriculture or urbanization not only reduces the planet's capacity to sequester carbon but also releases stored carbon back into the atmosphere. Agricultural practices add around 5% to total emissions, largely through soil management and fertilizer application. Furthermore, waste management practices, including landfilling and incineration, generate approximately 3% of global CO₂ emissions as organic materials decompose or are burned [10,11].

In Türkiye, the biggest contributor to CO₂ emissions from human activities is the energy, industrial processes and product use (IPPU), agriculture, and waste sectors. According to the National Greenhouse Gas (GHG) Emission Inventory Report, which covers the years 1990-2020 submitted as part of the United Nations Framework Convention on Climate Change, the energy sector accounts for 85.4% of total CO₂ emissions in 2020. The remaining 14.2% comes from IPPU, 0.4% from agriculture, and close to zero from waste. Total CO₂ emissions from all sectors have increased by approximately 173% in 30 years. This increase constitutes 86% of total GHG emissions in Türkiye [12].

Despite the challenges posed by CO₂ emissions, various natural and technological sinks exist that can absorb atmospheric carbon dioxide. Forests serve as one of the most significant carbon sinks, with the ability to sequester about 2.6 billion metric tons of CO₂ annually through photosynthesis. Initiatives focused on

reforestation and afforestation are crucial for enhancing this capacity [13]. Oceans also play a vital role, absorbing an estimated 2.5 billion metric tons of CO₂ each year. However, elevated CO₂ levels can lead to ocean acidification, which threatens marine ecosystems [14]. Soil is another critical carbon sink, with healthy soils capable of storing approximately 3.3 billion metric tons of carbon each year. Implementing sustainable agricultural practices can significantly enhance soil carbon storage, thereby acting as a buffer against CO₂ emissions [15]. On the technological front, solutions such as CCS aim to sequester CO₂ emissions from industrial processes, currently capturing about 40 million metric tons of CO₂ per year. Additionally, innovations like direct air capture (DAC) are emerging, showing potential for removing millions of tons of CO₂ from the atmosphere annually [16].

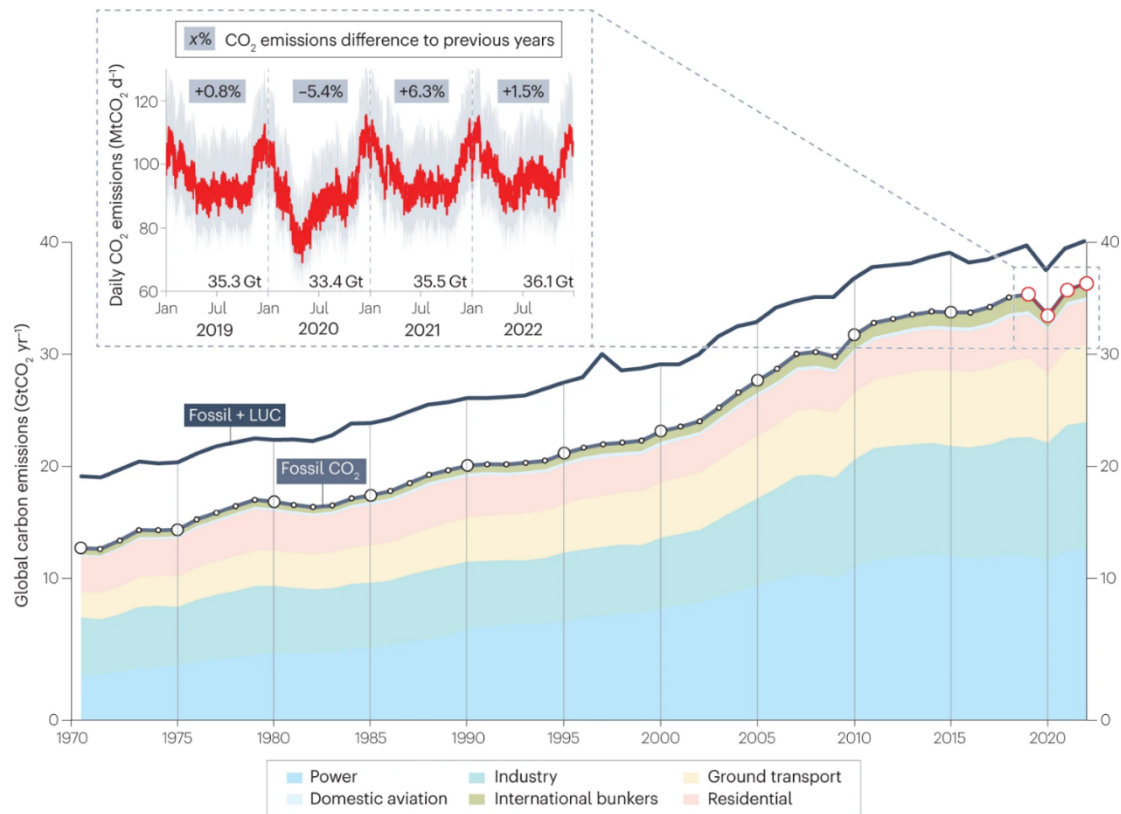


Figure 2. Global CO₂ emissions 1970-2022 [9].

Comprehending the sources and sinks of CO₂ emissions is crucial for creating effective solutions to address climate change. By targeting emissions from fossil fuel combustion, industrial activities, and land use changes, while simultaneously enhancing natural sinks like forests and soils, we can make significant strides toward a sustainable future. These combined efforts will be critical in tackling the multifaceted challenges posed by climate change and in attaining global carbon reduction targets.

3. Capture and Removal of CO₂

As the urgency to address climate change escalates, the development of effective carbon capture technologies has become crucial. These technologies aim to mitigate CO₂ emissions from major sources, such as power plants, industrial processes, and transportation systems [17,18]. Key strategies include pre-combustion capture, which involves removing CO₂ before combustion occurs, typically in integrated gasification combined cycle (IGCC) power plants [19]; post-combustion capture, which captures CO₂ from flue gases after fuel combustion using methods such as chemical absorption and adsorption [20]; and direct air capture (DAC), which extracts CO₂ directly from the atmosphere, presenting a pathway for achieving negative emissions [21]. Recent advancements are increasingly focused on integrating these methods with renewable energy sources to enhance efficiency and sustainability. Table 1 summarizes the principles, advantages, and disadvantages of CCS technologies. Accordingly, Chemical absorption enables the selective capture of CO₂ using amine or solvent solutions and is a method applicable at an industrial scale [22]. However, challenges such as high energy consumption during solvent regeneration, solvent degradation, and corrosion increase

the cost and environmental impacts of this method [23,24]. Physical absorption, on the other hand, involves the capture of CO₂ using physical solvents at low temperatures. This method is highly efficient in high-pressure gas streams and has low solvent loss [25]. However, its reduced effectiveness at low pressures limits its large-scale application [26]. When comparing these two absorption methods, chemical absorption offers higher selectivity, while physical absorption has the advantage of reducing solvent costs.

Membrane technologies involve the separation of CO₂ from other gases through semi-permeable membranes. This method is advantageous due to its energy efficiency and modular design [27]. Various CO₂ capture technologies have reviewed the potential of membrane-based systems, particularly in applications such as CO₂-enhanced methane recovery. It is highlighted that membrane technologies when integrated with other CO₂ capture methods, can improve overall efficiency and feasibility in industrial applications [28]. However, limitations such as the chemical and thermal stability of membranes and the need for multi-stage processes to achieve high purity are notable challenges [27]. Nevertheless, innovative approaches such as thin-film composite membranes and graphene oxide modification show promise in enhancing membrane performance [29]. In this context, it was emphasized that novel materials and hybrid approaches, such as incorporating nanoparticles and advanced polymer structures, could improve membrane performance and longevity [30].

Adsorption methods involve the physical or chemical capture of CO₂ using high-surface-area materials [31]. The use of materials like metal-organic frameworks (MOFs) improves selectivity and recovery rates. However, high material costs and long-term stability issues are among the disadvantages of this method [32-34]. Innovations such as hybrid graphene-MOF materials and surface engineering are improving the effectiveness of adsorption technology [35,36]. Cryogenic separation allows producing high-purity CO₂ through liquefaction at low temperatures. The absence of solvent use is a significant advantage [37]. However, the requirement for extremely low temperatures leads to high energy consumption, limiting its economic feasibility [38]. Biological capture involves the sequestration of CO₂ using microalgae or other biological agents. This method offers additional benefits, such as biofuel production [39]. However, challenges such as sensitivity to growth conditions and the need for large areas limit their practical applications [40,41].

Chemical looping CO₂ capture (CLC) is a method that uses metal oxides and enables the direct separation of CO₂ from fossil fuels. CLC is a promising method for decreasing carbon emissions from fossil fuels by enabling highly efficient and direct CO₂ separation [42]. Pilot-scale studies indicate that technology is still in the developmental phase for large-scale commercial applications [43]. On the other hand, the selection of oxygen carriers plays a crucial role in system performance. In this context, it was found that Fe₂O₃/CaO-based oxygen carriers are effective for hydrogen-rich syngas production. Thus, CLC has potential not only for carbon capture but also for hydrogen production [44]. However, despite its high efficiency, its limited commercial adoption and high initial costs are restrictive factors [45]. Moreover, the high reactor design costs were highlighted as a major challenge [46]. With these characteristics, CLC presents a significant opportunity for transitioning to a low-carbon economy by offering sustainable energy production and effective CO₂ emission reduction, but large-scale applicability and cost reduction are needed.

In summary, while chemical and physical absorption methods are among conventional approaches, membrane and adsorption technologies offer innovative solutions. With the latest developments, membrane technologies present a promising pathway for CO₂ separation, but overcoming challenges related to multi-stage processing, chemical stability, and thermal resistance is crucial for their widespread adoption in carbon capture applications. Designing mixed-matrix membranes and incorporating advanced nanomaterials with superior properties are essential to addressing these challenges.

Table 1. Carbon capture technologies.

Technology	Principles	Advantages	Disadvantages	References
Chemical absorption	Absorb CO ₂ with amine or solvent solutions.	High selectivity, can operate at low temperatures and can be applied on an industrial scale.	Solvent regeneration is energy-intensive, risks solvent degradation and corrosion	[22-24]
Physical absorption	CO ₂ is absorbed at low temperatures with physical solvents	Efficient in high-pressure gas flows, low solvent loss.	Poor efficiency at low pressures	[25,26]
Membrane technologies	Separates CO ₂ and other gases by semi-permeable membranes	High energy efficiency, modular structure	Requires multi-stage process for high purity, limited chemical and thermal resistance of membranes	[27-30]
Adsorption	CO ₂ is physically or chemically trapped in materials with a high surface area	High selectivity and recovery rate, low energy consumption	Material costs can be high, long-term stability can be an issue	[31-36]
Cryogenic separation	Separation of CO ₂ by liquefaction at low temperatures	High-purity CO ₂ can be obtained, and no solvent is required	High energy consumption for low temperatures	[37,38]
Biological capture	Capturing and converting CO ₂ with microalgae or other biological methods	Renewable provides side benefits such as biofuel production	Efficiency is low, requires a large area and growth conditions are sensitive	[39-41]
Chemical looping capture	Capture and storage of CO ₂ with metal oxides	High efficiency, direct separation of CO ₂ from fossil fuels	Technology is not yet commercially available. The initial cost is high	[42-46]

3.1. Membrane-based CO₂ separation

Membrane-based separation technologies have attracted considerable interest in CO₂ capture because of their potential for high selectivity and energy efficiency. These systems utilize semi-permeable membranes to separate CO₂ from other gases, offering a compact and scalable solution for reducing emissions. Fig. 3 schematically illustrates how gas mixtures are separated using membranes. In the figure, the feed gas, which typically consists of CO₂ and other components, enters the membrane system. The membrane is a semi-permeable structure that exhibits selective permeability to certain gases, allowing some gases to pass through more easily while others are retained. The gases that pass through the membrane are referred to as permeate gas, whereas the gases that are retained by the membrane are called retentate gas. In CO₂ capture processes, the primary goal is usually to separate CO₂ as the permeate gas. In membrane-based CO₂ separation, permeability (P) and selectivity (α) are two key parameters used to assess performance. Permeability indicates the amount of gas passing through a unit thickness of the membrane and is typically measured in Barrer. This parameter reflects how quickly CO₂ can permeate the membrane, which is crucial for achieving high flow rates and efficiency in industrial applications. Selectivity, on the other hand, denotes the degree of selectivity between two gases, often measured for gas pairs like CO₂/N₂, and determines the membrane's ability to separate CO₂ effectively from other gases. Membranes with high permeability and high selectivity allow for the rapid and efficient separation of CO₂ from other gases, making the optimization of these two parameters essential for achieving ideal performance.

Membrane-based CO₂ separation technologies are characterized by several advantages, including energy efficiency, as they typically require less energy than traditional amine scrubbing processes, resulting in lower operational costs [28]. Moreover, the modular nature of membrane systems allows for their deployment in various scales and applications, ranging from large industrial plants to small-scale operations, facilitating ease of integration into existing infrastructures. The various types of membranes employed in CO₂ separation include organic (polymeric), inorganic (ceramic), and nanocomposite (mixed matrix membranes – MMMs) [29]. Polymeric membranes are known for their flexibility and ease of processing, while ceramic membranes offer superior thermal and mechanical stability. Mixed matrix membranes combine the advantages of both polymeric and inorganic materials, leading to enhanced performance characteristics such as increased

permeability and selectivity for CO₂ over other gases.

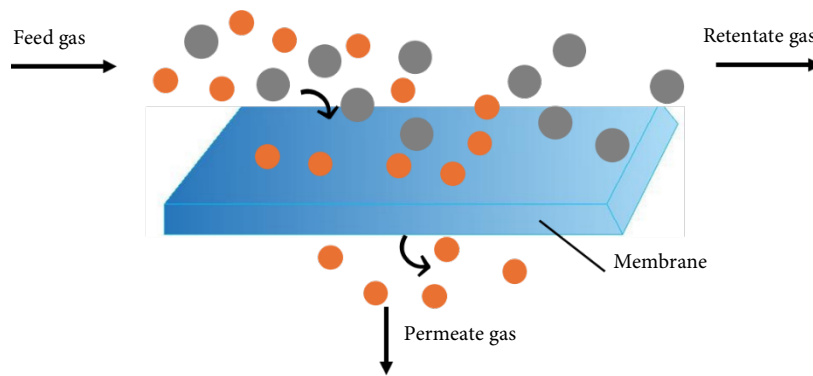


Figure 3. The diagram of gas mixture separation with membranes.

3.2. Design of mixed matrix membranes (MMMs)

MMMs are composite membranes formed by embedding inorganic or organic particles in a polymeric matrix. The particles (e.g. MOF, zeolites, carbon nanotubes) combine with the polymer matrix to further customize and improve the separation properties of the membrane. In this context, the most promising advancement in membrane technology is the development of MOF-based MMMs. These advanced materials combine the beneficial properties of MOFs with nanoparticles, creating a new class of membranes that present superior gas separation characteristics [47,48]. The incorporation of MOFs enhances selectivity for CO₂ due to their high surface area and tunable pore structures, allowing for precise adjustments to optimize gas adsorption properties.

Fig. 4 illustrates the production of a MMM by embedding a nanoparticle-doped MOF composite into a polymer matrix. Initially, nanoparticles and the MOF are combined to form a homogeneous nanocomposite, leveraging the structural and chemical properties of the MOF with the functionality of the nanoparticles to enhance carbon capture performance. The nanocomposite is then added to a polymer solution to achieve uniform dispersion. This step aims to improve the membrane's properties, such as gas permeability and selectivity. The prepared polymer-nanocomposite mixture is cast into a polytetrafluoroethylene (PTFE) mold and then dried and solidified to form the MMM. The casting step is followed by a controlled drying and solidification phase, where solvent removal is carefully managed to prevent defects and ensure the formation of a robust and uniform membrane structure. This process also allows for the fine-tuning of the membrane's porosity and thickness, which are critical for optimizing gas transport and separation. The resulting MMM is optimized for carbon capture applications with enhanced porosity, permeability, and thermal and mechanical stability. These features make the membrane highly effective in capturing CO₂.

3.3. Recent advances in MMMs for CO₂ separation

Table 2 provides examples of MMMs prepared with various polymer and MOF compounds for CO₂ separation applications. In these MMMs, significant increases in CO₂ permeability and selectivity have been observed using MOF fillers like UIO-66, UIO-66-NH₂, MIL-96-(Al), MOF-808, and Mg₂(dobpdc) combined with polymers such as PIM-1, 6FDA-DAM, ODPA-DAM, Matrimid, and PDA [49-54]. The high surface area and porous structures of MOF fillers contribute to the effective capture of CO₂ while facilitating rapid CO₂ transport and maintaining stable selectivity. A high-performance membrane was developed for CO₂/N₂ selectivity by combining 6FDA-DAM polymer with Mg₂(dobpdc), offering significant advantages for industrial applications, especially in CO₂ separation from other gases [51,53]. These studies on membrane selectivity have produced high-performance MMMs using various fillers, with optimized separation parameters. These findings demonstrate that MOFs can enhance CO₂ separation performance in different polymer matrices, and each MOF-polymer combination can be tailored for specific gas separation needs. On the other hand, MMMs obtained by embedding nanoparticle-doped MOF composites in polymer membranes improve the permeability of the membranes by facilitating more efficient pathways for gas transport, leading to a synergistic effect that optimizes both adsorption and diffusion processes. The studies highlighted a range of MOFs, such as ZIF-8 and MIL-53(Al), combined with different nanomaterials, including graphene oxide and porous carbon, within diverse polymer matrices like PSF [55-57]. This results in increased CO₂ uptake

while maintaining mechanical stability, which is crucial for consistent membrane performance under diverse operational conditions.

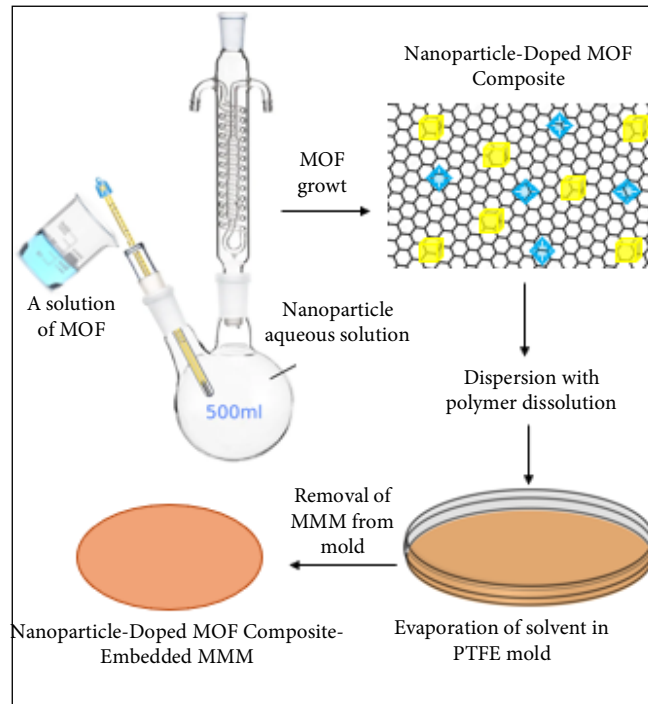


Figure 4. Fabrication flowchart of nanoparticle-doped MOF composite-embedded MMM

Table 2. Application of MOFs as a filler in MMMs for CO₂ capture.

Membrane Materials	Fillers	Application	References
PIM-1	UiO-66-CN	Polymeric membranes with embedded MOF in CO ₂ separation	[49]
6FDA-DAM	Mg ₂ (dobpdc)	Membranes designed for CO ₂ permeability and CO ₂ /N ₂ selectivity	[50]
6FDA-DAM	MIL-96-(Al)	Processing of MMMs for CO ₂ /N ₂ post-combustion separation.	[51]
ODPA-DAM	UiO-66-NH ₂	High-performance MOF-based MMMs for gas separation	[52]
	UiO-66-NH ₂ @PI		
Matrimid	MOF-808	CO ₂ /N ₂ separation performance of MMMs.	[53]
PDA	UiO-66	CO ₂ /N ₂ and CO ₂ /CH ₄ separation performance of MOF membranes	[54]

Composite membranes contribute to sustainability efforts by utilizing abundant and often environmentally friendly materials in their production. However, challenges remain in scaling these materials for commercial use, necessitating further research into cost-effective manufacturing processes and the long-term stability of these membranes under various environmental conditions. The cost of MOF-based MMMs is primarily influenced by the synthesis of MOF materials, polymer matrix selection, and fabrication processes. Studies have shown that MOF production can contribute up to 60% of the total membrane cost, with solvent-based synthesis being one of the major cost drivers [51,52]. Although MOFs offer superior CO₂ separation efficiency, their large-scale application is often hindered by the high cost of raw materials and complex synthesis routes. Several studies have highlighted the need for cost reduction in MMM fabrication. One approach involves using lower-cost precursors for MOF synthesis while maintaining the structural integrity and performance of the final membrane. For example, solvent-free synthesis and scalable continuous production methods have been explored to reduce costs by approximately 30% [54]. Therefore, it is important to develop alternatives such as solvent-free synthesis and continuous production techniques to make MMMs more economical in the future. Additionally, optimizing polymer-MOF interactions through surface modifications has been suggested to improve compatibility and reduce processing costs [53]. Finally, the use of nanoparticle-doped MOF composites can provide economic advantages in membrane fabrication by optimizing gas migration pathways [55,57].

3.4. Nanomaterials effect on carbon capture performance of membranes

In recent years, nanocomposite membranes obtained using nanomaterials have been frequently used in CO₂ capture. The filler material used in the production of nanocomposite membranes is selected based on the desired performance. Common nanomaterials include metal nanoparticles (Au, Ag, ZnO), carbon-based nanomaterials (carbon nanotubes, graphene oxide), metal-organic frameworks (MOFs), and zeolites. Additionally, functionalization processes can be applied to improve the surface properties of these nanomaterials. Moreover, by combining these nanomaterials, it is possible to produce filler materials with new properties such as high permeability, selectivity, and durability (e.g., MOF-graphene oxide composites). The findings presented in Table 3 provide a comparative assessment of the CO₂ capture performance of nanocomposite membranes. The HKUST-1@Graphene Oxide (GO) membrane was synthesized using the electrodeposition method, achieving a CO₂ adsorption capacity of 194.1 cm³/g and a CO₂/N₂ ideal adsorption selectivity of 276.5, demonstrating that MOF structures modified with graphene oxide can enhance CO₂ adsorption capacity [58]. The Pebax/ZIF-8/NH₂-MIL-53(Al) membrane exhibited a CO₂ permeability of 488 ± 9 Barrer and a CO₂/CH₄ selectivity of 37.5 ± 0.6, indicating that the incorporation of amine-functionalized ZIF-8 and MIL-53(Al) MOFs improves CO₂ separation properties [59]. Similarly, the PEI-functionalized cerium nanosheet (PEI-F-Ce) mixed with a crosslinked polyethylene oxide (XLPEO) membrane demonstrated a CO₂ permeability of 641 Barrer and a CO₂/N₂ selectivity of 70.1, highlighting that the controlled pore structure provided by amine-functionalized F-Ce nanosheets enhances CO₂ permeability [60]. The Polyethersulfone (PES) blended with polyurethane (PU) and nano-clay membrane showed that the addition of PU and nano-clay fillers increased CO₂ permeability by 7.8 times and CO₂/N₂ and CO₂/CH₄ selectivity by 1.8 and 2.2 times, respectively [61]. The Pebax®1657-MOF-74(Ni)@GO membrane exhibited a significant improvement in CO₂/N₂ separation [29]. On the other hand, during the nanomaterial drop-casting

process, some agglomeration occurred within the membrane structure, which could impact gas transport efficiency. Finally, carbon nanotube (CNT) incorporated with NH₂-functionalized MIL-101 and 6FDA-durene polyimide-based mixed matrix membranes (MMMs) demonstrated both high CO₂ permeability and CO₂/CH₄ selectivity, confirming the positive impact of MOF and CNT combinations on CO₂ separation performance [62]. The findings in the table highlight the significant potential of nanomaterial-incorporated membranes in enhancing selectivity and permeability, particularly emphasizing that hybrid membranes based on MOF, CNT, and GO can optimize CO₂ capture efficiency. The integration of nanoparticle-doped MOF composite-embedded MMMs within the wider context of carbon capture technologies and membrane-based separation provides a promising pathway for effective CO₂ removal. By addressing these challenges and leveraging the unique properties of advanced membrane materials, we can enhance the efficiency of CO₂ capture technologies and significantly contribute to global actions aimed at decreasing carbon emissions and addressing climate change.

Table 3. Performance of nanocomposite membranes in CO₂ separation.

Nanocomposite membrane	Method	Findings	References
HKUST-1@GO	Electrodeposition	High CO ₂ adsorption capacity of 194.1 cm ³ /g and CO ₂ /N ₂ adsorption ideal selectivity of 276.5 at 273 K	[58]
Pebax/ZIF-8/NH ₂ -MIL-53(Al)	Solution-casting technique	A CO ₂ permeability of 488 ± 9 Barrer and a CO ₂ /CH ₄ selectivity of 37.5 ± 0.6	[59]
PEI-F-Ce/XLPEO	Solution-casting technique	Excellent CO ₂ permeability (641 Barrer) and outstanding CO ₂ /N ₂ selectivity (70.1)	[60]
PES/PU/nano-clay	Solution-casting and solvent evaporation methods	The combined use of PU and nano-clay as fillers improved the CO ₂ permeability, CO ₂ /N ₂ , and CO ₂ /CH ₄ selectivity of PES by 7.8, 1.8, and 2.2 times.	[61]
Pebax*1657-MOF-74 (Ni)@GO	One-pot and solvent casting methods.	A substantial increase in CO ₂ /N ₂ separation selectivity,	[29]
CNT-MIL/6FDA-durene NH ₂ -MIL-101/6FDA-durene CNT-COOH/6FDA-durene	Solution casting method	MMMs containing the synthesized MOF/CNT composite exhibited high CO ₂ permeability and CO ₂ /CH ₄ selectivity.	[62]

4. Conclusion

This study underscores the pivotal role of advanced membrane-based carbon capture technologies, concentrating on the integration of nanoparticle-doped MOF composite-embedded MMMs. The innovative use of MOFs within polymer matrices has demonstrated significant potential in enhancing both the selectivity and permeability for CO₂ separation. By leveraging the high surface area, tunable porosity, and customizable properties of MOFs, these MMMs have emerged as promising candidates for effective and efficient carbon capture. However, the application of MOF-composites produced by incorporating carbon-based materials into MOF for use in polymer membranes is critical in enhancing the membranes' thermal and water stability. These materials ensure that the membranes maintain structural integrity under harsh industrial conditions while also functionalizing the membrane pores to make them more CO₂-attractive. The selection of nanoparticles is crucial; they must be carefully chosen to align with the morphological structure of the MOF to achieve optimal synergy. This compatibility enhances the overall performance, as the right nanomaterial can create efficient gas transport pathways, facilitating selective CO₂ adsorption and improving separation efficiency. The use of nanocomposites in membrane production has significantly improved performance, increasing CO₂ permeability by 7.8 times, CO₂/N₂ selectivity by 1.8 times, and CO₂/CH₄ selectivity by 2.2 times. In this context, the amount of filler material incorporated into the membrane is a significant factor. While an optimal filler concentration can maximize CO₂ capture performance, excessive loading of nanomaterials can lead to agglomeration. This agglomeration can block the pores of the membrane, restricting gas flow and thereby diminishing the overall efficiency of the gas separation process. Thus, precise control over the filler amount is essential to maintain a balance between performance and structural stability.

Despite significant advancements in nanoparticle-doped MOF-based MMMs for CO₂ separation, challenges such as scaling up production, economic feasibility, and long-term stability persist. Continued research is needed to optimize material compositions and manufacturing processes for industrial applications. Considering that MOF production can account for up to 60% of the total membrane cost, solvent-free synthesis and continuous production methods could reduce costs by approximately 30%. These findings highlight that MOF and nanoparticle-doped MMMs are promising candidates for cost-effective and efficient carbon capture processes. Progress in this field presents a promising opportunity for reducing CO₂ emissions and contributing to climate change mitigation and global sustainability efforts.

Conflict of Interest Statement

The authors declare that there is no conflict of interest

References

- [1] A. Raihan and A. Tuspekova, "Dynamic impacts of economic growth, energy use, urbanization, agricultural productivity, and forested area on carbon emissions: New insights from Kazakhstan," *World Development Sustainability*, vol. 1, 100019, 2022. doi: 10.1016/j.wds.2022.100019
- [2] S. Bolan, L. P. Padhye, T. Jasemizad, M. Govarthan, N. Karmegam, H. Wijesekara, D. Amarasiri, D. Hou, P. Zhou, B. Kumar Biswal, R. Balasubramanian, H. Wang, K. H. M. Siddique, J. Rinklebe, M. B. Kirkham, and N. Bolan, "Impacts of climate change on the fate of contaminants through extreme weather events," *Science of The Total Environment*, vol. 909, 168388, 2024. doi: 10.1016/j.scitotenv.2023.168388
- [3] M. Filonchyk, M. P. Peterson, H. Yan, A. Gusev, L. Zhang, Y. He and S. Yang, "Greenhouse gas emissions and reduction strategies for the world's largest greenhouse gas emitters," *Science of The Total Environment*, vol. 944, 173895, 2024. doi: 10.1016/j.scitotenv.2024.173895
- [4] International Energy Agency, "CO₂ Emissions in 2023," *iea.org*, March 2024. [online]. Available: <https://www.iea.org/reports/co2-emissions-in-2023>, [Accessed: Oct. 28, 2024].
- [5] A. Jahanger, I. Ozturk, J. C. Onwe, T. E. Joseph and M. R. Hossain, "Do technology and renewable energy contribute to energy efficiency and carbon neutrality? Evidence from top ten manufacturing countries," *Sustainable Energy Technologies and Assessments*, vol. 56, 103084, 2023. doi: 10.1016/j.seta.2023.103084
- [6] B. Dziejarski, R. Krzyżyńska and K. Andersson, "Current status of carbon capture, utilization, and storage technologies in the global economy: A survey of technical assessment," *Fuel*, vol. 342, 127776, 2023. doi: 10.1016/j.fuel.2023.127776
- [7] Y. Cheng, S. J. Datta, S. Zhou, J. Jia, O. Shekhah and M. Eddaoudi, "Advances in metal-organic framework-based membranes," *Chemical Society Reviews*, vol. 51, pp. 8300-8350, 2022. doi: 10.1039/D2CS00031H
- [8] R. Chen, M. Chai and J. Hou, "Metal-organic framework-based mixed matrix membranes for gas separation: Recent advances and opportunities," *Carbon Capture Science & Technology*, vol. 8, 100130, 2023. doi: 10.1016/j.ccst.2023.100130
- [9] Z. Liu, Z. Deng, S. Davis and P. Ciaia, "Monitoring global carbon emissions in 2022," *Nature Reviews Earth & Environment*, vol. 4, pp. 205-206, 2023. doi: 10.1038/s43017-023-00406-z
- [10] L. Wang, "Assessment of land use change and carbon emission: A Log Mean Divisa (LMDI) approach," *Heliyon*, vol. 10, no 3, e25669, 2024. doi: 10.1016/j.heliyon.2024.e25669
- [11] European Environment Agency, "Greenhouse gas emissions from land use, land use change and forestry in Europe," *eea.europa.eu*, Oct. 31, 2024. [Online]. Available: <https://www.eea.europa.eu/en/analysis/indicators/greenhouse-gas-emissions-from-land?activeAccordion=546a7c35-9188-4d23-94ee-005d97c26f2b>, [Accessed: Nov. 5, 2024].
- [12] United Nations Climate Change, "Turkey. 2022 National Inventory Report (NIR)," *unfccc.int*, Apr. 14, 2022. [Online]. Available: <https://unfccc.int/documents/461926>, [Accessed: Oct. 18, 2024]
- [13] K. Psistaki, G. Tsantopoulos and A. K. Paschalidou, "An Overview of the Role of Forests in Climate Change Mitigation," *Sustainability*, vol. 16, 6089, 2024. doi: 10.3390/su16146089
- [14] C. L. Sabine, R. A. Feely, N. Gruber, R. M. Key, K. Lee, J. L. Bullister, R. Wanninkhof, C. S. Wong, D. W. R. Wallace, B. Tilbrook, F. J. Millero, T.-H. Peng, A. Kozyr, T. Ono, and A. F. Rios "The Oceanic Sink for Anthropogenic CO₂," *Science*, vol. 305, pp. 367-371, 2004. doi: 10.1126/science.1097403
- [15] C. I. D. Rodrigues, L. M. Brito and L. J. R. Nunes, "Soil Carbon Sequestration in the Context of Climate Change Mitigation: A Review," *Soil Systems*, vol. 7, no 3, pp. 64, 2023. doi: 10.3390/soilsystems7030064
- [16] M. Ozkan, S. P. Nayak, A. D. Ruiz and W. Jiang, "Current status and pillars of direct air capture technologies," *iScience*, vol. 25, no 4, 103990, 2022. doi: 10.1016/j.isci.2022.103990

- [17] B. Dziejarski, R. Krzyżyńska and K. Andersson, "Current status of carbon capture, utilization, and storage technologies in the global economy: A survey of technical assessment," *Fuel*, vol. 342, 127776, 2023. doi: 10.1016/j.fuel.2023.127776
- [18] T. M. Gür, "Carbon Dioxide Emissions, Capture, Storage and Utilization: Review of Materials, Processes and Technologies," *Progress in Energy and Combustion Science*, vol. 89, 100965, 2022. doi: 10.1016/j.pecs.2021.100965
- [19] A. Padurean, C. C. Cormos and P. S. Agachi, "Pre-combustion carbon dioxide capture by gas-liquid absorption for Integrated Gasification Combined Cycle power plants," *International Journal of Greenhouse Gas Control*, vol. 7, pp. 1-11, 2012. doi: 10.1016/j.ijggc.2011.12.007
- [20] C. Wu, Q. Huang, Z. Xu, A. T. Sipra, N. Gao, L. P. d. S. Vandenberghe, S. Vieira, C. R. Soccol, et al., "A comprehensive review of carbon capture science and technologies," *Carbon Capture Science and Technology*, vol. 11, 100178, 2024. doi: 10.1016/j.ccst.2023.100178
- [21] N. McQueen, K. V. Gomes, C. McCormick, K. Blumanthal, M. Pisciotta, and J. Wilcox, "A review of direct air capture (DAC): Scaling up commercial technologies and innovating for the future," *Progress in Energy*, vol. 3 no 3, 032001, 2021. doi: 10.1088/2516-1083/abf1ce
- [22] F. O. Ochedi, J. Yu, H. Yu, Y. Liu and A. Hussain, "Carbon dioxide capture using liquid absorption methods: a review," *Environmental Chemistry Letter*, vol. 19, pp. 77-109, 2021. doi: 10.1007/s10311-020-01093-8
- [23] M. Perumal, D. Jayaraman and A. Balraj, "Experimental studies on CO₂ absorption and solvent recovery in aqueous blends of monoethanolamine and tetrabutylammonium hydroxide," *Chemosphere*, vol. 276, 130159, 2021. doi: 10.1016/j.chemosphere.2021.130159
- [24] D. Hospital-Benito, J. Lemus, C. Moya, R. Santiago and J. Palomar, "Process analysis overview of ionic liquids on CO₂ chemical capture," *Chemical Engineering Journal*, vol. 390, 124509, 2020. doi: 10.1016/j.cej.2020.124509
- [25] R. Ben-Mansour, M. A. Habib, O. E. Bamidele, M. Basha, N. A. A. Qasem, A. Peedikakkal, T. Laoui and M. Ali, "Carbon capture by physical adsorption: Materials, experimental investigations and numerical modeling and simulations – A review," *Applied Energy*, vol. 161, pp. 225-255, 2016. doi: 10.1016/j.apenergy.2015.10.011
- [26] X. Zhang, Z. Song, R. Gani and T. Zhou, "Comparative Economic Analysis of Physical, Chemical, and Hybrid Absorption Processes for Carbon Capture," *Industrial & Engineering Chemistry Research*, vol. 59, no 5, pp. 2005-2012, 2020. doi: 10.1021/acs.iecr.9b05510
- [27] R. Hou, C. Fong, B. D. Freeman, M. R. Hill and Z. Xie, "Current status and advances in membrane technology for carbon capture," *Separation and Purification Technology*, vol. 300, 121863, 2022. doi: 10.1016/j.seppur.2022.121863
- [28] S. F. Cannone, A. Lanzini, and M. Santarelli, "A review on CO₂ capture technologies with focus on CO₂-enhanced methane recovery from hydrates," *Energies*, vol. 14 no 2, 387, 2021. doi: 10.3390/en14020387
- [29] L. Feng, Q. Zhang, J. Su, B. Ma, Y. Wan, R. Zhong, and R. Zou, "Graphene-Oxide-Modified Metal-Organic Frameworks Embedded in Mixed-Matrix Membranes for Highly Efficient CO₂/N₂ Separation," *Nanomaterials*, vol. 14 no 1, 24, 2024. doi: 10.3390/nano14010024
- [30] M. Liu, M. D. Nothling, S. Zhang, Q. Fu and G. G. Qiao, "Thin film composite membranes for postcombustion carbon capture: Polymers and beyond," *Progress in Polymer Science*, vol. 126, 101504, 2022. doi: 10.1016/j.proppolymsci.2022.101504
- [31] F. Raganati, F. Miccio and P. Ammendola, "Adsorption of Carbon Dioxide for Post-combustion Capture: A Review," *Energy & Fuels*, vol. 35, no 16, pp. 12845-12868, 2021. doi: 10.1021/acs.energyfuels.1c01618
- [32] T. Ghanbari, F. Abnisa and W. M. A. W. Daud, "A review on production of metal organic frameworks (MOF) for CO₂ adsorption," *Science of The Total Environment*, vol. 707, 135090, 2020. doi: 10.1016/j.scitotenv.2019.135090
- [33] O. T. Qazvini, R. Babarao and S. G. Telfer, "Selective capture of carbon dioxide from hydrocarbons using a metal-organic framework," *Nature Communications*, vol.12, 197, 2021. doi: 10.1038/s41467-020-20489-2
- [34] D. Britt, H. Furukawa, B. Wang, T. G. Glover and O. M. Yaghi, "Highly efficient separation of carbon dioxide by a metal-organic framework replete with open metal sites," *Proceedings of the National Academy of Sciences of the United States of America*, vol. 106, no 49, pp. 20637-20640, 2009. doi: 10.1073/pnas.0909718106
- [35] B. Szczyński, J. Choma and M. Jaroniec, "Gas adsorption properties of hybrid graphene-MOF materials," *Journal of Colloid and Interface Science*, vol. 514, pp. 801-813, 2018. doi: 10.1016/j.jcis.2017.11.049
- [36] C. Petit and T. J. Bandoz, "Engineering the surface of a new class of adsorbents: Metal-organic framework/graphite oxide composites," *Journal of Colloid and Interface Science*, vol. 447, pp. 139-151, 2015. doi: 10.1016/j.jcis.2014.08.026
- [37] M. Shen, L. Tong, S. Yin, C. Liu, L. Wang, W. Fen and Y. Ding, "Cryogenic technology progress for CO₂ capture under carbon neutrality goals: A review," *Separation and Purification Technology*, vol. 299, 121734, 2022. doi: 10.1016/j.seppur.2022.121734
- [38] C. Font-Palma, D. Cann and C. Udemu, "Review of Cryogenic Carbon Capture Innovations and Their Potential Applications," *Journal of Carbon Research*, vol. 7, no 3, 58, 2021. doi: 10.3390/c7030058
- [39] S. K. Bhatia, R. K. Bhatia, J.-M. Jeon, G. Kumar and Y.-H. Yang, "Carbon dioxide capture and bioenergy production using biological

- system – A review,” *Renewable and Sustainable Energy Reviews*, vol. 110, pp. 143-158, 2019. doi: 10.1016/j.rser.2019.04.070
- [40] E. Daneshvar, R. J. Wicker, P.-L. Show and A. Bhatnagar, “Biologically-mediated carbon capture and utilization by microalgae towards sustainable CO₂ biofixation and biomass valorization – A review,” *Chemical Engineering Journal*, vol. 427, 130884, 2022. doi: 10.1016/j.cej.2021.130884
- [41] M. U. Sieborg, A. K. H. Nielsen, L. D. M Ottosen, K. Daasbjerg and M. V. W. Kofoed, “Bio-integrated carbon capture and utilization: at the interface between capture chemistry and archaeal CO₂ reduction,” *Nature Communications*, vol. 15, 7492, 2024. doi: 10.1038/s41467-024-51700-3
- [42] H. A. Alalwan and A. H. Alminshid, “CO₂ capturing methods: Chemical looping combustion (CLC) as a promising technique,” *Science of The Total Environment*, vol. 788, 147850, 2021. doi: 10.1016/j.scitotenv.2021.147850
- [43] I. Gogolev, C.Linderholm, D. Gall, M. Schmitz, T. Mattisson, J. B. C. Pettersson and A. Lyngfelt, “Chemical-looping combustion in a 100 kW unit using a mixture of synthetic and natural oxygen carriers – Operational results and fate of biomass fuel alkali,” *International Journal of Greenhouse Gas Control*, vol. 88, pp. 371-382, 2019. doi: 10.1016/j.ijggc.2019.06.020
- [44] Q. Hu, Y. Shen, J. W. Chew, T. Ge and C.-H. Wang, “Chemical looping gasification of biomass with Fe₂O₃/CaO as the oxygen carrier for hydrogen-enriched syngas production,” *Chemical Engineering Journal*, vol. 379, 122346, 2020. doi: 10.1016/j.cej.2019.122346
- [45] B. Jin, R. Wang, D. Fu, T. Ouyang, Y. Fan, H. Zhang and Z. Liang, “Chemical looping CO₂ capture and in-situ conversion as a promising platform for green and low-carbon industry transition: Review and perspective,” *Carbon Capture Science & Technology*, vol. 10, 100169, 2024. doi: 10.1016/j.ccst.2023.100169
- [46] J. Adanez, A. Abad, F. Garcia-Labiano, P. Gayan and L. F. d. Diego, “Progress in Chemical-Looping Combustion and Reforming technologies,” *Progress in Energy and Combustion Science*, vol. 38, no 2, pp. 215-282, 2012. doi: 10.1016/j.pecs.2011.09.001
- [47] X. W. Liu, T. J. Sun, J. L. Hu, and S. D. Wang, “Composites of metal-organic frameworks and carbon-based materials: Preparations, functionalities and applications,” *Journal of Materials Chemistry A*, vol. 4, no 10, pp. 3584–3616, 2016. doi: 10.1039/C5TA09924B
- [48] L. Hu, K. Clark, T. Alebrahim, and H. Lin, “Mixed matrix membranes for post-combustion carbon capture: From materials design to membrane engineering,” *Journal of Membrane Science*, vol. 644, 120140, 2022. doi: 10.1016/j.memsci.2021.120140
- [49] G. Yu, X. Zou, L. Sun, B. Liu, Z. Wang, P. Zhang and G. Zhu, “Constructing Connected Paths between UiO-66 and PIM-1 to Improve Membrane CO₂ Separation with Crystal-Like Gas Selectivity,” *Advanced Materials*, vol. 31, no 15, 1806853, 2019. doi: 10.1002/adma.201806853
- [50] L. Maserati, S. M. Meckler, J. E. Bachman, J. R. Long and B. A. Helms, “Diamine-Appended Mg₂(dobpdc) Nanorods as Phase-Change Fillers in Mixed-Matrix Membranes for Efficient CO₂/N₂ Separations,” *Nano Letters*, vol. 17, no 11, pp. 6828–6832, 2017. doi: 10.1021/acs.nanolett.7b03106
- [51] M. Benzaqui, R. S. Pillai, A. Sabetghadam, V. Benoit, P. Normand, J. Marrot, N. Menguy, D. Montero, W. Shepard, A. Tissot, C. Martineau-Corcoss, C. Sicard, M. Mihaylov, F. Carn, I. Beurroies, P. L. Llewellyn, G. De Weireld, K. Hadjiivanov, J. Gascon and C. Serre, “Revisiting the Aluminum Trimesate-Based MOF (MIL-96): From Structure Determination to the Processing of Mixed Matrix Membranes for CO₂ Capture,” *Chemistry of Materials*, vol. 29, no 24, pp. 10326–10338, 2017. doi: 10.1021/acs.chemmater.7b03203
- [52] H. Wang, S. He, X. Qin, C. Li and T. Li, “Interfacial Engineering in Metal-Organic Framework-Based Mixed Matrix Membranes Using Covalently Grafted Polyimide Brushes,” *Journal of the American Chemical Society*, vol. 140, no 49, pp. 17203–17210, 2018. doi: 10.1021/jacs.8b10138
- [53] R. Thür, D. Van Havere, N. Van Velthoven, S. Smolders, A. Lataire, J. Wieme, V. V. Speybroeck, D. De Vos and I. F. J. Vankelecom, “Correlating MOF-808 parameters with mixed-matrix membrane (MMM) CO₂ permeation for a 2 more rational MMM development,” *Journal of Materials Chemistry A*, vol. 9, pp. 12782-12796, 2021. doi: 10.1039/D0TA10207E
- [54] W. Wu, Z. Li, Y. Chen and W. Li, “Polydopamine-Modified Metal-Organic Framework Membrane with Enhanced Selectivity for Carbon Capture,” *Environmental Science & Technology*, vol. 53, no 7, pp. 3764–3772, 2019. doi: 10.1021/acs.est.9b00408
- [55] S. Anastasiou, N. Bhoria, J. Pokhrel, K. S. Kumar Reddy, C. Srinivasakannan, K. Wang and G. N. Karanikolos, “Metal-organic framework/graphene oxide composite fillers in mixed-matrix membranes for CO₂ separation,” *Materials Chemistry and Physics*, vol. 212, pp. 513–522, 2018. doi: 10.1016/j.matchemphys.2018.03.064
- [56] M. van Essen, R. Thür, M. Houben, I. F. J. Vankelecom, Z. Borneman and K. Nijmeijer, “Tortuous mixed matrix membranes: A subtle balance between microporosity and compatibility,” *Journal of Membrane Science*, vol. 635, 119517, 2021. doi: 10.1016/j.memsci.2021.119517
- [57] A. Khan, A. M. Elsharif, A. Helal, Z. H. Yamani, A. Saeed Hakeem and M. Yusuf Khan “Mixed Dimensional Nanostructure (UiO-66-Decorated MWCNT) as a Nanofiller in Mixed-Matrix Membranes for Enhanced CO₂/CH₄ Separation,” *Chemistry - A European Journal*, vol. 27, no 43, pp. 11132–11140, 2021. doi: 10.1002/chem.202101017
- [58] B. Yao, Y. Wang, Z. Fang, Y. Hu, Z. Ye and X. Peng, “Electrodepositing MOFs into laminated graphene oxide membrane for CO₂ capture,” *Microporous and Mesoporous Materials*, vol. 361, 112758, 2023. doi: 10.1016/j.micromeso.2023.112758

- [59] J. Wang, L. Li, X. Li and J. Zhang, "Constructing double-faced CO₂-capture domains by sandwich-like fillers in membranes for efficient CO₂ separation," *Chemical Engineering Science*, vol. 283, 119374, 2024. doi: 10.1016/j.ces.2023.119374
- [60] M. Zhao, J. Guo, Q. Xin, Y. Zhang, X. Li, X. Ding, L. Zhang, L. Zhao, H. Ye, H. Li, G. Xuan and Y. Zhang, "Novel aminated F-Ce nanosheet mixed matrix membranes with controllable channels for CO₂ capture," *Separation and Purification Technology*, vol. 324, 124512, 2023. doi: 10.1016/j.seppur.2023.124512
- [61] M. S. Maleh, S. Kiani and A. Raisi, "Study on the advantageous effect of nano-clay and polyurethane on structure and CO₂ separation performance of polyethersulfone based ternary mixed matrix membranes," *Chemical Engineering Research and Design*, vol. 179, pp. 27-40, 2022. doi: 10.1016/j.cherd.2022.01.011
- [62] R. Lin, L. Ge, S. Liu, V. Rudolph and Z. Zhu, "Mixed-Matrix Membranes with Metal-Organic Framework-Decorated CNT Fillers for Efficient CO₂ Separation," *ACS Applied Materials & Interfaces Journal*, vol. 7, no 27, pp. 14750-14757, 2015. doi:10.1021/acsami.5b02680

* This article is an extended version of the paper presented at the International Conference on Engineering Technologies (ICENTE'22).

This is an open access article under the CC-BY license



GAZİ

JOURNAL OF ENGINEERING SCIENCES

Multiobjective Mathematical Model Proposal For Mid-Term Capacity Planning In A Bearing Manufacturing Company

Begüm Polat^a, Esra Dinler^b, Alptekin Demiray^c

Submitted: 03.09.2023 Revised: 01.01.2025 Accepted: 17.03.2025 doi: 10.30855/gmbd.070525N09

ABSTRACT

Keywords: Medium Term Capacity Planning, Multiobjective Mathematical Programming, Pareto Solution

^a Baskent University,
Engineering Faculty,
Dept. of Industrial Engineering
06810 - Ankara, Türkiye
Orcid: 0000-0002-5582-6091
e mail: polatbegum12@gmail.com

^b Baskent University,
Engineering Faculty,
Dept. of Industrial Engineering
06810 - Ankara, Türkiye
Orcid: 0000-0001-8868-8484

^c Ortadoğu Rulman Sanayii ve Ticaret
A.Ş.
06900 - Ankara, Türkiye
Orcid: 0009-0000-7667-7796

^{*}Corresponding author:
polatbegum12@gmail.com

Businesses aim to use their resources efficiently and increase their income by planning their production processes. Capacity planning is of great importance in this area. Capacity planning evaluates idle capacity and aims to reduce costs by organizing workflow and using resources efficiently. One of the mathematical techniques used in capacity planning studies is linear programming. Within the scope of this study, the determination of the products to be produced on the lines and their quantities were carried out with the linear programming technique for medium term capacity planning in a company that produces bearings. A multiobjective mathematical model was created by considering the resources of the enterprise and Pareto solutions were obtained. With the proposed mathematical model, capacity planning has been carried out by determining which products the enterprises will produce on which line and how much. In the proposed multi-objective mathematical model, the first purpose is to minimize the number of working days, and the second is to determine the lot sizes according to the characteristics of the products and to manage the stock status effectively. In the proposed model, these two objective functions are weighted and expressed as a single objective function, and Pareto solutions are obtained by taking into account system-specific constraints. The results were compared according to performance criteria.

Rulman Üretimi Yapan Bir Firmada Orta Dönem Kapasite Planlama İçin Çok Amaçlı Matematiksel Model Önerisi

ÖZ

İşletmeler üretim süreçlerini planlayarak kaynaklarını verimli kullanmayı ve gelirlerini artırmayı hedefler. Kapasite planlama bu alanda büyük önem taşır. Kapasite planlama, iş akışını düzenleyip kaynakları verimli kullanarak atıl kapasiteyi değerlendirir ve maliyetleri azaltmayı hedefler. Kapasite planlama çalışmalarında kullanılan matematiksel tekniklerden biri doğrusal programlamadır. Bu çalışmada, rulman üretimi yapılan bir firmada gerçek bir orta dönem kapasite planlaması için matematiksel bir model geliştirilerek hatlarda üretilecek ürünlerin ve miktarlarının belirlenmesi gerçekleştirilmiştir. İşletmenin sahip olduğu kaynaklar gözetilerek çok amaçlı matematiksel bir model geliştirilmiş ve Pareto çözümler elde edilmiştir. Önerilen matematiksel model ile işletmelerin hangi ürünleri hangi hatta ne kadar üreteceğinin belirlenerek kapasite planlaması gerçekleştirilmiştir. Önerilen çok amaçlı matematiksel modelde ilk amaç çalışılan gün sayısının en küçüklenmesi, ikincisi ise ürünlerin özelliklerine göre parti büyüklüklerinin belirlenerek stok durumlarının etkin bir biçimde yönetiminin gerçekleştirilmesidir. Önerilen modelde bu iki amaç fonksiyonu Ağırlıklı Toplam yöntemi kullanılarak tek bir amaç fonksiyonu biçiminde ifade edilmiş ve sistemde özel kısıtlar göz önünde bulundurularak Pareto çözümler elde edilmiştir. Sonuçlar performans kriterlerine göre karşılaştırılmıştır.

Anahtar Kelimeler: Orta Dönem Kapasite Planlama, Çok Amaçlı Matematiksel Programlama, Pareto Çözüm

1. Giriş

Üretim, insani ihtiyaçların karşılanması, mal ve hizmetlerin elde edilmesi için yapılan çalışmalar bütününe verilen addır. İşletmeler, mal ve hizmetleri üretmek amacıyla, üretim fonksiyonlarını doğru bir biçimde planlamalı ve yönetimlerini gerçekleştirmelidirler. Bu nedenle üretim planlama, üretimdeki senaryoları en iyilemek amacıyla geliştirilmiştir. İşletmeler, mal ve hizmetlerin tasarlanması ve üretilmesi için kritik bir rol oynayan üretim planlamasından yararlanmaktadır.

Üretim planlama, müşteri ve organizasyonların ihtiyacına göre üretim için verimli bir süreç oluşturmayı hedeflemektedir. Teslimatların zamanında gerçekleşmesi gibi müşteriye bağlı süreçleri ve üretimin çevrim süresi gibi müşteriden bağımsız süreçleri en iyilemek için çalışmalar yürütülmektedir. İyi bir üretim planının amacı, bir siparişin verilmesi ile o siparişin tamamlanması ve teslim edilmesi arasında geçen süreyi yani tedarik süresini en aza indirmektir. Firmaya ve üretim planlamasının tipine bağlı olarak, tedarik süresinin tanımı değişebilmektedir.

Kapasite planlama ise bir üretim planlama türüdür. Tedarik zincirinin talebinin karşılanması kapsamında, işgücü ihtiyaçlarını ve üretim kapasitesini belirlemek için kullanılmaktadır. Kapasite planlama, işletmelerde üretim verimliliğini en üst seviyeye çıkararak sorunsuz bir iş akışı sağlamayı hedefleyen temel bir araç olarak rol almaktadır. Bu biçimde, işletmelerin taleplerdeki değişikliklerin öngörülmesine ve planlanmasına, kaynakları en iyilenmesine, ürün eksikliklerinin önlenmesine ve darboğazların belirlenmesine yardımcı olmakta ve işletmeler tarafından sıklıkla kullanılmaktadır.

Kapasite planlama uzun, orta ve kısa dönem kapasite planlama olmak üzere üç farklı düzeyde incelenmektedir. Uzun dönem planlama kapsamında, işletmelerin yatırım planlamaları ile ilgili çalışmalar yapılmaktadır. Kısa dönem planlama kapsamında ise gereksinim planlamaları ve üretim çizelgeleme çalışmaları gerçekleştirilmektedir. Yapılan bu çalışma kapsamında kullanılan orta dönem kapasite planlamasında ise, işletmelere ait kaba kapasite planlaması yapılmaktadır. Orta dönem planlama kapsamında hammadde, işgücü, makine saati gibi kritik ve sınırlı kaynakların en iyi biçimde kullanımı sağlanarak, işletmelerin verimliliklerinin en iyi seviyeye çıkarılması amaçlanmaktadır [1].

Bu çalışma, ürünlerin farklı kriterlere göre özelliklerinin değerlendirilerek elde atıl olarak kalmasının engellenmesi hedefi ile literatürdeki çalışmalardan ayrılmaktadır. Böylelikle riskli ürünler az sayıda partiler halinde üretilecek, ürünün talep edilmemesi durumunda stokta kalması engellenebilecektir. Ancak talep durumu belirli ve riskli olmayan ürünler tek seferde üretilerek talep karşılanacak ve diğer yandan hazırlık süresi ve toplam gün sayısı en küçüklenebilecektir. Bu amaç sayesinde sadece üretim ve hazırlık maliyetleri değerlendirmemiş olacak ve ayrıca ürünlerin riskli olmalarından kaynaklanacak maliyetlerin de önüne geçilmiş olunacaktır.

Bu çalışmada, rulman üretimi yapan bir firmada gerçek üretim süreçleri incelenmiş ve kapasite planlaması yapılmıştır. Çalışmanın ikinci bölümde çalışma ile ilgili yapılan literatür araştırmasında incelenen örnek çalışmalara değinilmiştir. Üçüncü bölümde çalışmada kullanılan verilerin alındığı işletmedeki süreçler, mevcut durumda kullandıkları yöntemler ve oluşturulan matematiksel model tanımlanmıştır. Dördüncü bölümde ise önerilen matematiksel modelin sonuçlarına yer verilmiştir. Bu çözümlerin değerlendirmesi farklı performans kriterlerine göre yapılmıştır.

2. Literatür Taraması

Doğrusal Programlama, karar vericilerin mevcutta bulunan sınırlı kaynaklardan en iyi biçimde yararlanmak istediği kapasite planlama ve karar verme gibi birçok alanda kullanılan matematiksel programlamanın bir alanıdır [2]. Doğrusal programlama problemleri, ihtiyaçları karşılamak için sınırlı kaynakların etkin dağılımı ya da kullanımı ile ilgilenmektedir [3]. Literatürde üretim planlama ve kapasite planlama kapsamında

doğrusal programlamanın ve sezgisel tekniklerin kullanıldığı çok sayıda çalışma bulunmaktadır. İncelenen çalışmalarda pek çok farklı amaç fonksiyonu ile çalışıldığı görülmüştür. Çoğunlukla karın en büyüklenmesi, maliyetin en küçüklenmesi gibi ekonomik amaçlarla modeller önerilmiştir. Bu amaçların yanı sıra çevrim sürelerinin en küçüklenmesi, işçi atamalarının en küçüklenmesi ve problemde verilen üretim planına uyulması gibi amaç fonksiyonları ile de çalışılmıştır. Çalışma kapsamında incelenen örnek çalışmalardan bölümün devamında bahsedilmiştir.

Bir elektronik üreticisinde yapılan çalışmada Tavaghof-Gigloo, Minner ve Sibelmayr (2016) üretim planlama problemi için karma tamsayılı doğrusal programlama modelini ele almışlardır [4]. Çok ürünlü, çok tesisli ve çok aşamalı, talebin bilindiği bir sistemde sonlu kapasite planlaması çalışılmıştır. Çalışma kapsamında vardiyalar, fazla mesailer göz önünde bulundurularak toplam maliyet en küçüklenmek istenmiştir.

Üretim sektöründe sipariş üzerine üretim yapan bir firmada kısa dönem kapasite planlama problemi ele alınmıştır [5]. Chen, Mestry, Damodaran ve Wang (2009) tüm siparişlerin teslim tarihini geçirmeden üretilmesi için operasyonel karı en yüksek düzeye çıkaracak biçimde matematiksel model sunmuştur. Önerilen modelde normal mesai, fazla mesai ve dış kaynak kullanımları da dikkate alınmıştır.

Prefabrik evler için yapı elemanları üreten bir firmada karma model montaj hattının kapasite planlama çalışması, Huka, Grenzfurtnner, Zauner, Gronalt (2023) tarafından Endüstri 4.0 uygulamalarından yararlanılarak yapılmıştır [6]. Paralel üretim hatlarında belirli bir planlama dönemi için personel tahsisi ve iş yükü atamalarını gerçekleştirecek doğrusal programlama çalışması yapılmış ve çalışma sonucunda ürün çıktıları en büyüklenmek istenmiştir.

Yapılan başka bir kaynak kapasite planlama çalışmasında Ojstersek, Buchmeister (2021) üretim sistemi kısıtlamalarına bağlı olarak, yeni bir karar modeli geliştirmişlerdir [7]. Orta ve kısa vadeli işçi dağılımı için matematiksel bir karar modeli geliştirilerek minimum işçi tahsisi yapmak amaçlanmıştır. Bu çalışmalara ek olarak bir simülasyon modeli geliştirilmiş ve üretimdeki dinamik olaylar ile oluşturulan karar modeline uygulanmıştır.

Yapılan bir başka çalışmada güneş enerjisi ve yenilenebilir enerji sektöründe yer alan bir firmada 12 aylık üretim planlaması problemi Ekmekçi (2015) tarafından ele alınmıştır [8]. Çalışmada doğrusal programlamadan yararlanılarak kısıtlar oluşturulmuş ve amaç fonksiyonunda kar en büyüklenmeye çalışılmıştır. Bu çalışmada karın en büyüklenmesinin yanında üretim planlama sürecinde doğrusal programlama ile hem sürecin hızlandırılması sağlanmış hem de kaynaklar en iyi biçimde kullanılmıştır.

Tekstil sektöründe yapılan bir diğer çalışmada ise kar maksimizasyonunu sağlayan üretim miktarları hesaplanmıştır [9]. Bunun için Deste, Karabulut (2021) doğrusal programlamadan yararlanarak farklı niteliklerde ürün üretimi gerçekleştiren işletmenin kısıtlı kaynakları sayısal verilerle ifade edilerek kısıtlar oluşturmuş ve matematiksel model kurulmuştur. Modelin sonuçlarına göre işletmenin en iyi üretim miktarları belirlenmiştir.

Konfeksiyon işletmesinde yapılan bir çalışmada, Çetindere, Sevim ve Duran (2010) siparişe göre çalışan ve çok farklı niteliklerde ürün üretimi gerçekleştiren bir firmanın makine, işgücü ve hammadde olmak üzere kısıtlı kaynakları sayısal olarak ifade etmiş ve bu doğrultuda matematiksel model önerisinde bulunmuşlardır [10]. İşletmenin sahip olduğu kaynakların verimli kullanımının sağlandığı takdirde karını arttırabileceği tespit edilmiştir.

Demircioğlu ve Demircioğlu (2016) bir işletmede üretme-satın alma kararlarında ilgili sistem için bir doğrusal programlama modeli geliştirmişlerdir [11]. Bu modelin sonuçları mevcutta kullanılan sistem ile kıyaslanmıştır. Çalışma kapsamında işletmedeki karlılığın arttırılması amaçlanmaktadır.

Gıda sektöründe tatlı üretimi yapan bir işletmede Kara ve Savaş (2015) optimal üretim miktarlarının

hesaplanması için doğrusal programlamadan yararlanmışlardır [12]. Bu kapsamda doğrusal programlama modelinin çözüm yöntemlerinden simpleks metodundan yararlanılmıştır. Çalışmada asıl amaç, uygun üretim miktarlarının belirlenmesiyle işletmenin karını en büyükmeye çalışmaktır.

Tek amaçlı doğrusal programlamaya ek olarak çok amaçlı doğrusal programlama çözüm yöntemlerinden yararlanılarak bu kapsamda belirlenen farklı amaçların aynı anda gerçekleşmesi koşulu üzerinden literatürde çok sayıda çalışma yapılmıştır. Literatürde yer alan çok amaçlı doğrusal programlama modeli örneklerine aşağıda yer verilmiştir.

Özcan ve Erol (2013) elektrik üretim planlaması kapsamında yapılan bu çalışmada maliyetlerin en küçüklenmesi, CO2 salınımının en küçüklenmesi, fosil yakıt kullanımının en küçüklenmesi ve sosyal kabulün en büyüklenmesi amaçlarını aynı anda eniyileyen eden çok amaçlı bir karışık tam sayılı doğrusal programlama modeli kurmuşlardır [13]. Kurulan bu model ile çok amaçlı optimizasyon probleminin çözümünde minimum sapma yöntemi kullanılmıştır.

Üretim işletmesinde yapılan bir çalışmada, Büyükkelik (2007) müşteri memnuniyeti ve termin süreleri dikkate alınarak mesai sürelerinin en iyi biçimde kullanılması, kalıpların mümkün olduğunca doluluğunun sağlanması gibi amaçları yerine getirecek çok amaçlı bir doğrusal programlama modeli önermiştir [14]. Modelde, işletmenin önceliklerine uygun olarak amaçlar ağırlıklandırılmıştır.

Liu ve Papageorgiou (2013) tedarik zinciri kapsamında üretim, dağıtım ve kapasite planlaması yapılırken aynı anda maliyet, yanıt verebilirlik ve müşteri hizmet düzeyleri göz önüne alınarak karma tamsayı doğrusal programlama modeli kurmuşlardır [15]. Toplam maliyet, toplam akış süresi ve toplam satış kayıplarının en küçüklendiği çok amaçlı programlama modelinde e-kısıt tekniği kullanılarak model çözdürülmüştür.

Sezgisel algoritmalar günümüzde pek çok alanda sıkça kullanıldığı gibi kapasite planlama alanında da fazlaca örnekleri mevcuttur. Bu kapsamdaki örneklere bölümün devamında yer verilmiştir. Yapılan bir çalışmada Mhiri, Jacomino, Mangione, Vialletelle ve Lepelletier (2015) düşük hacimli üretim, karmaşık süreçler, değişken çevrim süreleri ve tekrarlı akış özelliklerine sahip yarı iletken üretimi için bir sonlu kapasite planlama sezgisel geliştirmişlerdir [16]. Önerilen algoritma ile kalan süreç adımları için üretim partileri başlangıç ve bitiş tarihleri hesaplanmış, tüm makineler için beklenen iş yükü tahmin edilmiş ve iş yükünü darboğaz araçlarının kapasitelerine karşı dengelenmiştir.

Kazakovtsev, Gudyma, Antamoshkin (2014) dökümhanede verilen bir çıktı planına uygun olarak proses üretim hatlarının optimal kapasite planlaması problemi, bir ağ üzerinde ayrık bir konum problemi olarak ele almışlardır [17]. Problemi çözmek için ağgözlü sezgisellere sahip genetik algoritmayı kullanmışlardır. Bu sayede kapasite planlama probleminin çalışma süresi mevcut algoritmanın çalışma süresinden daha düşük olarak gözlemlenmiştir.

Chen, Chen, Lin, Chen ve Yang (2011) düşük sipariş hacmi, yüksek sipariş çeşitliliği, karmaşık süreçler, belirsiz sipariş ve sık sipariş değişikliği özelliklerine sahip bir silah üretim sistemi için sezgisel geliştirmişlerdir [18]. Önerilen yöntem ile siparişleri kaynaklara tahsis ederek fabrikaya uygun sipariş tamamlama zamanı belirlenmiş ve tüm makinelerin beklenen iş yükü tahmin edilmiştir.

Yarı iletken ürün üretimi yapan bir firmada Iwata, Tajii ve Tamura (2003) çok amaçlı bir kapasite planlama metodolojisi üzerinde çalışmışlardır [19]. Çalışmada çevrim süresinin ve maliyetin enküçüklenmesi hedef olarak verilmiştir.

Khalili ve Khah (2020) otel kapasitesini optimal bir biçimde belirlemek için kuyruk teorisini kullanan yeni bir matematiksel optimizasyon modeli sunmuşlardır [20]. Çalışma kapsamındaki problem büyük ölçeklerde çok karmaşık olduğundan problemi çözmek için Taguchi yöntemi ile geliştirilmiş bir Genetik Algoritma yaklaşımı kullanılmıştır.

Literatürdeki örneklerden görüldüğü üzere kapasite planlama kapsamında doğrusal programlama ve sezgisel tekniklerin kullanımlarına sıklıkla rastlanılmaktadır. Ayrıca çalışmalar incelendiğinde çoğunlukla maliyet en küçüklemesi veya karın en büyüklmesi gibi amaçlar ele alınmıştır. Bu çalışmada literatürden farklı olarak ürünlerin farklı kriterlere göre özellikleri değerlendirilmiş ve ürünlerin elde atıl olarak kalmasının engellenmesi hedeflenmiştir. Bu aşamada çalışma kapsamında çok kriterli karar verme yöntemlerinden TOPSIS (Technique for Order Preference by Similarity to Ideal Solution) metodundan yararlanılmıştır. Literatürde çok kriterli karar verme yöntemlerinden TOPSIS metodunun kullanıldığı birçok örnek yer almaktadır. Bunlardan üretim alanında yapılan çalışmalar incelenmiştir.

Ayvaz, Boltürk ve Kaçtıoğlu (2015) tarafından gerçekleştirilen çalışmada, işletmeler için en uygun ERP yazılımının seçimi amacıyla Analitik Ağ Süreci (ANP), TOPSIS ve doğrusal programlama yöntemleri kullanılmıştır [21]. Bu kapsamında TOPSIS metodundan yararlanarak fiyat, kalite, hizmet, teslimat ve güvenlik gibi kriterler değerlendirilmiş ve en uygun yazılım belirlenmiştir.

Ev tekstili ürünleri satışı yapan bir işletmede gerçekleştirilen çalışma, Oğuz, Pençe, Şişeci Çeşmeli ve Çetinkaya Bozkurt (2021) tarafından ele alınarak, işletmenin tedarikçileri arasından en iyisinin belirlenmesi sağlanmıştır [22]. Bu çalışmada, tedarikçi seçim sürecinde Analitik Hiyerarşi Süreci (AHP), TOPSIS ve çok amaçlı doğrusal olmayan programlama yöntemleri kullanılmış ve ürün kalitesi, defosuz ürün miktarı, iletişim kolaylığı gibi kriterlere göre en uygun tedarikçi belirlenmiştir. Bu yöntemlerin kullanımının karar verme sürecinin etkinliğini arttırdığı görülmüştür.

Ömürbek, Makas ve Ömürbek (2015), bir üniversitede kullanılmak üzere en uygun istatistiksel yazılımın belirlenmesi için çalışma yürütmüşlerdir [23]. Bu kapsamda, Analitik Hiyerarşi Süreci (AHP) ve TOPSIS yöntemleri kullanılmıştır. Çalışmada ilk olarak ana kriterler belirlenmiş ve bu ana kriterlerin altında alt kriterler belirlenerek kriterlerin değerlendirmeleri yapılmıştır.

Supçiller ve Çapraz (2011), bir oluklu mukavva kutu üreticisi için tedarikçi seçimi sorununu ele almıştır [24]. Çalışmada, çok kriterli karar verme yöntemlerinden AHP ve TOPSIS birlikte kullanılarak kalite, maliyet, teslimat ve hizmet ana kriterleri ile bunların alt kriterleri tanımlanmıştır.

Literatür taramasının sonucunda, gerçekleştirilen bu çalışmada firma çalışanları tarafından belirlenen kriterler, çok kriterli karar verme tekniklerinden TOPSIS metodu ile ağırlıklandırılmıştır. Bu sayede karar verme süreçlerinin karmaşıklığı önlenmeye çalışılmış ve verilen iki amaç fonksiyonuna göre sonuçlar elde edilmiştir.

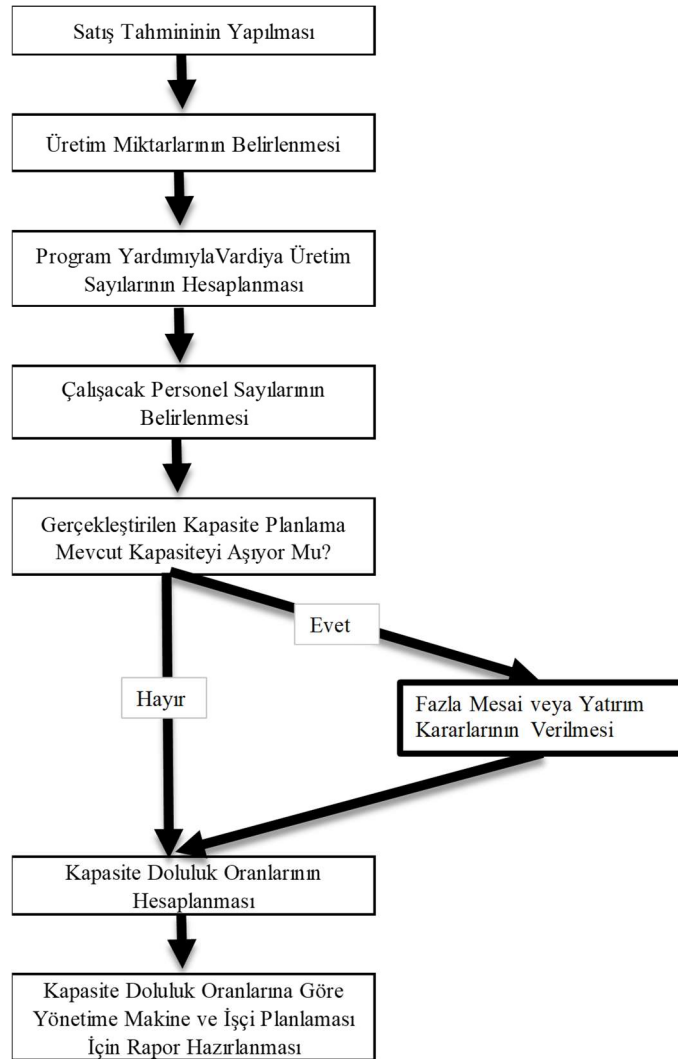
3. Uygulama

Bu çalışmada rulman üretimi yapılan bir firmada farklı amaçlar gözetilerek matematiksel model önerisi yapılmış ve uygulama gerçekleştirilmiştir. Alt bölümlerde mevcut durum analizi ve önerilen çok amaçlı matematiksel model anlatılmaktadır.

3.1. Mevcut durum analizi

Mevcut durumda rulman üretimi yapılan işletmede kapasite planlama için gerçekleştirilen çalışmalar Şekil 1'de verilmiştir. Mevcut durumda yıllık olarak müşteri talepleri doğrultusunda satış planı için ürün bazında üretim planları yapılmaktadır. Yapılan bu planlar ile her bir ürün için yıllık üretim miktarları belirlenmektedir. Üretim miktarlarının belirlenmesinden sonra ana imalat programı üzerinde çalışmalar yapılarak program yardımıyla her bir hat için, hattın bir günde kaç vardiya çalışarak gerekli üretimleri karşılayabileceği hesaplanmaktadır. Bu aşamadan sonra gerektiği takdirde yönetsel kararlar verilebilmektedir. Örneğin, normal mesainin yetmediği durumlarda fazla mesai kullanımı devreye girmektedir. Ancak fazla mesai ücretlerinin yüksek olması ve normal mesaiye dönülebilmesi durumunda

firma yatırım kararları da verebilmektedir.



Şekil 1. Kapasite planlama adımları

İşletmede mevcut durumda ana imalat programında yıllık kapasite planlaması, yılda iki defa olmak üzere altı ayda bir gerçekleştirilmektedir. Ürünlerin talep miktarları önceki senelerde gerçekleşen üretim miktarlarına göre yıllık olarak satış planında tahmin edilebilmektedir.

Firmada çalışan mühendisler tahmin edilen talep miktarlarını baz alarak, program yardımıyla manuel olarak ürün-hat eşleştirmelerini yapmaktadır. Bu işlem yaklaşık bir hafta kadar sürmektedir. Bu sebeple kapasite planlama çalışmaları bir yılda iki defadan fazla yapılamamaktadır. Ancak firma bu hesaplamaları belli dönemlerde yaparak kapasite planlamasını daha etkili kullanmak istemektedir. Ek olarak işlem manuel olarak gerçekleştirildiği için en iyi ürün-hat eşleşmesinin yapılıp yapılamadığı bilinmemekte ve yapılan kapasite planlama, çalışanların tecrübesine ve yorumuna göre farklılık gösterebilmektedir.

İşletmede sekiz saat olmak üzere günde üç vardiya aralıksız üretim gerçekleştirilmektedir. İşletmenin kurumsal kaynak planlaması programından alınan verilerle ve program yardımıyla her bir hattın günde kaç vardiya çalışarak yıllık ihtiyacı karşılayabileceği hesaplanmaktadır. Yapılan bu çalışmalarda tezgâh verimliliği, üretilen miktar ve bir vardiyada üretilen miktarlar çalışanlar tarafından bilinmektedir. Bu veriler ile ilgili hattın bir yılda kaç gün çalışması gerektiği, toplam kapasitesi ve günlük çalışması gereken vardiya sayısı hesaplanmaktadır.

İşletmede amaç ilk olarak fazla mesai yapılmadan, normal mesai süresinde tüm ürünlerin taleplerinin karşılanmasıdır. Bunun sebebi fazla mesai ücretlerinin normal mesai ücretlerinden yüksek olmasıdır. Normal mesai süresinin talebi karşılamaya yetmediği durumlarda fazla mesai sürelerinden yararlanılmaktadır. Bu kapsamda yapılan çalışmalardan 1 numaralı hat için örnek bir kesit Tablo.1’de verilmiştir. Tablo 1’de Ürün 15 ve Ürün 51 için üçüncü sütunda vardiya üretim miktarları, dördüncü sütunda yıllık üretim miktarları ve beşinci sütunda ise tezgah verimliliği bilgileri gösterilmiştir. Bu bilgiler sayesinde, parçaların üretimi için gereken ihtiyaç iş günü ve ihtiyaç vardiyalar hesaplanmaktadır.

Tablo 1. Mevcut durum örnek çalışma

Hat No	Parça Tanımı	Vardiya Üretim Miktarı	Yıllık Üretim Miktarı	Tezgah Verimliliği	İş günü	İhtiyaç işgünü	Yıllık Kapasite	Toplam işgünü	İhtiyaç vardiya
1	Ürün15	3600	2.750.000	%91	279,8	280	2.751.840	280	3,0
	Ürün51	3600	750	%91	0,1				

Her bir hat için hangi ürünlerin o hat üzerinde üretilebileceği bilinmektedir. Aynı biçimde, vardiya üretim miktarları daha önce yapılan çalışmalardan yararlanılarak vardiya üretim miktarı listesinden alınmaktadır. Bir iş günü üç vardiyadan oluşmaktadır. Yıllık üretim miktarları ise her bir hattın ilgili üründen bir yılda kaç adet üretebildiğini göstermekte ve imalat programından bu veri elde edilebilmektedir. Tezgâh verimliliği verisi ise işletme kapsamında kullanılan kurumsal kaynak planlaması programı sayesinde önceki yıllarda yapılan üretim ve kapasitelere göre hesaplanarak kullanılabilir. Bu veriler ile program yardımıyla yıllık üretim miktarı, iş günü ve ihtiyaç vardiya sayıları hesaplanmaktadır.

Bu kapsamda firmanın ihtiyacı gereği, ürün-hat eşleştirmelerinin hem optimum değerlerinin bulunabilmesi hem de bu işlemlerin mühendisler tarafından daha kısa sürede yapılabilmesi için matematiksel model oluşturulmuştur.

3.2. Çok amaçlı kapasite planlama modeli

Çalışma kapsamında, firmada mevcut durumda gerçekleştirilen orta dönem kapasite planlamasının farklı amaçlar göz önüne alınarak yapılması için çok amaçlı doğrusal programlama modeli önerilmiştir. Önerilen çok amaçlı matematiksel modelde ilk amaç çalışılan gün sayısının en küçüklenmesi, ikinci amaç ise ürünlerin özelliklerine göre parti büyüklüklerinin belirlenmesi ve stok durumlarının etkin bir biçimde yönetiminin gerçekleştirilmesidir. Bu amaçlar doğrultusunda matematiksel model oluşturulmuştur. Çalışma kapsamında önerilen matematiksel model gerçek bir sistem üzerinde yer alan varsayımlar, sistem kısıtları ve amaçlar doğrultusunda oluşturulmuş ve sisteme ait gerçek veriler elde edilerek çözümü gerçekleştirilmiştir.

3.2.1. Modele ilişkin varsayımlar

Rulman üretim fabrikasında yapılan çalışma kapsamında önerilen matematiksel modelde çalışmaların yapılabilmesi için bazı varsayımlar bulunmaktadır. Bu varsayımlar aşağıda belirtildiği gibidir:

1. Ana imalat programı kapsamında kapasite planlama yılda iki defa yapılmaktadır.
2. Yıllık çalışılan gün sayısı 280 gün olarak alınmaktadır.
3. Her bir hat bazında fazla mesai 50 günü aşmayacaktır.
4. Ürün-hat eşleştirmeleri yapılırken hangi hatlarda hangi ürünlerin üretilebileceği bilinmektedir.
5. Ürünler belirtilen talep miktarlarından daha az üretilemeyecektir.
6. Vardiya üretim miktarı (VÜM), bir vardiyada (8 saat) %100 verimle ilgili hattın ilgili üründen üretebilme miktarıdır ve önceki çalışmalardan bu miktarlar hat bazında bilinmektedir.
7. Tezgâh verimlilikleri işletmede kullanılan kurumsal kaynak planlaması programı sayesinde önceki yıllardaki performanslara bakılarak hesaplanabilmektedir.

8. Hatlara ürün atamaları yapılırken hazırlık süreleri de dikkate alınacak ve her ürün değişiminde hazırlık süresi 1 vardiya olarak toplam süreye eklenecektir. Eğer ilgili hatta tek bir ürün üretimi yapılıyorsa o hatta hazırlık süresi hesaplanmayacaktır.

9. Çalışma kapsamında montaj aşamasındaki ürün-hat eşleşmeleri ile ilgili çalışılacaktır.

Çalışma kapsamında, montaj aşamasında seçilen 72 ürün ve 40 hat için ürün-hat eşleşmeleri üzerinde çalışılmıştır. Önerilen modelde, firmaya ait genel kısıtlar talep ve kapasite kısıtlarıdır. Buna ek olarak modelde parti büyüklüklerinin belirlenerek bu partilerin üretim sıralarının bulunması amacı ile ek kısıtlar bulunmaktadır. Çok amaçlı matematiksel model için iki amaç bulunmaktadır. Önerilen matematiksel modelde kullanılan indisler, parametreler ve karar değişkenlerine ilişkin tanımlamalar aşağıda verilmektedir.

İndisler

i, k ürünler $i, k \in \{1, \dots, n\}$

j hatlar $j \in \{1, \dots, m\}$

t üretim sırası $t \in \{1, \dots, p\}$

Parametreler

A_i i . ürünün bir yıllık talep miktarı

M Çok büyük bir sayı

Nm Her bir hat için normal mesai süresi

Fm Her bir hat için fazla mesai süresi

C Fazla mesai katsayısı

k_i i . ürün için hesaplanan kriter puanı

a_{ij} i . ürünün j . hattaki birim üretim süresi

Karar Değişkenleri

Z_{ijt} i . ürünün j . hatta t . sıradaki üretim parti miktarı

X_j j . hatta üretim yapılan toplam gün sayısı

Y_j j . hattın yıllık çalıştığı fazla mesai gün sayısı

$A_{ijt} \begin{cases} i. \text{ ürün } j. \text{ hatta } t. \text{ sırada üretilirse } 1, \\ \text{Diğer durumlarda } 0. \end{cases}$

$W_{ikjt} \begin{cases} i. \text{ üründen } k. \text{ ürüne } j. \text{ hatta } t. \text{ sırada geçiş yapılıyorsa } 1, \\ \text{Diğer durumlarda } 0. \end{cases}$

$P_{ijt} \in \{0, 1\}$, yardımcı değişken

3.2.2. Önerilen modele ilişkin amaç fonksiyonları

Çok amaçlı matematiksel model için iki amaç belirlenmiştir. Birinci amaç fonksiyonu toplam çalışılan gün sayısının en küçüklenmesidir. Eş. (1) ile gösterilen bu amaç fonksiyonunda hedef normal mesai ve fazla mesai ile geçirilen toplam sürenin en küçüklenmesidir. Burada fazla mesai için ayrılan sürenin en küçüklenmesi için bir ceza katsayısı bulunmaktadır. Böylelikle hatların doluluk oranlarının artırılarak fazla mesai süresine ihtiyaç duyulması durumunda en az sürenin kullanılması sağlanmaktadır. Ayrıca ürün geçişlerinde gerçekleşen hazırlık süresinin de en küçüklenmesi hedeflenmiştir.

$$Z \min = \sum_j X_j + C \sum_j Y_j + 0.33 \sum_i \sum_k \sum_j \sum_t W_{ikjt} \quad (1)$$

İkinci amaç fonksiyonu ise ürünlerin belirli kriterler göz önüne alınarak ürün özelliklerinin belirlenmesi ve bu özelliklere göre parti büyüklüklerinin belirlenerek üretimlerinin gerçekleştirilmesidir. Buradaki amaç,

ürünlerin müşteriler tarafından talep edilmemesi durumunda ürünlerin elde kalma riskini azaltmak ve stokların etkinliğini artırmaktır.

Bu çalışmada, ürünler farklı kriterlere göre değerlendirilmiş ve ürünlerin elde atıl olarak kalmasının engellenmesi hedeflenmiştir. Böylelikle riskli ürünlerin üretimi az sayıda partiler halinde üretilecek, ürünün talep edilmemesi durumunda stokta kalması engellenebilecektir. Ancak talep durumu belirli ve riskli olmayan ürünler tek seferde üretilerek talep karşılanacak ve diğer yandan hazırlık süresi ve toplam gün sayısı en küçüklenebilecektir. Bu amaç sayesinde sadece üretim ve hazırlık maliyetleri değerlendirmemiş olacak ve ayrıca ürünlerin riskli olmalarından kaynaklanacak maliyetlerinde önüne geçilmiş olunacaktır.

İkinci amaç fonksiyonu için öncelikle ürünlerin risk durumlarını belirlemek amacı ile kriterler belirlenmiş ve bu kriterlere göre puanlamaları yapılmıştır. Belirlenen kriterler aşağıda açıklanmaktadır.

- **Frekans (Süreklilik):** İlgili ürünün son bir yıldaki alım miktarını ifade eder. 0-12 ay arasında bir değerdir. Frekansın yüksek olması ürünü alacak olan müşterinin talebinin yüksek olduğu ve ürünün stokta kalma riskinin düşük olduğu anlamına gelmektedir.
- **Görünürlük (Planlama Ufku):** İlgili ürün için gelecekteki talep tahminine göre elde edilen değerdir. 0-6 ay arasında değer almaktadır. Talep tahmininin yüksek olması ilgili ürünün bölünerek üretilmesine gerek olmadığı, müşteri tarafından ilgili talep tahmini döneminde alınacağını ifade etmektedir.
- **Ürün Durumu:** İlgili ürünün standart veya özel bir ürün olduğunu ifade eder. Standart ürün tüm müşteriler tarafından talep edilebilirken, özel ürünler müşteri bazlı olarak üretilir. Standart ürün "1" olarak, özel ürün ise "0" olarak ifade edilmiştir. Ürünün standart olması, stokta kalsa bile başka bir müşteri tarafından satın alınabileceğini göstermektedir. Ürünün özel olması ise, müşteriye özel üretim olduğunu ve müşteri almazsa stokta kalacağı anlamına gelmektedir.

Ürün bazlı kriter puanlarının belirlenmesinde TOPSIS yönteminden yararlanılmıştır. TOPSIS çok kriterli karar verme problemlerini çözmede kullanılan yaygın bir yöntemdir. Bu yöntem, alternatifleri ideal çözüme ve negatif ideal çözüme olan uzaklıklarına göre sıralar. TOPSIS, alternatiflerin sıralanmasında tamamen sayısal verilere dayanır. Bu sayede, subjektif yorumlardan ve kişisel önyargılardan kaçınılır. Yöntem, objektif bir değerlendirme sağlar. TOPSIS, en iyi ve en kötü çözümün belirlenmesini sağlayarak, karar vericilerin her alternatifin ideal çözüme ne kadar yakın olduğunu net bir şekilde görmelerine yardımcı olur. Bu, karar vericilerin daha bilinçli tercihler yapmasını sağlar. TOPSIS yöntemi, karar vericilere hızlı, objektif ve çok yönlü analizler yapma imkânı sağlar. Ayrıca, büyük veri setleriyle çalışırken işlem kolaylığı, kriterlerin esnek şekilde değerlendirilmesi ve alternatiflerin net sıralanması gibi faktörler bu yöntemi cazip kılar.

TOPSIS yöntemi için öncelikle ürünlerin özelliklerini yansıtacak kriterler firma yetkililerinin yardımıyla belirlenmiştir. Çalışma kapsamında kriter puanları hesaplanırken aşağıdaki TOPSIS adımları takip edilmiştir. İlk olarak ürünler için performans kriterlerinin değerleri fabrikadaki yetkiler ile belirlenmiştir. Bu sayede karar matrisi oluşturulmuştur. Tablo 2’de örnek ürünler için belirlenen kriter değerleri verilmiştir.

Tablo 2. Ürünlere ilişkin kriter değerleri

Parça Tanımı	Talep Miktarı	Frekans	Planlama Ufku	Ürün Durumu
Ürün 30	720000	11	6	0
Ürün 31	420000	6	2	0
Ürün 32	78000	12	2	1
Ürün 33	510000	12	6	1
Ürün 34	130000	12	6	1
Ürün 35	0	12	6	1
Ürün 36	190000	12	6	1

Performans kriterlerinin değerleri ürün bazlı belirlendikten sonra bu verilen değerler Eş. (2)'ye göre normalize edilerek normalize matris elde edilmiştir.

$$r_{ij} = \frac{x_{ij}}{\sqrt{\sum_{j=1}^n x_{ij}^2}} \quad (2)$$

Sonraki adımda ağırlıklandırılmış normalize matrisin elde edilmesi için kriterler için firma yetkilileri ile ağırlıklar belirlenmiş (Frekans için 0.5, planlama ufku için 0.2 ve ürün durumu için 0.3) ve bu ağırlıklar ile normalize matris değerleri çarpılarak ağırlıklandırılmış normalize matris elde edilmiştir. Bu yöntemde her alternatifin yakınlık indeksi hesaplanılarak alternatiflerin sıralaması yapılır. Bu, alternatifin ideal çözümlerle olan yakınlığına ve negatif ideal çözümlerle olan uzaklığına dayanır. Bu uzaklıklar yardımı ile sıralamanın yapılabilmesi için ürünlerin ideal ve negatif ideal çözümlere olan uzaklıkları hesaplanmış ve buna göre her bir ürün için kriter puanları hesaplanmıştır. Toplam 72 adet ürün için hesaplanan kriter puanları Tablo 3'te verilmiştir.

Tablo 3. Ürün bazlı kriter puanları

Parça	Kriter Puanı	Parça	Kriter Puanı	Parça	Kriter Puanı	Parça	Kriter Puanı
Ürün 1	0.2280	Ürün 19	0.6273	Ürün 37	0.1124	Ürün 55	0.2465
Ürün 2	0.7556	Ürün 20	0.7043	Ürün 38	0.8728	Ürün 56	0.6414
Ürün 3	0.8098	Ürün 21	0.5761	Ürün 39	0.8448	Ürün 57	0.7649
Ürün 4	0.7391	Ürün 22	0.8540	Ürün 40	0.5081	Ürün 58	0.7771
Ürün 5	0.8098	Ürün 23	0.7499	Ürün 41	0.1124	Ürün 59	0.6414
Ürün 6	0.7043	Ürün 24	0.5761	Ürün 42	1.0000	Ürün 60	0.1779
Ürün 7	0.2280	Ürün 25	0.0000	Ürün 43	0.1124	Ürün 61	0.1500
Ürün 8	0.8554	Ürün 26	0.5314	Ürün 44	0.6152	Ürün 62	0.1249
Ürün 9	0.8098	Ürün 27	0.0000	Ürün 45	0.7915	Ürün 63	0.2041
Ürün 10	0.5761	Ürün 28	0.0000	Ürün 46	0.9208	Ürün 64	0.1500
Ürün 11	0.7570	Ürün 29	0.0000	Ürün 47	0.6189	Ürün 65	0.7771
Ürün 12	0.8448	Ürün 30	0.0569	Ürün 48	0.4249	Ürün 66	0.1124
Ürün 13	0.7391	Ürün 31	0.8448	Ürün 49	0.8952	Ürün 67	0.1124
Ürün 14	0.5636	Ürün 32	0.7069	Ürün 50	0.6189	Ürün 68	0.1124
Ürün 15	0.0000	Ürün 33	0.1124	Ürün 51	0.9600	Ürün 69	0.1124
Ürün 16	0.2840	Ürün 34	0.1124	Ürün 52	0.8448	Ürün 70	0.1124
Ürün 17	0.2840	Ürün 35	0.1124	Ürün 53	0.8126	Ürün 71	0.1124
Ürün 18	0.0000	Ürün 36	0.1124	Ürün 54	0.3497	Ürün 72	0.1124

Tablo 3'te verilen kriter puanlarına göre yüksek çıkan kriter puanlarına sahip ürünler bölünerek üretilmek istenirken, düşük kriter puanına sahip ürünler ideal ürün olmaya yakındır ve bölünmeden üretilbilirler. Yani yüksek kriter puanına sahip ürünler kritik parçalardır ve sipariş verilmediği zaman elde stok olarak kalma riski olan ürünlerdir. TOPSIS yönteminin uygulanması sonucunda ürünlere ilişkin elde edilen kriter puanları ikinci amaç fonksiyonu için kullanılmıştır. Eş. (3) ile verilen amaç fonksiyonunda k_i ile gösterilen değerler kriter puanlarını oluşturmaktadır. Burada yüksek kriter puanına sahip ürünler yani elde kalma olasılığı yüksek olan ürünlerin küçük partiler halinde üretilmesi için ilgili karar değişkeni ile çarpımlarının toplamlarının enbüyüklenmesi hedeflenmiştir. Böylelikle riskli ürünler tek seferde değil, birden fazla partide üretilecek ve tahmin edilen üretim miktarları bir defa da karşılanmamış olacaktır.

$$Z \max = \sum_i \sum_j \sum_t k_i A_{ijt} \quad (3)$$

3.2.3. Önerilen çok amaçlı matematiksel model

Yukarıda verilen varsayımlar, tanımlamalar, sistem kısıtları ve açıklanan amaç fonksiyonlarına göre çalışmada önerilen çok amaçlı doğrusal programlama modeli aşağıda verilmiştir. Verilen model çok amaçlı bir modeldir ve amaçların tek bir amaç fonksiyonunda birleştirilmesi için Ağırlıklı Toplam Yöntemi kullanılmıştır. Ağırlıklı Toplam Yöntemi ile elde edilen amaç fonksiyonu Eş. (4)'de verilmiştir. Bu yöntemde, birleştirilmiş amaç fonksiyonu, amaç fonksiyonlarının önem derecelerine karşı gelen ağırlıklar ile çarpılarak toplanması ile elde edilmektedir. Amaç fonksiyonlarının değerlerinin birbirinden farklı birimlere sahip olması nedeni ile toplanabilmesi için öncelikle normalize edilmesi gerekmektedir. Burada Verilen denklemde $f_i min$ değeri i . amaç fonksiyonu değerinin en küçük değeri, $f_i max$ değeri ise ilgili amaç fonksiyonunun en büyük değeridir.

$$\text{Amaç fonksiyonu} \\ \text{Min } z = \omega_1 \left(\frac{f_1(x) - f_1 min}{f_1 max - f_1 min} \right) + \omega_2 \left(\frac{f_2 max - f_2(x)}{f_2 max - f_2 min} \right) \quad (4)$$

Kısıtlar

$$\sum_j \sum_t Z_{ijt} \geq A_i, \forall i \quad (5)$$

$$\sum_i \sum_t a_{ij} Z_{ijt} \leq Nm + Fm, \forall j \quad (6)$$

$$X_j \leq Nm, \forall j \quad (7)$$

$$Y_j \leq Fm, \forall j \quad (8)$$

$$\sum_i \sum_k W_{ikjt} \leq 1, i \neq k; \forall j, t \quad (9)$$

$$\sum_i A_{ijt} + \sum_k A_{kjt} - \sum_i \sum_k W_{ikjt} \leq 1, i \neq k; \forall j, t \quad (10)$$

$$\sum_i A_{ijt} + \sum_k A_{kjt} \leq 1, i \neq k; \forall j, t \quad (11)$$

$$\sum_i A_{ijt} - \sum_i A_{ij(t+1)} \geq 0, \forall j, t \quad (12)$$

$$Z_{ijt} + M P_{ijt} \leq M, \forall i, j, t \quad (13)$$

$$A_{ijt} + M P_{ijt} \geq 1, \forall i, j, t \quad (14)$$

$$A_{ijt} \leq Z_{ijt}, \forall i, j, t \quad (15)$$

$$Z_{ijt} \geq 0, \forall i, j, t \quad (16)$$

$$A_{ijt} \in \{0, 1\}, \forall i, j, t \quad (17)$$

$$W_{ikjt} \in \{0, 1\}, \forall i, k, j, t \quad (18)$$

$$P_{ijt} \in \{0, 1\}, \forall i, j, t \quad (19)$$

Eş. (5) talep kısıtıdır ve bu kısıt kapsamında ürün bazında hatlarda üretilecek toplam miktar talep edilen miktarın altında kalmayacaktır. Eş. (6)'da hat bazında üretilen ürünlerin toplam üretim günü, normal mesai ve fazla mesai günlerinin toplamından fazla olmayacaktır. Eş. (7)'de çalışılabilecek gün sayısının belirtilen normal mesai gün sayısını aşamayacağı ve Eş. (8)'de ise çalışılabilecek fazla mesainin belirtilen gün sayısını aşamayacağı belirtilmiştir. Eş. (9)'da hat içerisinde aynı sıraya aynı anda birden fazla ürünün atanması engellenmektedir. Eş. (10), A_{ijt} ile W_{ikjt} değişkenleri arasındaki tutarlılığı garanti etmektedir. Hat bazında atanacak ürünlerin her bir sıra için 1'den az olması Eş. (11) ile garanti edilmiştir. Eş. (12) hatta atanan ürünlerin sıralamasının düzgün bir biçimde ilerlemesini sağlar. Eğer hat boş kalacaksa bunu planlama ufkunun sonuna yerleştirme sağlanır. Eş. (13)-(15) A_{ijt} ve Z_{ijt} değişkenleri arasındaki ilişkiyi sağlamaktadır. Eş. (16)-(19) ise karar değişkenlerine ait işaret kısıtlarıdır.

3.3. Deneysel sonuçlar

Önerilen çok amaçlı matematiksel modelin çözümü için CPLEX 22.1.1 kullanılmıştır. Kullanılan ağırlıklandırma metodunda farklı ağırlıklar ile çözümler elde edilmiştir. 19 farklı ağırlık ile model çalıştırılmış ve Pareto optimal çözümler elde edilmiştir. Kullanılan amaç fonksiyonu ağırlıkları Tablo 4'te belirtilmiştir.

Tablo 4. Ağırlıklı toplam yönteminde kullanılan ağırlıklar

Amaç Fonksiyonu-1	Amaç Fonksiyonu-2
0.95	0.05
0.90	0.10
0.85	0.15
0.80	0.20
0.75	0.25
0.70	0.30
0.65	0.35
0.60	0.40
0.55	0.45
0.50	0.50
0.45	0.55
0.40	0.60
0.35	0.65
0.30	0.70
0.25	0.75
0.20	0.80
0.15	0.85
0.10	0.90
0.05	0.95

Ayrıca kriterlere ilişkin uygun ağırlıkların elde edilmesi için farklı TOPSIS ağırlıkları verilerek çözümler elde edilmiştir. Bölüm 3.2.2’de TOPSIS yönteminin uygulanması sırasında kriterler için verilen ağırlık değerleri değiştirilerek farklı problemlerin çözümü gerçekleştirilmiştir. Böylelikle hem amaç fonksiyonu ağırlıklarının değişimi hem de TOPSIS ağırlıklarının değişimi ile toplamda 285 problemin çözümü gerçekleştirilmiştir. TOPSIS ağırlıkları belirlenirken süreklilik kriterinin en önemli kriter olduğu, görünürlük kriterinin ise bu kriterler arasında en az önemli kriter olduğu firma yetkilileri tarafından belirlenmiştir. TOPSIS çalışmasında kullanılan ağırlıklar Tablo 5’te verilmiştir.

Tablo 5. TOPSIS ağırlıklar

No	Süreklilik	Ürün Durumu	Görünürlük
1	0.90	0.05	0.05
2	0.85	0.10	0.05
3	0.80	0.10	0.10
4	0.75	0.15	0.10
5	0.70	0.20	0.10
6	0.65	0.20	0.15
7	0.60	0.20	0.20
8	0.60	0.30	0.10
9	0.55	0.25	0.20
10	0.50	0.30	0.20
11	0.50	0.40	0.10
12	0.45	0.35	0.20
13	0.40	0.40	0.20
14	0.40	0.30	0.30
15	0.35	0.35	0.30

Elde edilen sonuçlara göre yüksek ağırlıkta olan amaç fonksiyonuna göre ürünlerin parti büyüklüklerinin değiştiği görülmüştür. Tablo.10’da verilen örnekte olduğu gibi, modelin birinci amaç fonksiyonununun 0.95,

ikinci amaç fonksiyonunun 0.05 olduğu bir durumda elde edilen sonuçlara göre 14. ürünün 13. hatta 2170000 adet tek seferde üretildiği görülmüştür. Ancak birinci amaç fonksiyonunun 0.05, ikinci amaç fonksiyonunun 0.95 olduğu durumda ise 14. ürünün 13 ve 19. hatlara sırasıyla 944833 ve 1225167 adet olmak üzere iki parti şeklinde üretildiği görülmüştür. Buna göre ikinci amaç fonksiyonuna verilen ağırlığın artması durumunda yani ürünlerin kritiklik durumuna göre amaç fonksiyonu ağırlığı arttığında kritik olan ürünlerin küçük partiler halinde üretimi sağlanmıştır. Katsayı değişimi ile elde edilen bazı örnek parti büyüklüğü değişiklikleri Tablo 6'da paylaşılmıştır.

Tablo 6. Örnek üretim miktarı değişimleri

Amaç Fonk-1	Amaç Fonk-2	Ürün	Hat	Üretim Miktarı
0.95	0.05	14	13	2170000
0.05	0.95	14	13	944833
0.05	0.95	14	19	1225167
0.95	0.05	21	18	570000
0.05	0.95	21	4	467700
0.05	0.95	21	18	102300
0.95	0.05	31	4	420000
0.05	0.95	31	4	210850
0.05	0.95	31	18	209150
0.95	0.05	41	20	2522522
0.95	0.05	41	28	2767478
0.05	0.95	41	6	55450
0.05	0.95	41	20	2522522

Birden fazla birbiriyle çelişen amaç fonksiyonuna sahip modellerde Pareto optimal çözümler elde edilir. Elde edilen bu çözümlerin karşılaştırılması için çeşitli performans değerlendirme kriterleri kullanılır. Bu çalışmada elde edilen çözümlerin değerlendirilmesi için kullanılan performans kriterleri aşağıda açıklanmıştır.

Pareto optimal çözüm oranı (Ratio of Pareto Optimal Solutions-Rpos), her bir Pareto cephesi kapsamında sunulan çözümlerin sayısının toplam elde edilen çözüme oranını göz önüne almaktadır. Pareto çözüm oranı ne kadar yüksek olursa, çözüm yöntemi o kadar tercih edilebilir olacaktır. Ortalama ideal uzaklık (Mean Ideal Distance-MID) metriği Pareto çözümlerinin ideal noktadan ortalama uzaklığını hesaplamak için kullanılmaktadır ve Eş. (20)'de verildiği gibi hesaplanmaktadır. Bu metrik ne kadar az olursa, yöntem verimliliği de o kadar yüksek olacaktır [21].

$$MID = \sum_{i=1}^n \sqrt{\frac{(f_{1,i} - f_1^{best})^2}{(f_{1,total}^{max} - f_{1,total}^{min})^2} + \frac{(f_{2,i} - f_2^{best})^2}{(f_{2,total}^{max} - f_{2,total}^{min})^2}}{n}} \quad (20)$$

Aralık (Spacing Metric-SM) metriği çözümlerin çözüm uzayındaki dağılımını gösterir ve Eş. (21)'de gösterildiği gibi hesaplanır. Burada d_i çözüm uzayındaki iki Pareto optimal çözüm arasındaki Öklid mesafesidir. \bar{d} ortalama mesafeyi ve n toplam Pareto optimal sayısını ifade etmektedir. SM değeri ne kadar küçük olursa yöntemin performansı o kadar iyi olmaktadır [22].

$$d_i = \sqrt{(f_{2,i+1} - f_{2,i})^2 + (f_{1,i+1} - f_{1,i})^2}$$

$$SM = \frac{\sum_{i=1}^{n-1} |\bar{d} - d_i|}{(n-1)\bar{d}} \quad (21)$$

Çeşitlendirme (Diversification Metric-DM) metriği Pareto optimal çözümlerin çeşitliliğini göstermektedir.

Bu değer ne kadar büyük elde edilirse çözümler o kadar çeşitlenir ve Eş. (22)'de verildiği gibi hesaplanmaktadır. Burada m değeri amaç fonksiyonu sayısını ifade etmektedir [22].

$$DM = \sqrt{\sum_{m=1}^2 (\max f_m^i - \min f_m^i)^2} \quad (22)$$

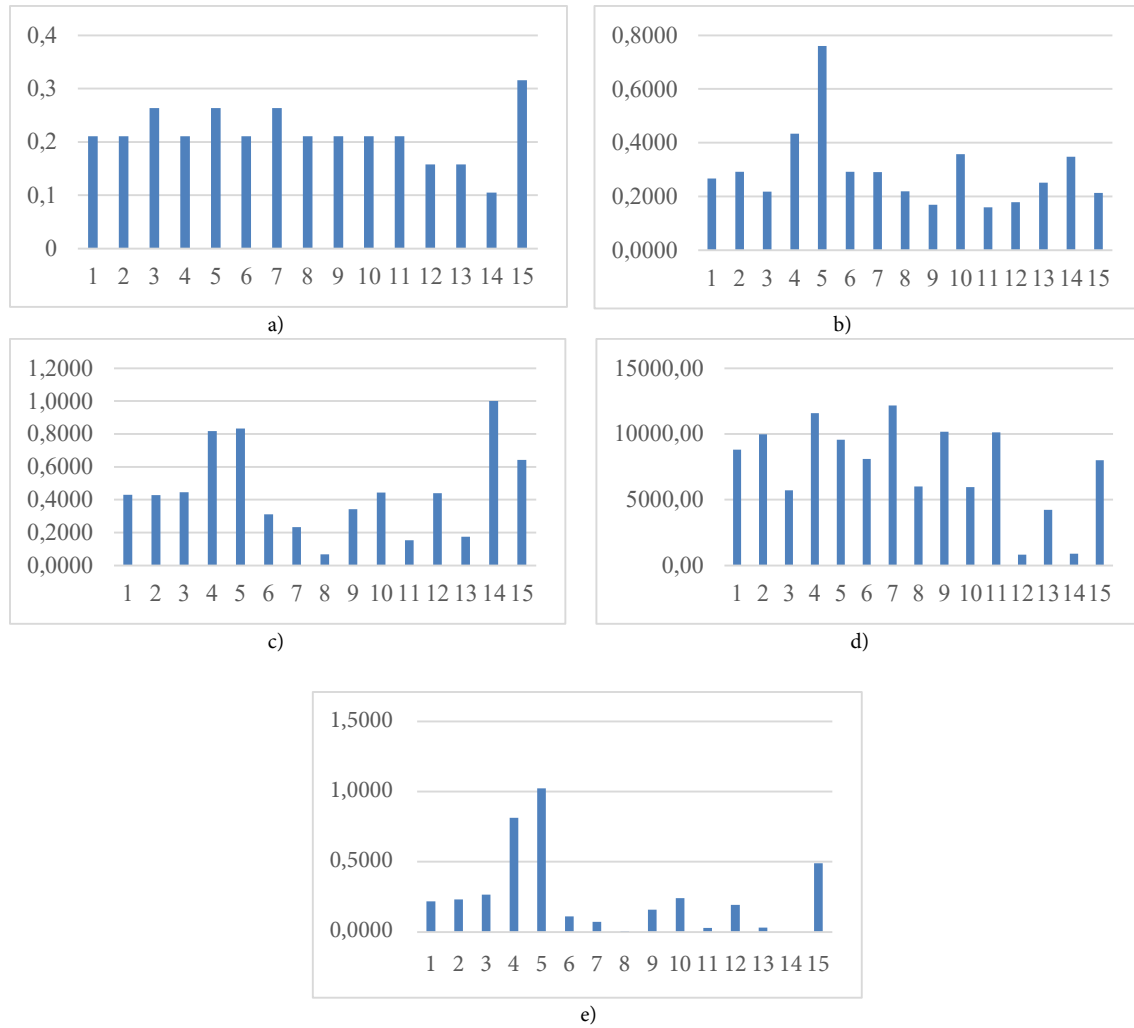
Pareto cephesinin tekdüzelığı (Non-uniformity of Pareto Front-NPF) metriğinde Pareto cephesinin düzensizliği ne kadar düşük olursa, tekdüzelik o kadar büyük olmakta ve dolayısıyla çözüm yönteminin daha fazla tercih edilir olmasını sağlamaktadır. Eş. (23)'de Pareto cephesinin tekdüzelığının hesaplanması gösterilmiştir [22].

$$NPF = \sqrt{\frac{\sum_i (\frac{d_i}{d} - 1)^2}{n-1}} \quad (23)$$

Elde edilen 285 adet çözüm sonucunda farklı performans kriterleri ile çözümler karşılaştırılmıştır. Burada karar vericinin hangi amaca yönelmek istediğine bağlı olarak uygun kriter ağırlıklarının belirlenmesi ve karar vericiye sunulması hedeflenmiştir. Tablo 7'de her bir ağırlık değerine ilişkin belirtilen metriklerden elde edilen sonuçlar yer almaktadır. Bu tabloda her satır, mevcut problem için kullanılan TOPSIS ağırlıklarını temsil etmektedir. Sütunlarda ise kullanılan performans değerlendirme metriklerinin sonuçları yer almaktadır. Performans değerlendirmesinde kullanılan metriklerin sonuçlarının incelenebilmesi için ayrı ayrı beş adet çubuk grafiği Şekil 2'de paylaşılmıştır.

Tablo 7. Elde edilen çözümlerin performans kriterlerine göre sonuçları

Ağırlık	Rpos	MID	SM	DM	NPF
1	0.2105	0.2663	0.4299	8798.12	0.2175
2	0.2105	0.2915	0.4281	9971.00	0.2309
3	0.2632	0.2176	0.4451	5709.22	0.2659
4	0.2105	0.4330	0.8182	11574.00	0.8122
5	0.2632	0.7603	0.8334	9550.20	1.0219
6	0.2105	0.2920	0.3111	8095.25	0.1095
7	0.2632	0.2907	0.2330	12172.00	0.0713
8	0.2105	0.2190	0.0674	6012.04	0.0057
9	0.2105	0.1694	0.3422	10178.00	0.1575
10	0.2105	0.3573	0.4435	5947.01	0.2402
11	0.2105	0.1592	0.1538	10118.00	0.0282
12	0.1579	0.1783	0.4392	828.87	0.1929
13	0.1579	0.2517	0.1755	4220.09	0.0308
14	0.1053	0.3481	1.0000	907.32	-
15	0.3158	0.2134	0.6414	8012.20	0.4894



Şekil 2. Kriter karşılaştırma grafikleri a) Pareto çözüm oranı, b) MID, c) SM, d) DM, e)NPF

Kapasite planlama problemi kapsamında çok amaçlı bir model ile çalışılmıştır. İlk amaç toplam çalışılan gün sayısını en küçükmek isterken, ikinci amaç fonksiyonunda ise belirlenen frekans, görünürlük ve ürün durumu olmak üzere üç adet performans kriteri doğrultusunda, kriter puanı yüksek olan ürünlerin bölünerek üretilmesi sağlanmıştır. Bu durumda ürünler bölünerek üretildiğinde hazırlık süreleri artacağı için çalışılan gün sayısı da arttırılmış olacaktır ve amaç fonksiyonları arasında bir ödünleşme söz konusudur.

Problem kapsamında elde edilen Pareto optimal sonuçlar ve kriterlere göre bu sonuçların karşılaştırmalı grafikleri Şekil-2'de paylaşılmıştır. Paylaşılan metriklerden Şekil-2(a)'da Pareto çözüm oranları verilmiş ve oransal olarak daha yüksek olan ağırlıklar tercih edilebilir olacaktır. Bu kapsamda TOPSIS ağırlıkları frekansın 0.6, görünürlüğün 0.2, ürün durumunun 0.2 olduğu durum diğer ağırlıklara göre daha çok tercih edilebilir konumdadır. Şekil-2(b)'de MID metriğine göre her bir Pareto optimal çözüm grubu için ideal noktaya yani en iyi amaç fonksiyonu değerine olan uzaklıklar hesaplanmıştır. Metrik değerinin az olması çözümün performansının iyi olduğunu gösterdiği için frekans kriterinin 0.35-0.55 aralığında, görünürlük kriterinin 0.10-0.30 aralığında ve ürün durumu kriterinin 0.25-0.40 değerleri aralığında olan ağırlıkların diğer durumlara göre daha verimli olduğu söylenebilmektedir. Şekil-2(c) SM metriği kapsamında Pareto optimal çözümlerin çözüm uzayındaki dağılımlarını göstermektedir. Metrik ne kadar düşük olursa yöntemin performansı da o kadar iyi olmaktadır. Problem kapsamında hesaplanan ağırlıklara göre en iyi sonucu veren ağırlıkların frekans kriteri için 0.40-0.60, görünürlük için 0.10-0.40 ve ürün durumu için 0.20-0.40 aralığında olan ağırlıklar olduğu görülmektedir. Şekil-2(d) DM metriğine göre Pareto optimal çözümlerin çeşitliliği hakkında bilgi vermektedir. Metrik büyüdükçe çözümler çeşitlenmektedir ve buna göre frekans kriteri için 0.50-0.75, görünürlük için 0.10-0.20 ve ürün durumu için 0.15-0.25 aralıklarında bulunan ağırlıklarda daha

iyi sonuç verdiği söylenebilmektedir. Son olarak Şekil-2(e)'de NPF metriğine ait sonuçlar yer almaktadır. Pareto cephesinin düzensizliğinin düşük olması, tekdüzeliği arttırmakta ve dolayısıyla çözüm yönteminin daha fazla tercih edilir olmasını sağlamaktadır. Pareto optimal çözümler sonucunda elde edilen en iyi NPF değerleri frekans kriteri için 0.40-0.60, görünürlük için 0.10-0.40 ve ürün durumu için 0.20-0.40 aralığındaki ağırlıklar vermektedir. Her bir metrik için elde edilen en iyi sonuçlar belirli aralıklar verilerek sunulmuştur.

Hesaplanan sonuçlar doğrultusunda bazı ağırlık değerlerinin diğerlerine göre hem metrikler bazında hem de genel bir Pareto analizi yapıldığında daha iyi sonuçlar verdiği gözlemlenmiştir. Bu durumda karar verici durumundaki firma çalışanları hem amaç fonksiyonları hem de TOPSIS kriterleri bazında hangi ağırlıklar şirket politikasına daha uygun ise ona göre karar verebileceklerdir. Bu sayede en iyi ürün-hat eşleşmesi elde edilebilecek ve ürünlere ait parti büyüklüğü belirlenebilecektir. Buna ek olarak firmada bu çalışmanın yapılmasının mühendislerin bir haftadan fazla süresini aldığı bilinmektedir. Bu durumda aynı çalışma için, gerekli parametreler ayarlandıktan sonra, dakikalar içinde sonuç alınabilecektir ve zaman açısından büyük bir iyileştirme sağlanacaktır.

4. Sonuçlar ve Değerlendirme

Kapasite planlama firmaların rekabetinde büyük bir öneme sahiptir. Firmalar kapasite planlamalarını ne kadar doğru yapabilirse diğer firmalarla rekabette o kadar öne çıkabilmektedirler. Bu çalışma kapsamında rulman üretimi yapılan bir firmada orta dönem kapasite planlama çalışması yapılmıştır. Firmada mevcut durumda kapasite planlama çalışma manuel olarak yapılmaktadır. Bu durumda yapılan kapasite planlama, mühendisin deneyimine bağlı olarak değişiklik göstermektedir ve en iyi sonucun elde edilip edilemediği bilinmemektedir. Ayrıca program ile yapılan bu çalışma mühendislerin yaklaşık bir haftalık süresini almaktadır. Bu sebeple yapılan kapasite planlama çalışmaları bir yılda iki defadan fazla yapılamamaktadır.

Çalışma kapsamında orta dönem kapasite planlama problemi doğrusal programlama yaklaşımıyla çözülmüştür. Gerçek hayatın doğası gereği aynı anda birbiriyle çelişen birden çok amaç olabileceği göz önünde bulundurularak, çalışmada çok amaçlı bir programlama yapılmıştır. Birinci amaç fonksiyonu üretim için gereken toplam çalışılacak gün sayısını en küçüklerken, ikinci amaç fonksiyonu ise müşterilerin güvenilirlikleri, ürünlerin gelecekteki üretim öngörülebilirlikleri ve üretilecek ürünlerin standart ve özel olmasına göre üretim planlarını belirlemek için kullanılmıştır.

Çalışmada her bir ürün için farklı kriter puanları belirlenmiş ve ürünlerin özellikleri değerlendirilerek elde edilmiş olarak kalmasının engellenmesi hedeflenmiştir. Böylelikle kriter puanı yüksek olan ürünlerin üretimi az sayıda partiler halinde üretilecek, ürünün talep edilmemesi durumunda stokta kalması engellenebilecektir. Ancak talep durumu belirli ve kriter puanı düşük olan ürünler tek seferde üretilerek talep karşılanacak ve öte yandan hazırlık süresi ve toplam gün sayısı en küçüklenebilecektir. Bu amaç sayesinde sadece üretim ve hazırlık maliyetleri değerlendirmemiş olacak ve ayrıca ürünlerin riskli olmalarından kaynaklanacak maliyetlerinde önüne geçilmiş olacaktır.

Çalışmada genel kapasite planlama kısıtlarına ek olarak bazı kısıtlar belirlenmiş ve matematiksel model çok amaçlı olarak oluşturulmuştur. Modelin çözümü sonucunda Pareto optimal çözümler elde edilmiş ve bu çözümler Pareto çözüm oranı, ortalama ideal uzaklık, aralık, çeşitlendirme ve Pareto cephesinin tekdüzeliği olmak üzere beş farklı metrik ile performansları açısından değerlendirilmiştir. Bu aşamadan sonra firmadaki mühendisler firma için en uygun ağırlıkları seçerek sonuçları mevcut duruma göre çok kısa bir sürede elde edebileceklerdir.

Gelecek çalışmalarda, çalışmadaki problemin geliştirilmesi kapsamında mevcut durumda kurulmuş olan modele maliyet, karlılık gibi ek amaç fonksiyonları eklenebilir ve modelin vereceği sonuçlar değerlendirilebilir. Ek olarak, belirlenen performans kriterleri genişletilebilir ve problemin doğrusal olmayan modelleme yaklaşımı kullanılarak modellenmesi ve çözümü gerçekleştirilebilir. Ayrıca probleme yeni amaçlar

eklemeden, çok amaçlı metasezgisel yöntemler kullanılarak Pareto çözüm kümesi elde edilmesi de gelecek çalışmalarda değerlendirilebilir.

Kaynaklar

- [1] M. Tanyaş and M. Baskak, *Üretim Planlama ve Kontrol*, 7th ed. İstanbul: İrfan Yayıncılık, 2017.
- [2] K. Şimşek Alan, "Doğrusal tamsayılı programlama problemlerinin çözümü için yeni alternatif bir algoritma," *Avrupa Bilim ve Teknoloji Dergisi*, vol. 29, pp. 93-98, 2021. doi: 10.31590/ejosat.1019251
- [3] S. I. Gass, *Linear Programming*. New York: McGraw-Hill, 1982.
- [4] D. Tavaghof-Gigloo, S. Minner, and L. Sibelmayr, "Mixed integer linear programming formulation for flexibility instruments in capacity planning problems," *Computers & Industrial Engineering*, vol. 101, pp. 101-110, 2016. doi: 10.1016/j.cie.2016.04.013
- [5] C. Chen, S. Mestry, P. Damodaran, and C. Wang, "The capacity planning problem in make-to-order enterprises," *Mathematical and Computer Modelling*, vol. 50, pp. 1461-1473, 2009. doi: 10.1016/j.mcm.2009.07.010
- [6] M. A. Huka, W. Grenzfurtnr, B. Zauner, and M. Gronalt, "Capacity planning of a mixed-model assembly line for prefabricated housebuilding elements," *Procedia Computer Science*, vol. 280, pp. 706-713, 2021. doi: 10.1016/j.procs.2021.01.293
- [7] R. Ojstersek and B. Buchmeister, "Simulation based resource capacity planning with constraints," *International Journal of Simulation Modelling*, vol. 4, pp. 672-683, 2021. doi: 10.2507/IJSIMM20-4-578
- [8] N. Ekmekçi, "Sanayi işletmelerinde üretim planlaması ve doğrusal programlama ile bir sanayi işletmesinde optimizasyon uygulaması," M.S. thesis, Selçuk Univ., Konya, Türkiye, 2015.
- [9] M. Deste and M. Karabulut, "Doğrusal programlama tekniğiyle üretim planlama yaklaşımı ve tekstil sektöründe bir uygulama," *Süleyman Demirel Üniversitesi İktisadi ve İdari Bilimler Fakültesi Dergisi*, vol. 26, no. 3, pp. 247-258, 2021.
- [10] A. Çetindere, Ş. Sevim, and C. Duran, "Üretim planlama problemlerinde doğrusal programlama tekniğinin kullanımı bir konfeksiyon işletmesinde uygulama," *Erciyes Üniversitesi İktisadi ve İdari Bilimler Fakültesi Dergisi*, no. 35, pp. 271-300, 2010.
- [11] E. N. Demircioğlu and M. Demircioğlu, "Üretme satın alma kararlarında faaliyete dayalı maliyet sistemi ve kısıtlar teorisi: Doğrusal programlama ile örnek uygulama," *Mustafa Kemal Üniversitesi Sosyal Bilimler Enstitüsü Dergisi*, pp. 316-333, 2016.
- [12] H. Kara and H. Savaş, "Doğrusal programlama metoduyla Diyarbakır ili gıda sektöründe bir üretim planlama uygulaması," *International Periodical for the Languages, Literature and History of Turkish or Turkic*, pp. 491-506, 2015. doi: 10.7827/TurkishStudies.7636
- [13] E. C. Özcan and S. Erol, "Türkiye'de elektrik üretim planlaması için çok amaçlı bir karışık tam sayılı doğrusal programlama modeli," *Selçuk Üniversitesi Mühendislik Bilim ve Teknoloji Dergisi*, vol. 1, no. 1, 2013.
- [14] M. Büyükkelik, "Üretim planlama problemlerinde doğrusal programlama modellerinin kullanımı: Bir üretim işletmesinde uygulama," M.S. thesis, Niğde Üniversitesi, Niğde, Türkiye, 2007.
- [15] S. Liu and L. G. Papageorgiou, "Multiobjective optimisation of production, distribution and capacity planning of global supply chains in the process industry," *Omega*, vol. 41, pp. 369-382, 2013. doi: 10.1016/j.omega.2012.03.007
- [16] E. Mhiri, M. Jacomino, F. Mangione, P. Vialletelle, and G. Lepelletier, "Finite capacity planning algorithm for semiconductor industry considering lots priority," *IFAC-PapersOnLine*, vol. 48, no. 3, pp. 1598-1603, 2015. doi: 10.1016/j.ifacol.2015.06.314
- [17] L. A. Kazakovtsev, M. N. Gudyma, and A. N. Antamoshkin, "Genetic algorithm with greedy heuristic for capacity planning," in *Proc. of the 6th International Congress on Ultra Modern Telecommunications and Control Systems and Workshops (ICUMT)*, St. Petersburg, Russia, 2014, pp. 607-613. doi: 10.1109/ICUMT.2014.7002170
- [18] J. C. Chen, K. H. Chen, C. H. Lin, C. W. Chen, and C. L. Yang, "A study of a heuristic capacity planning algorithm for weapon production system," *International Journal of Electronic Business Management*, vol. 9, no. 1, pp. 46-57, 2011.
- [19] Y. Iwata, K. Tajii, and H. Tamura, "Multi-objective capacity planning for agile semiconductor manufacturing," *Production Planning & Control*, vol. 14, no. 3, pp. 244-254, 2003. doi: 10.1080/09537280310000102586
- [20] S. Khalili and M. M. Khah, "A new queuing-based mathematical model for hotel capacity planning: A genetic algorithm solution," *Journal of Applied Research on Industrial Engineering*, vol. 7, no. 3, pp. 203-220, 2020. doi: 10.22105/jarie.2020.244708.1187
- [21] B. Ayvaz, E. Boltürk, and S. Kaçtıoğlu, "Supplier selection with TOPSIS method in fuzzy environment: An application in banking sector," *Sigma Journal of Engineering and Natural Sciences*, vol. 33, no. 3, pp. 351-362, 2015.

- [22] C. Oğuz, İ. Pençe, M. Ş. Çeşmeli, and Ö. Çetinkaya Bozkurt, "Tedarikçilerin TOPSIS ile seçilmesi ve gelişim durumlarının sezgisel optimizasyon ile belirlenmesi," *Acta Infologica*, vol. 5, no. 1, pp. 53-64, 2021. doi: 10.26650/acin.868427
- [23] N. Ömürbek, Y. Makas, and V. Ömürbek, "AHP ve TOPSIS yöntemleri ile kurumsal proje yönetim yazılımı seçimi," *Süleyman Demirel Üniversitesi Sosyal Bilimler Enstitüsü Dergisi*, vol. 21, no. 1, pp. 59-83, 2015.
- [24] A. Supçiller and Ö. Çapraz, "Oluklu mukavva kutu üreticisi için tedarikçi seçiminde AHP ve TOPSIS yöntemlerinin kullanımı," *İstanbul Üniversitesi İktisat Fakültesi Ekonometri ve İstatistik Dergisi*, no. 13, pp. 1-22, 2011.

This is an open access article under the CC-BY license



GAZİ

JOURNAL OF ENGINEERING SCIENCES

Heading Estimation for Agricultural Vehicles with Multi-Antenna RTK/GNSS, Tactical-Grade and Low-Cost IMUs

Hasan Dilmac^a, Veli Ilci^{*b}, Emirhan Kaya^c

Submitted: 28.01.2025 Revised: 25.03.2025 Accepted: 13.04.2025 doi:10.30855/gmbd.070525N10

ABSTRACT

Keywords: Autonomous vehicles, heading determination, GNSS, IMU

^a Ondokuz Mayıs University,
Faculty of Engineering,
Dept. of Geomatics Engineering
55139 - Samsun, Türkiye
Orcid: 0000-0001-6877-8730
e mail: hasan.dilmac@omu.edu.tr

^{b*} Ondokuz Mayıs University,
Faculty of Engineering,
Dept. of Geomatics Engineering
55139 - Samsun, Türkiye
Orcid: 0000-0002-9485-874X

^c Ondokuz Mayıs University,
Faculty of Engineering,
Dept. of Geomatics Engineering
55139 - Samsun, Türkiye
Orcid: 0009-0007-2633-3419

*Corresponding author:
veli.ilci@omu.edu.tr

Nowadays, Autonomous Vehicles (AVs) are employed for various tasks, including spraying, harvesting, and planting. For AVs to navigate autonomously, accurate heading knowledge of the vehicle is essential. Sensors such as the Global Navigation Satellite System (GNSS) and Inertial Measurement Unit (IMU) are used on AVs to produce heading information. Dual-frequency and Real-Time Kinematic (RTK) capable systems with multiple antennas are used to increase the heading accuracy of GNSS. For IMUs, heading accuracy is directly related to the quality of the sensors, so high accuracy is achieved with expensive IMUs. However, with the development of micro-electro-mechanical system (MEMS) technology, studies are also being carried out on low-cost IMU solutions. This study tested the heading performances of three different sensors: a low-cost RTK/GNSS with multiple antennas, a tactical-grade IMU, and a low-cost MEMS IMU. An Unmanned Ground Agricultural Vehicle (UGAV) designed for spraying was driven on a line, and the sensors' data mounted on the UGAV were collected. Heading accuracy was also examined according to the distance between the RTK/GNSS system antennas. As a result of the analysis, the average errors of RTK/GNSS, tactical-grade IMU, and low-cost IMU are 0.58, 0.60, and 4.24 degrees, respectively.

Tarım Araçları için Çok-Antenli RTK/GNSS, Taktiksel-Sınıf ve Düşük-Bütçeli IMU ile Yön Tahmini

ÖZ

Günümüzde Otonom Araçlar (AVs), ilaçlama, hasat ve ekim gibi çok çeşitli görevlerde kullanılmaktadır. OA'ların otonom bir şekilde hareket edebilmesi için aracın doğru yön bilgisi esastır. OA'larda yön bilgisi üretmek için Küresel Navigasyon Uydu Sistemi (GNSS) ve Ataletsel Ölçü Birimi (IMU) gibi sensörler kullanılır. Gerçek Zamanlı Kinematik (RTK) çözümü sağlayabilen çift frekanslı çoklu antenlere sahip sistemler, GNSS'in yön belirleme doğruluğunu artırmak için kullanılabilir. IMU'lar için yön doğruluğu sensörlerin kalitesiyle ilgilidir, bu nedenle pahalı IMU'larla yüksek doğruluk elde edilir. Ancak Mikro-Elektro Mekanik Sistem (MEMS) teknolojisinin gelişmesiyle birlikte düşük maliyetli IMU çözümleri üzerinde de çalışmalar yürütülmektedir. Bu çalışmada, çoklu antene sahip düşük maliyetli bir RTK/GNSS, taktiksel sınıf bir IMU ve düşük maliyetli bir MEMS IMU olmak üzere üç farklı sensörün yön belirleme performansları test edilmiştir. İlaç püskürtme için tasarlanmış İnsansız Kara Tarım Aracıyla (UGAV) bir hat üzerinde sürüş gerçekleştirilmiş ve üzerine monte edilmiş sensörlerle veriler toplanmıştır. Ayrıca, RTK/GNSS sisteminin antenleri arasındaki mesafeye göre elde ettiği yön doğruluğu da incelenmiştir. Analiz sonucunda, RTK/GNSS, taktiksel sınıf IMU ve düşük maliyetli IMU'nun ortalama hataları sırasıyla 0,58, 0,60 ve 4,24 derece bulunmuştur.

Anahtar Kelimeler: Otonom araçlar, yön tahmini, GNSS, IMU

1. Introduction

Precision agriculture is becoming an important research area due to population growth, climate change, and global warming. Furthermore, by 2050, 70% of the world's population is expected to reside in cities, creating a shortage of workers in rural areas [1]. Because of this, there is an increasing need for automation, and new techniques and tools are required to monitor and examine plants and crops in addition to increasing farming output [2]. Future agricultural concepts include more sophisticated farms with sensors, machinery, and robots that are more productive and environmentally sustainable. Autonomous Vehicles (AVs) and robotics have the potential to be crucial in achieving the demands of agricultural products in this regard [3]. Many tasks, including weeding [4], spraying [5], planting and harvesting [6-8], monitoring the environment [9], and supplying water and fertilisers [10], are being performed by autonomous vehicles and robots in agriculture.

Self-localization is an essential component of AVs in fulfilling their mission in the field. Early navigation systems are primarily based on vision sensors and computer vision techniques [11]. Over the past decades, autonomous localisation of AVs has been addressed by different kinds of methods, including Global Navigation Satellite Systems (GNSS), Light Detection and Ranging (LiDAR), and Inertial Measurement Units (IMUs) [12]. GNSS-based localisation has been the most applied approach for AVs [13,14]. By implementing three different control strategies, Alonso-Garcia et al. [15] assessed the effectiveness of low-cost GNSS receivers in enabling the autonomous navigation of agricultural tractors. Han et al. [16] introduced a path planning and tracking system for an autonomous agricultural sprayer using a single-frequency GNSS Real-Time Kinematic (RTK), achieving a positional accuracy of 0.01 m.

Estimating the vehicle's heading is another crucial task in autonomous navigation [17]. Even though the price of GNSS devices has been dropping recently, most studies still use IMU sensors like 3-axis Fiber Optical Gyroscopes (FOG) for vehicle heading estimation [18]. Three-axis FOGs are typically paired with three-axis accelerometers and magnetometers to find and track vehicles' position and heading. However, since sensor drift causes them to accumulate motion estimation errors, their primary purpose in navigation is short-range [19]. Besides, FOG sensors are quite costly, making their usage in agricultural robots unfeasible [20]. This has led to the widespread use of commercially available, low-cost Micro-Electro-Mechanical System (MEMS) IMUs in low-grade inertial systems. However, this technology is still in its infancy, and its benefits come at the risk of poor accuracy [21]. Compared to its optical equivalents, low-cost MEMS exhibit much worse accuracy because of more significant biases, axis misalignment errors, scale factor, and increased temperature drift susceptibility [22]. Since MEMS IMUs have a limited capacity, they are generally combined with other sensors to improve heading accuracy [23,24]. A vehicle's position, velocity, and heading can be accurately determined via GNSS, which is suitable for autonomous driving operations. By utilising the vehicle's current position and heading, the GNSS-based autonomous driving approach computes the optimal steering angle and wheel speed based on predefined waypoints, enabling the vehicle to accurately follow a predetermined route [25]. GNSS can typically provide a position solution with an accuracy of a few meters. It is possible to attain sub-meter precision, but it will take extra processing and external data. For instance, the RTK method is used in GNSS to obtain cm-level accuracy [26]. RTK/GNSS is typically used to find a stationary rover's position. However, it can also be used to determine the exact location of a moving rover antenna on a vehicle. It is even possible to ascertain the platform's heading by installing many antennas on it [27]. Nadarajah et al. [28] examined the single-frequency GNSS attitude determination performance utilising a combination of GPS and Galileo measurements. Zhu et al. [29] combined MEMS IMU with dual-antenna GNSS to get attitude information in a GNSS-limited environment with high accuracy.

Today, the accuracy and precision required for the heading and location of AVs can be achieved with costly systems. However, this is one of the biggest obstacles to the commercialisation and widespread use of AVs. Therefore, some studies were undertaken to provide the required accuracy and sensitivity with low-cost sensors [30, 31]. This study analysed the heading estimation accuracies of a low-cost RTK/GNSS with triple

antennas, tactical grade, and low-cost MEMS IMUs. For this purpose, a vehicle designed for agricultural spraying was driven along a straight line, and heading predictions were made with sensors. In addition, it was evaluated how the distance between the antennas of the RTK/GNSS affected the heading accuracy. This paper is organised as follows. Section II presents the vehicle system and sensor placement, heading estimation methods of sensors, analysis methods, and field experiment. Section III gives the heading estimation results for the sensors. Finally, the conclusions of this study are included in Section IV.

2. Material and Methods

2.1. The vehicle system and sensor placement

An Unmanned Ground Agricultural Vehicle (UGAV) designed for agricultural spraying was used to analyse the heading performances of the sensors. The design of the vehicle is shown in Figure 1a. However, to analyse the heading accuracy of RTK/GNSS according to the distances between the antennas, additional parts were mounted on UGAV, and the distance between the antennas was adjusted accordingly (Figure 1b). A total of 7 separate drives was made to determine the heading accuracy according to the varying distance between RTK/GNSS antennas. The position of the first antenna (ANT1) was fixed, and the second antenna (ANT2) was moved at intervals of 30 cm in a north-south direction, at most 210 cm and at least 30 cm away from the ANT1. In each drive, heading estimation was also obtained with tactical grade and low-cost IMUs for comparison purposes. Since the content of the study is related to the heading, the ANT3 was not used even though it was placed on the vehicle.

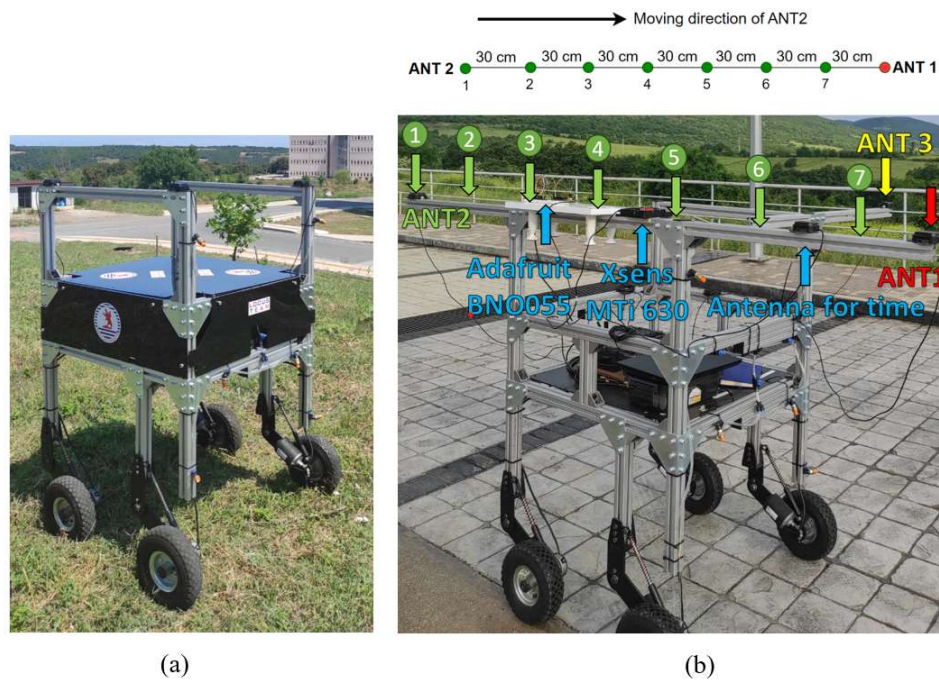


Figure 1. UGAV (a) standard design; (b) modified design for setting antenna distance.

2.2. Heading estimation based on RTK/GNSS

A simpleRTK2B SBC development board [32], a multi-frequency GNSS sensor, was utilised in the study. Three u-blox ZED-F9 modules and three GNSS antennas can be used simultaneously on this board (Figure 2). This development board is open code and programmable. This allows the development of algorithms for many different applications. This development card can receive RTK corrections for all three antennas, so the position of each antenna can be obtained with cm precision (Table 1). It is a low-cost RTK-GNSS sensor compared to its equivalents in the market.

Table 1. Sensor specifications

Specifications	SimpleRTK2B SBC	Xsens Mti 630	Adafruit BNO055
Price	• \$1,033.85	• €1,009.00	• \$34.95
Type	• Low-cost GNSS	• Tactical-Grade IMU	• Low-Cost IMU
Positional Accuracy	• <1-4 cm with corrections • <1.5m in standalone mode	-	-
Heading Accuracy	• Sub-degree	• ± 1 degree	• ± 2.5 degree
Update Rate	• Up to 20Hz	• Up to 400Hz	• Up to 100Hz
Advantages	<ul style="list-style-type: none"> • High positional accuracy (RTK cm-level precision) • Three-Dimensional (3D) position information beside the heading • Optimal in open-sky environment • Provide Coordinated Universal Time (UTC) time 	<ul style="list-style-type: none"> • High heading accuracy • High frequency • Provide UTC 	<ul style="list-style-type: none"> • Low-cost compared to the other sensors • Compact and easy to integrate • Suitable for basic orientation tracking
Disadvantages	<ul style="list-style-type: none"> • Requires GNSS signal for operation (limited indoor use) 	<ul style="list-style-type: none"> • Requires calibration • Susceptible to magnetic interference affecting heading accuracy 	<ul style="list-style-type: none"> • Requires calibration • Highly sensitive to magnetic interference • Lower heading accuracy compared to high-end IMUs

GNSS delivers two primary types of measurements: carrier phase and pseudorange. If the carrier phase ambiguity can be successfully resolved, the positioning based on the carrier phase yields a more precise range than those using pseudorange.



Figure 2. SimpleRTK2B SBC

Ambiguity resolution is one of the most challenging issues in GNSS and is a necessary first step for all RTK positioning-related applications [33]. In the RTK approach, which presents the ideas of a base and a rover, one or more rovers receive a continuous differential correction data stream (per the RTCM 3.3 protocol) from the base over a communication channel (Figure 3). In the standard RTK, the base stays in a static known position. However, this is not the case for mobile vehicles carrying both the base and the rover. For this, a moving base RTK approach is developed so that both base and rover receivers can move. With the moving base RTK approach, heading estimation of a moving vehicle can be obtained [27].

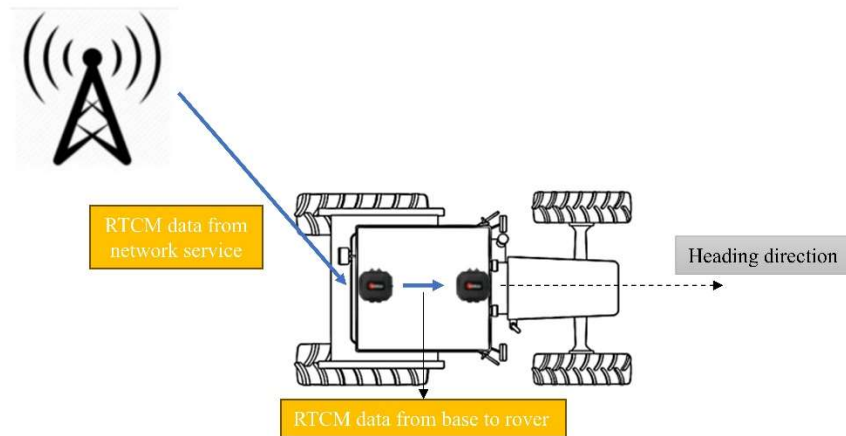


Figure 3. Moving base setup for heading estimation [34]

Several coordinate systems are utilised in heading determination using GNSS. The local level coordinate system is commonly employed as the reference for calculating the heading of a moving vehicle. This topocentric coordinate system is defined relative to a reference ellipsoid, such as GRS80. Another coordinate system is the vehicle platform coordinate system defined by the user. The heading direction coincides with the vehicle's direction of travel [35]. Then, the heading of the vehicle to the reference system can be estimated by using two GNSS antennas as below:

$$\Psi_G = \text{atan} \left(\frac{Y_{\text{ANT}2} - Y_{\text{ANT}1}}{X_{\text{ANT}2} - X_{\text{ANT}1}} \right) \quad (1)$$

Here, Ψ_G is grid heading. The SimpleRTK2B SBC development board provides GNGGA via the National Marine Electronics Association (NMEA) messages containing the geographic coordinates, time, and other information about the antennas. The grid coordinates of the points in the Transverse Mercator (TM) projection were generated for the heading estimation.

2.3. Heading estimation based on IMUs

In this study, a tactical-grade MEMS IMU (Xsens Mti 630), and a low-cost IMU (Adafruit BNO055) were used to estimate the vehicle's heading. Xsens Mti-630 includes a 3-axis gyroscope, 3-axis accelerometer, 3-axis magnetometer, control and fusion unit. With the control unit, timing and synchronisation of the sensors is ensured. At the same time, it provides motion data at high frequencies using calibration models and an Xsens-optimized strap-down algorithm. Thanks to the sensor fusion units inside, Xsens combines the information from all sensors and, as a result, provides location and true north-referenced heading data at frequencies up to 400 Hz [36]. Xsens Mti Manager software was used to communicate with the Xsens Mti 630 to get data files and set some parameters (coordinate system, time update, output preference, filter settings to get true north-referenced heading or true heading (Ψ_T)).

Adafruit BNO055 sensor also has a 3-axis gyroscope, 3-axis accelerometer, and 3-axis magnetometer sensors [37]. However, it is a low-cost MEMS sensor with a lower capacity than Xsens Mti 630. Some raw data such as linear acceleration (a_x, a_y, a_z in m s^{-2}), angular velocity (w_x, w_y, w_z in deg s^{-1}), magnetic field vector (m_x, m_y, m_z in Tesla m^{-2}), and calibration information can be received from the Adafruit BNO055 sensor.

Arduino Nano was used to receive and process the data of the Adafruit BNO055 sensor. Unlike other sensors (SimpleRTK2B SBC and Xsens MTi 630), BNO055 does not provide UTC. In the study, another sensor, SimpleRTK 2B, was used to allow the comparison of different sensor outputs based on UTC. Both sensors were connected via Arduino, and raw IMU data was obtained along with UTC (Figure 4).

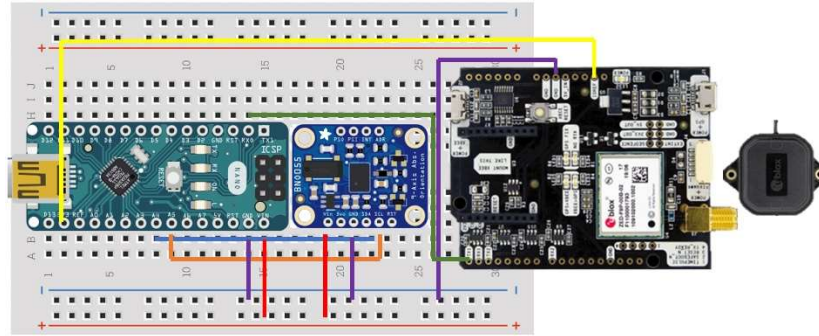


Figure 4. Arduino Nano, Adafruit, and SimpleRTK2B connection diagram

Just as a gravitational vector (g) is applied to objects towards the center of the earth, a magnetic vector is coming towards objects from the magnetic north. For a situation where pitch and roll angles also come into play, that is, where there is movement in 3D space rather than in a horizontal plane, heading calculation is made as follows [38]:

$$\Psi_M = \text{atan} \left(\frac{m_y \cdot \cos(\theta) + m_z \cdot \sin(\theta)}{m_x \cdot \cos(\theta) - m_y \cdot \sin(\theta) \cdot \sin(\theta) + m_z \cdot \cos(\theta) \cdot \sin(\theta)} \right) \quad (2)$$

Here, Ψ_M is the magnetic heading, θ and ϕ are the roll and pitch angles obtained using raw data from the accelerometer and gyroscope by applying various filters.

2.4. Heading transformations

Several north directions are taken as a reference when calculating the heading angle. True North (TN), Magnetic North (MN), and Grid North (GN) are the different norths, each of one point in different directions (Figure 5). The magnetometer sensor is the main component of IMU, which allows heading estimation. This sensor gives a magnetic vector based on Earth's magnetic field. The heading determined by measuring the magnetic field is known as the magnetic heading since the Earth's geographic and magnetic poles do not coincide. Removing a magnetic declination from the magnetic heading is necessary to determine the true heading or the heading referred to the geographical North direction [39, 40]. GN refers to the direction of the grid in a plane coordinate system, typically aligned with the grid of a map projection. Converting the spherical surface of the globe into a flat surface results in the distinction between true north and grid north, also known as convergence. The projection and map location determine a given map's convergence [41].

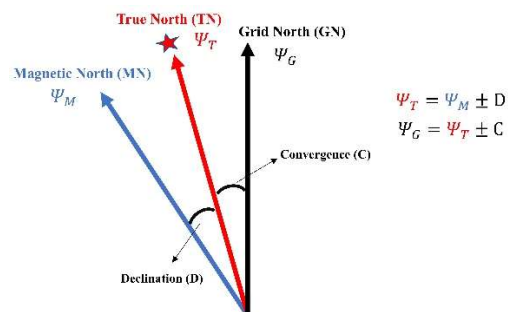


Figure 5. Magnetic, true, and grid north

Since the headings obtained with each sensor are in different systems, heading transformations were performed to compare them. The grid heading is taken as a reference for comparison.

2.5. Reference heading calculation

A line was determined for the study to compare the headings generated from sensors. In order to calculate

the reference heading of this line, 15 points were determined on it and marked with spray, then three measurements of 30 epochs were made on each point, and 3D coordinates were obtained precisely by taking their averages (Figure 6). These point coordinates were obtained using Topcon Hiper V, which is based on the RTK/GNSS observation method, with an accuracy of 1-2 cm level. Then, the grid heading of the line was calculated using the coordinate data of 15 points. The reference heading of the line was calculated as 235.2594 degrees.

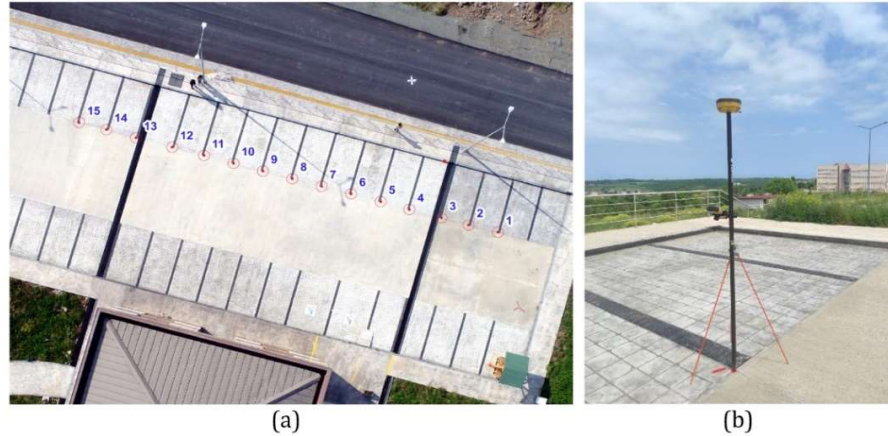


Figure 6. Test area (a) the line determined on which UGAV will track, (b) the measurement of the points on the line.

2.6. Field experiment: data collection of sensors

For the comparison of heading estimation capabilities of the sensors described in the previous sections, they were mounted on the UGAV. While collecting data with sensors, UGAV was driven along a line with starting point 1 and ending point 15. Before beginning the drive to get RTK fix solutions, convergence time was waited for the ambiguity resolution to be resolved. Sensor data collections were repeated seven times for seven different antenna conditions, and each measurement took approximately one minute. The manual calibration of IMUs was realised each time before starting the driving. The frequency of GNSS data collection was 1 Hz, whereas the IMU data were collected at 100 Hz.

3. Results and Discussion

After data collection in the field was completed, the heading values were estimated from the sensors' data using MATLAB software. For this purpose, geographical coordinates in GNGGA message type in NMEA format collected with GNSS were converted to the projection system (TM 3°). Then, the grid heading values were obtained using the coordinate values of each measurement according to Eq. 1. This makes approximately 60 measurements for GNSS data with a frequency of 1 Hz because each drive lasted approximately one minute. UTC has been converted to GPS Time of Week (ToW) to ensure time synchronization by using MATLAB software.

Xsens MTi 630 can generate true-heading, Euler angles, quaternions, and UTC in addition to the raw data, depending on the output options. In order to compare the heading of Xsens MTi 630 with the heading obtained from RTK/GNSS, time and heading transformations were made in MATLAB software. Thus, grid heading values of Xsens MTi 630 were obtained with GPS ToW. The data update frequency of Xsens MTi 630 was 100 Hz. This makes approximately 6000 measurements for one drive.

Magnetic heading values of Adafruit BNO055 were estimated using raw data of the sensors according to Eq. 2. Magnetic heading calculations from the raw data, transitions from magnetic heading to grid heading, and transitions from UTC to GPS ToW for time synchronisation were performed in MATLAB software. The data update frequency and number of measurements were the same with Xsens Mti 630.

The plots of the grid heading values and the reference grid heading value of each sensor in the same time interval for each antenna condition are shown in Figure 7. Antenna condition refers to the distances (baselines) between ANT1 and ANT2. In the 1st condition, the distance between the antennas is the farthest (210 cm), while in the 7th condition, the distance between the antennas is the closest (30 cm). The distance between antennas decreases by 30 cm from the 1st condition to the 7th condition.

For the first six cases where the baseline is long compared to condition seven, the heading accuracies of RTK/GNSS and Xsens MTi 630 are very close to each other and have almost the same characteristics. However, in condition seven, as the distance between antennas decreases to 30 cm, the heading accuracy of RTK/GNSS also decreases and is not like Xsens Mti 630. The heading accuracy of the Adafruit BNO055 is much noisier and more unstable than the other two sensors in all cases. Even though it seems to produce the most accurate results in case six, it is still below the other two sensors due to its noise. The sensors' respective comparisons in each case show that the Xsens MTi 630 provides similar accuracies for all conditions. Adafruit BNO055 appears to produce results with similar noise within a certain range. In the heading values obtained with RTK/GNSS, it is seen that the heading accuracy begins to decrease as the distance between antennas decreases. This decrease is not directly proportional to antenna distances. This decrease is not directly proportional to antenna distances as in the difference between conditions six and seven.

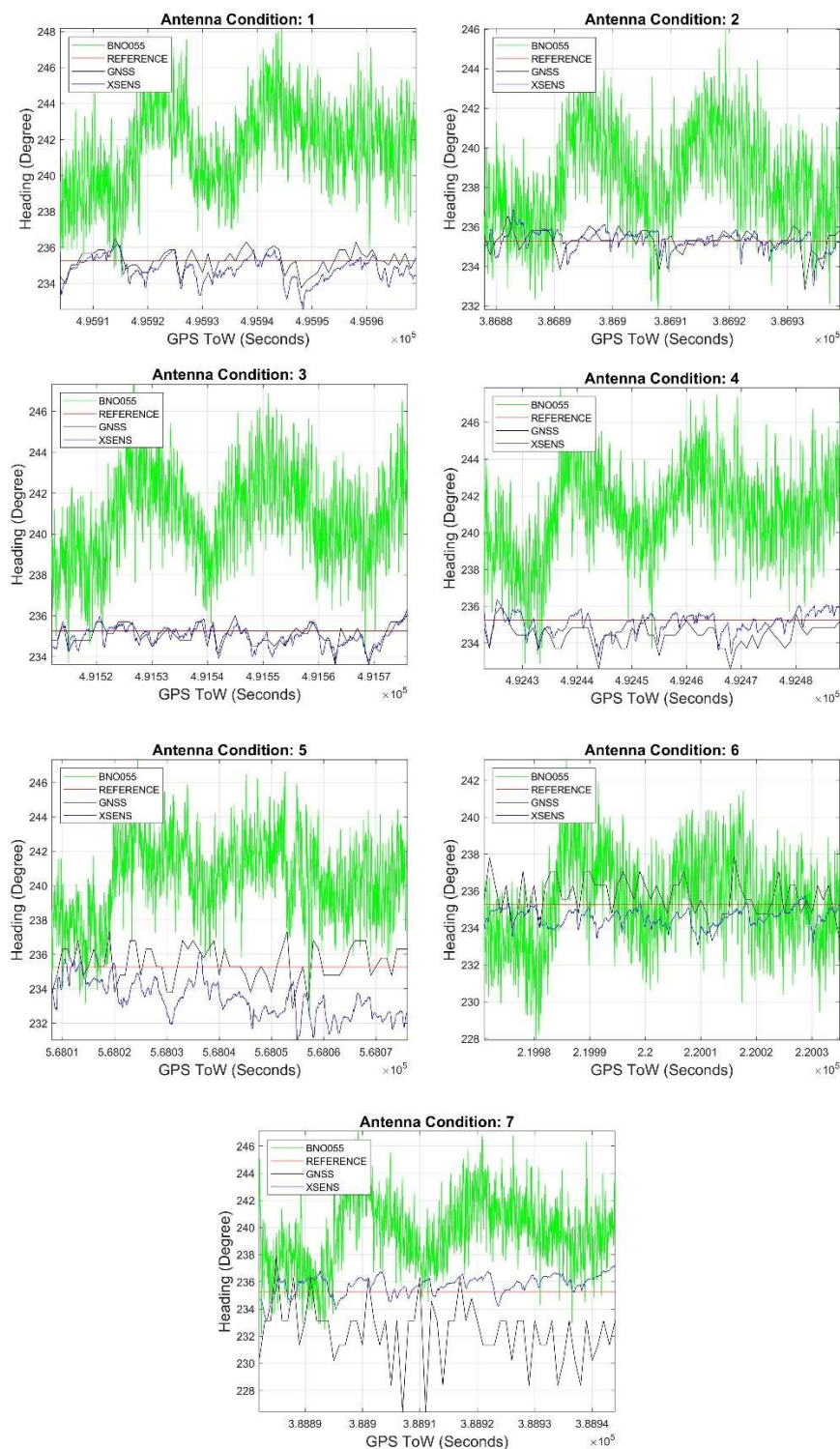


Figure 7. Heading plots of sensors and reference value

For a more quantitative comparison, the root mean square (RMS) error and mean values of the sensor headings in each case were calculated (Table 2). When the RMSs of GNSS-based headings are examined, the heading errors are relatively stable at first, with slight variations in RMS and mean values across the initial antenna conditions (one to three), where the antenna distance is 210 cm to 150 cm. As the antenna distance decreases (Conditions four through seven), both RMS and Mean heading errors tend to increase significantly. In Condition seven (30 cm distance), there is a sharp increase in heading error, with RMS rising from 0.8 to 3.7 degrees and the mean error increasing from 0.6 to 3.2 degrees. The significant increase in heading errors as the antenna distance decreases indicates that this sensor relies heavily on antenna separation for accurate

heading determination. This matches the theoretical expectation that a larger baseline leads to better heading accuracy. The greater the baseline between the two antennas, the more accurate the measurement of the relative direction between the antennas as the relative position change between the two antennas becomes more noticeable, improving the accuracy of the heading calculation. Also, with a longer baseline, errors in individual position estimates of the antennas (due to noise or multipath) are less likely to affect the heading calculation. An extended baseline allows for better differentiation between the signals, making the heading determination less sensitive to minor errors.

Since the seventh condition does not accurately reflect the heading accuracy that can be achieved with RTK/GNSS, it is not included in calculating the average of the means of all conditions. When calculated this way, the average mean error of RTK/GNSS headings in all conditions except the seventh condition is 0.58 degrees.

The RMS values of the Xsens Mti 630 in each drive are generally close to each other, so it can be said that it has very high precision. The average mean error of Xsens Mti 630 headings in all conditions is 0.60 degrees. The Adafruit BNO055 sensor produced the worst results in terms of both accuracy and precision. The average mean error of BNO055, which produces quite noisy heading values, is 4.24 degrees.

Table 2. RMS and mean error values of sensors

Antenna Condition	RMS (Degree)			Mean (Degree)		
	SimpleRTK2B SBC	Xsens Mti 630	Adafruit BNO055	SimpleRTK2B SBC	Xsens Mti 630	Adafruit BNO055
1	0.6	0.8	6.8	0.5	0.6	6.3
2	0.6	0.5	3.9	0.4	0.4	3.3
3	0.6	0.5	6.0	0.5	0.4	5.6
4	0.8	0.9	4.5	0.6	0.7	4.0
5	0.8	0.8	4.7	0.6	0.6	4.1
6	1.1	0.8	2.4	0.9	0.7	2.0
7	3.7	0.9	5.0	3.2	0.8	4.4

Considering the sensor specifications, such as prices, advantages, and disadvantages (Table 1), the SimpleRTK2B is one of the most suitable sensors for high-accuracy applications in open-sky environments. In addition to providing heading performance and price equal to that of a tactical-grade IMU, it offers cm-level 3D position information. However, the distance between antennas affects the sensor's heading accuracy. The vehicle's dimensions used in the application must be considered to achieve maximum heading accuracy. The distance between the antennas should be above 60 cm for optimal results. In situations where the vehicle dimensions do not allow for optimal antenna spacing or indoor applications (e.g., greenhouses), the Xsens MTi 630 sensor should be preferred for high accuracy. This sensor can also generate position information indoors using a strap-down navigation approach. However, IMU sensors are sensitive to nearby metal objects. Calibration should be performed every time to minimise the effects of magnetic interference factors in the surroundings. For agricultural applications where high heading accuracy is not required, such as basic orientation tracking, the Adafruit BNO055 sensor, with its affordable price, may meet the user's needs. However, it should be noted that it does not provide UTC information. Additionally, the update rate in applications can also be an important component. The advantage of IMU sensors in this regard is noticeable. A high update rate allows for more precise tracking of fast-moving objects, making it especially beneficial in agricultural applications like automated machinery, crop monitoring, or robotic vehicles that require rapid response times. With a higher update rate, IMUs can provide more accurate and real-time orientation and movement data, leading to improved performance in dynamic environments. However, the trade-off is that high update rates can consume more power, which may be a consideration for battery-powered systems. Moreover, in applications where slower movement or less frequent updates are sufficient, the high update rate may lead to unnecessary data processing, potentially increasing computational load without providing significant benefits. Therefore, it is essential to balance the required accuracy with the system's power and computational capabilities.

In many studies, the performance of low-cost IMUs has not been tested independently. Instead, integrated solutions combining dual-antenna RTK/GNSS and low-cost IMUs have been developed to enhance robustness and accuracy. Furthermore, accuracy assessments in these studies are typically reported in terms of positional error [4, 15, 16, 25, 42, 43] rather than heading accuracy. Nevertheless, a comparative analysis has been conducted with a few studies that employ low-cost IMUs and RTK-GNSS sensors using similar accuracy evaluation criteria. Cui et al. [44] implemented a geometric-based path-tracking algorithm to guide an autonomous vehicle with a dual-antenna RTK and a navigation controller along a continuous U-shaped path. With an antenna baseline of 0.785 m, the system achieved a lateral position error within ± 3 cm for 86.30% of the time and maintained a heading deviation within ± 2 degrees for 90.61% of the time. Chen et al. [45] developed a coarse initial heading estimation method for the low-cost MEMS IMUs aided by the GNSS sensor. The initial heading is computed by comparing the two trajectories obtained with IMU-based and GNSS-based methods. The algorithm was tested on a car, a wheeled robot, and a tractor under various conditions. Results indicate that the initial heading was determined within 5 seconds with accuracies of 0.25, 0.6, and 1.6 degrees for the car, robot, and tractor, respectively. Galati et al. [46] developed a cost-efficient autonomous navigation system for agriculture by using a dual-antenna GPS and low-cost IMUs. The system utilises a Gaussian Sum Filter integrating multiple Extended Kalman Filters to address IMU bias and GPS signal loss. It achieved position and heading estimation, with average errors of 0.2 m and 0.2 degrees. Huang et al. [47] developed an integrated navigation system based on IMU and RTK-GNSS sensors to improve the positioning accuracy of autonomous agricultural vehicles. During operation on open roads, the system's position and heading errors are within 3 cm and 0.6 degrees, respectively. Pini et al. [48] evaluated the performance of the FANTASTIC GNSS receiver (simply FANTASTIC), which has dual antennas and integrated IMU. This sensor uses a loosely coupled GNSS/IMU integration to provide RTK-level position accuracy and GNSS-assisted attitude estimation. Three high-performance commercial GNSS receivers (Bmk1, Bmk2, and Bmk3) capable of delivering RTK measurements were considered benchmarks to compare FANTASTIC's performance. The performance of FANTASTIC was tested in four different environments: open-sky, kiwifruit orchard, vineyard, and greenhouse, alongside the benchmark GNSS receivers. Two reference systems, one GNSS-based and the other robotic total station-based, were used for evaluation. The heading error of FANTASTIC in open-field conditions was around 0.5 degrees. In the kiwifruit orchard, the heading error was 0.56 degrees with a 95% confidence level, while in the vineyard, it increased to 2.5 degrees with the same confidence level. Lastly, the heading error consistently remained above 1 degree in the greenhouse environment. Compared to previous studies, the results of this study are generally consistent with the high-precision findings reported in the literature.

4. Conclusion

In the agriculture industry, AVs and robots are useful tools for increasing productivity while lowering the need for human labour in various tasks. One of the most essential elements for AVs to successfully perform their tasks in the field is the ability to determine their heading correctly. GNSS and IMU are the most commonly used sensors to determine the heading of a vehicle. With the latest developments in sensor technology, systems with different accuracy and sensitivity have come along in every price range. This has initiated a quest for the most accurate results with the lowest possible price systems. Manufacturers of GNSS equipment have just begun to market small, RTK-capable, affordable receivers (less than \$1,000). With the development of MEMS (Micro-Electro-Mechanical Systems) technology, IMU sensor sizes and costs have decreased.

The heading accuracies of low-cost RTK/GNSS, tactical grade, and low-cost MEMS IMUs were analysed in this context. Real driving tests were performed to study the heading performances of these sensors mounted on UGAV. Heading accuracies of GNSS RTK according to the distance between antennas and heading comparisons of GNSS RTK and other IMU sensors were evaluated. According to the RMS values in Table 2, RTK/GNSS produced the most accurate results when the antennas were furthest from each other. It shows that heading accuracy gradually deteriorates when the distance between antennas falls below 1.5 meters and

deteriorates further when it falls below 60 cm. Therefore, a minimum antenna distance of 60 cm is recommended to obtain an accurate heading value with RTK/GNSS. RTK/GNSS and Xsens MTi 630 sensor generally gave similar results except for the 7th condition. If the distance between antennas is sufficient, it can be seen that RTK/GNSS can achieve the accuracy of a tactical-grade IMU.

The low-cost Adafruit BNO055 IMU sensor produced the noisiest results. It has an average mean error that may be sufficient for applications that do not require very precise heading information. For example, it can track the general movement direction of tractors or agricultural vehicles in large fields or where precise row planting is not required. However, for precision agriculture applications such as auto-steering, precise spraying systems and row planting, this accuracy may not be acceptable. In such cases, RTK-GNSS or high-accuracy IMUs should be preferred.

Acknowledgment

This work was supported by the Ondokuz Mayıs University under Grant PYO.MUH.1908.22.078.

Conflict of Interest Statement

The authors declare that there is no conflict of interest

References

- [1] D. T. Fasiolo, L. Scalera, E. Maset, and A. Gasparetto, "Towards autonomous mapping in agriculture: A review of supportive technologies for ground robotics," *Rob Auton Syst*, vol. 169, Nov. 2023. doi: 10.1016/j.robot.2023.104514
- [2] K. R. Aravind, P. Raja, and M. Pérez-Ruiz, "Task-based agricultural mobile robots in arable farming: A review," *Spanish Journal of Agricultural Research*, vol. 15, no. 1, 2017. doi: 10.5424/sjar/2017151-9573
- [3] A. Ghobadpour, G. Monsalve, A. Cardenas, and H. Mousazadeh, "Off-Road Electric Vehicles and Autonomous Robots in Agricultural Sector: Trends, Challenges, and Opportunities," *Vehicles*, vol. 4, no. 3, pp. 843-864, 2022. doi: 10.3390/vehicles4030047
- [4] M. Nørremark, H. W. Griepentrog, J. Nielsen, and H. T. Sogaard, "The development and assessment of the accuracy of an autonomous GPS-based system for intra-row mechanical weed control in row crops," *Biosystems Engineering*, vol. 101, no. 4, pp. 396-410, 2008. doi: 10.1016/j.biosystemseng.2008.09.007
- [5] A. T. Meshram, A. V. Vanalkar, K. B. Kalambe, and A. M. Badar, "Pesticide spraying robot for precision agriculture: A categorical literature review and future trends," *Journal of Field Robotics*, vol. 39, no. 2, pp. 153-171, 2022. doi: 10.1002/rob.22043
- [6] W. Ji, D. Zhao, F. Cheng, B. Xu, Y. Zhang, and J. Wang, "Automatic recognition vision system guided for apple harvesting robot," *Computers and Electrical Engineering*, vol. 38, no. 5, pp. 1186-1195, 2012. doi: 10.1016/j.compeleceng.2011.11.005
- [7] Y. Zhao, L. Gong, C. Liu, and Y. Huang, "Dual-arm Robot Design and Testing for Harvesting Tomato in Greenhouse," *IFAC-PapersOnLine*, vol. 49, no. 16, pp. 161-165, 2016. doi: 10.1016/j.ifacol.2016.10.030
- [8] H. Zhou, X. Wang, W. Au, H. Kang, and C. Chen, "Intelligent robots for fruit harvesting: recent developments and future challenges," *Precision Agriculture*, vol. 23, pp. 1856-1907, 2022. doi: 10.1007/s11119-022-09913-3
- [9] P. Gonzalez-de-Santos, A. Ribeiro, C. Fernandez-Quintanilla, et al., "Fleets of robots for environmentally-safe pest control in agriculture," *Precision Agriculture*, vol. 18, no. 4, pp. 574-614, 2017. doi: 10.1007/s11119-016-9476-3
- [10] T. L. Oluwabunmi, O. Adenugba, I. A. Ayoade, J. Azeta, and C. A. Bolu, "Development of an Autonomous Vehicle for Smart Irrigation," in *2022 5th Information Technology for Education and Development (ITED)*, Abuja, Nigeria, November 1-3, 2022, IEEE, pp. 1-7. doi: 10.1109/ITED56637.2022.10051388
- [11] A. Bechar and C. Vigneault, "Agricultural robots for field operations. Part 2: Operations and systems," *Biosystems Engineering*, vol. 153, pp. 110-128, 2017. doi: 10.1016/j.biosystemseng.2016.11.004

- [12] Y. Bai, B. Zhang, N. Xu, J. Zhou, J. Shi, and Z. Diao, "Vision-based navigation and guidance for agricultural autonomous vehicles and robots: A review," *Computers and Electronics in Agriculture*, vol. 205, no. 107584, 2023. doi: 10.1016/j.compag.2022.107584
- [13] T. Bakker, K. van Asselt, J. Bontsema, J. Müller, and G. van Straten, "Autonomous navigation using a robot platform in a sugar beet field," *Biosystems Engineering*, vol. 109, no. 4, pp. 357–368, 2011. doi: 10.1016/j.biosystemseng.2011.05.001
- [14] X. Han, H. J. Kim, C. W. Jeon, H. C. Moon, J. H. Kim, and S. Y. Yi, "Application of a 3D tractor-driving simulator for slip estimation-based path-tracking control of auto-guided tillage operation," *Biosystems Engineering*, vol. 178, pp. 70–85, 2019. doi: 10.1016/j.biosystemseng.2018.11.003
- [15] S. Alonso-Garcia, J. Gomez-Gil, and J. I. Arribas, "Evaluation of the use of low-cost GPS receivers in the autonomous guidance of agricultural tractors," *Spanish Journal of Agricultural Research*, vol. 9, no. 2, pp. 378–388, 2011. [Online]. Available: www.inia.es/sjar
- [16] J. H. Han, C. H. Park, Y. J. Park, and J. H. Kwon, "Preliminary results of the development of a single-frequency GNSS RTK-based autonomous driving system for a speed sprayer," *Journal of Sensors*, vol. 2019, no. 1, 2019. doi: 10.1155/2019/4687819
- [17] A. Leanza, R. Galati, A. Ugenti, E. Cavallo, and G. Reina, "Where am I heading? A robust approach for orientation estimation of autonomous agricultural robots," *Computers and Electronics in Agriculture*, vol. 210, Jul. 2023. doi: 10.1016/j.compag.2023.107888
- [18] A. Mizushima, K. Ishii, N. Noguchi, Y. Matsuo, and R. Lu, "Development of a low-cost attitude sensor for agricultural vehicles," *Computers and Electronics in Agriculture*, vol. 76, no. 2, pp. 198–204, May 2011. doi: 10.1016/j.compag.2011.01.017
- [19] D. Jiang, L. Yang, D. Li, F. Gao, L. Tian, and L. Li, "Development of a 3D ego-motion estimation system for an autonomous agricultural vehicle," *Biosystems Engineering*, vol. 121, pp. 150–159, 2014. doi: 10.1016/j.biosystemseng.2014.02.016
- [20] A. Roshanianfard, N. Noguchi, H. Okamoto, and K. Ishii, "A review of autonomous agricultural vehicles (The experience of Hokkaido University)," *Journal of Terramechanics*, vol. 91, pp. 155–183, October 2020. doi: 10.1016/j.jterra.2020.06.006
- [21] S. Sasaki, J. Asgari, and A. R. Amiri-Simkooei, "Improving MEMS-IMU/GPS integrated systems for land vehicle navigation applications," *GPS Solutions*, vol. 20, no. 1, pp. 89–100, Jan. 2016. doi: 10.1007/s10291-015-0471-3
- [22] Y. Li, M. Efatmaneshnik, and A. G. Dempster, "Attitude determination by integration of MEMS inertial sensors and GPS for autonomous agriculture applications," *GPS Solutions*, vol. 16, no. 1, pp. 41–52, Jan. 2012. doi: 10.1007/s10291-011-0207-y
- [23] L. Cong, E. Li, H. Qin, K. V. Ling, and R. Xue, "A performance improvement method for low-cost land vehicle GPS/MEMS-INS attitude determination," *Sensors*, vol. 15, no. 3, pp. 5722–5746, Mar. 2015. doi: 10.3390/s150305722
- [24] J. Si, Y. Niu, J. Lu, and H. Zhang, "High-Precision Estimation of Steering Angle of Agricultural Tractors Using GPS and Low-Accuracy MEMS," *IEEE Transactions on Vehicular Technology*, vol. 68, no. 12, pp. 11738–11745, Dec. 2019. doi: 10.1109/TVT.2019.2949298
- [25] J. H. Han, C. H. Park, Y. Y. Jang, J. D. Gu, and C. Y. Kim, "Performance evaluation of an autonomously driven agricultural vehicle in an orchard environment," *Sensors*, vol. 22, no. 1, Jan. 2022. doi: 10.3390/s22010114
- [26] J. Jackson, R. Saborio, S. A. Ghazanfar, D. Gebre-Egziabher, and B. Davis, "Evaluation of Low-Cost, Centimeter-Level Accuracy OEM GNSS Receivers," *the University Digital Conservancy*, 2018. Available: <https://hdl.handle.net/11299/197453.2018>
- [27] M. Farkas, S. Rózsa, and B. Vanek, "Multi-sensor Attitude Estimation using Quaternion Constrained GNSS Ambiguity Resolution and Dynamics-Based Observation Synchronization," *Acta Geodaetica et Geophysica*, vol. 59, pp. 51–71, Mar. 2024. doi: 10.1007/s40328-024-00441-2
- [28] N. Nadarajah, P. J. G. Teunissen, and N. Raziq, "Instantaneous GPS-galileo attitude determination: Single-frequency performance in satellite-deprived environments," *IEEE Transactions on Vehicular Technology*, vol. 62, no. 7, pp. 2963–2976, 2013. doi: 10.1109/TVT.2013.2256153
- [29] F. Zhu, Z. Hu, W. Liu, and X. Zhang, "Dual-Antenna GNSS Integrated with MEMS for Reliable and Continuous Attitude Determination in Challenged Environments," *IEEE Sensors Journal*, vol. 19, no. 9, pp. 3449–3461, May 2019. doi: 10.1109/JSEN.2019.2891783
- [30] J. Y. Huang, Z. Y. Huang, and K. H. Chen, "Combining Low-Cost Inertial Measurement Unit (IMU) and Deep Learning Algorithm for Predicting Vehicle Attitude," in *IEEE Conference on Dependable and Secure Computing*, Taipei, Taiwan, October 7–10, 2017, IEEE, pp. 237–239. doi: 10.1109/DESEC.2017.8073847
- [31] A. H. Işık and Ö. Çetin, "Multifunctional and Low Cost Autonomous Mobile Robot," *Gazi Journal of Engineering Sciences*, vol. 6, no. 2, pp. 105–110, Aug. 2020. doi: 10.30855/gmbd.2020.02.02

- [32] ArduSimple, "SimpleRTK2B SBC - Development Kit." Accessed: May 28, 2024. [Online]. Available: <https://www.ardusimple.com/product/simplertk2b-sbc-development-kit/>
- [33] S. Ji, R. Du, W. Chen, Z. Wang, K. He, and Z. Nie, "Partial GNSS ambiguity resolution in coordinate domain," *Survey Review*, vol. 51, no. 369, pp. 525–532, Nov. 2019. doi: 10.1080/00396265.2018.1490870
- [34] u-blox, "ZED-F9P Moving base applications Application note: ZED-F9P-MovingBase_AppNote_UBX-19009093," 2023. [Online]. Available: www.u-blox.com
- [35] J. Keong and G. Lachapelle, "Heading and Pitch Determination Using GPS/GLONASS," *GPS Solutions*, vol. 3, pp. 26-36, 2000. Available: <https://doi.org/10.1007/PL00012800>
- [36] Xsens, "Xsens MTi 630." Accessed: May 28, 2024. [Online]. Available: <https://www.movella.com/products/sensor-modules/xsens-mti-630-ahrs>
- [37] Adafruit, "BNO055 Intelligent 9-axis absolute orientation sensor," 2016. [Online]. Available: <https://www.bosch-sensortec.com/products/smart-sensor-systems/bno055/>
- [38] X. Cui, Y. Li, Q. Wang, M. Karaim, and A. Noureldin, "Vehicle heading estimation of INS/magnetometer integrated system based on constant hard iron interference calibration," *Measurement and Control*, vol. 54, no. 7–8, pp. 1208–1218, Sep. 2021, doi: 10.1177/00202940211021876
- [39] P. Kaniewski and J. Kazubek, "Integrated System for Heading Determination," *Acta Physica Polonica A*, vol. 116, no. 3, pp. 325-330, 2009.
- [40] B. Li, T. Gallagher, A. G. Dempster, and C. Rizos, "How feasible is the use of magnetic field alone for indoor positioning?" in *2012 International Conference on Indoor Positioning and Indoor Navigation*, Sydney, NSW, Australia, November 13-15, 2012, IEEE, pp. 1-9. doi: 10.1109/IPIN.2012.6418880
- [41] USGS, "What do the different north arrows on a USGS topographic map mean?" Accessed: May 29, 2024. [Online]. Available: <https://www.usgs.gov/faqs/what-do-different-north-arrows-usgs-topographic-map-mean>
- [42] A. Stoll and H. D. Kutzbach, "Guidance of a Forage Harvester with GPS," *Precision Agriculture*, vol. 2, pp. 281–291, 2000.
- [43] J. Carballido, M. Perez-Ruiz, L. Emmi, and J. Agüera, "Comparison of Positional Accuracy between RTK and RTX GNSS based on The Autonomous Agricultural Vehicles under Field Conditions," *Applied Engineering in Agriculture*, vol. 30, no. 3, pp. 361–366, 2014. doi: 10.13031/aea.30.10342
- [44] B. Cui, J. Zhang, X. Wei, X. Cui, Z. Sun, Y. Zhao, and Y. Liu, "Improved Information Fusion for Agricultural Machinery Navigation Based on Context-Constrained Kalman Filter and Dual-Antenna RTK," *Actuators*, vol. 13, no. 5, 2024. doi: 10.3390/act13050160
- [45] Q. Chen, H. Lin, J. Kuang, Y. Luo, and X. Niu, "Rapid Initial Heading Alignment for MEMS Land Vehicular GNSS/INS Navigation System," *IEEE Sensors Journal*, vol. 23, no. 7, pp. 7656–7666, 2023. doi: 10.1109/JSEN.2023.3247587
- [46] R. Galati, G. Mantriota, and G. Reina, "RoboNav: An Affordable Yet Highly Accurate Navigation System for Autonomous Agricultural Robots," *Robotics*, vol. 11, no. 5, 2022. doi: 10.3390/robotics11050099
- [47] Y. Huang, J. Fu, S. Xu, T. Han, and Y. Liu, "Research on Integrated Navigation System of Agricultural Machinery Based on RTK-BDS/INS," *Agriculture*, vol. 12, no. 8, 2022. doi: 10.3390/agriculture12081169
- [48] M. Pini, G. Marucco, G. Falco, M. Nicola, and W. De Wilde, "Experimental Testbed and Methodology for the Assessment of RTK GNSS Receivers Used in Precision Agriculture," *IEEE Access*, vol. 8, pp. 14690–14703, 2020. doi: 10.1109/ACCESS.2020.2965741

This is an open access article under the CC-BY license



Optimization of Tensile Properties in 3D-Printed PETG Honeycomb Structures via Taguchi Method: Influence of Cell Size and Geometric Orientation

Ahmet Fatih Yılmaz^{*a}

Submitted: 04.03.2025 Revised: 24.04.2025 Accepted: 28.04.2025 doi:10.30855/gmbd.070525N11

ABSTRACT

Keywords: Honeycomb structures, FDM, Taguchi optimization, PETG, Mechanical properties

^{a,*} Karabük University,
Engineering Faculty,
Dept. of Mechanical Engineering
78100-Karabük, Türkiye
Orcid: 0000-0001-5784-0121
e mail: ahmetfatihyilmaz@karabuk.edu.tr

^{*}Corresponding author:
ahmetfatihyilmaz@karabuk.edu.tr

Honeycomb structures are extensively used in engineering applications due to their high strength-to-weight ratio, energy absorption capacity, and customizable mechanical behavior. However, optimizing their tensile performance remains a significant challenge. This study systematically investigates the effects of cell size (1.75 mm, 1.5 mm, 1.25 mm) and geometric orientation (0°, 15°, 30°) on the tensile behavior of 3D-printed PETG honeycomb structures, fabricated using FDM. Nine different specimens were manufactured and tested following the ASTM D638 standard. The optimal configuration was determined using Taguchi's signal-to-noise (S/N) ratio analysis, while Analysis of Variance (ANOVA) was conducted for statistical evaluation. The results indicate that a cell size of 1.25 mm and a 30° orientation provided the highest fracture force (277.03 N), while the 1.75 mm cell size at 30° exhibited the greatest energy absorption (335.59×10^{-3} J). ANOVA confirmed that cell size significantly influenced tensile strength, whereas geometric orientation had a greater impact on energy absorption. This study contributes to optimizing three-dimensional (3D) printing parameters for enhanced mechanical performance and provides insights for designing lightweight, high-strength structures in aerospace and structural applications.

Taguchi Yöntemi ile 3B Baskılı PETG Bal Peteği Yapılarında Çekme Özelliklerinin Optimizasyonu: Hücre Boyutu ve Geometrik Yönelimin Etkisi

ÖZ

Bal peteği yapıları, yüksek mukavemet/ağırlık oranı, enerji sönümlenme kapasitesi ve özelleştirilebilir mekanik davranışları nedeniyle mühendislik uygulamalarında yaygın olarak kullanılmaktadır. Ancak, çekme dayanımının optimize edilmesi halen önemli bir araştırma konusudur. Bu çalışma, hücre boyutu (1.75 mm, 1.5 mm, 1.25 mm) ve geometrik yönelim (0°, 15°, 30°) değişkenlerinin, EYM yöntemiyle üretilen PETG bal peteği yapılarının çekme mekanik özellikleri üzerindeki etkisini sistematik olarak incelemektedir. Toplamda dokuz farklı numune üretilmiş ve ASTM D638 standardına uygun olarak test edilmiştir. Taguchi sinyal-gürültü (S/N) oranı analizi ile optimum parametreler belirlenmiş, Varyans Analizi (ANOVA) ile istatistiksel değerlendirme yapılmıştır. Sonuçlar, 1.25 mm hücre boyutu ve 30° yönelime sahip yapıların en yüksek kırılma kuvvetine (277.03 N) ulaştığını, 1.75 mm hücre boyutu ve 30° yönelimdeki numunelerin ise en yüksek enerji sönümlenme kapasitesine (335.59×10^{-3} J) sahip olduğunu göstermektedir. ANOVA analizleri, hücre boyutunun çekme dayanımı üzerinde önemli bir etkiye sahip olduğunu, geometrik yönelimin ise enerji sönümlenme kapasitesini daha fazla etkilediğini doğrulamıştır. Bu çalışma, üç boyutlu (3D) baskı parametrelerinin mekanik performans açısından optimize edilmesine katkı sağlamakta ve havacılık ile yapısal uygulamalar için hafif ve yüksek dayanımlı yapıların tasarımına yönelik önemli bilgiler sunmaktadır.

Anahtar Kelimeler: Bal peteği yapıları, EYM, Taguchi yöntemi, PETG, Mekanik özellikler

1. Introduction

The growing need for lightweight to high strength materials in aerospace, automotive, biomedical, and structural applications has driven significant interest in honeycomb structures. These structures provide exceptional mechanical properties such as a high strength to weight ratio, superior energy absorption, and customizable deformation behavior [1]. Advances in additive manufacturing (AM), especially Fused Deposition Modeling (FDM), have enabled the precise fabrication of intricate honeycomb geometries using various thermoplastic materials [2]. Among these, polyethylene terephthalate glycol-modified (PETG) is a popular choice due to its excellent balance of mechanical performance, durability, and printability [3]. However, the performance of 3D-printed honeycomb structures is highly dependent on cell size, geometric orientation, and printing parameters, which remain an open field of optimization. Optimizing these parameters is crucial for ensuring reliable mechanical performance while minimizing material waste and production time. By employing the Taguchi optimization method, this research seeks to systematically explore the influence of cell size and geometric orientation on the tensile behavior of PETG honeycomb structures, thereby providing valuable insights for performance-driven design improvements [4].

A honeycomb structure consists of a periodic arrangement of hollow cells, typically hexagonal, rectangular, or auxetic in shape, designed to optimize mechanical properties while minimizing material usage [5]. Fused Deposition Modeling (FDM) is an additive manufacturing technique that extrudes thermoplastic filaments layer-by-layer to create 3D-printed objects. PETG is a widely used polymer in FDM printing due to its high impact resistance, ductility, and chemical resistance compared to other common materials such as PLA and ABS [6]. The Taguchi optimization method is a statistical approach used to determine the most influential parameters affecting product performance while reducing experimental iterations [7].

Numerous studies have investigated the mechanical behavior of honeycomb structures manufactured using 3D printing. Recent advancements focus on understanding how geometric variations, printing orientation, and cell design affect mechanical properties, since gaps remain in systematically optimizing these parameters for tensile performance [8]. Several research efforts have explored the effects of honeycomb geometry and printing parameters. Studies have found that hexagonal honeycombs offer superior mechanical properties compared to square or triangular designs due to their higher in-plane stiffness and energy absorption capacity [9]. Other studies indicate that the orientation of printed layers significantly impacts mechanical strength, with vertical and diagonal orientations often displaying lower strength due to weak interlayer adhesion [10]. PETG has gained attention as a favorable material due to its higher ductility and impact resistance compared to PLA and ABS, making it appropriate for high performance applications [11]. The use of optimization methodologies, including statistical and computational approaches, has shown potential in improving honeycomb structure performance [12]. Taguchi and response surface methodologies have been applied in optimizing 3D-printing parameters, particularly for impact and compressive strength [13]. Moreover, several computational and experimental studies have examined the mechanical performance of honeycomb structures. Finite Element Analysis (FEA) models have been developed to predict compressive and bending behavior of different honeycomb cell configurations [14]. Experimental studies have explored the anisotropic mechanical properties of FDM-printed structures with varying infill densities and orientations [15]. FFT-based modeling techniques have also been proposed to enhance the predictive accuracy of in plane elastic properties of honeycomb structures beneath large elastic deformations [16]. Recent advancements in integrating machine learning and AI-based models have enhanced mechanical prediction accuracy of honeycomb structures [12]. However, while these studies provide valuable insights, the impact of cell size and geometric orientation on tensile properties remains underexplored. Moreover, a few studies have employed robust optimization techniques such as Taguchi methods to fine-tune design parameters for optimal tensile strength [17]. Despite the extensive research on honeycomb structures and their mechanical properties, several gaps and limitations persist. Most studies focus on compressive or bending performance, neglecting tensile properties, which are critical in structural applications [18]. There has been limited investigation on the combined effects of cell size and geometric orientation in PETG honeycombs [19]. Few studies have

employed systematic optimization using the Taguchi method for enhancing tensile performance. Challenges remain in accurately modeling the anisotropic behavior of FDM-printed structures due to interlayer adhesion issues and print-induced defects [20]. In addition, the thermo-mechanical interactions in honeycomb materials require further modeling efforts [21]. Recent studies have explored bioinspired functionally graded honeycomb structures, revealing promising impact resistance properties [22]. Moreover, efforts to enhance energy absorption capabilities in honeycomb structures are ongoing, especially for corrugated honeycomb aluminum designs [23]. These limitations highlight the need for an optimized approach to improve the tensile behavior of PETG honeycomb structures, guiding the development of lightweight to high-strength materials.

This research aims to examine the effect of honeycomb cell size and geometric orientation on the tensile properties of 3D-printed PETG structures. The research employs the Taguchi optimization method to determine the most influential parameters for maximizing tensile strength. Furthermore, the study provides experimental validation and statistical analysis to guide optimal design configurations for PETG honeycomb-based applications. This investigation is particularly significant for its originality, as it is among few to investigate the impact and optimization of geometric orientation and cell size on the tensile mechanical properties of FDM-printed PETG honeycomb structures. Consequently, 9 distinct specimens were fabricated utilizing 3 different cell sizes (1,25 mm, 1,5 mm, 1.75 mm) and 3 different geometric orientations (0° , 15° , and 30°) through the FDM technique using the same PETG material. The Taguchi method was utilized to optimize the maximum fracture force and energy absorption by determining the optimum combination of cell size and geometric orientation. The results were additionally examined utilizing analysis of variance (ANOVA). This study aimed to address a gap in literature by investigating the tensile properties of honeycomb structures printed using FDM-printed PETG.

2. Material And Method

2.1. Design of honeycomb structure

The ASTM D638-14 standards employed a dog-bone-shaped specimen with appropriately placed honeycomb structures within the testing section for the tension test [24]. Specimen dimensions were obtained from a Type IV model, as shown in Figure 1, and SolidWorks software was chosen to create the computer-aided design (CAD) shape.

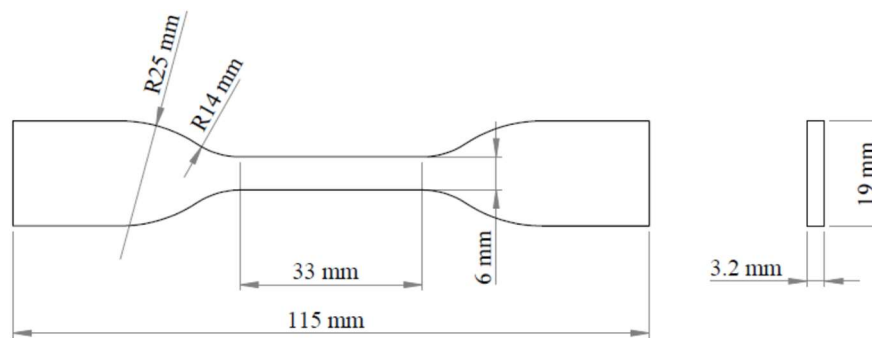


Figure 1. The geometry of the experimental specimen, based on ASTM D638-14 standards.

The tensile test specimens had a thickness of 0.6 mm (2h) and were designed to accommodate 2, 3, and 4 honeycomb unit cells, as illustrated in Figure 2, within the 6 mm width of the test zone in the 0° geometric orientation. Consequently, cell sizes (c) of 1.75 mm, 1.5 mm, and 1.25 mm were selected based on minimum and maximum value constraints, considering both design objectives and manufacturability. Additionally, geometric orientation values of 0° , 15° , and 30° were chosen within the specified range of minimum, maximum, and average values.

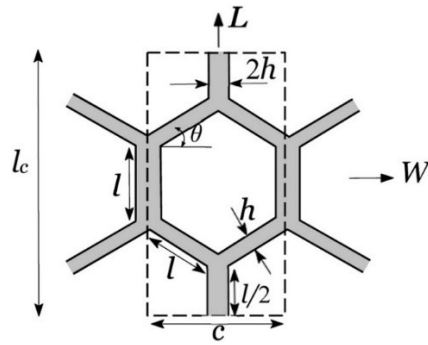


Figure 1. The unit cell of the honeycomb structure.

These cells were then rotated by 15° and 30° and placed in the test area and then the geometric orientations of the honeycomb structures were designed using SolidWorks software as shown in Figure 3, resulting in three distinct plans (0° , 15° , 30°).

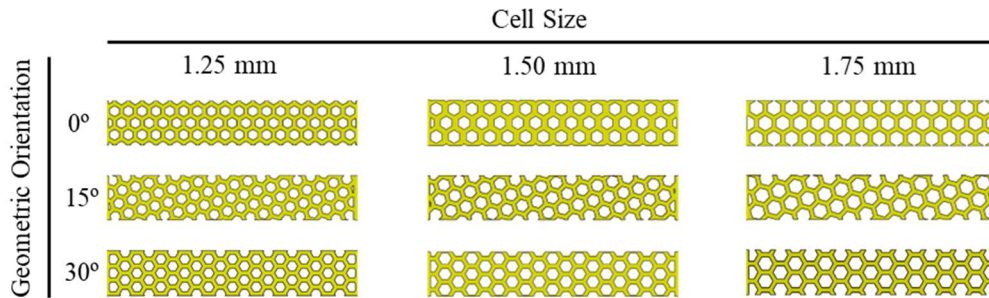


Figure 2. Designs of the test areas of the tensile specimens.

2.2. Manufacturing test specimens

The honeycomb structures were first saved as STL files and then imported into the Ultimaker Cura slicing software to define the print settings and optimize the arranging of the specimens on the build plate. The specimens were fabricated using polyethylene terephthalate glycol (PETG) filament with a Creality Ender 3 Pro 3D printer. The study followed the recommended print settings for PETG, specifically a layer height of 0.2 mm, a speed of print is 50 mm/s, a lines infill pattern, and an infill density of 25%. Figure 4 presents images of the fabricated specimens in the test area.

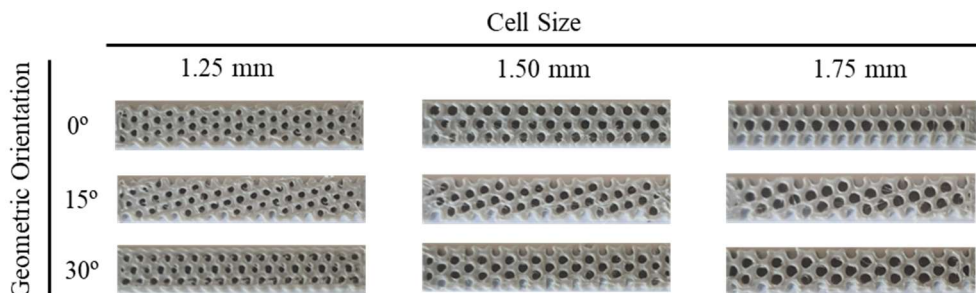


Figure 3. Images of the test areas of the manufactured tensile specimens.

In accordance with the principles of Design of Experiments (DOE) methodology, a total of nine distinct specimens were manufactured, as shown in Figure 5. To minimize the influence of random error sources and variability, three specimens were produced for each sample.

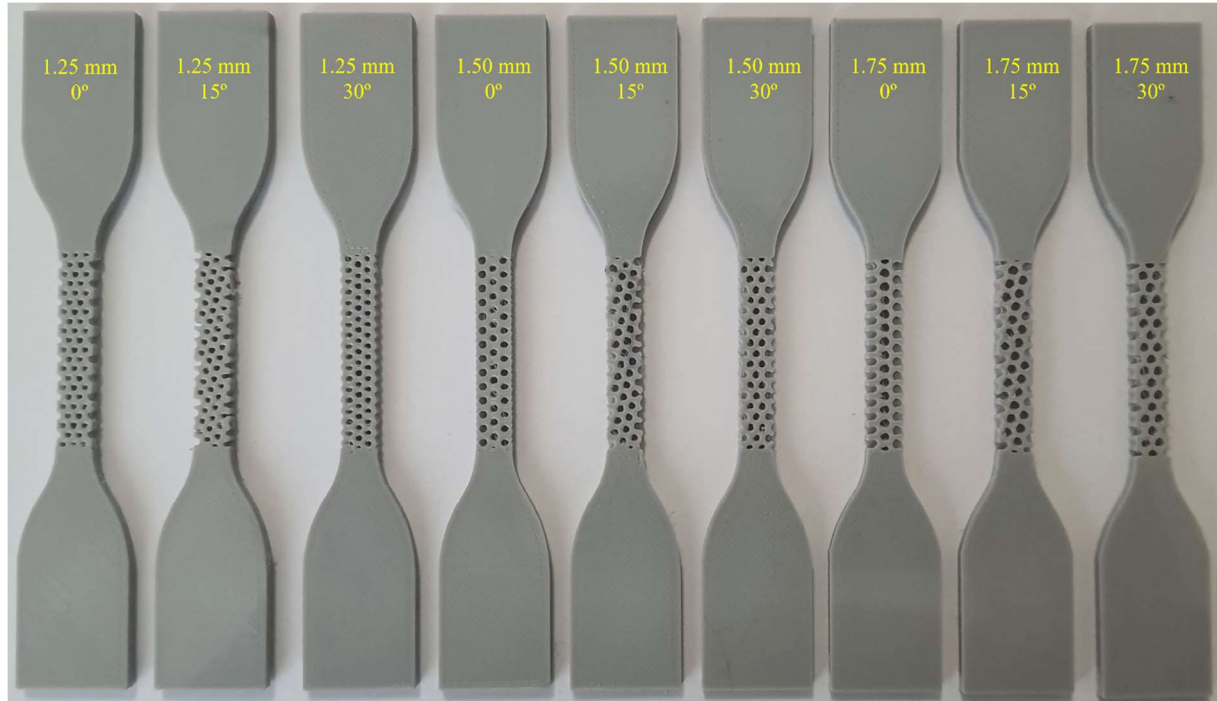


Figure 4. 3d printed tensile specimens.

2.3. Tensile Test

The tensile test was accomplished utilizing a Shimadzu Autograph universal testing machine in compliance with the ASTM D638 standard. The displacement rate was adjusted at 5 mm/min, and the specimens were subjected to a gradually increasing load until failure. Load and displacement data were systematically recorded during the experiment and subsequently analyzed to determine the mechanical properties. A representative tensile test specimen is shown in Figure 6.



Figure 6. A specimen of the tensile test.

2.3. Optimization

The Taguchi method offers a statistically robust approach that facilitates the identification of optimal operating conditions while reducing the number of required experiments, thus reducing both the time and cost associated with experimental investigations [25]. A major advantage of this method is its use of orthogonal arrays for experimental design, which not only simplifies the planning process but also accounts for uncontrolled variables commonly referred to as noise factors that contribute to variability.

In this study, a full factorial design was employed, incorporating two factors at three levels each, to systematically explore their interactions and effects on a specified response variable [26]. The primary factors influencing force at break and energy absorption were identified as the dimensions and orientations of the honeycomb structures. Table 1 presents these factors alongside their respective levels.

Table 1. Taguchi L9 orthogonal array.

Factors	Levels		
	1.75 mm	1.5 mm	1.25 mm
Cell size	1.75 mm	1.5 mm	1.25 mm
Geometric orientation	0°	15°	30°

To optimize the experimental design, Taguchi's L9 orthogonal array was chosen. The experimental setup was designed using Minitab's L9 Taguchi orthogonal array, facilitating the generation of main effects plots for the signal-to-noise (S/N) ratio related to mechanical properties. Given that the primary objective of this study was to enhance tensile strength specifically, force at break and energy absorption the "larger-is-better" criterion was applied in accordance with Equation (1).

$$S/N = -10 \log_{10} \left[\frac{1}{n} \sum_{i=1}^n \frac{1}{y_i^2} \right] \quad (1)$$

3. Results and Discussion

This section analyzes the mechanical performance of three individual honeycomb structures with varying geometric orientations, as determined through tensile testing. The tensile tests were conducted to evaluate the force at break and absorbed energy, with each measurement averaged across multiple specimens. The mean values, along with their standard deviations, are presented in Table 2. The results indicate that the highest force at break was recorded at 277.03 N in run 9, whereas the lowest value was observed in run 1 at 128.43 N. Similarly, absorbed energy varied across the samples, with run 3 exhibiting the highest value of 335.59×10^{-3} J and run 5 the lowest at 151.95×10^{-3} J. Based on these findings, the optimal combination of cell size and geometric orientation for maximizing both force at break and absorbed energy is 1.25 mm and 30°, respectively, yielding values of 277.03×10^{-3} J and 288.47×10^{-3} J. In order to further improve the clarity and interpretability of the results, descriptive statistical data are presented in Table 2. These data include the minimum and maximum values, mean values, and standard deviations for each test run.

Table 2. Results of the tensile test.

Run	Cell size	Geometric orientation	Force (N)	Energy (x10-3 J)
1	1.75 mm	0°	128.43	165.64
2	1.75 mm	15°	137.10	200.69
3	1.75 mm	30°	164.06	335.59
4	1.50 mm	0°	143.75	272.74
5	1.50 mm	15°	141.66	151.95
6	1.50 mm	30°	146.87	130.26
7	1.25 mm	0°	253.62	220.26
8	1.25 mm	15°	169.732	152.74
9	1.25 mm	30°	277.03	288.47

Figure 7 illustrates the force-displacement curves obtained from tensile tests conducted on specimens with honeycomb cell orientations of 0°, 15°, and 30°, across three different cell sizes within the test area: 1.75 mm, 1.5 mm, and 1.25 mm. For the 1.75 mm cell size configuration, the 30° orientation exhibited the highest force resistance, whereas the 0° and 15° orientations demonstrated lower force responses. Notably, the 15° orientation experienced structural failure at an elongation of approximately 1.68 mm. In the 1.50 mm cell size configuration, the 30° orientation continued to show the highest force at break. The 0° and 15° orientations followed trends similar to those observed in the 1.75 mm configuration, displaying a gradual increase in force until failure; however, in this case, their force values were closer to the 30° orientation. The overall force capacity in this configuration exceeded that of the 1.75 mm cell size, indicating that increasing the number of cells enhances the structural strength of the specimen. The 1.25 mm cell size configuration maintained this trend, with the 30° orientation again exhibiting the highest force resistance, reaching a peak force of approximately 290 N. This suggests that reducing the cell size results in a structure with greater strength and stiffness. The 0° and 15° orientations demonstrated comparable behavior, though they exhibited slightly higher force values prior to yielding compared to the larger cell size configurations.

Figure 8 illustrates the force-displacement curves obtained from tensile tests performed on specimens with varying geometric orientations of 0°, 15°, and 30°. Each graph presents a comparative analysis of three different cell size configurations: 1.75 mm, 1.50 mm, and 1.25 mm. In the 0° geometric orientation, the specimen with a 1.25 mm cell size exhibits the highest force capacity, followed by the 1.50 mm and 1.75 mm configurations, which display similar values. This observation aligns with findings in the existing literature, which suggest that specimens with smaller cell sizes can endure greater forces before structural failure [23]. The force-displacement curve for the 1.25 mm configuration shows a significant increase in force, indicative of a stronger material response, whereas the 1.75 mm configuration exhibits a comparatively lower force resistance. For the 15° geometric orientation, the force capacities of all three cell sizes are closely aligned, in contrast to the more pronounced differences observed in the 0° and 30° orientations. This behavior is unique and noteworthy from a structural perspective. Nonetheless, the 1.25 mm cell size configuration continues to demonstrate the highest force resistance. While the displacement at failure remains consistent across configurations, it is slightly lower than that observed in the 0° orientation. In the 30° geometric orientation, the specimen with a 1.25 mm cell size once again exhibits the highest force capacity, followed closely by the 1.75 mm configuration. In contrast, the 1.50 mm cell size displays the lowest force resistance, showing a significant difference compared to the other configurations. The displacement patterns in this orientation resemble those observed in the 0° configuration. This suggests that the material maintains its structural integrity in the 30° orientation almost as effectively as in the 0° orientation.

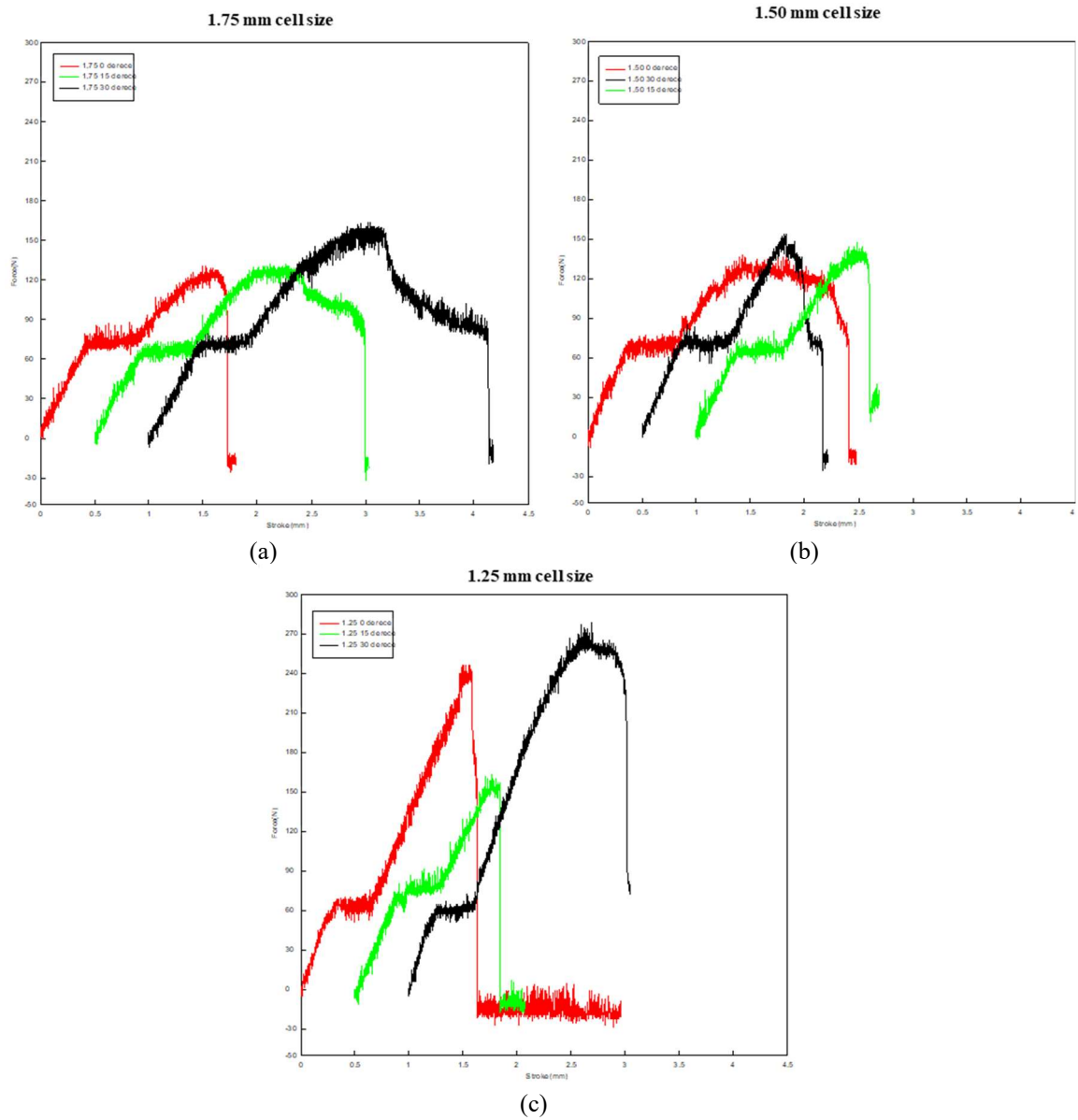


Figure 5. Force-displacement curves of tensile specimens containing different cell sizes in the test area (a) 1.75 mm, (b) 1.50 mm and (c) 1.25 mm.

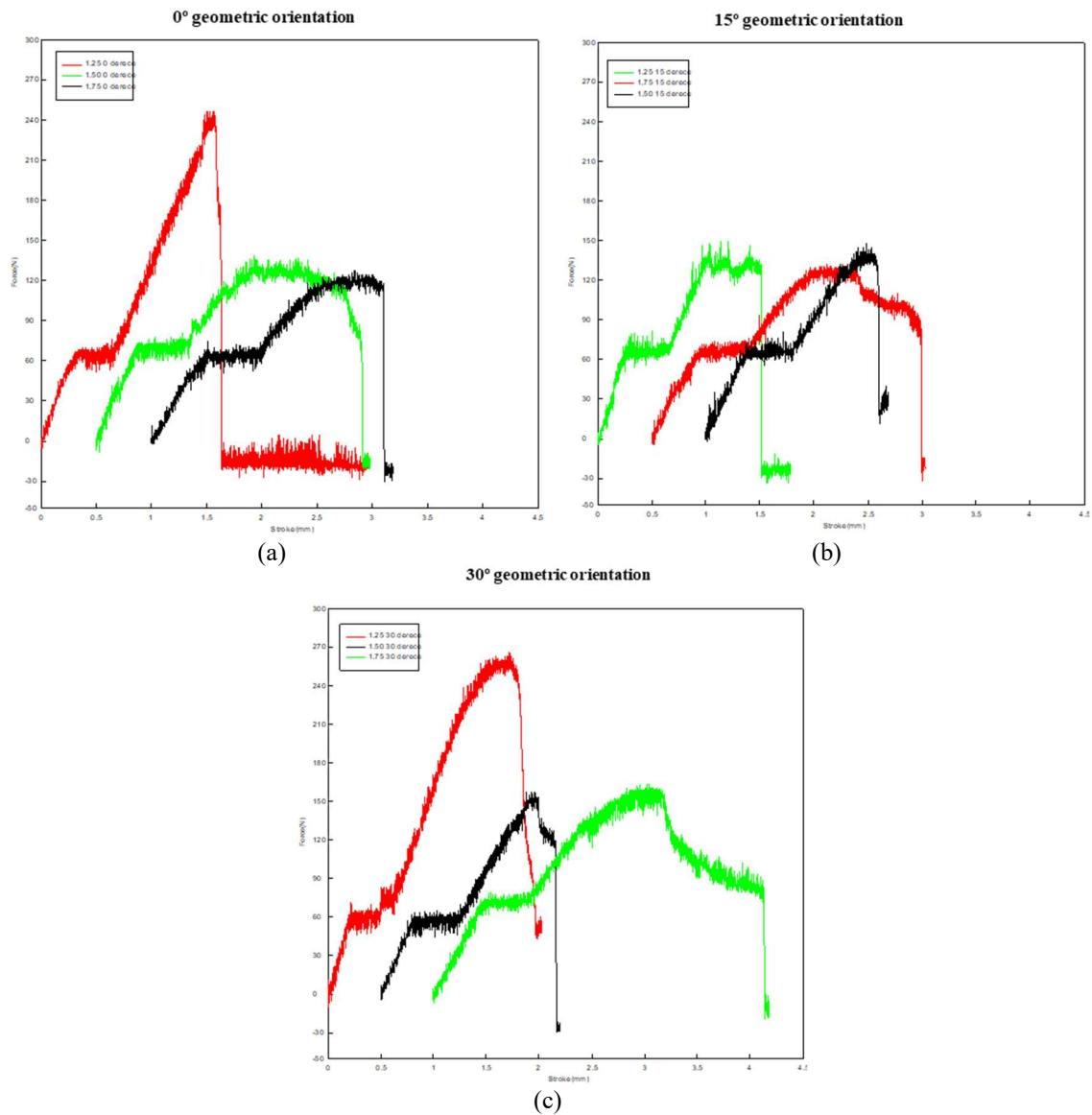


Figure 6. Force-displacement curves of tensile specimens containing different geometric orientations in the test area (a) 0°, (b) 15° and (c) 30°.

Table 3 shows that the influence of cell size and geometric orientation of the honeycomb structure on force at break and absorbed energy. As seen in the table, while cell size is 69.53% on force at break, it's only 9.38% on absorbed energy. And also, for geometric orientation, there is reverse contribution on force at break and absorbed energy. Geometric orientation effect is 14.03% whereas it is significantly higher than in absorbed energy as 25.68%. Most models with P-values above 0.05 are worthless, but a component with a P-value below 0.05 definitely influenced the final model [27,28]. The P-values are below 0.05 only on the effect of cell size on force at break within four values as indicated in Table 3. The cell size of the honeycomb structure has a P value higher than 0.05 for absorbed energy. However geometric orientation of the honeycomb structure has a P-value higher than 0.05 both on force at break and absorbed energy. As with different porous structures [29], for honeycomb structure, cell size is an important determinant for the force at break. Additionally, a computational technique for model validation has made use of the coefficient of determination R^2 . A strong correlation between experimental results and model predictions is indicated by R^2 values near to 1 [30]. The fact that the P values for both cell size and geometric orientation exceed 0.05, combined with the R^2 value remaining at approximately 35%, indicates a weak predictive relationship. Since this R^2 value is significantly lower than the generally accepted threshold of 85%, it suggests that these parameters do not provide a reliable basis for accurately estimating the absorbed energy of honeycomb cells printed using the FDM method with

PETG. Table 3 shows that the model's accuracy is indicated by the R2 values for force at break (83.56%) and absorbed energy (35.06%).

Table 3. ANOVA for force at break and absorbed energy.

Source	Force at break			Absorbed energy		
	DF	Contribution	P-value	DF	Contribution	P-value
Cell size	2	69.53%	0.037	2	9.38%	0.763
Geometric orientation	2	14.03%	0.291	2	25.68%	0.514
Error	4	16.44%		4	64.94%	
Total	8	100%		8	100%	
R2		83.56%			35.06%	

Figure 9 presents two main effects plots illustrating the impact of cell size and shape orientation on signal-to-noise (S/N) ratios for specific performance metrics. In S/N ratio figures, the highest S/N ratio results in the most optimal settings for operational parameters. In subplot (a), the plot shows S/N ratios for force at break, with distinct trends for each factor. For cell size, the S/N ratio increases as cell size decreases, suggesting that a smaller cell size positively influences the force at break, enhancing the system's robustness to noise. Regarding geometric orientation, a significant variation is observed. An orientation of 15° results in a reduction in the S/N ratio, while orientations of 0° and 30° yield higher ratios, with 30° achieving the highest value. This trend implies that aligning shape orientation to 30° could help optimize force at break. Subplot (b) displays the mean values for absorbed energy across the same factor levels. For cell size, a significant variation is observed again. An orientation of 1.50 mm results in a reduction in the S/N ratio, while orientations of 1.75 mm and 1.25 mm yield higher ratios, with 1.75 mm achieving the highest value. For geometric orientation, the relationship is again non-linear like cell size. An orientation of 15° leads to notably lower means absorbed energy, whereas an orientation of 30° yields the highest mean value. This observation is consistent with the literature, demonstrating that geometric orientation significantly influences energy absorption capacity [31,32].

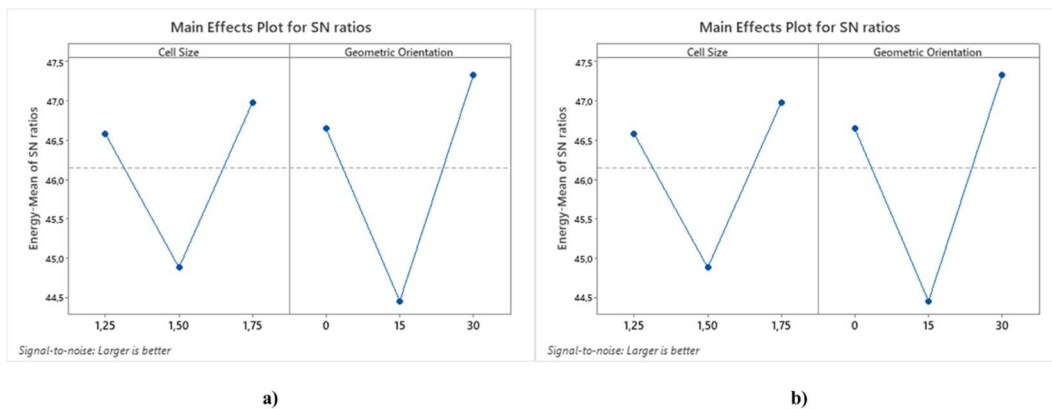


Figure 7. S/N ratios of factor levels for (a) force at break and (b) absorbed energy.

4. Conclusions

This study examines the tensile mechanical characteristics of honeycomb structures manufactured with varying cell sizes and geometric orientations, comparing them to specimens fabricated through FDM method using PETG material. The objective of the research was to identify the cell sizes and geometric orientations that yield the highest fracture force and energy absorption. During the production process, configurations with cell sizes of 1.75 mm, 1.5 mm, and 1.25 mm, as well as geometric orientations of 0°, 15°, and 30°, were evaluated. The findings are summarized as follows:

- The highest fracture force (277.03 N) was achieved with a 1.25 mm cell size and a 30° geometric orientation, while the highest energy absorption (335.59 J) was observed in 1.75 mm cell size and a 30° orientation.
- The lowest fracture force (128.43 N) was recorded for the 1.75 mm cell size at a 0° orientation, whereas the lowest energy absorption (151.95 J) was measured in the 1.50 mm cell size at a 15° orientation.
- Cell size accounted for 69.53% of the variation in fracture force, while geometric orientation contributed 25.68% to energy absorption.
- The influence of cell size on both fracture force and energy absorption was greater than geometric orientation.

A systematic evaluation of these parameters enables the advancement and optimization of engineering systems that incorporate honeycomb-structured materials for enhanced performance. The findings from this study hold significant potential for applications in aerospace manufacturing, medical device development, protective equipment, and various other industries where high force resistance, energy absorption, adaptability, and mechanical durability are critical.

This study provides valuable insights; however, it is limited by the specific material, manufacturing parameters, and testing conditions. Future research could expand on these findings by exploring additional variables and employing computational methods to enhance applicability and robustness.

Conflict of Interest Statement

The authors declare that there is no conflict of interest.

References

- [1] X. Zhou, L. Ren, Z. Song, and others, "Advances in 3D/4D printing of mechanical metamaterials: From manufacturing to applications," *Composites Part B*, vol. 254, p. 110585, 2023. doi: 10.1016/j.compositesb.2023.110585
- [2] J. Fan et al., "A review of additive manufacturing of metamaterials and developing trends," *Materials Today*, vol. 50, pp. 303–328, 2021. doi: 10.1016/j.mattod.2021.04.019
- [3] Y. Garbatov, S. S. Marchese, G. Epasto, and V. Crupi, "Flexural response of additive-manufactured honeycomb sandwiches for marine structural applications," *Ocean Engineering*, vol. 302, p. 117732, 2024. doi: 10.1016/j.oceaneng.2024.117732
- [4] J. Zhang, G. Lu, and Z. You, "Large deformation and energy absorption of additively manufactured auxetic materials and structures: A review," *Compos B Eng*, vol. 201, p. 108340, 2020. doi: 10.1016/j.compositesb.2020.108340
- [5] C. Qi, F. Jiang, and S. Yang, "Advanced honeycomb designs for mechanical properties: A review," *Composites Part B*, vol. 227, p. 109393, 2021. <https://doi.org/10.1016/j.compositesb.2021.109393>. doi: 10.1016/j.compositesb.2021.109393
- [6] G. Palomba, G. Epasto, L. Sutherland, and V. Crupi, "Aluminium honeycomb sandwich as a design alternative for lightweight marine structures," *Ships and Offshore Structures*, vol. 17, pp. 2355–2366, 2022. doi: 10.1080/17445302.2021.1996109
- [7] S. L. Omairey, P. D. Dunning, and S. Sriramula, "Development of an ABAQUS plugin tool for periodic RVE homogenisation," *Eng Comput (Swansea)*, vol. 35, pp. 567–577, 2019. doi: 10.1007/s00366-018-0616-4
- [8] F. Pehlivan, F. H. Öztürk, S. Demir, and A. Temiz, "Optimization of functionally graded solid-network TPMS meta-biomaterials," *J Mech Behav Biomed Mater*, vol. 157, p. 106609, 2024. doi: 10.1016/j.jmbbm.2024.106609
- [9] G. Sun, X. Huo, H. Wang, and others, "On the structural parameters of honeycomb-core sandwich panels against low-velocity impact," *Composites Part B*, vol. 216, p. 108881, 2021. doi: 10.1016/j.compositesb.2021.108881
- [10] Z. Huang, X. Zhang, and C. Yang, "Experimental and numerical studies on the bending collapse of multi-cell Aluminum/CFRP hybrid tubes," *Composites Part B*, vol. 181, p. 107527, 2020. doi: 10.1016/j.compositesb.2019.107527

- [11] A. Singh, B. Koohbor, and G. Youssef, "Full-field characterizations of additively manufactured composite cellular structures," *Composites Part B*, vol. 272, p. 111208, 2024. doi: 10.1016/j.compositesb.2024.111208
- [12] X. Zheng, T. Chen, X. Jiang, and others, "Deep-learning-based inverse design of three-dimensional architected cellular materials with the target porosity and stiffness using voxelized Voronoi lattices," *Sci Technol Adv Mater*, vol. 24, p. 2157682, 2023. doi: 10.1080/14686996.2022.2157682
- [13] P. Nampally, A. T. Karttunen, and J. N. Reddy, "Nonlinear finite element analysis of lattice core sandwich plates," *Int J NonLinear Mech*, vol. 121, p. 103423, 2020. doi: 10.1016/j.ijnonlinmec.2020.103423
- [14] H. Yang, Z. Liu, Y. Xia, and others, "Mechanical properties of hierarchical lattice via strain gradient homogenization approach," *Composites Part B*, vol. 271, p. 111153, 2024. doi: 10.1016/j.compositesb.2023.111153
- [15] L. Mizzi, D. Attard, R. Gatt, and others, "Implementation of periodic boundary conditions for loading of mechanical metamaterials using finite element analysis," *Eng Comput (Swansea)*, vol. 37, pp. 1765–1779, 2021. doi: 10.1007/s00366-019-00910-1
- [16] Z. Zhao, C. Liu, X. Xu, L. Sun, J. Wang, Y. Li, "An FFT-based method for estimating the in-plane elastic properties of honeycomb considering geometric imperfections at large elastic deformation," *Thin-Walled Structures*, vol. 185, p. 110570, 2023. doi: 10.1016/j.tws.2023.110570
- [17] A. F. Yilmaz and M. Konal, "Enhanced Container Ship Hatch Cover using Topology Optimization Method for Lightweight Design and Optimal Costs," *Journal of Offshore Mechanics and Arctic Engineering*, pp. 1–16, 2025. doi: 10.1115/1.4067799
- [18] T. Wu, M. Li, X. Zhu, and X. Lu, "Research on non-pneumatic tires with gradient anti-tetrachiral structures," *Mechanics of Advanced Materials and Structures*, vol. 28, pp. 2351–2359, 2021. doi: 10.1080/15376494.2020.1734888
- [19] S. Liu, F. Zhang, B. Chao, and others, "Based on the preparation of dual-absorber agents using Ni and Ni/rGO for the fabrication of a dual honeycomb nested structure for wideband microwave absorption," *Composites Part B*, vol. 284, p. 111735, 2024. doi: 10.1016/j.compositesb.2024.111735
- [20] X. Zhang, L. Zhang, and P. Zhang, "Equivalent constitutive equations of honeycomb material using micro-polar theory to model thermo-mechanical interaction," *Composites Part B*, vol. 43, pp. 3081–3087, 2012. doi: 10.1016/j.compositesb.2012.04.056
- [21] Y. Le, N. S. Ha, and N. S. Goo, "Advanced sandwich structures for thermal protection systems in hypersonic vehicles: A review," *Composites Part B*, vol. 226, p. 109301, 2021. doi: 10.1016/j.compositesb.2021.109301
- [22] C. Peng and P. Tran, "Bioinspired functionally graded gyroid sandwich panel subjected to impulsive loadings," *Composites Part B*, vol. 188, p. 107773, 2020. doi: 10.1016/j.compositesb.2020.107773
- [23] X. Xing, S. Yang, S. Lu, and others, "Energy absorption and optimization of bi-directional corrugated honeycomb aluminum," *Composites Part B*, vol. 219, p. 108914, 2021. doi: 10.1016/j.compositesb.2021.108914
- [24] F. Pehlivan, "Optimizing 3D-Printed Auxetic Structures for Tensile Performance: Taguchi Method Application on Cell Size and Shape Orientation," *Manufacturing Technologies and Applications*, vol. 5, no. 3, pp. 284–294, 2024. doi: 10.52795/mateca.1576416
- [25] S. Demir, A. Temiz, and F. Pehlivan, "The investigation of printing parameters effect on tensile characteristics for triply periodic minimal surface designs by Taguchi," *Polym Eng Sci*, vol. 64, no. 3, pp. 1209–1221, 2024. doi: 10.1002/pen.26608
- [26] N. Ben Ali, M. Khelif, D. Hammami, and C. Bradai, "Experimental optimization of process parameters on mechanical properties and the layers adhesion of 3D printed parts," *J Appl Polym Sci*, vol. 139, no. 9, p. 51706, 2022. doi: 10.1002/app.51706
- [27] F. H. Öztürk, "Optimization of adherend thickness and overlap length on failure load of bonded 3D printed PETG parts using response surface method," *Rapid Prototyp J*, vol. 30, no. 8, pp. 1579–1591, 2024. doi: 10.1108/RPJ-02-2024-0090
- [28] A. F. Yilmaz, "Assessment of Combinability of S235JR-S460MC Structural Steels on Fatigue Performance," *Transactions of the Indian Institute of Metals*, vol. 77, no. 2, pp. 323–331, Feb. 2024. doi: 10.1007/s12666-023-03113-x
- [29] P. Wang, Y. Bian, F. Yang, H. Fan, and B. Zheng, "Mechanical properties and energy absorption of FCC lattice structures with different orientation angles," *Acta Mech*, vol. 231, pp. 3129–3144, 2020. doi: 10.1007/s00707-020-02710-x
- [30] A. Temiz, "The Effects of Process Parameters on Tensile Characteristics and Printing Time for Masked Stereolithography Components, Analyzed Using the Response Surface Method," *J. of Materi Eng and Perform.*, vol. 33, pp. 9356–9365, 2024. doi: 10.1007/s11665-023-08617-7

[31] M. Günay, S. Gündüz, H. Yılmaz, N. Yaşar, and R. Kaçar, "PLA Esaslı Numunelerde Çekme Dayanımı İçin 3D Baskı İşlem Parametrelerinin Optimizasyonu," *Politeknik Dergisi*, vol. 23, no. 1, pp. 73–79, Mar. 2020. doi: 10.2339/politeknik.422795

[32] M. Xu, Z. Xu, Z. Zhang, H. Lei, Y. Bai, and D. Fang, "Mechanical properties and energy absorption capability of AuxHex structure under in-plane compression: Theoretical and experimental studies," *Int J Mech Sci*, vol. 159, pp. 43–57, 2019. doi: 10.1016/j.ijmecsci.2019.05.044

This is an open access article under the CC-BY license

